



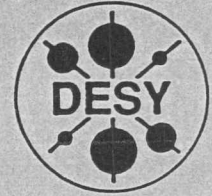
\*X1998-00736\*

DEUTSCHES ELEKTRONEN-SYNCHROTRON

DESY-THESIS-1998-007

RAL-TH-97-004

April 1998

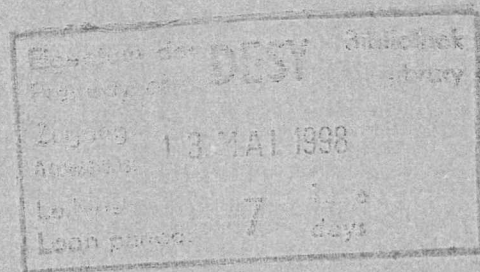


*C.P.*

Measurement and QCD Analysis of  
the Proton Structure Function  $F_2$   
from the 1994 HERA Data  
Using the ZEUS Detector

by

A. Quadt



ISSN 1435-8085

NOTKESTRASSE 85 - 22603 HAMBURG

DESY behält sich alle Rechte für den Fall der Schutzrechtserteilung und für die wirtschaftliche Verwertung der in diesem Bericht enthaltenen Informationen vor.

DESY reserves all rights for commercial use of information included in this report, especially in case of filing application for or grant of patents.

To be sure that your reports and preprints are promptly included in the  
HEP literature database  
send them to (if possible by air mail):

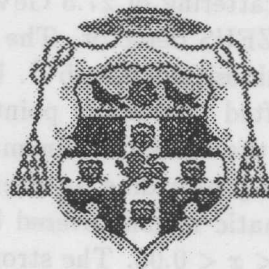
DESY  
Zentralbibliothek  
Notkestraße 85  
22603 Hamburg  
Germany

DESY  
Bibliothek  
Platanenallee 6  
15738 Zeuthen  
Germany

Measurement and QCD Analysis of  
the Proton Structure Function  $F_2$   
from the 1994 HERA Data  
using the ZEUS Detector.

Arnulf Quadt ✓

Christ Church  
University of Oxford



Thesis submitted in partial fulfilment  
of the requirements for the degree of  
Doctor of Philosophy

University of Oxford, Michaelmas Term 1996

# Measurement and QCD Analysis of the Proton Structure Function $F_2$ from the 1994 HERA Data using the ZEUS Detector.

Arnulf Quadt

Christ Church, University of Oxford

Thesis submitted in partial fulfilment of the  
requirements for the degree of Doctor of Philosophy.

University of Oxford, Michaelmas Term 1996

## Abstract

The proton structure function  $F_2(x, Q^2)$  has been measured in neutral current deep inelastic scattering of 27.5 GeV electrons and 820 GeV protons at the HERA collider using the ZEUS detector. The data sample, collected in 1994, corresponds to an integrated luminosity of  $2.4 \text{ pb}^{-1}$ . By using a new kinematic reconstruction method, events with a shifted interaction point and events with collinear photon radiation in the initial state, the accessible kinematic region is extended down to  $Q^2$  as low as  $1.5 \text{ GeV}^2$  and to low  $y$  providing an overlap with measurements from fixed target experiments. The kinematic region covered by these measurements is  $1.3 < Q^2 < 15000 \text{ GeV}^2$  and  $2.8 \cdot 10^{-5} < x < 0.08$ . The strong rise of  $F_2$  with decreasing  $x$  persists to the lowest  $Q^2$  and becomes more pronounced as  $Q^2$  increases.

The data are shown to exhibit double logarithmic scaling in  $x$  and  $Q^2$ . The significance of this observation for unitarity bounds is discussed. The data are also shown to exhibit double asymptotic scaling. Based on this the strong coupling is determined to  $\alpha_s(M_z^2) = 0.115 \pm 0.002(\text{exp.}) \pm 0.006(\text{sys.}) \pm 0.009(\text{theor.})$  in next to leading order. Using the next to leading order Altarelli-Parisi evolution a QCD analysis of the  $F_2$  data is performed. The  $Q^2$  evolution of  $F_2$  is found to be consistent with perturbative QCD over the entire kinematic region. The gluon momentum distribution of the proton is extracted and found to rise strongly at small  $x$ .

## Acknowledgements

Quite a number of people helped me and gave me guidance during the last three years of my D.Phil. studies. I would like to take this opportunity to thank all of them.

First of all I am very grateful to my supervisor Prof. Robin C.E. Devenish, for his continuous support, encouragement, unwavering faith in me from the very beginning and his many words of wisdom. He has given me the freedom to study whatever my curiosity lead me to as well as the guidance I needed to finish my projects successfully. Particularly his inexhaustible patience in reading and commenting on all my reports and this thesis as well as the many conversations about physics were extremely helpful.

I am also very grateful to Dr. A.M.S. Cooper-Sarkar for enlightening discussions on theoretical aspects of DIS physics and for always being prepared to comment on my reports, notes and this thesis. Special thanks go to Prof. R.J.Cashmore for accepting me as a D.Phil. student despite the exceptional circumstances and also for numerous inspiring and stimulating discussions.

During the last year Dr. R.G. Roberts, who kindly provided me with his DGLAP evolution program, gave me a deeper insight into structure functions, QCD analyses and particle physics in general. Conversations with him always resulted in a much clearer picture of the theory and the enthusiasm to test it.

I gratefully acknowledge the help and support of the *Studienstiftung des deutschen Volkes* during my entire University education. It has been a pleasure to get to know Mrs. K. Schuster, who encouraged me to study at Oxford. I also thank Mrs. I. Czolbe and Dr. U. Lange for their far-sighted advice and non-bureaucratic help.

The work in the ZEUS collaboration and especially in the DIS group was an enjoyable experience. I thank the DIS-coordinators Prof. R.C.E. Devenish, Dr. A. Doyle, Prof. Dr. G. Wolf, Dr. E. Gallo and Dr. R. Yoshida for setting up such a friendly and fruitful atmosphere. They and also Prof. Dr. R. Klanner provided helpful comments and suggestions, thank you !

Many thanks go to Dr. A. Bargende, Dr. A. Byrne, Dr. J. Crittenden and Dr. M. Lancaster for introducing me to the exciting field of particle physics and the secrets of structure function measurements.

Not only in the context of these measurements the close collaboration with Dr. E. Barberis, Dr. F.S. Chlebana, Dr. A. Frey, Dr. L. Lindemann, Dr. M. Roco and Dr. M. Vreeswijk and helpful advice of Dr. S. Schlenstedt and Dr.habil. N. Pavel made my time in the  $F_2$ - and DIS-group most enjoyable and productive. I also thank the CTD-SLT experts Dr. H.A.J.R. Uijterwaal, S. Topp-Jørgensen and the ZEUS trigger experts Dr. R. Carlin, Dr. L. Wiggers, Prof. W. Smith and Dr. K. Tokushuku for demonstrating how successful proper teamwork can be.

I am very grateful to Mr. G. Bung, Mr. G.Danne, Prof. B. Foster, Prof. Dr. E. Hilger, Dr. U. Katz, Prof. Dr. M.J. Lentze and Prof. Dr. E. Lohrmann for awakening my serious interest in physics and mathematics and the invaluable advice and encouragement in scientific as well as administrative matters.

It is thanks to Dave Gilkinson, Olaf Manczak, Peter Grönbech, Ian McArthur and Dr. David Bailey, who kept ZARAH and the computer cluster in Oxford and Hamburg up and running, that I could torture these machines with my CPU intensive jobs and carry out my analyses.

I thank my ZEUS-UK colleagues for introducing me to their 'sense of humour' and the great time we had in Hamburg and Oxford.

The generous award of a 'Senior Scholarship' from *Christ Church* as well as financial support by the *British Chamber of Commerce in Germany* and the *German Academic Exchange Service (DAAD)* gave me the opportunity to concentrate on my research and these are most gratefully acknowledged.

That I did not get completely lost in the deep structure of the proton but also enjoyed life outside physics is thanks to the friendship of Dave and Susan Daniels, James and Sarah Tickner, Steve Campbell-Robson, Ulrich Münch, Olaf Ruske, Christian Tölkes, Nicola Stein, Christian Düsterberg, Thilo Michel, Thorsten Mausbach, Jens Müller, Heike Landfermann, Bianka Degen, Michael Fausten, Bert Kiel, Hans-Gerd Wolf, Frank Weigand, Jörg Gotzmann and many others.

Finally, I would like to express my gratitude to my parents and grandparents who have always been patient, loving, caring and understanding. They have always supported and encouraged me to make the most out of opportunities they never had. This thesis and work towards it would not have been possible without them.

THANK YOU !!!

# Contents

<b>Abstract</b>	<b>i</b>
<b>Acknowledgements</b>	<b>iv</b>
<b>Contents</b>	<b>vi</b>
<b>1 Introduction.</b>	<b>1</b>
<b>2 Deep-Inelastic Scattering.</b>	<b>3</b>
2.1 A Short Historical Review.	3
2.2 The DIS Variables	5
2.3 DIS Cross Section and Structure Functions.	7
2.4 The Naive Quark Parton Model.	9
2.5 Outline of QCD.	11
2.6 Factorisation.	13
2.7 The DGLAP Evolution.	15
2.8 The BFKL Equation.	17
2.9 Unifying DGLAP and BFKL.	18
2.10 Shadowing.	19
2.11 Modern Parametrisations of Parton Densities.	21
2.12 DIS Experiments.	24
<b>3 The ZEUS Detector at HERA.</b>	<b>26</b>
3.1 The HERA Accelerator.	26
3.2 The ZEUS Detector.	29
3.2.1 The Central Tracking Detector (CTD).	32
3.2.2 The Vertex Detector (VXD).	32
3.2.3 The Uranium Calorimeter (UCAL).	33
3.2.4 The Small Angle Rear Tracking Detector (SRTD).	35
3.2.5 The Luminosity Monitor (LUMI).	36
3.3 The ZEUS Trigger and Data Acquisition System.	37

<b>4 Monte Carlo Simulation.</b>	<b>39</b>
4.1 Introduction.	39
4.2 Electroweak Radiation at the Lepton Vertex.	39
4.3 Parton Distribution Functions.	42
4.4 QCD-Cascade and Hadronic Final State.	43
4.5 Photoproduction Events.	44
4.6 Detector Simulation.	44
<b>5 The Data Sample</b>	<b>46</b>
5.1 Introduction.	46
5.2 Trigger and Preselection.	48
5.3 Vertex Reconstruction.	50
5.4 Electron Identification and Reconstruction.	55
5.4.1 Introduction.	55
5.4.2 The Algorithm.	56
5.4.3 Electron Finding Efficiency.	56
5.4.4 Positron Position Measurement	60
5.4.4.1 SRTD Region	60
5.4.4.2 Inner RCAL Region	65
5.4.4.3 Outer RCAL and BCAL Region	66
5.4.5 Positron Energy Measurement	67
5.4.5.1 Kinematic Peak Correction	69
5.4.5.2 Energy Calibration based on Tracking	76
5.5 Luminosity Calorimeters.	86
5.6 Hadronic Event Parameters.	89
5.6.1 Introduction.	89
5.6.2 Noise Simulation.	89
5.6.3 Noise Cuts.	90
5.6.4 Hadronic Energy Scale.	91
5.6.5 Large Rapidity Gap Events.	94
5.7 Backgrounds.	97
5.7.1 Photoproduction Background.	97
5.7.1.1 Tagged Photoproduction.	98
5.7.1.2 Photoproduction Monte Carlo.	98
5.7.2 Bremsstrahlung Background.	100
5.7.3 Beam Induced Background.	100
5.7.4 Fake FCAL Electrons.	103
5.7.5 Cosmic and Halo Muons.	103
5.7.6 QED-Comptons.	104
5.7.7 Sparks.	105

<b>6 Reconstruction of Event Kinematics.</b>	<b>106</b>	<b>9 Phenomenological Analysis of <math>F_2</math>.</b>	<b>181</b>
6.1 Introduction.	106	9.1 Introduction.	181
6.2 Observables in DIS.	106	9.2 Double-Logarithmic Scaling.	182
6.3 Electron Method.	108	9.2.1 The Scaling of the $F_2$ Data.	182
6.4 Jacquet-Blondel Method.	110	9.2.2 Interpretation and Unitarity Constraints.	185
6.5 Double Angle Method.	112	9.3 Double-Asymptotic Scaling.	187
6.6 ' $P_T$ '-Method.	112	9.3.1 Introduction.	187
6.6.1 Introduction.	112	9.3.2 The Leading-Order Case.	188
6.6.2 $P_T$ -Balancing.	113	9.3.3 The Next-to-Leading-Order Case.	190
6.6.3 $\Sigma$ -Correction.	116	9.3.4 $\alpha_s$ -Extraction from $F_2$ using NLO-DAS.	193
6.6.4 Kinematic Reconstruction of the $p_T$ -Method.	117	9.4 The Bjorken Plot.	198
6.7 Radiative Events.	118	<b>10 QCD-Analysis of the <math>F_2</math>-Data.</b>	<b>200</b>
6.8 Resolution and Migration.	121	10.1 Introduction.	200
6.9 Distributions of the Kinematic Variables for the $F_2$ Data Sample.	125	10.2 The NLO-Evolution.	202
<b>7 Extraction of <math>F_2</math>.</b>	<b>129</b>	10.2.1 The Data Sets.	202
7.1 Introduction.	129	10.2.2 The Quality of the Fit.	203
7.2 Bin Selection.	130	10.2.3 Parametrisations of the Parton Distribution Functions.	203
7.3 Remaining Backgrounds.	134	10.2.4 $Q^2$ -Evolution of Singlet and Non-Singlet Quantities.	204
7.4 Unfolding.	136	10.2.5 Calculation of $\alpha_s$ .	206
7.4.1 Bin-by-Bin Unfolding.	137	10.3 Results.	208
7.4.2 Matrix Inversion.	138	10.3.1 The Central Fit.	208
7.4.3 Matrix Unfolding.	138	10.3.2 Sensitivity to the Input Data.	214
7.4.4 Bayes Unfolding.	139	10.3.3 Sensitivity to the Normalisation.	216
7.5 From the Cross Section to $F_2$ .	140	10.3.4 Sensitivity to $\alpha_s$ .	218
7.6 Test of the $F_2$ -Extraction.	142	10.3.5 Error Estimate on the PDFs, the gluon and $F_2$ .	219
7.7 Statistical Error.	143	10.3.6 $F_2^{charm}$ Comparison.	222
7.8 Systematic Uncertainties.	144	<b>11 Conclusion.</b>	<b>226</b>
7.8.1 Systematic Checks in the NVTX Analysis.	144	<b>12 The Photon Lifetime.</b>	<b>228</b>
7.8.2 Systematic Checks in the SVTX Analysis.	153	<b>13 <math>F_2</math> Tables.</b>	<b>230</b>
7.8.3 Systematic Checks in the ISR Analysis.	157	<b>References</b>	<b>240</b>
<b>8 Final Results on <math>F_2</math>.</b>	<b>161</b>		
8.1 Introduction.	161		
8.2 Shifted Vertex $F_2$ .	162		
8.3 Initial State Radiation- $F_2$ .	164		
8.4 Nominal Vertex $F_2$ .	166		
8.5 Scaling Behaviour.	175		
8.6 Total Cross Section.	177		

1	Introduction	1
2	Deep inelastic scattering	10
3	The Standard Model	15
4	Quantum electrodynamics	20
5	Quantum chromodynamics	25
6	Electroweak theory	30
7	Hadron structure	35
8	Deep inelastic scattering at HERA	40
9	The ZEUS detector	45
10	Event reconstruction	50
11	Structure function $F_2$	55
12	Structure function $F_L$	60
13	Structure function $R$	65
14	Structure function $F_3$	70
15	Structure function $S_1$	75
16	Structure function $S_2$	80
17	Structure function $S_3$	85
18	Structure function $S_4$	90
19	Structure function $S_5$	95
20	Structure function $S_6$	100
21	Structure function $S_7$	105
22	Structure function $S_8$	110
23	Structure function $S_9$	115
24	Structure function $S_{10}$	120
25	Structure function $S_{11}$	125
26	Structure function $S_{12}$	130
27	Structure function $S_{13}$	135
28	Structure function $S_{14}$	140
29	Structure function $S_{15}$	145
30	Structure function $S_{16}$	150
31	Structure function $S_{17}$	155
32	Structure function $S_{18}$	160
33	Structure function $S_{19}$	165
34	Structure function $S_{20}$	170
35	Structure function $S_{21}$	175
36	Structure function $S_{22}$	180
37	Structure function $S_{23}$	185
38	Structure function $S_{24}$	190
39	Structure function $S_{25}$	195
40	Structure function $S_{26}$	200
41	Structure function $S_{27}$	205
42	Structure function $S_{28}$	210
43	Structure function $S_{29}$	215
44	Structure function $S_{30}$	220
45	Structure function $S_{31}$	225
46	Structure function $S_{32}$	230
47	Structure function $S_{33}$	235
48	Structure function $S_{34}$	240
49	Structure function $S_{35}$	245
50	Structure function $S_{36}$	250
51	Structure function $S_{37}$	255
52	Structure function $S_{38}$	260
53	Structure function $S_{39}$	265
54	Structure function $S_{40}$	270
55	Structure function $S_{41}$	275
56	Structure function $S_{42}$	280
57	Structure function $S_{43}$	285
58	Structure function $S_{44}$	290
59	Structure function $S_{45}$	295
60	Structure function $S_{46}$	300
61	Structure function $S_{47}$	305
62	Structure function $S_{48}$	310
63	Structure function $S_{49}$	315
64	Structure function $S_{50}$	320
65	Structure function $S_{51}$	325
66	Structure function $S_{52}$	330
67	Structure function $S_{53}$	335
68	Structure function $S_{54}$	340
69	Structure function $S_{55}$	345
70	Structure function $S_{56}$	350
71	Structure function $S_{57}$	355
72	Structure function $S_{58}$	360
73	Structure function $S_{59}$	365
74	Structure function $S_{60}$	370
75	Structure function $S_{61}$	375
76	Structure function $S_{62}$	380
77	Structure function $S_{63}$	385
78	Structure function $S_{64}$	390
79	Structure function $S_{65}$	395
80	Structure function $S_{66}$	400
81	Structure function $S_{67}$	405
82	Structure function $S_{68}$	410
83	Structure function $S_{69}$	415
84	Structure function $S_{70}$	420
85	Structure function $S_{71}$	425
86	Structure function $S_{72}$	430
87	Structure function $S_{73}$	435
88	Structure function $S_{74}$	440
89	Structure function $S_{75}$	445
90	Structure function $S_{76}$	450
91	Structure function $S_{77}$	455
92	Structure function $S_{78}$	460
93	Structure function $S_{79}$	465
94	Structure function $S_{80}$	470
95	Structure function $S_{81}$	475
96	Structure function $S_{82}$	480
97	Structure function $S_{83}$	485
98	Structure function $S_{84}$	490
99	Structure function $S_{85}$	495
100	Structure function $S_{86}$	500

## Chapter 1

# Introduction.

“What is matter made of ? ” is simultaneously a simple and very fundamental question. Several generations of scientists tackled this question and managed to give partial answers revealing some of nature’s secrets. The general idea is to understand the characteristics of matter from its building blocks and the interactions between them. The current understanding of these is comprised in the *Standard Model* of elementary particle physics reflecting the beauty of their underlying symmetries.

Deep inelastic lepton nucleon scattering (DIS) experiments have played a crucial role in the understanding of hadronic matter. They have disclosed the structure of hadrons being made out of constituents and the interaction between the latter. HERA now offers the possibility to study the structure of the proton with a resolution of  $10^{-18}$  m, about three orders of magnitude smaller than the proton itself.

This thesis presents an independent measurement of the proton structure function  $F_2$  using the HERA data collected with the ZEUS detector in 1994. Three complementary analyses have been performed on a data set corresponding to an integrated luminosity of  $2.4 \text{ pb}^{-1}$ . They are based on events with a shifted interaction point (‘SVTX analysis’), events with collinear photon radiation in the initial state (‘ISR analysis’) and a conventional analysis (‘NVTX analysis’).

The thesis is organised as follows:

- The second chapter gives an overview of the theory of deep inelastic scattering. The concept of structure functions is introduced and related to the experimentally measurable cross sections. Theoretical predictions for the evolution of the structure functions are discussed.
- In the third chapter the HERA collider and the ZEUS experiment are described.
- Chapter four introduces the Monte Carlo simulation of the  $ep$  scattering process and of the detector performance.
- The selection and reconstruction of the analysed events is described in chapter five.

Particular emphasis is put on electron energy corrections which are necessary to compensate the electron energy loss in inactive material in front of the calorimeter.

- Chapter six gives an overview of conventional reconstruction methods of event kinematics. A new method, which incorporates their advantages and gives a good resolution in the entire kinematic region, is introduced.
- The  $F_2$  extraction from the measured events using several unfolding techniques is discussed in chapter seven. Details on the investigations of systematic uncertainties for the three analyses are given.
- The final  $F_2$  results are presented in chapter eight. They are compared to other  $F_2$  data as well as to parametrisations obtained from global QCD analyses.
- In chapter nine the present  $F_2$  data are analysed in the context of phenomenological models. Also the determination of the strong coupling constant  $\alpha_s$  is carried out in a model dependent way.
- In chapter ten a QCD analysis of the present  $F_2$  data and NMC data is performed, based on the Altarelli-Parisi evolution equations. The gluon momentum distribution in the proton is determined and its uncertainty estimated.
- A conclusion is given in chapter eleven.

## Chapter 2

# Deep-Inelastic Scattering.

### 2.1 A Short Historical Review.

The idea of investigating the structure of matter by scattering pointlike projectiles off a target and measuring the distributions of quantities such as scattering angles or energies goes back to Rutherford [1]. This famous experiment, in which  $\alpha$ -particles were scattered off a gold foil, showed that the mass of an atom is concentrated in a 'nucleus' much smaller than the atom.

However, when using spin- $\frac{1}{2}$  particles, such as electrons, the scattering cross section receives corrections to the Rutherford formula, which were calculated by Mott [2].

Electron scattering has been extensively used to investigate the structure of matter. Already in 1913 Franck and Hertz [3] scattered electrons on various gases showing that atoms have discrete energy levels.

In 1950, Rosenbluth calculated the cross section for elastic electron proton scattering, assuming the proton to have spin  $\frac{1}{2}$  and allowing for an extended structure [4].

In 1953, Hofstadter et al. observed elastic electron proton ( $ep$ ) scattering at the Mark III line at Stanford [5] with electron energies up to 188 MeV. The results showed the excitation of higher energy states in the nuclei, the resonances, and allowed a measurement of the proton form factors for its electric charge and magnetic moment distribution. As evidence for a distributed structure the proton form factor was found to drop sharply with increasing momentum transfer, compared to that of a point charge, with a proton radius estimated to be  $(0.7 \pm 0.2)10^{-13}$  cm. The success of these early scattering experiments led to the proposal for a two mile long linear accelerator, the Stanford Linear Accelerator Center (SLAC).

In 1961, Gell-Mann and Ne'eman independently proposed the 'Eightfold Way' [6], a classification scheme to group the observed baryons and mesons with the same spin according to their charge and strangeness, using SU(3) symmetry. As the classification scheme had a missing entry for the spin  $\frac{3}{2}$  baryons, they predicted a particle with charge -1 and strangeness -3. The discovery of this particle, the  $\Omega^-$ , in 1964 led to a

wide acceptance of the Eightfold Way.

Also in 1964, Gell-Mann and Zweig independently proposed hadrons to be composed of elementary constituents, called 'quarks' [7], providing a deeper understanding of the Eightfold Way. The quarks, coming in three flavours up (u), down (d) and strange (s) and carrying spin  $\frac{1}{2}$ , were assigned fractional charge: the u has  $+\frac{2}{3} \cdot e$ , the d and s have  $-\frac{1}{3} \cdot e$ , where  $e$  is the charge of the proton. In the quark model, which was found to reproduce the multiplet structure of all observed hadrons, each baryon consists of three quarks, later called 'valence quarks', while mesons are composed of quark-antiquark pairs.

However, in order to make the baryons' wave function consistent with the Pauli Exclusion principle, stating that no two identical fermions can occupy the same state, a new quantum number, called colour, was introduced [8]. Quarks were assumed to come in three colours (red, green and blue) where only quark combinations forming colourless<sup>1</sup> particles can occur in nature. Despite this attempt to explain the 'confinement' of quarks in hadrons and hence the failure to observe free quarks directly, quite a number of physicists were rather sceptical about the reality of quarks, including even one of their inventors<sup>2</sup>.

In August 1967, a long series of experiments on deep-inelastic (i.e. large energy loss of the lepton)  $ep$  scattering experiments started at the Stanford Linear Accelerator center (SLAC) [9].

The most famous result was that the deep-inelastic *Structure Function*, which can be interpreted as the momentum distribution of the proton constituents, showed little dependence on the momentum transfer, but depended only on the fractional proton momentum carried by the struck constituent. This surprising feature, called 'scale invariance' or simply scaling, is expected for scattering from a point-like object and was found following a suggestion by Bjorken. In 1968, he had predicted the scaling of the proton structure function in the deep-inelastic scattering region. However, he expected it at high  $Q^2$  so when it was found at relatively low  $Q^2$  it was called 'precocious' scaling. Confronted with the early SLAC data in 1968, Feynman explained the results by applying his parton model [10]. This model assumes that the proton is composed of free point-like partons, and that the electrons scatter from the partons incoherently. In an application of the parton model, Bjorken and Paschos identified the partons with the spin- $\frac{1}{2}$  quarks in 1969 [11]. The neutral gluons, the field quanta responsible for the binding of the quarks, were added to the parton model in 1971 [12].

The identification of partons as quarks and gluons opened the door to the development of a comprehensive field theory of quarks and gluons and their strong interactions,

<sup>1</sup>Quark combinations, i.e. particles, are colourless if the total amount of each colour cancels to zero (red + anti-red, ...) or if all three colours are present to equal amounts (red + green + blue = white).

<sup>2</sup>"Such particles [quarks] presumably are not real but we may use them in our field theory anyway" (Gell-Mann, 1964).

called Quantum Chromodynamics (QCD). QCD in conjunction with electroweak theory constitutes the *Standard Model* of elementary particle physics.

A more detailed discussion of the history of deep-inelastic scattering and its results can be found in [9, 13].

The first deep-inelastic  $ep$  scattering results from SLAC were followed by several fixed target experiments at CERN and FNAL, using muon and neutrino beams of higher energies. Up to the late 1980's, the proton and neutron structure functions have been measured with increased precision and in an extended kinematic region.

The World's first  $ep$  collider HERA<sup>3</sup> follows this long tradition of deep-inelastic scattering experiments, and, as the centre of mass energy at HERA is more than one order of magnitude higher than at the fixed target experiments, it opens a new kinematic regime. In contrast to many fixed target experiments the hadronic final state at the HERA experiments is also the subject of detailed studies. Therefore HERA yields qualitatively and quantitatively new insights into the structure of matter and allows tests of the underlying theory in unprecedented detail.

## 2.2 The DIS Variables

The scattering of high energetic electrons off protons generally results in an inelastic reaction, i.e. the proton disintegrates, and a large number of particles with a very high total invariant mass can be produced in the final state. This process is called 'deep-inelastic scattering' (DIS).

There are two fundamental classes of DIS events (figure 2.1)

$$e^\pm + P \rightarrow e^\pm X \quad \text{and} \quad e^\pm + P \rightarrow \begin{pmatrix} - \\ \nu \end{pmatrix} X \quad (2.1)$$

where  $X$  represents the spray of particles produced by the break-up of the proton

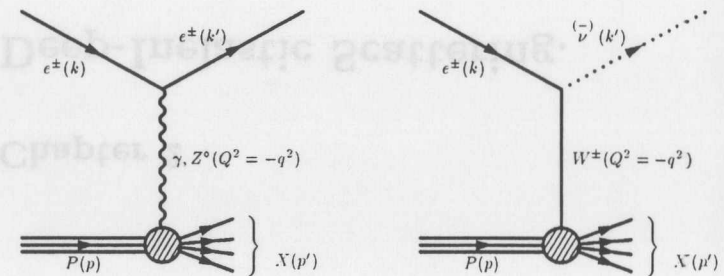


Figure 2.1: Feynman diagrams of neutral current (left) and charged current (right) DIS.

<sup>3</sup>HERA = 'Hadron-Elektron Ring Anlage'.

(the 'hadronic final state'). The 4-momenta of the incoming and scattered lepton are  $k = (E, \mathbf{k})$ ,  $k' = (E', \mathbf{k}')$  and those of the proton and the photon are  $p = (E_p, \mathbf{p})$  and  $q = (E_\gamma, \mathbf{q})$ .

In the first process the charge of the lepton is conserved, the intermediate vector boson is neutral. This process is referred to as neutral current (NC) DIS. In the second process the lepton converts to an (anti-) neutrino via the exchange of a charged vector boson. Therefore this process is called charged current (CC) DIS.

At a given centre of mass energy  $\sqrt{s}$  the kinematics of inclusive DIS scattering are completely described by two of the following three Lorentz-invariant quantities.

$$Q^2 = -q^2 = -(k - k')^2 \quad (2.2)$$

$$x = \frac{Q^2}{2p \cdot q} \quad (2.3)$$

$$y = \frac{p \cdot q}{p \cdot k} \quad (2.4)$$

$Q^2$  is the negative square of the momentum transfer and specifies the virtuality of the exchanged boson. If  $Q^2 > 0$  the exchanged boson can have longitudinal as well as transverse polarisation, while  $Q^2 = 0$  photons are only transversely polarised. If  $M$  is the proton mass and  $Q^2 \gg (2Mx)^2$  then the wavelength of the virtual photon is

$$\lambda = \frac{h}{|q|} = \frac{hc}{\sqrt{\nu^2 + Q^2}} \approx \frac{2Mx}{Q^2} \quad (2.5)$$

where  $\nu = \frac{E - E'}{M}$  is the photon energy in the proton rest frame.

Thus, for a given  $x$ , the wavelength of the photon is inversely proportional to  $Q^2$ , implying that with increasing  $Q^2$  the virtual photon probes smaller distances.

$x$  is the Bjorken scaling variable. In the parton model  $x$  can be interpreted as the proton momentum fraction carried by the struck quark (see section 2.4).

In the proton rest frame  $y$  corresponds to the fractional energy transfer from the lepton to the proton,  $y = \frac{E - E'}{E} = \frac{\nu}{E}$

Ignoring the particle masses the three quantities are related via

$$Q^2 = s \cdot x \cdot y \quad (2.6)$$

where  $s = (k + P)^2$  is the square of the centre of mass energy.

The square of the invariant mass  $W^2$  of the hadronic final state  $X$  is related to  $x$  and  $Q^2$  by the momentum conservation at the hadronic vertex:

$$W^2 = (P')^2 = (P + q)^2 = Q^2 \cdot \left(\frac{1}{x} - 1\right) + M^2 \quad (2.7)$$

Throughout the rest of this thesis, the natural system of units is used, where  $\hbar = c = 1$ .

### 2.3 DIS Cross Section and Structure Functions.

As the masses of the  $W^\pm$ - and the  $Z^0$ -boson are large, 80.2 GeV and 91.2 GeV respectively [162] their exchange is suppressed with respect to the photon exchange by a factor  $\frac{Q^4}{(Q^2 + M_{Z,W}^2)^2}$  and the  $\gamma - Z$  interference is suppressed by a factor  $\frac{Q^2}{(Q^2 + M_Z^2)}$ . Figure 2.2 shows the comparison of the NC and the CC cross section as measured by ZEUS [14], clearly demonstrating this propagator effect at  $Q^2 \lesssim 2000 \text{ GeV}^2$ . At large  $Q^2 \gtrsim M_{Z,W}^2$  the neutral current and the charged current cross section are found to be of comparable size which is a direct result of electroweak unification. However, in most of the kinematic region considered in the present analyses, the single-photon exchange dominates by far. In the following only NC reactions are considered.

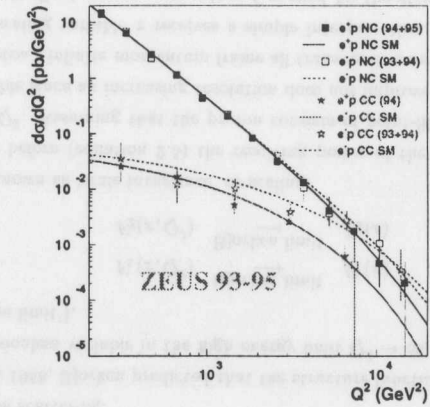


Figure 2.2: Measurement of the NC- and CC-cross section by ZEUS.

In the single boson exchange approximation the cross section for deep inelastic  $ep$  scattering can be factorised into a leptonic tensor  $L_{\mu\nu}$  and a hadronic tensor  $W^{\mu\nu}$

$$d\sigma \sim L_{\mu\nu} W^{\mu\nu} \quad (2.8)$$

The leptonic tensor, which is symmetric in  $\mu$  and  $\nu$ , can be calculated exactly using Quantum Electrodynamics (QED).

$$L_{\mu\nu} = 2 \left[ k'_\mu k_\nu + k'_\nu k_\mu + \left(\frac{q^2}{2}\right) g_{\mu\nu} \right] \quad (2.9)$$

where the electron mass has been neglected and  $g_{\mu\nu}$  is the metric tensor. The ignorance of the structure of the proton and hence the details of the interaction at the hadronic vertex are parametrised in the hadronic tensor  $W^{\mu\nu}$ . The most general form of the tensor  $W^{\mu\nu}$ , taking Lorentz-invariance and the symmetry of  $L^{\mu\nu}$  in  $\nu$  and  $\mu$  into account is

[15]

$$W^{\mu\nu} = -W_1 g^{\mu\nu} + \frac{W_2}{M^2} p^\mu p^\nu + i\epsilon^{\mu\nu\rho\sigma} p_\rho q_\sigma W_3 + \frac{W_4}{M^2} q^\mu q^\nu + \frac{W_5}{M^2} (p^\mu q^\nu + q^\mu p^\nu) \quad (2.10)$$

Imposing the conservation of the four-vector current yields

$$W_5 = -\frac{p \cdot q}{q^2} W_2 \quad \text{and} \quad W_4 = \left(\frac{p \cdot q}{q^2}\right)^2 W_2 + \frac{M^2}{q^2} W_1 \quad (2.11)$$

The three remaining functions  $W_1, W_2$  and  $W_3$  depend on two independent Lorentz-invariant scalar variables, here chosen to be  $\nu$  and  $Q^2$ . The dynamics of the strong interaction are contained in the  $\nu$  and  $Q^2$  dependence of the  $W_i$ . Nowadays the slightly different notation

$$\begin{aligned} F_1(x, Q^2) &= M \cdot W_1(\nu, Q^2) \\ F_2(x, Q^2) &= \nu \cdot W_2(\nu, Q^2) \\ \text{and} \quad F_3(x, Q^2) &= \nu \cdot W_3(\nu, Q^2) \end{aligned} \quad (2.12)$$

is used. The  $F_i$  are called *proton structure functions*. As  $F_3(x, Q^2)$  describes the parity violation contribution this structure function is small in the medium and low  $Q^2$  range. It only becomes relevant in the region  $Q^2 \approx M_p^2$ .

The deep-inelastic  $ep \rightarrow eX$  scattering cross section can now be written as

$$\frac{d^2\sigma^{\text{NC}}(\epsilon^\pm p)}{dx dQ^2} = \frac{4\pi\alpha^2}{x Q^4} \left[ \frac{y^2}{2} 2x F_1(x, Q^2) + (1-y) F_2(x, Q^2) \mp (y - \frac{y^2}{2}) x F_3(x, Q^2) \right] \quad (2.13)$$

or with the definition of  $F_L = F_2 - 2xF_1$

$$\frac{d^2\sigma^{\text{NC}}(\epsilon^\pm p)}{dx dQ^2} = \frac{2\pi\alpha^2}{x Q^4} \left[ Y_+ F_2(x, Q^2) - y^2 F_L \mp Y_- x F_3(x, Q^2) \right] \quad (2.14)$$

where  $Y_\pm = 1 \pm (1-y)^2$

Within the single-photon exchange approximation, one may view inelastic electron scattering as photoproduction by 'virtual' photons. As the effective photon mass  $q^2$  is variable the exchanged photon may have longitudinal as well as transverse polarisation. According to [140] the  $ep$  cross section can then be written as a photon flux and the cross section  $\sigma_{\text{tot}}^{\gamma^* p}$  for virtual photon proton scattering, provided the lifetime of the photon is longer than its interaction time with the proton (see appendix 12). The total cross section is the sum of the absorption cross section of transverse,  $\sigma_T$ , and longitudinal,  $\sigma_L$ , virtual photons,  $\sigma_{\text{tot}}^{\gamma^* p} = \sigma_L + \sigma_T$ . These are related to the structure function as

$$F_1 = \frac{Q^2}{8x\pi^2\alpha} \cdot \sigma_T \quad (2.15)$$

$$F_2 = \frac{Q^2}{4\pi^2\alpha} \cdot (\sigma_T + \sigma_L) \quad (2.16)$$

The additional function

$$F_L = F_2 - 2xF_1 = \frac{Q^2}{4\pi^2\alpha} \cdot \sigma_L \quad (2.17)$$

is only related to the absorption cross section of longitudinal photons. It is therefore called *Longitudinal Structure Function*  $F_L$ .

## 2.4 The Naive Quark Parton Model.

There are various approaches to understanding the experimental results on the structure functions and the underlying structure of the proton. According to Feynman's parton model [10], the proton is composed of free point-like constituents, called partons. In this model the deep-inelastic  $ep$  scattering cross section is the incoherent sum of quasi-elastic electron parton scattering.

Already in 1968, Bjorken predicted that the structure functions would depend only on one dimensionless variable in the high energy limit  $Q^2 \rightarrow \infty, \nu \rightarrow \infty$ , but  $\omega = \frac{2M\nu}{Q^2}$  finite ('Bjorken limit').

$$\begin{aligned} F_1(x, Q^2) &\xrightarrow{\text{Bjorken limit}} F_1(x) \\ F_2(x, Q^2) &\xrightarrow{\text{Bjorken limit}} F_2(x) \end{aligned}$$

a behaviour known as 'scale invariance' or scaling.

As shown before (equation 2.5) the resolving power of the exchanged photon increases with  $Q^2$ . Assuming that the proton consists of point-like constituents, makes scaling plausible since an increasing resolution does not improve the view of a point!

In the proton's infinite momentum frame all transverse momenta are negligible and the Bjorken scaling variable  $x$  receives a simple interpretation.  $x$  corresponds to the fractional longitudinal proton momentum  $\xi$  carried by the struck parton. Neglecting the parton and proton mass, 4-momentum conservation implies for this fraction:

$$\begin{aligned} 0 \approx m^2 &= (\xi p + q)^2 = \xi^2 p^2 - Q^2 + 2\xi p \cdot q \\ \Rightarrow \xi &= \frac{Q^2}{2p \cdot q} = x \end{aligned}$$

In this frame, relativistic time dilation slows down the interaction rate of the partons, which can then be considered as non-interacting free particles.

The experimental results from SLAC showed the scaling behaviour very clearly (figure 2.3),  $F_2$  (or alternatively  $\nu W_2$ ) does not exhibit any  $Q^2$  dependence.

In the parton model the structure function  $F_2$  corresponds to the sum of the partons momentum distribution  $x \cdot f_i(x)$  weighted with the square of their electric charge  $e_i$

$$F_2(x) = \sum_i e_i^2 x f_i(x) \quad (2.18)$$

$$\text{and} \quad F_1(x) = \frac{1}{2x} F_2(x) \quad (2.19)$$

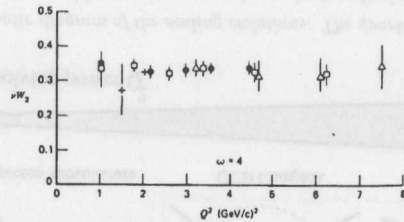


Figure 2.3:  $\nu W_2$  (corresponding to  $F_2$ ) as a function of  $Q^2$  for  $\omega = \frac{1}{x} = 4$ , as measured at SLAC. The scaling behaviour is evident.

where the latter is known as the Callan-Gross relation [16]. A comparison to equation 2.17 shows that this relation implies that the cross section for longitudinally polarised photons vanishes, as would be the case for scattering of spin- $\frac{1}{2}$  partons (illustrated in figure 2.4). In the Breit frame, where the virtual photon transfers only momentum

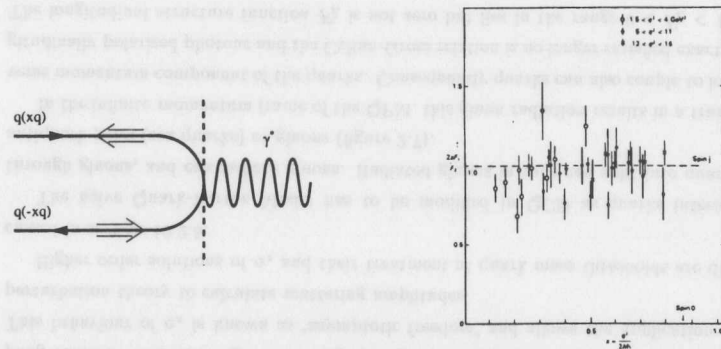


Figure 2.4: Left: Coupling of a spin- $\frac{1}{2}$  parton to a photon in the Breit frame. Right: Ratio of  $\frac{2xF_1}{F_2}$  from SLAC, showing that the proton constituents have spin- $\frac{1}{2}$ .

but no energy, the struck quark has 3-momentum  $x\mathbf{q}$  and  $-x\mathbf{q}$  before and after the collision with the photon respectively. Since the electromagnetic interaction is helicity conserving, spin- $\frac{1}{2}$  particles can only couple to photons of helicity  $\pm 1$ , i.e. transversely polarised photons, while spin-0 particles only couple to photons of helicity 0 [15].

Since the SLAC results (figure 2.4, plot taken from [17]) confirmed the Callan-Gross relation Feynman's partons were identified with Gell-Mann's quark and the model was called the Quark-Parton Model (QPM). The fractional charge of the partons was confirmed using neutrino-nucleon scattering<sup>4</sup> and the postulated number of 3 valence

<sup>4</sup>The ratio  $\frac{1}{2} \int [F_2^{\nu p}(x) + F_2^{\nu n}(x)] dx / \frac{1}{2} \int [F_2^{\nu p}(x) + F_2^{\nu n}(x)] dx = 2/(Q_u^2 + Q_d^2)$  were found to be  $3.6 \pm 0.3$

quarks ( $uud/duu$ ) in the proton /neutron was experimentally confirmed using the Gross-Llewellyn-Smith sum rule<sup>5</sup> [18].

If the proton consisted only of charged quarks, their momentum would be expected to add up to the proton momentum

$$\int_0^1 x \sum_i f_i(x) = 1$$

However, experimentally a value of  $\approx 0.5$  was found [19], implying that about half of the proton's momentum is carried by neutral partons. Direct evidence for the existence of these partons, called gluons, was provided in 1979 at DESY via the observation of three-jet events in  $e^+e^-$  annihilation [20].

## 2.5 Outline of QCD.

In the 1970's Quantum Chromodynamics (QCD) was developed as the field theory governing the strong interactions between quarks and gluons and therefore between hadrons in general. QCD is a non-abelian gauge theory based on the SU(3) symmetry group. Each quark (see table 2.1) has three possible 'charges' (colours red (r), green (g) and blue (b)) and the strong interaction can be mediated via the exchange of 8 different coloured gauge particles, called gluons, which transmit the colour force<sup>6</sup>. As

charge	Quark (mass)		
$+\frac{2}{3}$	u ( $\sim 4$ MeV)	c ( $\sim 1.5$ GeV)	t ( $\sim 175$ GeV)
$-\frac{1}{3}$	d ( $\sim 7$ MeV)	s ( $\sim 135$ MeV)	b ( $\sim 5$ GeV)

Table 2.1: The properties of the six quarks.

a consequence of the non-abelian structure of QCD the gluons also carry colour charge themselves and can therefore couple to each other. This self coupling of the gauge bosons in QCD is the main difference to QED. In the latter the coupling constant  $\alpha$  increases slightly with  $Q^2$  while in QCD the strong coupling constant  $\alpha_s$  is large at small  $Q^2$  (large distances) and decreases at high  $Q^2$  (small distances). The scale dependence of  $\alpha_s$  is given by the renormalisation group equation and the QCD  $\beta$ -function

$$\mu \frac{d\alpha_s}{d\mu} = \alpha_s \cdot \beta(\alpha_s) = -\frac{\beta_0}{2\pi} \alpha_s^2 - \frac{\beta_1}{4\pi^2} \alpha_s^3 - \frac{\beta_2}{64\pi^3} \alpha_s^4 - \dots \quad (2.20)$$

[18] as compared to the quark model prediction  $\frac{1}{2} = 3.6$

<sup>5</sup>The Gross-Llewellyn-Smith sum rule  $\int_0^1 \frac{dx}{x} \frac{1}{2} (F_2^{\nu p} + F_2^{\nu n}) = \int_0^1 dx (u_v + d_v)$  counts the number of valence quarks in the nucleon. Experimentally a value of  $3.2 \pm 0.6$  was obtained in [18].

<sup>6</sup>The gluons always carry a combination of colour and anti-colour such as  $r\bar{g}$ ,  $r\bar{b}$  etc.

$$\text{with } \beta_0 = 11 - \frac{2}{3}N_f; \beta_1 = 51 - \frac{19}{3}N_f; \beta_2 = 2857 - \frac{5033}{9}N_f + \frac{325}{27}N_f^2$$

where  $N_f$  is the number of (active) quark flavours with mass less than the energy scale  $\mu$ .

A solution of equation 2.20, in first order expansion, is

$$\alpha_s(Q^2) = \frac{12\pi}{(33 - 2N_f) \ln \frac{Q^2}{\Lambda_{QCD}^2}} \xrightarrow{Q^2 \rightarrow \infty} 0.$$

The QCD scale parameter  $\Lambda_{QCD}$  represents the energy scale at which the strong coupling constant becomes large. At a large energy scale  $Q^2$ ,  $\alpha_s$  vanishes logarithmically. This behaviour of  $\alpha_s$  is known as 'asymptotic freedom' and allows the application of perturbation theory to calculate scattering amplitudes.

Higher order solutions of  $\alpha_s$  and their treatment at quark mass thresholds are discussed in section 10.2.5.

The naive Quark-Parton Model has to be modified in QCD as quarks interact through gluons, and can radiate gluons. Radiated gluons in turn can split into quark-antiquark pairs (sea quarks) or gluons (figure 2.7).

In the infinite momentum frame of the QPM, this gluon radiation results in a transverse momentum component of the quarks. Consequently quarks can also couple to longitudinally polarised photons and the Callan-Gross relation is no longer satisfied exactly. The longitudinal structure function  $F_L$  is not zero but lies in the range  $0 < F_L < F_2$ . Due to its origin,  $F_L$  is largely dependent on the gluon distribution in the proton and is therefore considered to be a good measure of the latter. Unfortunately the measurement of  $F_L$  is experimentally difficult, particularly at HERA.

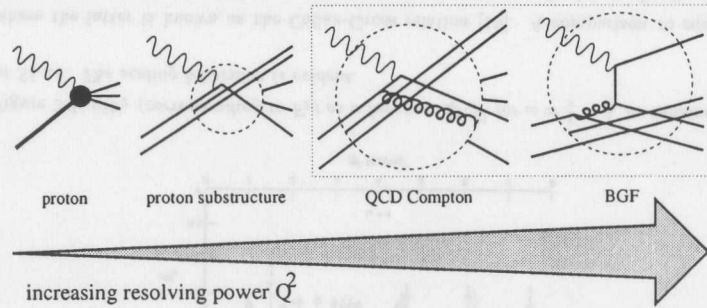


Figure 2.5: Schematic diagram of the scaling violations: The quark momentum densities depend of the resolution  $Q^2$  as processes such as gluon radiation or quark-antiquark splitting can be resolved with increasing  $Q^2$ . Two examples, the QCD Compton process and the Boson Gluon Fusion process, are shown on the right hand side.

Another, more important, consequence of the gluon radiation are scaling violations of the structure functions, which now exhibit a logarithmic dependence on  $Q^2$  at fixed  $x$ . This is interpreted as follows: At low  $Q^2$  the resolution of the exchanged photon is rather broad, so that only just the quark substructure of the proton is 'seen' (figure 2.5). At high  $Q^2$ , however, a finer resolution is achieved and quark-antiquark pairs originating from radiated gluons can be resolved. This means that the history of a quark before it interacts with the photon becomes important. It could radiate a gluon and thus, although the quark which is struck has momentum fraction  $x$ , the quark originally had a larger momentum fraction  $y > x$  (the process known as the QCD Compton process). Alternatively it may be that a gluon with momentum fraction  $y$  produced a  $q\bar{q}$  pair and one of these became the struck quark of momentum fraction  $x$  (the process known as Boson Gluon Fusion). Therefore the quark and gluon distributions  $f(y, Q^2)$  for all momentum fractions  $y$  such that  $x < y < 1$  contribute to the considered process. At large  $x$ , where valence quarks dominate, the quark density and hence  $F_2$  falls with  $Q^2$  as a result of the gluon radiation, while at small  $x$  the amount of  $q\bar{q}$  pairs and gluons in the partonic 'sea' increases, so that  $F_2$  rises with  $Q^2$ . These scaling violations in conjunction with a strong rise of  $F_2$  at small  $x$  for fixed  $Q^2$  have been found by both HERA experiments, ZEUS and H1 [108, 114].

It is this effect which allows studies of QCD in DIS since the parton being probed may not be an 'original' constituent, but arise from the strong interactions within the proton.

## 2.6 Factorisation.

In the QCD improved parton model a hadron scattering process is the result of an interaction between the quarks and gluons (hadron-hadron scattering) or the leptons and the quarks (DIS). The incoming hadrons can be viewed as providing 'broad band' beams of partons which carry varying fractions of the momenta of the parent hadrons.

The cross section for a hard scattering process initiated by two hadrons of 4-momenta  $P_1$  and  $P_2$  can be written as

$$\sigma(P_1, P_2) = \sum_{i,j} \int dx_1 dx_2 f_i(x_1, \mu^2) f_j(x_2, \mu^2) \sigma_{ij}(x_1, x_2, \mu^2, Q^2) \quad (2.21)$$

as illustrated in figure 2.6. The momenta of the partons which participate in the interaction are  $x_1 P_1$  and  $x_2 P_2$  where the characteristic scale of the hard scattering is  $Q^2$ .  $\sigma_{ij}(x_1, x_2, \mu^2, Q^2)$  is the short distance cross section for the hard scattering of partons of type  $i$  and  $j$ . Since the coupling is small at high energy, this cross section can be calculated in perturbation theory. It involves only high momentum transfers and is insensitive to low momentum scales. It is a purely short distance construct and independent of the type of the incoming hadrons.

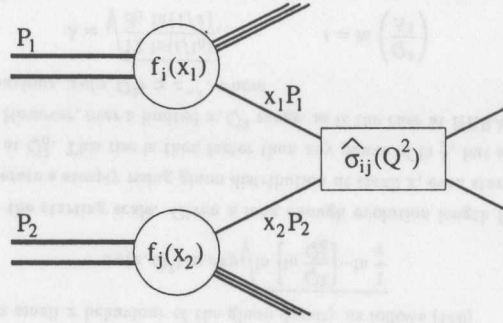


Figure 2.6: The parton model description of a hard scattering process.

The functions  $f_i(x, \mu^2)$  describe the distribution of longitudinal momentum fraction  $x$  and parton type  $i$  at an energy scale  $\mu^2$ . They depend on the type of hadron, but not on the particular scattering process considered. Thus they are a 'universal' description of the partons and their soft, long range interactions.

The separation of the scattering process in short and long range physics is called *factorisation* and set by the factorisation scale  $\mu_f^2$ .

In perturbative QCD the calculation of self energy diagrams such as a gluon splitting into a quark antiquark pair and the recombining into a gluon yields divergent integrals. These are dealt with by introducing a cut-off parameter  $\mu_R^2$  such that only momenta less than  $\mu_R$  are integrated over. The divergence is absorbed into the definition of the long range parton distribution functions. The energy scale  $\mu_R^2$ , defining the separation between the finite and the divergent contributions in the renormalisation procedure is called the renormalisation scale. In fact, in equation 2.21 the renormalisation and factorisation scales are set equal. The common practice is to choose  $Q^2$  as the relevant scale for both and this is adopted in chapter 10.

In addition to this scale one also has the freedom to choose a renormalisation scheme, defining how the divergences are absorbed. The most convenient scheme in deep-inelastic scattering is the DIS scheme as the definition of the parton distribution functions results in the relation

$$F_2(x, Q^2) = \sum_i e_i^2 [xq(x, Q^2) + x\bar{q}(x, Q^2)]$$

to all orders. However, for theoretical calculations a more attractive scheme is the  $\overline{MS}$  scheme<sup>7</sup>, which is also used for the studies described in chapter 10. The parton densities

<sup>7</sup> $\overline{MS}$  = 'minimal subtraction scheme'

can be transformed from one scheme into the other via

$$q_f^{DIS}(x, Q^2) = \left[ 1 + \alpha_s(Q^2) C_2^{f, \overline{MS}} \right] \otimes q_f^{\overline{MS}} + \frac{1}{2N_f} \alpha_s(Q^2) C_2^{g, \overline{MS}} \otimes g^{\overline{MS}} \quad (2.22)$$

$$g^{DIS}(x, Q^2) = \left[ 1 - \alpha_s(Q^2) C_2^{g, \overline{MS}} \right] \otimes g^{\overline{MS}} + \alpha_s(Q^2) \sum_f C_2^{f, \overline{MS}} \otimes q_f^{\overline{MS}}$$

where  $C_2^{f,g}$  are coefficient functions and  $\otimes$  represents the convolution integral in  $x$ .

## 2.7 The DGLAP Evolution.

The evolution of the quark ( $q_i(x)$ ) and gluon distributions ( $g(x)$ ) with  $Q^2$  is quantitatively described in perturbative QCD by the Dokshitzer-Gribov-Lipatov-Altarelli-Parisi equation [160, 161]

$$\begin{aligned} \frac{dq_i(x, Q^2)}{d \ln Q^2} &= \frac{\alpha_s(Q^2)}{2\pi} \int_x^1 \frac{dy}{y} \left[ q_i(y, Q^2) P_{qq} \left( \frac{x}{y} \right) + g(y, Q^2) P_{qg} \left( \frac{x}{y} \right) \right] \\ \frac{dg(x, Q^2)}{d \ln Q^2} &= \frac{\alpha_s(Q^2)}{2\pi} \int_x^1 \frac{dy}{y} \left[ \sum_i q_i(y, Q^2) P_{gq} \left( \frac{x}{y} \right) + g(y, Q^2) P_{gg} \left( \frac{x}{y} \right) \right] \end{aligned}$$

where the splitting function  $P_{ij}(z)$  represents the probability of a parton  $j$  emitting a parton  $i$  with momentum fraction  $z$  of the parent parton, when the scale changes from  $Q^2$  to  $Q^2 + d \ln Q^2$ . These splitting functions, calculated to first order, are illustrated in figure 2.7 and

$$\begin{aligned} P_{qq}(z) &= \frac{4}{3} \frac{1+z^2}{1-z} \\ P_{qg}(z) &= \frac{1}{2} [z^2 + (1-z)^2] \\ P_{gq}(z) &= \frac{4}{3} \frac{1+(1-z)^2}{z} \\ P_{gg}(z) &= 6 \left[ \frac{z}{1-z} + \frac{1-z}{z} + z(1-z) \right] \end{aligned}$$

In the context of perturbative QCD two types of terms can become large and hence important in the perturbation series in  $\ln Q^2$  and in  $\ln \frac{1}{x}$ .

The DGLAP equations are formally derived in the leading logarithm approximation (LLA) where terms of the form  $\alpha_s^n \cdot (\ln Q^2)^n$ , which give the dominant contribution at large  $Q^2$  and large  $x$ , are summed to all orders. In a field theory with asymptotic freedom such an approximation proves to be asymptotically exact. The amplitude for the inelastic  $ep$  scattering process can be obtained as the sum of ladder diagrams of consecutive gluon emissions (figure 2.8). The finally struck quark evolves from the incoming proton via this gluon emission thus losing, gradually, its longitudinal momentum. If, the rungs of the gluon ladder are labelled 1 to  $n$  from the proton to the photon, the fraction of longitudinal momentum  $x_i$  carried by the rungs are ordered

$$x_1 > x_2 > \dots > x_n$$

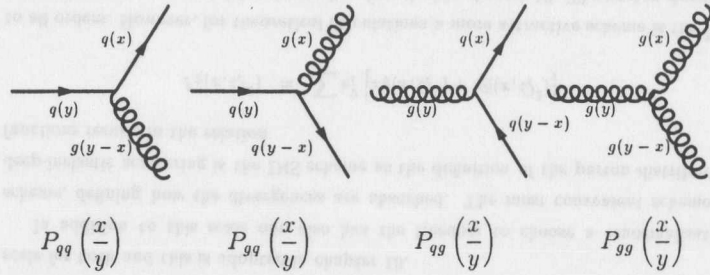


Figure 2.7: The splitting functions  $P_{ij}(\frac{x}{y})$ , that express the probability of finding a parton  $i$  inside parton  $j$  with a fraction  $\frac{x}{y}$  of the parent momentum. The two diagrams on the left show the gluon radiation, the diagrams on the right gluon splitting.

while the transverse momenta of the emitted gluons increase strongly as going up the ladder

$$k_{t_1}^2 \ll k_{t_2}^2 \ll \dots \ll k_{t_n}^2 \ll Q^2$$

The solutions of the DGLAP equations give the parton distributions as a function of  $x$  at any scale  $Q^2$ , provided their  $x$  dependence at an input scale  $Q_0^2$  is known. The latter can at present not be calculated but has to be determined experimentally. This procedure is described in more detail and applied in chapter 10.

At small  $x$  logarithms of  $\frac{1}{x}$  entering the cross section become important. In the moderate  $x$  region, where  $\alpha_s(Q^2) \ln Q^2 \ll 1$  and  $\alpha_s(Q^2) \ln \frac{1}{x} \ll 1$ , but  $\alpha_s(Q^2) \ln Q^2 \ln \frac{1}{x} \sim 1$ , the so-called Double Leading Logarithm Approximation (DLA) is used. In this approach leading terms in  $\ln \frac{1}{x}$  are summed when they are accompanied by leading  $\ln Q^2$ , resulting in a small  $x$  behaviour of the gluon density as follows [150]

$$xg(x, Q^2) \simeq \epsilon x p \sqrt{\ln \left[ \ln \frac{Q^2}{Q_0^2} \right] \cdot \ln \frac{1}{x}}$$

where  $Q_0$  is the starting scale. Given a long enough evolution length from  $Q_0^2$  to  $Q^2$ , this will generate a steeply rising gluon distribution at small  $x$ , even starting from a flat gluon input at  $Q_0^2$ . This rise is then faster than any power of  $\ln \frac{1}{x}$ , but slower than any power of  $x$ . However, over a limited  $x, Q^2$  range, as is the case at HERA, it may mimic a power behaviour,  $xg(x, Q^2) \simeq x^{-\lambda}$ , where

$$\lambda = \sqrt{\frac{12 \ln(t/t_0)}{\beta_0 \ln(1/x)}}, \quad t = \ln \left( \frac{Q^2}{\Lambda^2} \right)$$

In terms of the gluon ladders the DLA approach takes all contributions into account where strong ordering in  $x$  holds in addition to the strong  $k_t$  ordering (figure 2.8).

$$x \ll x_n \ll x_{n-1} \ll \dots \ll x_2 \ll x_1 \ll 1 \quad (2.23)$$

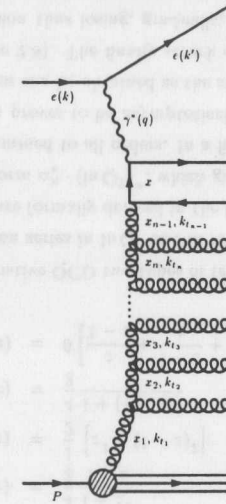


Figure 2.8: A ladder diagram, illustrating the parton evolution.

## 2.8 The BFKL Equation.

The steep behaviour of the gluon density and hence  $F_2$  at low  $x$  has led to further development in QCD. In the moderate- $x$  region the DLA approach already sums leading  $\ln \frac{1}{x}$  terms if accompanied by leading  $\ln Q^2$ . However, at low  $x$  it is also appropriate to sum diagrams which are leading in  $\ln \frac{1}{x}$  independent of  $\ln Q^2$ . This calculation has been done by Balitsky, Fadin, Kuraev and Lipatov [21], resulting in the BFKL equation which is named after them. Summing  $(\alpha_s \cdot \ln \frac{1}{x})^n$  terms involves the evolution of a gluon distribution which is not integrated over  $k_t$  and the gluon ladder does not have to be ordered in  $k_t$  anymore (rather it involves a 'random walk in  $k_t$ '). The unintegrated gluon distribution  $f(x, k_t^2)$  is related to the previously used  $g(x, Q^2)$  via

$$xg(x, Q^2) = \int_0^{Q^2} \frac{dk_t^2}{k_t^2} f(x, k_t^2). \quad (2.24)$$

The BFKL equation

$$\frac{df(x, k_t^2)}{d \ln \left( \frac{1}{x} \right)} = \int dk_t'^2 K(k_t^2, k_t'^2) \cdot f(x, k_t'^2) = \lambda \cdot f \quad (2.25)$$

describes the evolution of the unintegrated gluon density  $f(x, k_t^2)$  in  $\ln \frac{1}{x}$ . Its solution is dominated by the largest eigenvalue  $\lambda$  of the kernel  $K$ . To leading order in  $\ln \frac{1}{x}$  and fixed  $\alpha_s$  this solution is the steep power law behaviour

$$xg(x, Q^2) \sim f(Q^2) \cdot x^{-\lambda} \quad \text{with} \quad \lambda = \frac{3\alpha_s}{\pi} 4 \ln 2 \sim 0.5$$

which is reflected in a similarly steep expectation for the behaviour of  $F_2$  at low  $x$ .

This power law behaviour would violate unitarity in the limit  $x \rightarrow 0$ . However, the current form of the BFKL equation does not incorporate the running of  $\alpha_s$  with  $Q^2$  and the kernel has only been calculated to first order in  $\ln \frac{1}{x}$ . Furthermore cut-offs have to be introduced in the integral in the infrared and ultraviolet limit. These aspects have been studied [22] or are currently being worked on [23].

## 2.9 Unifying DGLAP and BFKL.

DGLAP deals with  $Q^2$  evolution and is probably inadequate at very low  $x$  while BFKL deals with  $\frac{1}{x}$  evolution and is inadequate at large  $Q^2$ . Ultimately one would like to achieve a 'unified' treatment of the  $x$  and  $Q^2$  dependence of the parton distributions and structure functions throughout the kinematic plane. Progress in this direction has been made [24] by the development of the so-called CCFM equation. It is based on the idea of coherent gluon radiation, which leads to angular ordering of gluon emission in the gluon ladder

$$\Theta_i > \Theta_{i-1}$$

where  $\Theta_i$  is the angle the  $i$ th gluon makes to the original direction. The maximum angle of gluon emission is specified by an additional scale, which can be taken to be  $Q^2$  of the probing photon. Hence the quantity dealt with is the unintegrated scale dependent gluon density  $f(x, k_T^2, Q^2)$ . At small  $x$  the integral equation for  $f(x, k_T^2, Q^2)$  reproduces the BFKL behaviour, while at moderate  $x$  it reproduces the DGLAP equation for the integrated gluon density  $g(x, Q^2)$  [25]. Numerical studies of the CCFM equation have shown that the gluon slope is reduced by  $\sim 0.1$  with respect to that of the BFKL equation but a flat gluon input at  $Q_0^2$  still yields a steeper rise of  $F_2$  at low  $x$  than would be obtained in the DLL approximation.

Technically the CCFM equation involves similar considerations to the BFKL equation concerning the incorporation of the running of  $\alpha_s$  and the UV and IR cut-offs.

Another approach to find an evolution equation that is valid over the whole kinematic plane is the attempt to take subleading  $\ln \frac{1}{x}$  terms into account. This 'resummation' of  $\ln \frac{1}{x}$  terms effectively requires a recalculation of the splitting functions. They can generally be written as

$$x \cdot P(x, \alpha_s) = \sum_{n=1}^{\infty} \sum_{m=-\infty}^n A_{nm} \alpha_s^n(Q^2) \ln^{m-1} \left( \frac{1}{x} \right) \quad (2.26)$$

The sum over  $m$  is here taken to extend to negative values to represent the contribution of terms which are non-singular as  $x \rightarrow 0$ . Since, at present, not all coefficients  $A_{nm}$  are known not all terms can be included in the sum. Depending in which terms are important different approximations are made (see figure 2.9). Only considering terms

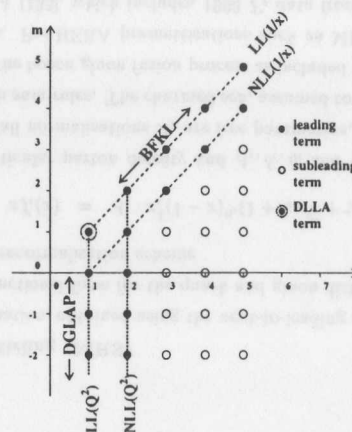


Figure 2.9: The  $(n, m)$  plane with the DGLAP and BFKL summations indicated.

which are leading in  $\ln Q^2$ , which gives the DGLAP equations, equation 2.26 is summed over  $m$ . For  $n = 1$  the leading  $\log(Q^2)$  approximation (LLA) is obtained, whereas  $n = 1, 2$  gives the next to leading  $\log(Q^2)$  approximation (NLLA). However, at very low  $x$  it is more appropriate to sum leading  $\ln \frac{1}{x}$  terms, i.e. terms for which  $n = m$  (leading  $\log \frac{1}{x}$  approximation -  $LL(1/x)$ ). This approximation gives the BFKL equation at  $LL(1/x)$ . Also including terms with  $m = n - 1$  yields the next to leading  $\log \frac{1}{x}$  approximation ( $NLL(1/x)$ ). The common term between the two approaches is the one with  $n = m = 1$ , which gives the double leading log approximation (DLLA).

## 2.10 Shadowing.

The considerations so far have yielded a steeply rising gluon density at small  $x$ . If this were the asymptotic behaviour of the gluon density the unitarity bound would eventually be saturated or even violated. Implications of the present data for the unitarity bound are discussed in section 9.2.2.

The evolution equations discussed above are linear integro-differential equations as they deal with the emission of gluons or their splitting into quarks or gluons. However, as  $x \rightarrow 0$  the gluon density gets very large, the self-coupling gluons may annihilate, or recombine to gluons. Such gluon shadowing or screening processes may compete with the usual evolution and eventually saturate the gluon density.

A measurement at  $Q^2$  probes a parton of transverse size  $\sim 1/Q$ . Assuming a homogenous distribution of gluons in the proton the  $xg(x, Q^2)$  gluons occupy a transverse area  $xg(x, Q^2) \frac{\pi}{Q^2}$ . If this area, which increases with decreasing  $x$ , gets comparable to

the transverse area of the proton,  $\pi R^2$ , shadowing effects are expected to set in

$$x \cdot g(x, Q^2) \frac{\pi}{Q^2} \gtrsim \pi R^2 \quad (2.27)$$

For a proton radius  $R \sim 1 \text{ fm} \doteq 5 \text{ GeV}^{-1}$  and  $Q^2 \sim 10 \text{ GeV}^2$  this limit is reached at  $xg(x, Q^2) \approx 250$ , which is well above the values found at HERA. However, in the scenario of 'hot spots' [26] the relevant size for  $R$  might be the radius of a constituent quark,  $\sim 0.4 \text{ fm}$ . No strong evidence for such an effect has so far been seen at HERA.

In order to take the recombination of gluons  $gg \rightarrow g$  into account Gribov, Levin and Ryskin added a quadratic correction to the evolution of the gluon distribution, yielding the so-called GLR equation [27]

$$\frac{d^2 xg(x, Q^2)}{d \ln Q^2 d \ln \frac{1}{x}} = \frac{3\alpha_s}{\pi} xg(x, Q^2) - \frac{\alpha_s}{Q^2 R^2} [xg(x, Q^2)]^2$$

This equation, however, can only be considered an approximation as possible interactions of gluon ladders before the recombination are not included and multi-ladder diagrams may also be important.

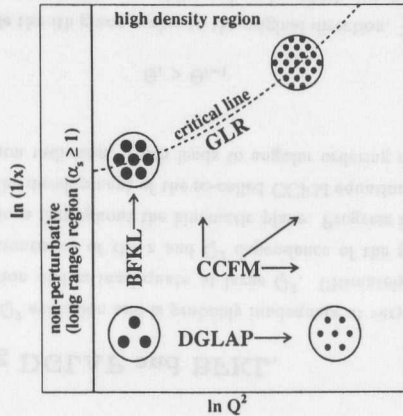


Figure 2.10: Schematic representation of the applicability of various evolution equations across the  $(x, Q^2)$  plane. The full circles indicate the parton density 'seen' at a particular  $x$  and  $Q^2$ . The critical line indicates the transition region between the dominance of gluon radiation and splitting, described by the linear evolution equations, and the saturation due to gluon recombination and shadowing.

The regions of phase space, where the different evolution equations can be applied, is schematically shown in figure 2.10.

## 2.11 Modern Parametrisations of Parton Densities.

The measurement of structure functions serves two main purposes, to test QCD as the theory of the strong interactions and to extract the, as yet, uncalculable parton distributions functions (PDFs). In this section the most recent parametrisations of the parton densities are introduced. Most of them are obtained using the DGLAP evolution equations to evolve parton densities to the measured values of  $Q^2$ . The  $x$  dependence of the parton densities are parametrised from a starting scale  $Q_0^2$ . The parameters are chosen by a  $\chi^2$  minimisation over data from structure functions in deep-inelastic  $e, \mu$  or  $\nu$  scattering; measurements of Drell-Yan production and  $W$ -asymmetry in  $p\bar{p}$  collision as well as prompt photon production in  $pN \rightarrow \gamma X$ .

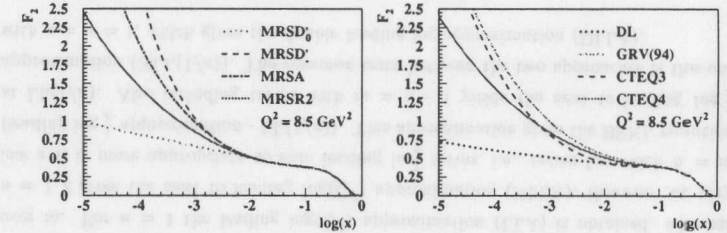


Figure 2.11: The proton structure function  $F_2$  according to the parametrisations of the MRS group (left) and the CTEQ group, GRV and Donnachie-Landshoff (right) at  $Q^2 = 8.5 \text{ GeV}^2$ .

### Martin-Roberts-Stirling (MRS)

The MRS parametrisation, obtained using the next-to-leading order DGLAP evolution, uses the following functional form for the quark and gluon distributions at the starting scale  $Q_0^2$  in the  $\overline{MS}$  renormalisation scheme

$$x f_i(x) = A_i \cdot x_i^\delta (1-x)^{\eta_i} (1 + \epsilon_i \sqrt{x} + \gamma_i x) \quad (2.28)$$

where  $f_i(x)$  is a particular parton density and  $A_i, \delta_i, \eta_i$  and  $\gamma_i$  are the parameters to be determined. Not all normalisations  $A_i$  are free parameters, but some are fixed from flavour or momentum sum rules. The charmed sea, assumed to be  $c(x, Q^2) = 0$  for  $Q^2 \leq m_c^2$ , is generated by the boson gluon fusion process as included in the DGLAP equations for massless partons. Pre-HERA parametrisations such as MRSD<sub>L</sub> and MRSD<sub>D</sub> [134] and the newer MRSA [135], which includes 1993  $F_2$  data from ZEUS and H1, start at  $Q_0^2 = 4 \text{ GeV}^2$ , whereas for the latest fits (MRSR) a low starting scale of  $Q_0^2 = 1 \text{ GeV}^2$  has been chosen. The main differences between the previous PDFs, apart from the data sets included in the fit, is the choice of the parameter  $\delta$ , which dominates the behaviour

at small  $x$

$$\begin{aligned} xg(x) &\sim x^0 && \text{MRSD}'_0 \\ xg(x) &\sim x^{-0.5} && \text{MRSD}'_- \\ xg(x) &\sim x^{-0.3} && \text{MRSa} \end{aligned}$$

where MRSD'\_0 and MRSD'\_- span the range of exponents as expected from lower energy DIS and hadron-hadron data or inspired by the solution of the BFKL equation respectively. The MRSa parameters are by construction consistent with the 1993 HERA data. Structure functions at  $Q^2 < Q_0^2$  have been determined by a backward evolution with a suppression factor  $\frac{Q^2}{Q^2 + \alpha^2}$  [136]. The  $\delta$  parameter for two of the four new MRSR fits is

	R <sub>1</sub>	R <sub>2</sub>	R <sub>3</sub>	R <sub>4</sub>
	$\lambda_s \neq \lambda_g$		$\lambda_s = \lambda_g$	
$\alpha_s(M_Z^2)$	0.113	0.120	0.113	0.120
$\Lambda_{\overline{MS}}^{(n_f=4)}$ (MeV)	241	344	241	344

Table 2.2: Characterising parameters of the four most recent MRS parametrizations MRSR.

varied independently for the gluon and sea quark distribution while in the other two, and in the older fits,  $\delta_s = \delta_g$  was chosen. The data available at that time did not have the precision to show any sensitivity to the expected small differences between  $\delta_s$  and  $\delta_g$ . In addition to two different treatments of the  $\delta$ 's the latest parton distributions are also given for two different assumptions on the values of  $\alpha_s$ , 0.113 and 0.120, or equivalently of  $\Lambda_{\overline{MS}}^{(4)} = 241$  MeV or 344 MeV. This is motivated by the tendency of HERA and TEVATRON data to prefer a larger value of  $\alpha_s$  than the high- $x$  DIS data, particularly that from BCDMS [164].

The MRSR parametrisation includes the 1994 HERA data on  $F_2$  with its much increased kinematic range (in particular to  $Q^2$  as low as 1.5 GeV<sup>2</sup>) and its improved precision.

A more detailed description of the MRS parametrisation is given in chapter 10. The  $x$  dependence of the old and new parametrizations is shown in figure 2.11.

#### CTEQ-Collaboration

The 'Coordinated Theoretical-Experimental Project on QCD' (CTEQ) uses a very similar approach to the MRS group. They parametrise their latest PDF, CTEQ4 [138], except a special low- $Q^2$  set, at  $Q_0^2 = 2.56$  GeV<sup>2</sup>. For the quark distributions the same

functional form as in equation 2.28 is chosen, whereas the gluon density is parametrised as

$$xg(x) = A_0 x^{A_1} (1-x)^{A_2} (1+A_3 x^{A_4})$$

Previously (CTEQ3) a 'minimal' parametrisation with  $A_4 = 1$  and  $\delta_s = \delta_g$  has been used. CTEQ chooses a slightly different set of data constraining the strange distributions. They do not suppress the charm distribution below threshold but use the 'variable flavour technique'.

#### Glück-Reya-Vogt (GRV)

Whereas the parton distributions of the MRS and CTEQ groups depend strongly on the input parametrizations at  $Q_0^2$  this is, to a much lesser extent, the case for the GRV group [102]. Their basic idea was that at very low starting scale  $Q_0^2 = 0.34$  GeV<sup>2</sup> the nucleon only consists of constituent valence quarks. With increasing  $Q^2$  the gluon and sea quarks would be generated dynamically from the valence quarks via the DGLAP evolution equations. As not all relevant data, in particular the prompt photon data, could be described adequately with this model, gluon and sea quark distributions had to be added at the starting scale. But these distributions have a valence like shape

$$xg(x, Q_0^2) = Ax^\alpha(1-x)^\beta; \quad x\bar{q}(x, Q_0^2) = A'x^{\alpha'}(1-x)^{\beta'}$$

Charm is treated as a heavy quark. There is no concept of charmed parton distributions. Their contribution to  $F_2$  comes from the Boson Gluon Fusion process and is calculated via the DGLAP evolution with massive quark coefficient functions. The DGLAP evolution from the very low starting scale  $Q_0^2$  ensures that the behaviour of the gluon and sea quark densities at small  $x$  for the  $Q^2$  range  $Q^2 \gtrsim 1$  GeV<sup>2</sup>, as described by GRV, is nearly a parameter free prediction of perturbative QCD dynamics.

#### Donnachie-Landshoff (DL)

In contrast to the parametrizations mentioned above the approach chosen by Donnachie and Landshoff [103] is based on Regge theory. The dependence of hadron-hadron or photon-hadron scattering cross sections as a function of the centre of mass energy square,  $s$ , is parametrised as

$$\sigma_{tot}(s) = A \cdot s^\epsilon + B \cdot s^{-\eta}$$

where  $\eta = 0.4524$  and  $\epsilon = 0.0808$  [104] are the values obtained in a global fit. This behaviour, extrapolated to  $Q^2 > 0$ , provides a parametrisation of  $F_2$ . The region of applicability is quoted to  $Q^2 < 10$  GeV<sup>2</sup>.

## 2.12 DIS Experiments.

A number of DIS experiments at SLAC, CERN and FNAL followed the first results on (unpolarised) deep-inelastic structure functions at SLAC and contributed to the effort of obtaining a fundamental and precise knowledge of properties of partons and of QCD. They used electron, muon and (anti-) neutrino beams on a variety of targets.

The SLAC experiments used electron beams with an energy range  $2.65 < E_e < 20$  GeV, on hydrogen and deuterium targets.

The CERN muon experiments EMC, BCDMS and NMC operated with beam energies  $100 < E_\mu < 280$  GeV, substantially extending the kinematic range to  $Q^2$  as large as 300 GeV and low values of  $x \simeq 7 \cdot 10^{-3}$ . They were complemented by the (anti-) neutrino program where the experiments CDHSW, CHARM, WA25, WA59 and BEBC-GGM studied the scattering of (anti-) neutrinos with  $100 < E_\nu < 280$  GeV off deuterium, iron, neon and other targets.

At FNAL the CCFR experiment used a neutrino beam of  $30 < E_\nu < 600$  GeV on an iron target and obtained structure function results at  $x$  as low as  $\sim 10^{-2}$ . The high muon beam energy of 490 GeV, used at the E665 experiment, in conjunction with special experimental techniques allowed structure function measurements to even lower values of  $x \sim 7 \cdot 10^{-4}$ . These, however, could only be reached at  $Q^2 \lesssim 1$  GeV.

The centre of mass energy at fixed target experiments, which were almost always inclusive, is given by

$$\sqrt{s} = \sqrt{2 m_{\text{target}} E_{\text{beam}}}$$

yielding a maximum value of  $\sqrt{s} \approx 35$  GeV. Their kinematic range in  $x$  and  $Q^2$  is shown in figure 2.12.

As HERA is an  $ep$  collider its centre of mass energy is related to the beam energies via

$$\sqrt{s} = \sqrt{4 E_e E_p}$$

With the design energies of  $E_e = 30$  GeV and  $E_p = 820$  GeV a centre of mass energy of  $\sqrt{s} \simeq 300$  GeV is achieved. As illustrated in figure 2.12 HERA extends the accessible kinematic range by almost two orders of magnitude in  $x$  and  $Q^2$ . While structure function measurements based on 1993 data were limited to  $Q^2 \gtrsim 6$  GeV<sup>2</sup> and left a gap to the fixed target region the 1994 data extend to  $Q^2$  values as low as  $\sim 1$  GeV<sup>2</sup> and provide an overlap with the NMC and E665 data. Additional detector components and special experimental techniques increased the HERA acceptance in 1995 even further down to  $Q^2 \simeq 0.1$  GeV<sup>2</sup> and  $x \simeq 2 \cdot 10^{-6}$ . This vastly extended kinematic region is the basis for exciting structure function results, a deeper insight into the structure of the proton and a better understanding of QCD.

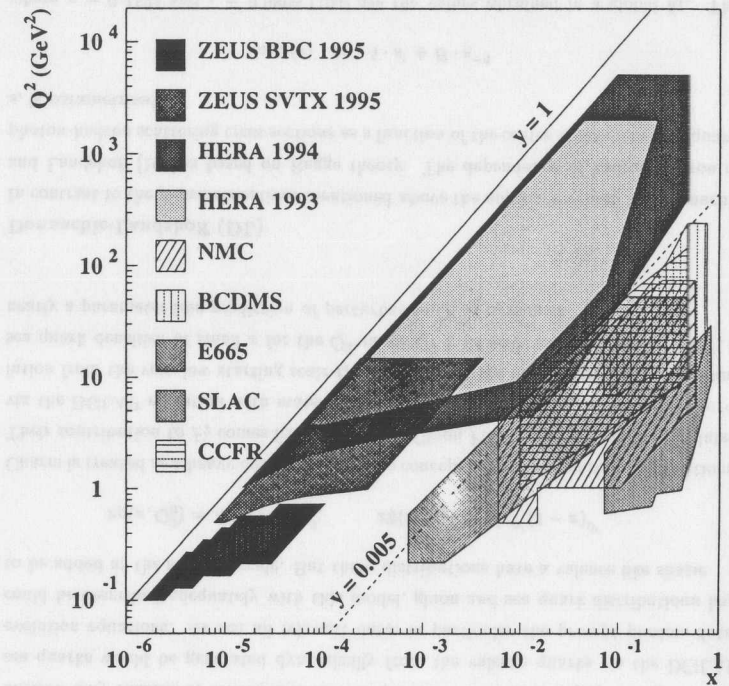


Figure 2.12:  $(x, Q^2)$  range of various DIS experiments that contributed to structure function data.

Further details about nucleon structure functions and their interpretation and role in QCD can be found in [38, 37, 39].

## Chapter 3

# The ZEUS Detector at HERA.

### 3.1 The HERA Accelerator.

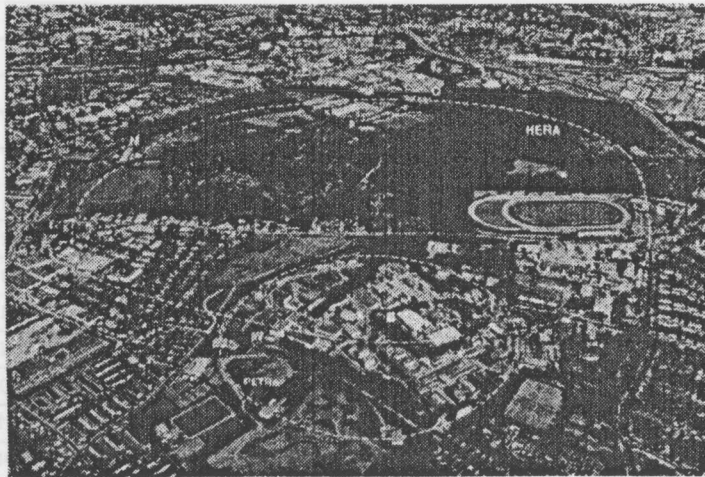


Figure 3.1: The 'Volkspark' in Hamburg surrounded by the HERA collider (dashed line). The pre-accelerator PETRA, enclosing the main DESY site, is shown in the foreground.

The 'Hadron Elektron Ring Anlage' (HERA) is the first lepton proton collider. HERA is designed to accelerate electrons or positrons to 30 GeV and protons to 820 GeV energy, yielding a centre of mass energy  $\sqrt{s} = 314$  GeV. The beams are brought into collision at zero crossing angle at four interaction points. The two main experiments, H1 and ZEUS, are located in the north and south hall respectively. The remaining two halls have been allocated to the HERMES and HERA-B experiments. HERMES is designed to study the spin structure of the nucleon using the scattering of longitudinally polarised photons

### 3.1 The HERA Accelerator.

27

off polarised gas jet targets of hydrogen, deuterium or  $He^3$ . Longitudinally polarised photons are produced from the naturally occurring transversely polarised electrons using spin rotators. HERA-B is designed to investigate  $CP$  violation in the  $B^0\bar{B}^0$  system. It uses a wire target for the production of  $B$ -mesons in the proton halo.

HERA is located under the 'Volkspark' in Hamburg, Germany, close to the main site of the DESY laboratory (figure 3.1). It was commissioned in 1991, first  $ep$  interactions were observed and recorded in H1 and ZEUS during spring 1992.

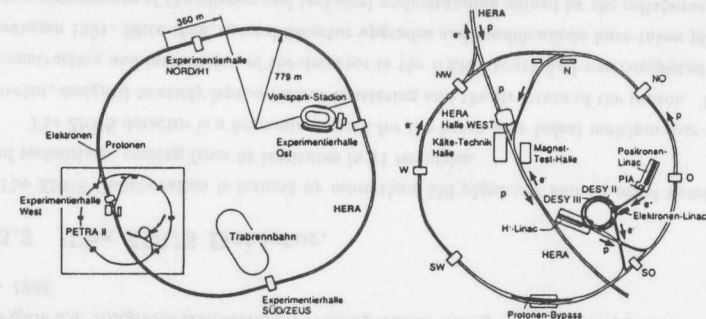


Figure 3.2: HERA accelerator complex with four experimental halls (left) and the pre-accelerator system (right).

Figure 3.2 shows a schematic layout of the HERA accelerator complex. Two separate rings for electrons<sup>1</sup> and protons, using conventional and superconducting magnets respectively, are housed in a 6.34 km long tunnel 10 – 30 m underground.

The proton acceleration chain starts with a  $H^-$  50 MeV linear accelerator. Before injection into the DESY III storage ring, the electrons are stripped off the hydrogen ions, yielding protons. DESY III is filled with 11 proton bunches, having the same bunch spacing as HERA, 96 ns, and accelerated to 7.5 GeV. The proton bunches are then transferred to PETRA<sup>2</sup>. Seventy bunches are accumulated there and accelerated to 40 GeV, then transferred to HERA. This process is repeated until HERA is filled with up to 210 bunches. After acceleration to 820 GeV the proton beam lifetime is of the order of several days.

The electron injection begins with the LINACs I and II which accelerate the electrons to 220 and 450 MeV, respectively, and fill the positron intensity accumulator (PIA) with a single bunch of up to 60 mA. This bunch is then transferred to DESY II and accelerated to 7.5 GeV. The transfer to the PETRA II storage ring is performed

<sup>1</sup>From the middle of 1994 on positrons were accelerated instead of electrons in order to increase the lepton beam lifetime. In the following electron is used as a generic expression for the colliding lepton.

<sup>2</sup>PETRA = 'Positronen-Elektronen Tandem Ring Anlage.'

HERA parameters	Design values		1994	
	electrons	protons	positrons	protons
Energy (GeV)	30	820	27.52	820
Centre of mass energy (GeV)	314		300	
Specific luminosity ( $\text{cm}^{-2}\text{s}^{-1}\text{mA}^{-2}$ )	$3.9 \cdot 10^{29}$		$3.4 \cdot 10^{29}$	
Instantaneous luminosity ( $\text{cm}^{-2}\text{s}^{-1}$ )	$1.7 \cdot 10^{31}$		$3.0 \cdot 10^{30}$	
Integrated luminosity (pb)	100		6	
Circumference (m)	6336			
Magnetic field (T)	0.165	4.65	0.165	4.65
Injection energy (GeV)	14	40	14	40
Current (mA)	58	163	20 - 33	30 - 55
Energy loss per turn (MeV)	127	$1.4 \cdot 10^{-10}$	127	$1.4 \cdot 10^{-10}$
Number of bunches	210		153 + 15	153 + 17
Bunch crossing time (ns)	96		96	
Beam $\sigma_x$ (mm) at IP	0.30	0.27	0.27	0.18
Beam $\sigma_y$ (mm) at IP	0.06	0.09	0.06	0.06
Beam $\sigma_z$ (mm) at IP	0.8	11	0.8	11
Injection time (min)	15	20	45	60

Table 3.1: HERA design parameters and performance during 1994 running

such that 70 bunches of 96 ns spacing are obtained. After acceleration to 14 GeV the electron bunches are transferred to HERA until this is filled with up to 210 bunches. After acceleration to 27.52 GeV the positron beam life time is about 8 hours<sup>3</sup>. In practice not all bunches are filled. Unpaired bunches, called pilot bunches, can be used to estimate beam related background rates, while empty bunches allow the estimation of background rates originating from cosmic rays. In the 1994 data taking period HERA operated with 153  $ep$  bunches, 15 electron- and 17 proton-pilot bunches.

The design parameters and performance of the HERA machine during the 1994 data taking period are summarised in table 3.1 [40, 41].

Since the first electron proton collisions in May 1992 the integrated luminosity delivered by HERA has been continuously increased (see figure 3.3). In 1994 HERA delivered  $\sim 6 \text{ pb}^{-1}$  integrated luminosity. For about  $2.5 \text{ pb}^{-1}$  ZEUS was operational, with all main components in good conditions. The present analyses are based on this data set.

<sup>3</sup>For electrons a life time of only 2 - 3 hours could be achieved.

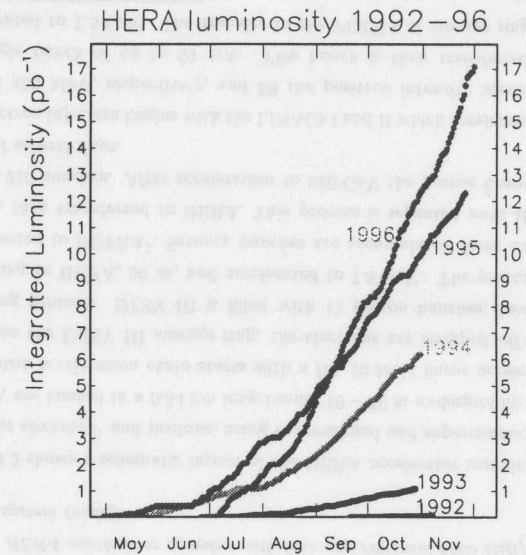


Figure 3.3: Integrated luminosity delivered by HERA during the data taking periods 1992 - 1996.

### 3.2 The ZEUS Detector.

The ZEUS Collaboration is formed by more than 450 physicists and an equal number of technicians, coming from 51 institutes in 11 countries.

The ZEUS detector is a hermetic (except for the beam-pipe holes) multipurpose detector, designed to study lepton-hadron scattering and the structure of the proton. The construction and installation of the detector in the HERA south hall was completed by autumn 1991. Since then, several detector upgrades and modifications have taken place as a consequence of the physics and technical understanding gained by the collaboration during the first years of data taking.

The ZEUS coordinate system is defined as a right-handed orthogonal system with the origin at the nominal interaction point (IP), and the  $z$ -axis pointing in the outgoing proton direction (defined as forward direction). In this frame, the  $x$ -axis points towards the centre of the HERA ring, the  $y$ -axis upwards. Thus, the proton beam polar angle is  $0^\circ$ , whereas the electron beam polar angle is  $180^\circ$ . The azimuthal angle  $\phi$  is measured with respect to the  $x$ -axis.

Figure 3.4 and 3.5 show the longitudinal and transverse (with respect to the beam direction) layouts of ZEUS, respectively.

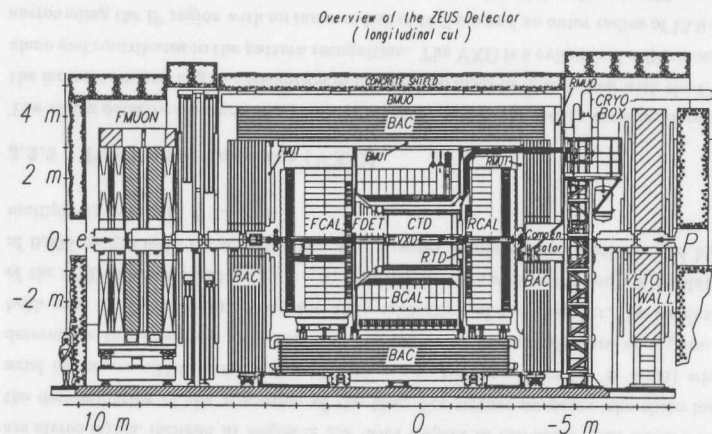


Figure 3.4: Cross section of ZEUS along the beam direction.

A brief outline of the major detector components is given in the following. The parts of the detector essential for the present analyses are described in more detail in the following sections. A more general and complete description can be found in [42].

Starting from the centre, ZEUS consists of charged particle tracking detectors (Vertex Detector, VXD, and Central Tracking Detector, CTD). The CTD is surrounded by a superconducting magnet providing a field of 1.43 T. Forward and rear tracking chambers (FTD and RTD) provide additional tracking information and particle identification in the forward and rear direction. The tracking chambers are surrounded by a high resolution Uranium Calorimeter (UCAL). The UCAL is divided into three sections: the FCAL in the forward direction, the RCAL in the rear direction, and the BCAL, a barrel section surrounding the central region. The small angle rear tracking detector (SRTD) is situated behind the RTD and covers the face of the RCAL to a radius of  $\sim 34$  cm around the centre of the beam-pipe hole. At a longitudinal depth of  $3 X_0$  in the RCAL the hadron-electron separator (HES), consisting of  $3 \times 3$  cm<sup>2</sup> silicon diodes, is installed for the discrimination between electromagnetic and hadronic showers originating from low energetic particles ( $< 5$  GeV). The UCAL is enclosed by muon identification chambers (FMUI, BMUI and RMUI) on the inner side of the iron yoke. The yoke itself serves as absorber for the backing calorimeter (BAC), which measures the energy of late showering particles, and as the return path for the solenoid magnetic field flux. On the other side of the yoke, the outer muon chambers are installed (FMUON, BMUON, RMUON). Behind the main detector at  $z = -7.5$  m an iron/scintillator VETOWALL is used to reject beam-related background. The C5 beam monitor, a small lead-scintillator counter, located around the beam pipe at  $z = -3.15$  m, monitors the synchrotron radiation

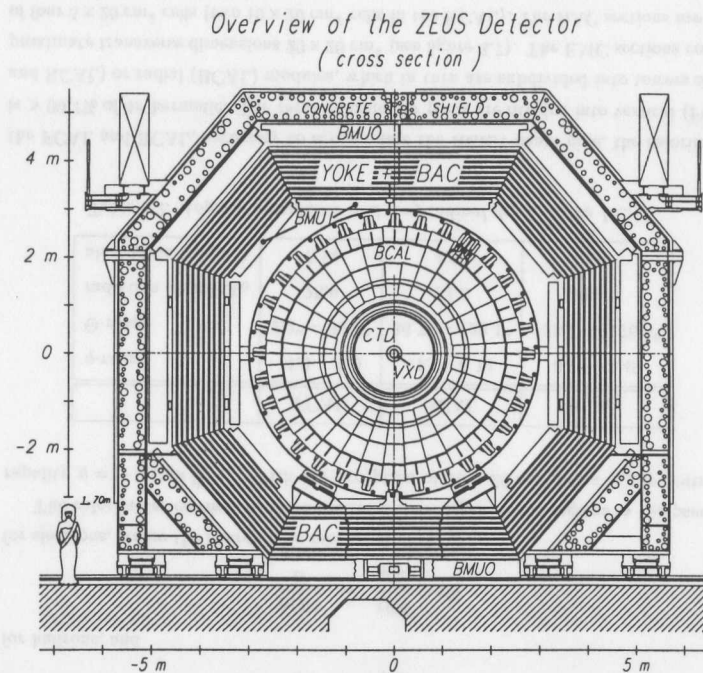


Figure 3.5: Cross section of ZEUS perpendicular to the beam direction.

accompanying the beams and the timing and longitudinal structure of the proton and electron bunches. At  $\sim 20 - 90$  m downstream in the proton beam direction the leading proton spectrometer (LPS) and the forward neutron calorimeter (FNC) detect protons and neutrons scattered through small angles, respectively. The proton remnant tagger (PRT), a lead-scintillator counter, located at  $z = 5.1$  m around the beam pipe, covers a pseudorapidity<sup>4</sup> range  $4.3 < \eta < 5.8$  and provides information about the hadronic final state particles in the very forward direction, i.e. about dissociating outgoing protons. In the electron beam direction two small lead/scintillator calorimeters are installed at  $-34$  m and  $-104$  m for the measurement of outgoing photons, used for the luminosity determination, tagging of  $Q^2 \approx 0$  scattering and radiative events.

The short time interval of 96 ns between the bunch crossing at HERA results in a nominal rate of 10 MHz. ZEUS uses a three-level trigger system to reduce the rate to a few Hz, a level at which data can be written to tape.

<sup>4</sup>The pseudorapidity is defined as  $\eta = -\ln(\tan \frac{\theta}{2})$ .

### 3.2.1 The Central Tracking Detector (CTD).

The central tracking detector (CTD) [43] measures the direction and momentum of charged particles with high precision and estimates the energy loss  $dE/dx$  used for particle identification. The CTD is a cylindrical drift chamber with an inner radius of 18.2 cm, outer radius 79.4 cm and length of 205 cm, filled with a gas mixture of argon,  $\text{CO}_2$  and ethane. It covers a polar angle of  $15^\circ < \Theta < 164^\circ$  and consists of 72 radial layers, organised into 9 superlayers (see figure 3.6). The odd superlayers are

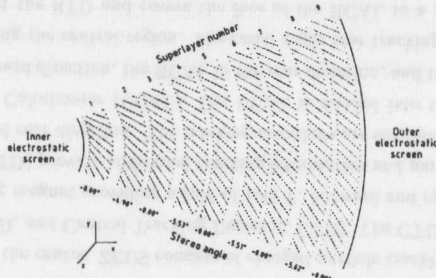


Figure 3.6: CTD wedge, showing the sense and field wires. The stereo angle for each superlayer is also given.

axial layers which have sense wires parallel to the beam axis, while the even superlayers are stereo layers, inclined at angles  $\simeq \pm 5^\circ$  with respect to the beam axis, which allows the determination of the  $z$ -position of the hits. For trigger purposes, the three inner axial layers are additionally equipped with a  $z$ -by-timing system ( $\sigma_z \simeq 4$  cm) which determines the  $z$ -position of a hit from the difference in arrival times of a pulse at both ends of the chamber. With the 1994 calibration of the chamber, the resolution of the CTD is around  $230 \mu\text{m}$  in  $r - \phi$ , resulting in a transverse momentum resolution of  $0.005 p_T \oplus 0.0016$  for long tracks. The  $z$ -vertex resolution for medium- and high-multiplicity events is  $\lesssim 1.5$  mm.

### 3.2.2 The Vertex Detector (VXD).

The vertex detector measures the event vertex and possibly secondary vertices, improves the momentum and angular resolution of charged particles as determined with the CTD alone and contributes to the pattern recognition. The VXD is a cylindrical drift chamber surrounding the IP region with an inner radius of 10.9 cm and an outer radius of 15.9 cm, equipped with 12 layers of 1.6 m long sense wires. In 1994 high voltage problems and damage due to synchrotron radiation caused part of the VXD to be off, particularly during the second half of the data taking period.

### 3.2.3 The Uranium Calorimeter (UCAL).

The ZEUS calorimeter is a high resolution uranium-scintillator compensating calorimeter [44]. The uranium calorimeter is one of the most essential detector components for the reconstruction of  $ep$ -scattering events and plays a crucial role for the present analyses. The UCAL is a sampling calorimeter, consisting of alternating layers of depleted uranium<sup>5</sup> as absorber and scintillator<sup>6</sup> as active material for readout purposes. The thickness of the plates (2.6 mm scintillator and  $3.3 \text{ mm} \doteq 1 X_0$  uranium) has been chosen to optimize the compensation of the calorimeter. Compensation means that electromagnetic and hadronic showers of equal energy yield equal response in the calorimeter ( $e/h = 1$ ). This characteristic is particularly important for the energy resolution of hadrons as hadronic showers have a statistically fluctuating electromagnetic component. The energy resolution of the ZEUS calorimeter, measured under test beam conditions, is

$$\frac{\sigma(E)}{E} = \frac{35\%}{\sqrt{E}} \oplus 2\%$$

for hadrons, and

$$\frac{\sigma(E)}{E} = \frac{18\%}{\sqrt{E}} \oplus 1\%$$

for electrons, where the energy  $E$  is measured in GeV.

The calorimeter consists of three sections, covering different regions in the pseudorapidity  $\eta = -\ln(\tan \frac{\Theta}{2})$ . With the exception of  $20 \times 20 \text{ cm}^2$  holes in the centre of

	FCAL	BCAL	RCAL
$\eta$ -range	-4.0 - -1.0	-1.1 - 0.74	0.72 - 3.49
$\Theta$ -range	$2.2^\circ - 39.9^\circ$	$36.7^\circ - 129.1^\circ$	$128.1^\circ - 176.5^\circ$
radiation length $X_0$	25.9	24.6	24.3
absorption length $\lambda$	7.14	4.92	3.99

Table 3.2: Angular acceptance and longitudinal depth of the UCAL.

the FCAL and RCAL, necessary to accommodate the HERA beam pipe, the calorimeter is  $> 99.7\%$  of  $4\pi$  hermetic. The three calorimeter parts are divided into vertical (FCAL and RCAL) or radial (BCAL) modules, which in turn are subdivided into towers of approximate transverse dimensions  $20 \times 20 \text{ cm}^2$  (see figure 3.7). The EMC sections consist of four  $5 \times 20 \text{ cm}^2$  cells (two  $10 \times 20 \text{ cm}^2$  cells in the RCAL). The HAC sections are cells

<sup>5</sup>An alloy of 98.4%  $U^{238}$ , 1.4% Nb and  $\leq 0.2\%$   $U^{235}$

<sup>6</sup>SCSN-38

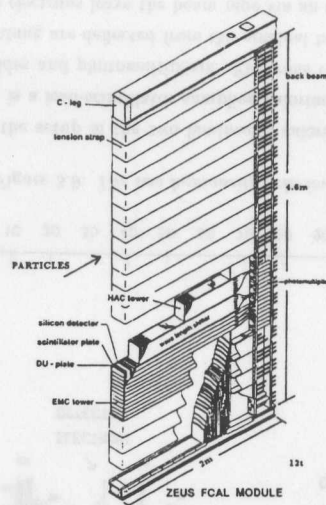


Figure 3.7: ZEUS FCAL module. The  $20 \times 20 \text{ cm}^2$  towers with their longitudinal division into EMC and HAC section are shown.

on their own. Each tower is segmented longitudinally into an inner, electromagnetic section (EMC) and two (RCAL only one) outer, hadronic sections (HAC1 and HAC2).

The longitudinal depth of the UCAL (table 3.2) is chosen such that 90% of all recorded jets deposit at least 95% of their energy in the UCAL [45].

Each calorimeter cell is read out on two opposite sides by two photomultiplier tubes (PMTs) coupled to the scintillator via wavelength shifters. As the energies corresponding to both PMTs are summed, the energy measurement is independent of the impact point of the particle within the cell. Comparison of the two PMT signals allows the determination of the horizontal impact point of the particles within a cell (see section 5.4.4.2).

The calorimeter is calibrated on channel-by-channel basis using the radioactive decay of  $U^{238}$ , which provides a constant reference signal. This calibration procedure is good to 1%. The PMTs can be calibrated via light emission of known intensity from LEDs. The rest of the electronic readout chain is calibrated using test pulses.

The calorimeter also provides accurate timing information with a time resolution better than 1 ns for energy deposits greater than 4.5 GeV. The total time of a calorimeter section (F/B/RCAL) is obtained from an energy weighted average of the times of all PMTs with energy deposits greater than 200 MeV.

### 3.2.4 The Small Angle Rear Tracking Detector (SRTD).

For a precise measurement of the scattered electron energy and angle, for low  $Q^2$  events in low- $x$  DIS, additional tracking is needed to improve the calorimeter reconstruction in regions close to the RCAL beam-pipe hole. It has also found to be useful to correct for energy loss due to the presence of inactive material in this detector region (VXD cables, flanges etc.).

The SRTD, installed at the beginning of 1994, is a scintillator strip detector at the face of the RCAL ( $z = -148 \text{ cm}$ ) and covers an area of  $68 \times 68 \text{ cm}^2$  around the RCAL beam-pipe hole (except for the  $20 \times 20 \text{ cm}^2$  hole itself) [46, 47]. Figure 3.8 shows a

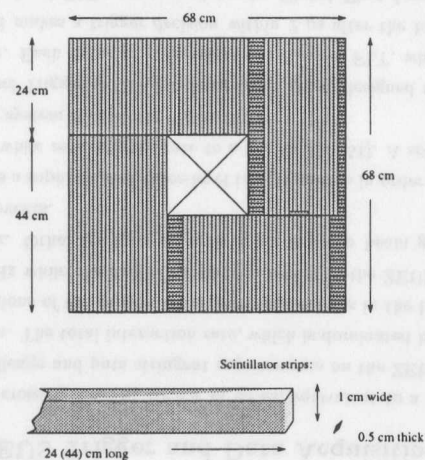


Figure 3.8: Schematic diagram of the SRTD showing the orientation of the scintillator strips, arranged in two planes and four quadrants.

schematic diagram of the detector layout. Charged particles are detected by two planes of orthogonally arranged ( $x, y$ ) strips with a 1 cm pitch which provide position and pulse height information via an optical fibre-photomultiplier readout. Each plane is divided into four quadrants.

SRTD hit information is used in conjunction with that from the CTD for track reconstruction. More importantly the SRTD can detect the preshowering of particles in the inactive material in front of the calorimeter. The energy deposit in the SRTD can be used to correct for these energy losses, so that the SRTD serves as a presampler. The SRTD also helps to reject background by providing a fast time measurement (resolution  $\sim 2 \text{ ns}$ ) to the trigger, complementing the rejection by the C5 and VETOWALL counters.

### 3.2.5 The Luminosity Monitor (LUMI).

The precise measurement of the time-integrated luminosity is a crucial aspect of all cross section and therefore of all structure function measurements. The  $ep$  luminosity at HERA is measured by the luminosity monitor using the rate of hard bremsstrahlung photons from the Bethe-Heitler process [48].

$$ep \rightarrow e'\gamma$$

The cross section for this process is high and well known from theoretical calculations to an accuracy of 0.5%.

## LUMINOSITY MONITOR 94

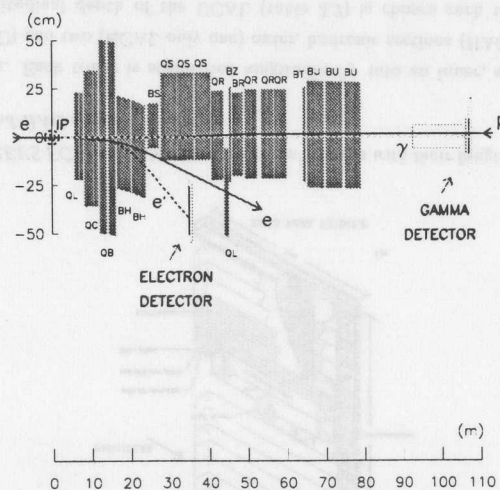


Figure 3.9: The two luminosity calorimeters.

Figure 3.9 shows the setup of the two luminosity calorimeters [49]. The electron calorimeter (LUMI-e) is a lead-scintillator sampling calorimeter. It is  $23 X_0$  deep and read out via light guides and photomultipliers. Electrons that have lost part of their energy via bremsstrahlung are deflected from the nominal beam orbit by the magnetic field of HERA. These electrons leave the beam pipe via an exit window at  $z = -27$  m and are detected by the LUMI-e at  $z = -34$  m. The geometrical acceptance is limited to the detection of electrons with  $0.2 \cdot E_{beam} < E'_e < 0.8 \cdot E_{beam}$ . The energy resolution is  $\frac{\sigma(E)}{E} = \frac{18\%}{\sqrt{E}}$  with  $E$  measured in GeV. The electron position is determined by scintillator

### 3.3 The ZEUS Trigger and Data Acquisition System.

fingers at a depth of  $7 X_0$ . The LUMI-e not only detects electrons from bremsstrahlung processes but also from photoproduction events, where the electron scattering angle is very small due to the negligible momentum transfer.

Photons radiated at angles  $\Theta_\gamma \leq 0.5$  mrad with respect to the beam axis leave the beam pipe undeflected via a copper/beryllium exit window at  $z = -92$  m and are detected in the photon calorimeter (LUMI- $\gamma$ ). The LUMI- $\gamma$  is a lead-scintillator calorimeter situated at  $z = -104$  m and is protected against synchrotron radiation by a  $3.5 X_0$  carbon/lead filter. The LUMI- $\gamma$  energy resolution under test beam conditions is  $18\%/\sqrt{E}$  (GeV), which is reduced to  $25\%/\sqrt{E}$  (GeV) by the filter. In the ISR analysis the LUMI- $\gamma$  is not only used for the measurement of the luminosity but also for the detection of collinearly radiated photons in the initial state.

### 3.3 The ZEUS Trigger and Data Acquisition System.

The short bunch crossing time at HERA of 96 ns, equivalent to a rate of  $\sim 10$  MHz, is a technical challenge and puts stringent requirements on the ZEUS trigger and data acquisition system. The total interaction rate, which is dominated by background from upstream interactions of the proton beam with residual gas in the beam pipe, is of the order 10 – 100 kHz while the rate of  $ep$  physics events in the ZEUS detector is of the order of a few Hz. Other background sources are electron beam gas collisions, beam halo and cosmic events.

ZEUS employs a sophisticated three-level trigger system in order to select  $ep$  physics events efficiently while reducing the rate to a few Hz [50, 51]. A schematic diagram of the ZEUS trigger system is shown in figure 3.10.

The First Level Trigger (FLT) is a hardware trigger, designed to reduce the input rate below 1 kHz. Each detector component has its own FLT, which stores the data in a pipeline, and makes a trigger decision within  $2 \mu\text{s}$  after the bunch crossing. The decision from the local FLT's are passed to the Global First Level Trigger (GFLT), which decides whether to accept or reject the event, and returns this decision to the component readout within  $4.4 \mu\text{s}$ .

If the event is accepted, the data are transferred to the Second Level Trigger (SLT), which is software-based and runs on a network of Transputers. It is designed to reduce the rate below 100 Hz. Each component can also have its own SLT, which passes a trigger decision to the Global Second Level Trigger (GSLT) [52]. The GSLT decides then on accepting or rejecting the event.

If the event is accepted by the GSLT, all detector components send their data to the Event Builder, which produces an event structure on which the Third Level Trigger (TLT) code runs. The TLT is software based and runs part of the offline reconstruction code on a farm of Silicon Graphics CPUs. It is designed to reduce the rate to a few Hz.

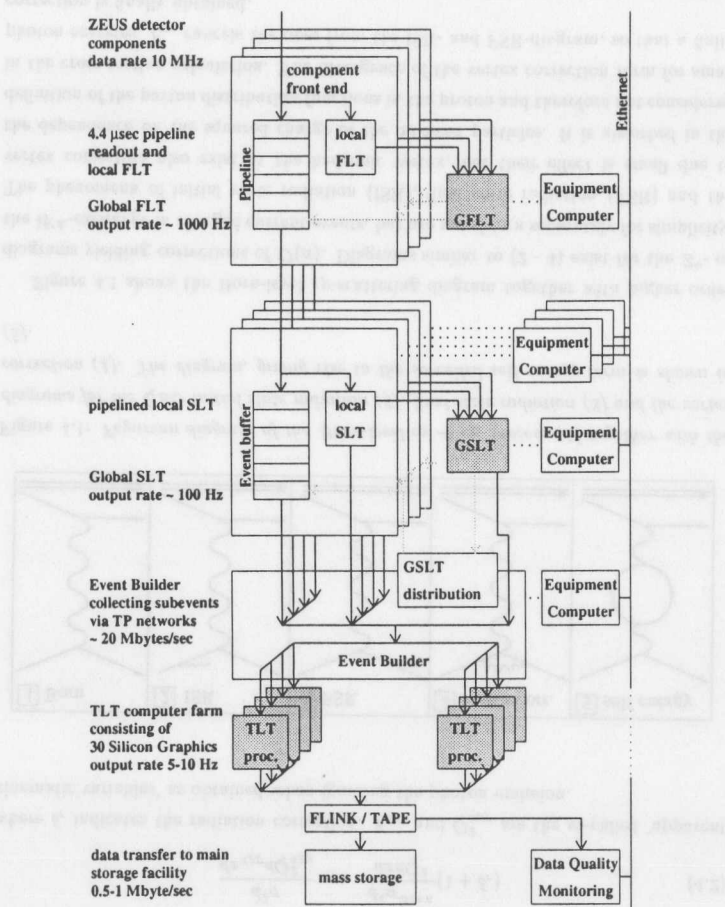


Figure 3.10: Schematic diagram of the ZEUS trigger and data acquisition system.

Events accepted by the TLT are written to tape via a fibre-link (FLINK) connection. The size of an event is typically  $\sim 100$  kBytes. From here on events are available for full offline reconstruction and data analysis.

The trigger logic used for the online selection of DIS events, on which the present analyses are based, is described in section 5.2.

## Chapter 4

# Monte Carlo Simulation.

### 4.1 Introduction.

Measurements of structure functions and cross sections require corrections for acceptance, efficiency and resolution effects of the detector and trigger system. As the detector components are highly complex and the trigger efficiency depends not only on the trigger hardware and its algorithms, but also on the event topology, analytic calculations are too complicated and hence not practical. Instead well established Monte Carlo techniques are used to simulate all relevant aspects of the ZEUS experiment. The simulation consists of two main parts. In the first part the  $ep$ -scattering process is simulated, focussing on the variation of the cross section with the event kinematics and the final state event topology. The second part simulates the detector and trigger response to the constellation of outgoing particles according to the detector geometry and testbeam results for the different components.

Not only the Born-level matrix element, but also QED and QCD corrections can be factorised in the Leading-Log-approximation (LLA). This is the basic property of higher order corrections which allows for a step-by-step procedure where the QED and QCD effects are described in separate programs.

The main concepts of the different simulation stages and their implementation in software packages is described in the following.

### 4.2 Electroweak Radiation at the Lepton Vertex.

On the Born-level the NC  $ep$ -scattering process is described by the single photon exchange between the electron and a quasi-free quark in the proton, as depicted in figure 4.1. The corresponding cross section is given by

$$\frac{d^2\sigma(\epsilon q \rightarrow \epsilon q)}{dx dy} = \frac{2\pi\alpha^2 e_q^2 s}{Q^4} [1 + (1-y)^2] \quad (4.1)$$

Higher order diagrams can lead to substantial corrections which have to be taken into account in the analysis. The emission of additional particles, mainly photons, does not only modify the cross section, but also affects the relation between event quantities measured in the detector, such as the scattered electron energy and angle, and the event kinematics at the hadronic vertex, where the proton structure is probed. Consequently the size of the radiative corrections depends on the chosen reconstruction method. The net effect is written as

$$\frac{d^2\sigma}{dx_{app}dQ_{app}^2} = \frac{d^2\sigma^{Born}}{dx_{app}dQ_{app}^2} (1 + \delta_r) \quad (4.2)$$

where  $\delta_r$  indicates the radiation correction.  $x_{app}$  and  $Q_{app}^2$  are the so-called 'apparent kinematic variables' as obtained when ignoring the photon emission.

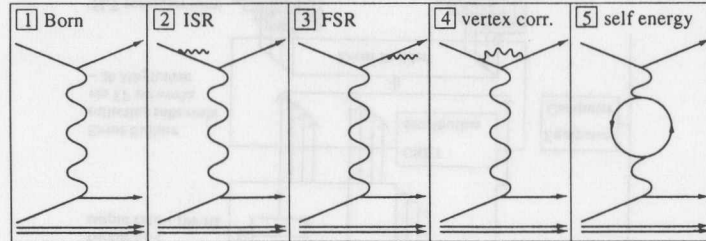


Figure 4.1: Feynman diagram of the Born-level  $eq \rightarrow eq$  process (1) together with the diagrams for the QED initial state radiation (2), final state radiation (3) and the vertex correction (4). The diagram, giving rise to the so-called self-energy term is shown in (5).

Figure 4.1 shows the Born-level  $ep$ -scattering diagram together with higher order diagrams yielding corrections of  $\mathcal{O}(\alpha)$ . Diagrams similar to (2 - 4) exist for the  $Z^0$ - or the  $W^\pm$ -exchange in charged current events, but are not shown separately for simplicity. The phenomena of initial state radiation (ISR), final state radiation (FSR) and the vertex correction also exist at the hadronic vertex, but their effect is small due to the dependence on the squared charge of the involved particles. It is absorbed in the definition of the parton distribution functions in the proton and therefore not considered in the cross section calculation. The divergence of the vertex correction term for small photon energies,  $E_\gamma$ , cancels the ones from the ISR- and FSR-diagram, so that a finite correction is finally obtained.

Additional contributions to  $\mathcal{O}(\alpha)$ -corrections originate from interferences between the Born diagram and two-photon exchanges (not shown) or the self-energy terms. In the latter all charged fermions with  $m^2 \leq Q^2$  have to be considered in the loop and this

results in the  $Q^2$ -dependence of the electromagnetic coupling  $\alpha_{em}$ .

The NC-DIS process  $eq \rightarrow eq\gamma$  including photon and  $Z^0$ -exchange and first order electroweak radiative corrections has been simulated using the Monte Carlo generator HERACLES [57]. The program operates at the parton level. Events are completely described by the flavour of the struck quark  $q$  and the four-momentum of the final state electron, quark and the potentially radiated photon.

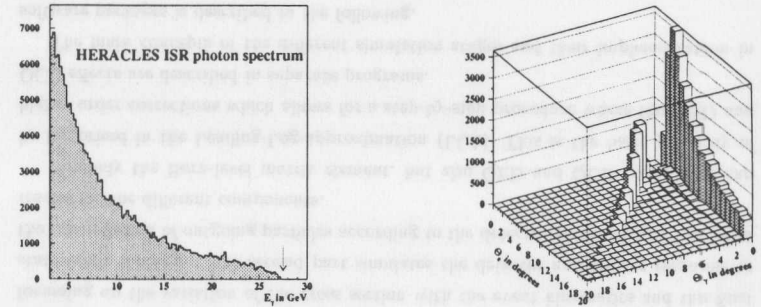


Figure 4.2: Left: ISR photon energy spectrum as generated using HERACLES. The arrow indicates the upper limit, given by the electron beam energy. Right: Correlation between the angular distributions of the scattered electron and the radiated photon. Two clear bands, originating from ISR and FSR events, are visible.

Figure 4.2 shows the photon energy spectrum in ISR events as generated by HERACLES. The electron beam energy of 27.52 GeV sets an upper limit on the photon energy. The correlation between the final state electron and photon angle (figure 4.2, right) shows two clear bands, one for events with  $\Theta_e \approx \Theta_\gamma$  (FSR) and one for  $\Theta_e \approx 0$  (ISR).

Figure 4.3 shows the radiative corrections as a function of  $y_{app}$  for the electron reconstruction method (section 6.3). For  $y_{app} \rightarrow 1$  the scattered electron energy decreases so that the available phase space for photon radiation increases and the resulting radiative correction can be as large as 200%. At low- $y$  only soft photons can be emitted, yielding rather small radiative corrections unless  $x$  is very large.

In addition to the leading order diagrams, already taken into account in HERACLES, the program HECTOR [93] can also evaluate all non-negligible second order leading log terms as well as third order and higher order terms originating from soft photon exponentiation.

For the ' $p_T$ '-method (section 6.6), which is used in the main  $F_2$ -analysis, the difference between the leading order and higher order calculations is about 0.2% at  $Q^2$  of a few  $\text{GeV}^2$  and rises to 0.5% at a few  $100 \text{ GeV}^2$ . This difference is almost independent of  $y$  [94].

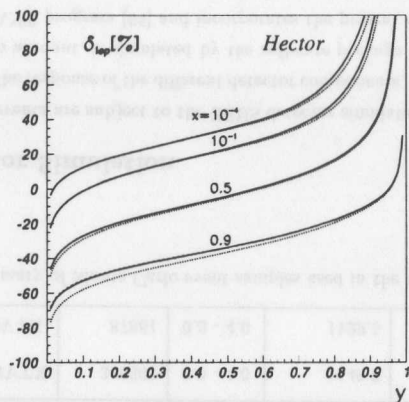


Figure 4.3: Radiative corrections in leptonic variables. Dotted lines:  $\mathcal{O}(\alpha)$ , dashed lines:  $\mathcal{O}(\alpha^2)$ , solid lines: in addition soft photon exponentiation.

In the analysis of ISR events the cross section is  $\mathcal{O}(\alpha^3)$  so that higher order corrections are  $\mathcal{O}(\alpha^4)$ . These corrections have been calculated [100], but are not included in HERACLES. However, additional final state radiation or the second emission of a collinear photon in the initial state do not contribute to the radiative corrections due to the electron and photon identification algorithms used in the present analyses. Hence the radiative corrections are estimated to be at most 5 – 10%.

### 4.3 Parton Distribution Functions.

The DIS NC cross sections in the Monte Carlo data sets of all three analyses have been generated according to the MRSA [135] structure function, modified at low- $Q^2$  as described in [136], using the PDFLIB software package [62]. These parametrisations, which have been obtained from fits to previous ZEUS and H1 measurements [109, 115] and other data sets, describe the density of quarks and gluons, i.e. the partons, in the proton at a given  $x$  and  $Q^2$ . These parametrisations provide an adequate description of the 1993- $F_2$  measurements at HERA.

However all Monte Carlo distributions, shown in the following chapters, have been reweighted to the parametrisations obtained from NLO-QCD fits to the respective data sets, as described in [118, 123, 124].

### 4.4 QCD-Cascade and Hadronic Final State.

In contrast to the single electron line at the lepton vertex the situation at the hadron vertex is more complicated. This is mainly due to the fact that the struck quark is not a free particle. As it carries net colour it is bound to the proton remnant by the colour flow. Also single free quarks are experimentally not observed but rather fragment into jets of hadrons.

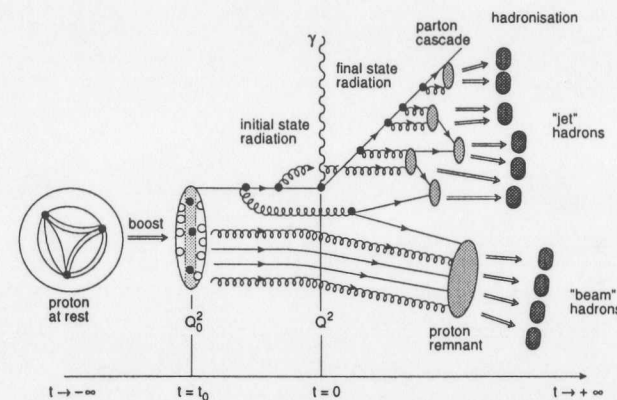


Figure 4.4: Schematic diagram of the DIS ep-scattering process, showing the different stages in the development of the hadronic final state.

Figure 4.4 shows the different stages of the virtual photon probing the proton structure and the development of the hadronic final state. The parton cascade is simulated using the colour dipole model (CDM) [58] supplemented by the Boson-Gluon-Fusion process (BGF). The BGF process is particularly important at low- $x$  due to the strong rise in the gluon density. In the CDM the colour dipole, formed by the struck quark and the proton remnant, radiates gluons, which can in turn emit softer gluons or split into quark-antiquark pairs.

The CDM-BGF model, as implemented in ARIADNE [59] provides at present the best description of the observed DIS non-diffractive hadronic final state [144]. In ARIADNE 4.06 diffractive events with a large rapidity gap, which have been observed in [54, 55], are thought to originate from a colour singlet exchange which is simulated by assuming that the struck quark originates from a colourless state in the proton, which carries only a small fraction of the latter's momentum. The parameters of the model are adjusted to be consistent with recent ZEUS measurements [56].

The output of the QCD-cascade serves as input to JETSET [60]. This program simulates the production of colourless hadrons in the final state using the LUND string

fragmentation model [61]. As partons move away from each other the colour strings between them expand and eventually fragment into shorter pieces which do not have enough energy to break further. Thereby hadrons are formed which are either long lived or resonances which decay rapidly to such states.

#### 4.5 Photoproduction Events.

In addition to the DIS Monte Carlo other Monte Carlo samples have been generated for studies and estimates of the photoproduction background contamination in the NVTX and the SVTX analysis. The minimum bias photoproduction events have been generated with  $0 \leq Q^2 \leq 4 \text{ GeV}^2$  at high- $y$  ( $y > 0.6$ ), using the PYTHIA 5.7 program [72]. Events with smaller  $y$  do not contribute to the photoproduction background. The cross sections are obtained from the ALLM parametrisations [139].

A summary of the Monte Carlo samples used in the three  $F_2$ -analyses is given in table 4.1.

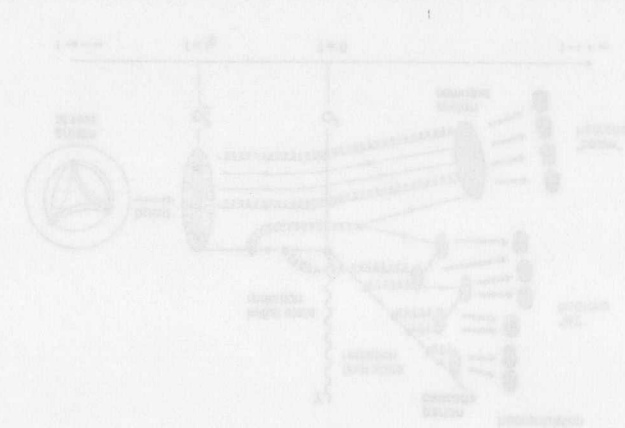
MC set	Nr. events	$Q^2$ range in $\text{GeV}^2$	cross section in $nbarn$	PDF para- metrisation
DIS - NVTX	1198287	$\geq 1.8$	862.27	MRSA'
DIS - SVTX	250833	$\geq 0.5$	3411.60	MRSA'
DIS - ISR	96310	$\geq 0.5$	78.32	MRSA'
PHP - NVTX	346301	0.0 - 4.0	1148.0	ALLM
PHP - SVTX	87861	0.0 - 4.0	1129.5	ALLM

Table 4.1: Summary of Monte Carlo event samples used in the three  $F_2$ -analyses.

#### 4.6 Detector Simulation.

All Monte Carlo events are subject to the ZEUS detector simulation and offline reconstruction chain. The response of the different detector components, taking their material and geometry into account, is simulated by the software package MOZART [63]. It is based on the GEANT program [65] and incorporates the present understanding of the detector and test beam results. The Monte Carlo samples considered here have been processed by the MOZART versions 12.1, 12.6 or 12.7. The differences between them do not affect components used in the presented  $F_2$ -analyses.

The ZEUS trigger decision is based on component signals and is simulated by the programme ZGANA [64]. The full offline event reconstruction, performed by the software package ZEPHYR, takes all calibration constants into account and treats data and Monte Carlo events in the same way. From here on the analyses do not differentiate between data or Monte Carlo events.



## Chapter 5

# The Data Sample

### 5.1 Introduction.

In this chapter the preselection, selection and reconstruction of the three samples of 1994 data used in the measurement of the proton structure function  $F_2(x, Q^2)$  are presented.

In order to extend the accessible kinematic range for the structure function measurement to lower values of  $Q^2$  two specific analyses have been performed. One is based on a small data set ( $\sim 58\text{nb}^{-1} \doteq 45379$  events), where the HERA setting was modified such that the interaction point was shifted from the nominal position of  $z = 0$  to  $z \simeq 65\text{cm}$ , yielding a larger detector acceptance for events with electrons scattered through a small angle ('shifted vertex - SVTX analysis').

The other analysis uses the main sample of  $2.4\text{pb}^{-1}$  ( $\doteq 1285668$  events) and exploits the fact that for constant energy and angle of the scattered electron the 4-momentum transfer  $Q^2$  depends linearly on the incoming electron energy ('initial state radiation - ISR analysis'). Therefore by selecting events with initial state photon radiation the electron beam energy is effectively lowered, resulting in an increased acceptance for low- $Q^2$  events.

The following description of the event reconstruction in the ZEUS detector focusses on the main analysis with the vertex at the nominal interaction point at  $+3\text{cm}$ , based on the  $\sim 2.4\text{pb}^{-1}$  sample ('nominal vertex - NVTX analysis'). Only for quantities of particular relevance or different characteristics in the various data sets a separate presentation is given.

In section 5.2 the event preselection and the requirements in the relevant trigger filters are presented.

The event vertex reconstruction is discussed in section 5.3. The vertex is of particular importance for the detector acceptance and trigger efficiencies as well as the reconstruction of kinematic variables via all angular quantities.

The essential tool in the identification of neutral current events is the electron finder. Crucial aspects such as its efficiency, the electron position reconstruction and the elec-

### 5.1 Introduction.

tron energy scale as well as appropriate correction methods are described in section 5.4.

In section 5.5 details of the use of the two luminosity calorimeters in the ISR analysis are given.

Subsequently the measurement of hadronic quantities and their corrections, particularly important for the ' $p_T$ '-method, are presented in section 5.6. The presence in the data sample of events with large rapidity gaps in the hadronic final state is also demonstrated and the resulting distributions of kinematic variables are shown and compared to those from the corresponding Monte Carlo samples.

Finally section 5.7 gives a discussion on backgrounds and appropriate subtraction methods.

## 5.2 Trigger and Preselection.

The main characteristics of a DIS event is the presence of the scattered electron in the final state. All three trigger stages of DIS events are therefore almost entirely based on the resulting electron signal in the calorimeter. The relevant quantities and their logical combination are described in the following.

### FLT

On the first trigger level the calorimeter trigger electronics provides several logical bits that indicate the presence of energy deposits above certain thresholds in the electromagnetic or hadronic calorimeter section. The required combination of these, arranged in the 1994 trigger slots, are:

- The **RCAL-IsoE** trigger [89] selects events with isolated electrons or muons in the RCAL. A group of up to 4 trigger towers with electromagnetic or minimum ionizing energy deposits is required to be surrounded by quiet trigger towers.
- The **RMECth** trigger requires the total electromagnetic energy deposit in the RCAL to be  $> 3.75$  GeV.
- The **REMC** trigger selects events with a total electromagnetic energy deposit in the RCAL of  $> 2.0(3.4)$  GeV, where the trigger towers next to the RCAL beamhole are ignored.
- The **BEMC** trigger selects events with more than 4.8 GeV total electromagnetic energy in the BCAL.
- Events with electrons in the FCAL are not specifically triggered on the electromagnetic FCAL energy, but on the event transverse energy,  $E_T$ .

The energy thresholds are tuned to obtain high trigger efficiencies with small background contamination and controllable trigger rates. For the later run range, corresponding to  $\approx 60\%$  of the luminosity one of the calorimeter FLT electronics cards (TEC) was not fully functioning, resulting in a reduced trigger efficiency. Selection cuts accounting for this effect are described in 5.4.4.1.

### SLT

On the second trigger level a logical **.OR.** of the FLT bits is required. In addition the quantity  $\delta$  is determined on the transputer network of the calorimeter SLT.  $\delta$  is defined as

$$\delta \equiv E - P_z = \sum_i E_i - P_{z,i} = \sum_i \delta_i$$

where  $E$  and  $P_z$  are the total energy and total longitudinal momentum of an event, and  $E_i$  and  $P_{z,i}$  are the same variables, but now referring to all final state particles in

an interaction. Since the positive  $z$ -direction in ZEUS has been chosen to point in the forward (the outgoing proton) direction, energy and longitudinal momentum for forward moving particles are essentially identical. Hence their contribution to  $\delta$  almost cancels to zero. For particles moving in the rear direction energy and longitudinal momentum are of opposite sign, so that their contribution to  $\delta$  is twice their energy.

$\delta$  is a conserved quantity. Ignoring possible particle losses in the forward or backward beamhole,  $\delta$  calculated from the initial state must be equal to the one from the final state.

$$\begin{aligned} \delta &= (E - P_z)_{proton} + (E - P_z)_{electron} \\ &\simeq (E_p - E_p) + (E_e - (-E_e)) \\ &= 2 \cdot E_e \end{aligned}$$

In all three analyses  $\delta$  is reconstructed from the calorimeter as

$$\delta = \sum_i E_i (1 - \cos \Theta_i)$$

where the sum is carried out over all calorimeter cells and the polar angle  $\Theta_i$  is determined from the cell centre and the primary event vertex.

In fully contained DIS events  $\delta$  is expected to peak at twice the electron beam energy, 55.04 GeV. However, in photoproduction events the contribution from the undetected electron is missing, resulting in much smaller values of  $\delta$ , peaking below 30 GeV.

In order to account for initial state radiation, where a significant fraction of the event  $E - P_z$  can be carried down the beampipe by the radiated photon, the DIS-SLT requires  $\delta' = E - P_z + 2 \cdot E_\gamma^{Lumi} > 24$  GeV. For studies of the  $\delta$ -distribution and photoproduction background contamination a prescaled<sup>1</sup> branch with  $\delta' > 15$  GeV was added.

### TLT

The third level trigger DIS filters used in the presented analyses require in addition to the afore defined FLT and SLT conditions also at least one of the electron identification algorithms 'Local' [97] or 'Elec5' [98] to find an electron candidate of 4 GeV or more.

In the following analyses only runs are considered in which the main detector components were fully functioning (as determined by EVTAK [90]) and in which the quality of relevant quantities such as the event timing lie within reasonable limits (as specified by DISTAKE94 [91]).

The luminosity of the finally selected runs corresponds to  $2.40 \text{ pb}^{-1} (\pm 1\%)$  in the NVTX and the ISR analyses and  $58.13 \text{ nb}^{-1} (\pm 2\%)$  in the SVTX analysis [101].

<sup>1</sup>Prescaling by a factor  $N$  means that only one out of  $N$  identified events is actually accepted and stored on tape.

### 5.3 Vertex Reconstruction.

It is important to understand the vertex reconstruction, both for the calculation of the detector and trigger acceptances as well as for the reconstruction of the event kinematics. Electrons, scattered through a small angle, are less likely to be detected in the rear calorimeter (RCAL) the closer their  $z$ -vertex is to the RCAL, since they simply vanish in the rear beam hole. The vertex also affects the determination of the electron scattering angle  $\Theta_e$ , the hadronic angle  $\gamma_h$  and the quantity  $E - P_z$ , where  $E$  is the total energy deposited in the calorimeter and  $P_z$  is the corresponding total longitudinal momentum. In addition the  $z$ -position of the event allows one to reduce background from beam-gas and cosmic ray events. In contrast to fixed target experiments the event vertex in ZEUS is determined predominantly from tracks originating from the charged particles of the hadronic final state.

The event vertex reconstruction uses primarily the central tracking detector and, if available, the vertex detector. The VCTRACK package [66] first performs the hit pattern recognition and reconstruction of tracks which are then fitted to a common vertex. In order to obtain a good vertex resolution, additional quality cuts are imposed on the tracking vertex in the analyses. The vertex fit from at least one track is required to give a  $\chi^2_{\text{vtx}}/ndf$  less than 5. Otherwise the event vertex is set to the mean value of the measured distribution, the nominal interaction point at +3 cm. For these events the vertex could be inferred from the time of flight of the final state particles to the FCAL and/or RCAL. The time resolution of  $\sim 1$  nsec for energy deposits larger than 400 MeV together with the requirement  $E_{\text{CAL}} > 5$  GeV result in a vertex resolution of  $\sim 12$  cm. However the timing behaviour of the ZEUS calorimeter is not yet simulated to the required precision in the Monte Carlo and hence is not used.

The fraction of events without a tracking vertex after final selection cuts is 22% for the NVTX analysis, 29% for the SVTX analysis and 28% for the ISR analysis.

Figure 5.1 shows the  $z$ -vertex distribution for the selected DIS data sample. The Monte Carlo vertex distribution has been generated according to a minimum-bias photoproduction sample in order not to bias the  $z$ -dependence of the tracking acceptance by the event kinematics and topology of DIS events. The width of the distribution reflects the length of the proton bunch. The  $z$ -vertex distribution is well reproduced in the central detector region and at  $z \approx +70$  cm. This second peak is due to  $\approx 3\%$  (5% in the SVTX case) spill over protons from the main bunch that arrive one bucket, i.e. 4.8 nsec, early ('satellite bunch') and can hence give rise to  $e\bar{p}$ -interactions at  $z \approx +70$  cm ('satellite events'). In the outer region a small discrepancy between data and Monte Carlo can be seen, where the Monte Carlo contributes more events than the data. This is presumably due to inclusion of beam-gas background in the photoproduction reference sample. In order to reduce any resulting uncertainty a vertex cut

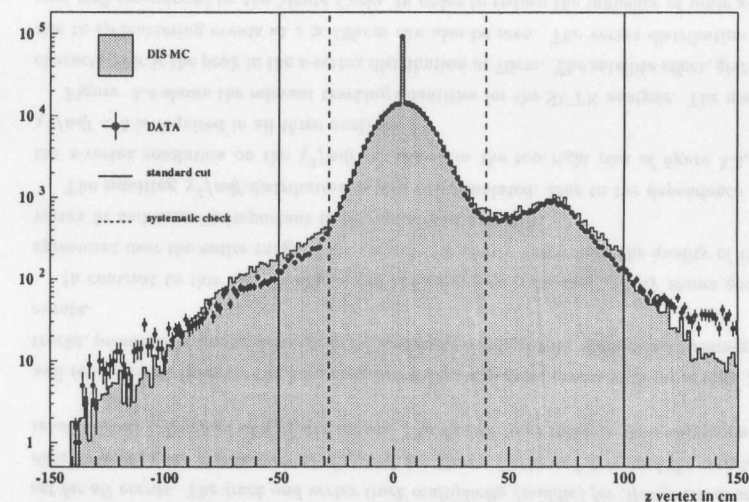


Figure 5.1:  $z$ -vertex distribution for the selected DIS-data sample. Overall good agreement between data (points) and Monte Carlo (histogram) can be seen, even for events without a tracking vertex, where the  $z$ -vertex is set to +3 cm.

$$-50 \text{ cm} < z_{\text{vtx}} < 100 \text{ cm} \quad \text{standard cut}$$

$$\text{or} \quad -28 \text{ cm} < z_{\text{vtx}} < 40 \text{ cm} \quad \text{systematic check for satellite contribution}$$

is applied.

At low- $Q^2$  the electron is scattered through too small an angle to be seen by the central tracking detector. Due to the  $\frac{1}{Q^4}$ -dependence of the cross section these events dominate the data sample. Hence the tracking vertex efficiency is a strong function of the direction of the hadrons in the detector as given by the kinematic variable  $y$  or the hadronic angle  $\gamma_h$ . Figure 5.2 shows the tracking efficiency and the corresponding vertex resolution as functions of these hadronic variables.

The tracking vertex efficiency drops very quickly for events with  $\log_{10}(y) < -1.2$ , which corresponds to  $\gamma_h \approx 60^\circ$ . This is also reflected in the vertex resolution, which grows from  $\sim 1.4$  mm at high  $y$  to several cm at low  $y$ , where an additional systematic shift of 5 – 10 mm towards the backward direction shows up. Although the overall agreement in track vertex efficiency between Monte Carlo and data is good, the efficiency is found to be slightly higher in the data than in the Monte Carlo at these low values of  $y$ . This effect is taken into account in the systematic error calculation.

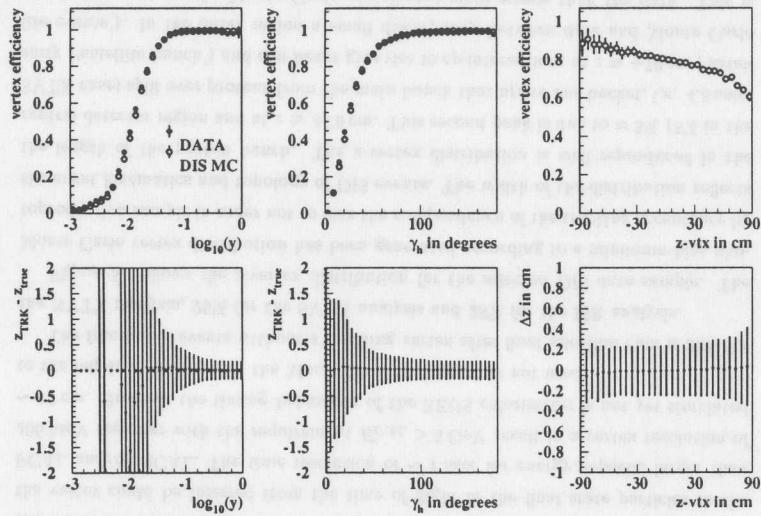


Figure 5.2: Track-vertex efficiency in  $z$  as a function of  $y$ ,  $\gamma_h$  and the  $z-vtx$  (top row). The corresponding resolutions for Monte Carlo (open circles) and data (closed circles) are shown in the bottom row.

The strong impact of the hadronic final state, which is boosted in the forward direction, on the tracking vertex efficiency can also be seen from its  $z$ -dependence. The closer the vertex is to the FCAL the less likely is a track vertex reconstruction, since the hadrons do not leave tracks in the CTD at such small angles. The efficiency drops from 90% for vertices at the rear CTD end to 60% for ones at the forward end. Simultaneously also the vertex resolution increases from  $\sim 2.5$  mm to more than 3 mm.

Since the tracking based vertex reconstruction gives about 1 mm wide distributions in  $x$  and  $y$  (see figure 5.3), while the actual beam width is only  $\approx 50 \mu\text{m}$ , the  $x$ - and  $y$ -vertex is always set to the mean of the corresponding distribution measured for the run range under consideration, 0.15 mm in  $x$  and  $-0.15$  mm in  $y$ .

The agreement between Monte Carlo and data in the  $x$ - and  $y$ -vertex distribution is reasonable, but not perfect. This is partially due to noise in the CTD. Another effect is, that the vertex chamber information can only be used for part of the data, while it is always present in the Monte Carlo. The small shoulders at  $x = 0$  and  $y = 0$  in the Monte Carlo are due to the tracking algorithm introducing pseudo-tracks at the origin in order to achieve a higher stability of the vertex fit.

The distribution of track multiplicities agrees very well between Monte Carlo and data for low track multiplicities, in particular the number of events without track is

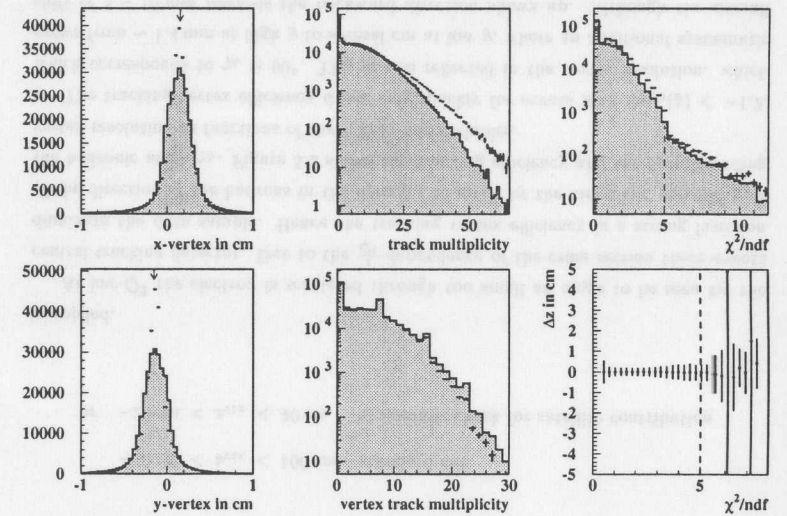


Figure 5.3: The  $x$ - and  $y$ -vertex distributions (left) for Monte Carlo (histogram) and data (dots) show reasonable agreement. The arrows indicate the vertex position which is set for all events. The track and vertex track multiplicity (middle) for Monte Carlo and data as well as the distribution of  $\chi^2_{vtx}/ndf$  for Monte Carlo and data and the  $z$ -vertex resolution as a function of  $\chi^2_{vtx}$  are shown. The dashed lines indicate the analysis cut.

well reproduced. However the data contain significantly more events with more than 20 tracks, presumably due to detector noise and event overlays with cosmics and beam-gas events.

In contrast to this the distribution of the on-vertex track multiplicity shows good agreement over the entire range. This quantity implicitly determines the quality of the vertex fit and hence is important to be reproduced correctly.

The resulting  $\chi^2_{vtx}/ndf$ -distribution is also well simulated. Due to the dependence of the  $z$ -vertex resolution on the  $\chi^2_{vtx}/ndf$ , as shown in the top right plot of figure 5.3, a  $\chi^2_{vtx}/ndf < 5$  is required in all three analyses.

Figure 5.4 shows the relevant tracking quantities for the SVTX analysis. The main characteristic is the peak in the  $z$ -vertex distribution at 70cm. The satellite effect, giving rise to  $e\bar{p}$ -scattering events at  $z \approx 130$  cm can also be seen. The vertex distribution is very well reproduced by the Monte Carlo. In order to reduce the influence of noise and spurious tracks, a vertex cut of

$$25 \text{ cm} < z_{vtx} < 200 \text{ cm}$$

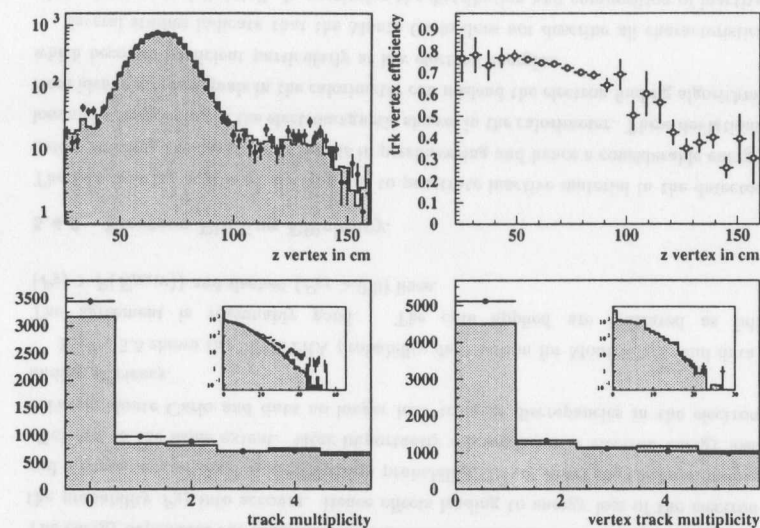


Figure 5.4: Tracking quantities of particular importance in the SVTX analysis.

is applied.

The tracking vertex efficiency is in very good agreement with the one obtained from the NVTX sample in the common vertex region. Since it drops to  $\sim 30 - 40\%$  at 130 cm, a large fraction of satellite events do not have a tracking vertex, which is then set to 67 cm, the default value in this analysis. The overall z-vertex resolution is correspondingly slightly degraded.

The track and vertex track multiplicities show essentially the good agreement between Monte Carlo and data as already seen in the NVTX case. However the fraction of events without tracking vertex differs by 14.0%, and the fraction of events without tracks at all by 9.4%. This effect is conservatively taken into account in the systematic error determination.

## 5.4 Electron Identification and Reconstruction.

### 5.4.1 Introduction.

The signature of neutral current DIS events is the presence of a scattered electron in the final state. Thus correct and efficient identification of the electron and precise reconstruction of its position and energy are of vital importance for the analysis of DIS events. Momentum conservation requires the scattered electron to balance the transverse momentum of the current jet, resulting in an azimuthal back-to-back event topology. Consequently the electron is well-isolated and relatively easy to find over a large part of the accessible  $(x, Q^2)$  plane. However at high  $y$  (low  $x$ ), where the energy transfer from the electron to the struck quark is relatively large, the current jet goes in the rear direction and the scattered electron has rather low energy. The resulting overlap of hadronic activity and the electron in the detector makes it difficult to separate them and identify the latter. Low energy electrons can also give rise to showers, very similar to hadron-initiated ones; the scattered electron can interact with inactive material, such as mechanical support structures or cables in the inner detectors, and start showering before entering the calorimeter. The resulting signal in the calorimeter is a broad, hadronic-like shower, that is difficult to identify as an electron. At such low energies the situation is complicated even further; electromagnetic showers from  $\pi^0 \rightarrow \gamma\gamma$  decays or low energetic hadrons in photoproduction can fake electron signals in the calorimeter and give rise to background, which has to be suppressed.

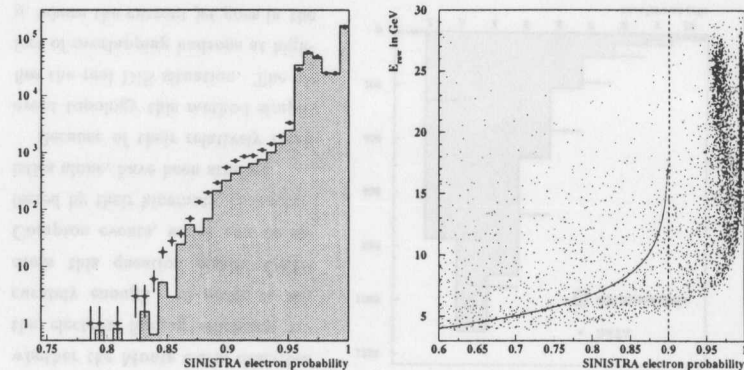


Figure 5.5: Left: SINISTRA probability for Monte Carlo (histogram) and data (dots). Right: Scatter plot of calorimeter energy versus SINISTRA probability. The full line indicates the energy dependent probability cut while a fixed cut at 0.9 is shown as dashed line.

### 5.4.2 The Algorithm.

In these analyses the neural network SINISTRA [67] is used for the electron identification. SINISTRA is based on islands of calorimeter cells. An island is defined as a group of cells that are contiguous to the cell with the highest energy (a  $3 \times 3$  array is the largest possible island). Only electromagnetic islands are processed by the network and tested for their probability of originating from an electron. The input consists of the PMT energies in the  $3 \times 3$  calorimeter towers around the highest energy cell of the island. In the RCAL  $9 \times 4$  EMC +  $9 \times 2$  HAC = 54 variables are projected to one output variable,  $P_{SI}$ , which can take values from 0 to 1. The output is interpreted as the probability that an island is the scattered beam electron ( $P_{SI} \sim 1$ ) or of hadronic origin ( $P_{SI} \sim 0$ ). In order for a candidate to be called an electron the probability, assigned by the network, is required to be

$$P_{SI} > 0.9$$

in the SVTX analysis. In the NVTX and ISR analysis a cut at

$$P_{SI} > 0.9 - 1.5 \times e^{-\frac{E_{raw}}{13}} \equiv P(E_{RAW})$$

is set, where  $E_{raw}$  is the candidate's energy as measured by the calorimeter in GeV. The energy dependent cut takes correlations between the calorimeter energy  $E_{RAW}$  and the probability  $P_{SI}$  into account. Hence effects leading to energy loss of the electron and a consequential drop in identification probability, do not lower the electron finding efficiency to the same extent. More importantly discrepancies in electron energy loss between Monte Carlo and data no longer lead to large discrepancies in the electron finding efficiency.

Figure 5.5 shows the SINISTRA probability distribution for Monte Carlo and data. The agreement is reasonably good. The cuts applied are indicated as full ( $P_{SI} > P(E_{RAW})$ ) and dashed ( $P_{SI} > 0.9$ ) lines.

### 5.4.3 Electron Finding Efficiency.

The fact that the scattered electron has to penetrate inactive material in the detector before reaching the calorimeter results in preshowering and hence a considerable energy loss and a broadening of the electromagnetic shower in the calorimeter. These deviations from ideal electron signals in the calorimeter can mislead the electron finding algorithm, which becomes inefficient particularly at low electron energies.

Several studies indicate that the Monte Carlo does not describe all characteristics of the detector in full detail. In particular the distribution and composition of inactive material in the detector is simplified and seems to be incomplete in some regions close to the beam-pipe. As an example the distributions of the number of cells assigned to

the electron, indicative of shower width, is shown in figure 5.6. As a consequence one might question whether the Monte Carlo describes the electron finding efficiency accurately enough. In order to address this question elastic QED-Compton events, which can be selected by their kinematic characteristics alone, have been studied.

Because of their relatively clean event topology this method simplifies the real DIS situation. The effect of overlapping hadrons at high- $y$ , where the current jet goes in the rear detector region, is not taken into account. The study of elastic QED-Compton events might therefore be compared to testbeam conditions.

In elastic QED-Compton events the incoming electron scatters off a quasi-real photon ( $q \simeq 0$ ; see figure 5.7). Due to the finite scattering angles both, electron and photon can be detected in the calorimeter. As the four-momentum transfer to the proton ( $q$ ) is approximately zero, it is essentially undeflected. From energy and momentum conservation the final state electron and photon balance each other in transverse momentum and carry the conserved event ( $E - P_z$ ), while the proton stays intact and is lost in the forward beamhole.

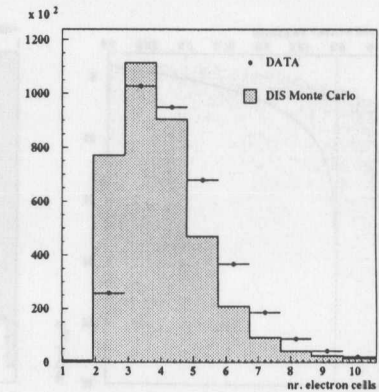


Figure 5.6: Number of cells assigned to an electron for Monte Carlo (histogram) and data (dots).

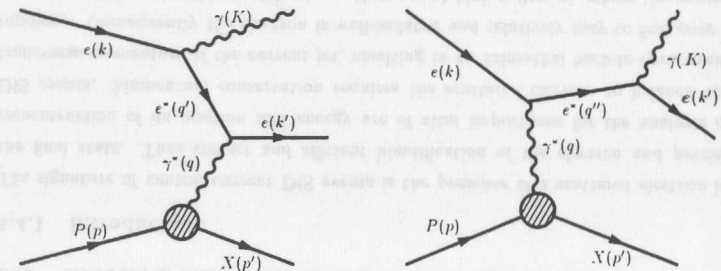


Figure 5.7: Feynman diagrams of the elastic QED-Compton process.

The elastic QED-Compton event sample has been selected with the following cuts:

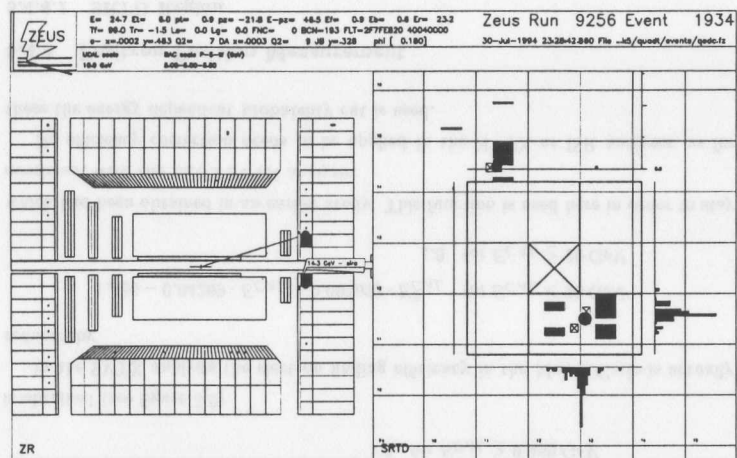


Figure 5.8: QED-Compton event in the ZEUS detector. The scattered electron leaves a track in the CTD, while the photon deposits 14.3 GeV in the calorimeter (left). One of the electromagnetic clusters is also detected in the SRTD (right).

- at least two electromagnetic islands with SINISTRA probability  $\geq 0.5$  and energy  $\geq 5$  GeV.
- both islands have to be at least 3 cm away from the edge of the calorimeter beam hole (referred to as 'box cut').
- total event energy when ignoring the photon and the electron islands:  $E_{HAD} < 2$  GeV
- $E - P_z > 30$  GeV
- $|\Delta p_x| \leq 4$  GeV obtained from the two highest energetic islands
- $|\Delta p_y| \leq 4$  GeV obtained from the two highest energetic islands

In order to be as unbiased as possible in the efficiency extraction a so-called 'trigger-electron' is required to have:

$$E_{CAL} > 10 \text{ GeV}$$

$$P_{SI} > 0.9$$

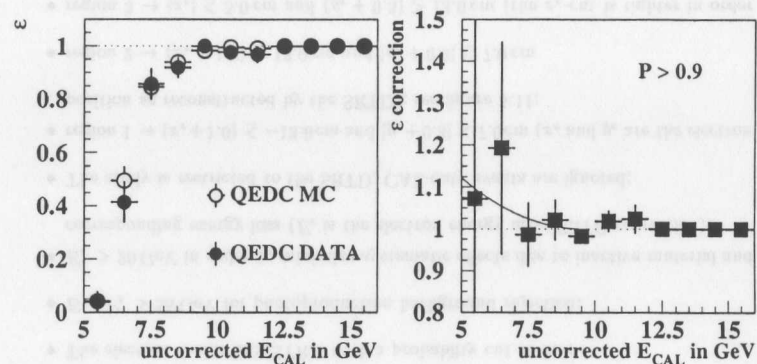


Figure 5.9: Electron finding efficiency (left) of SINISTRA for data (closed circles) and Monte Carlo (open circles) with a fixed probability cut at 0.9. The discrepancy between data and Monte Carlo for low energy electrons is also seen in the ratio of efficiencies, the efficiency correction, as illustrated in the right hand plot. A fit to a second order polynomial is shown as solid line

If such an electron is found its position and energy determine the parameters of the second electromagnetic island, which is considered the test object. The electron finding efficiency of the neural network SINISTRA is then tested by counting how often the test object is identified as an electron, requiring

$$\text{either } P_{SI} > 0.9$$

$$\text{or } P_{SI} > 0.9 - 1.5 \times e^{-\frac{E_{CAL}}{2.5}}$$

where the calorimeter energy  $E_{CAL}$  is specified in GeV. This procedure has been repeated for box cuts of 4 and 5 cm in order to test the stability of the method against the varying thickness of dead material in this region. No significant box cut dependence has been observed. The ratio of the electron finding efficiency in the Monte Carlo and the data for the different scenarios is fitted to a second order polynomial for electron energies below an energy  $E^0$ , which is also varied in the fit. For energies larger than  $E^0$  the ratio of efficiencies is unity.

The results are shown in figure 5.9 and 5.10. As can be clearly seen the energy dependent SINISTRA-probability cut not only gives a significantly higher efficiency for low energy electrons, but more importantly reduces the discrepancy between data and Monte Carlo efficiency. Taking the anti-correlation of the SINISTRA probability and the electron energy loss into account in the manner described, reduces the efficiency uncertainty.

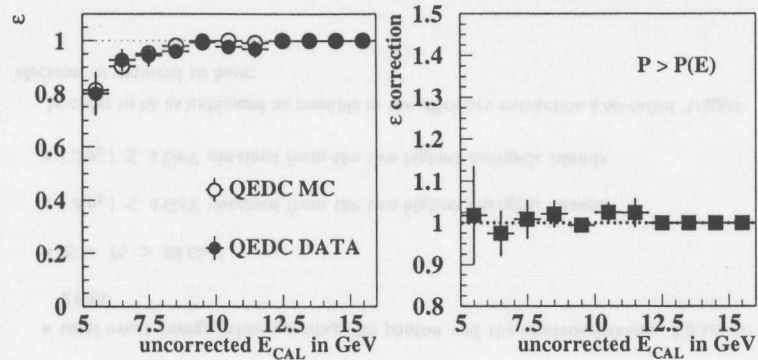


Figure 5.10: Electron finding efficiency (left) of SINISTRA for data (closed circles) and Monte Carlo (open circles) with an energy dependent probability cut. The efficiency is significantly higher than that for the fixed probability cut at 0.9. And even more importantly there is essentially no discrepancy between data and Monte Carlo efficiency observed as can be seen from the right hand plot.

For a fixed probability cut at 0.9 an efficiency correction of

$$\begin{aligned} &1.0 + 0.006128 \cdot (E_{CAL} - 9.469)^2 \quad \text{for } E_{CAL} < 9.469 \text{ GeV} \\ &1.0 \quad \text{for } E_{CAL} \geq 9.469 \text{ GeV} \end{aligned}$$

is obtained (see figure 5.9).

In the SVTX analysis the electron finding efficiency in the Monte Carlo is actually reduced by

$$\begin{aligned} &1.436 - 0.04269 \cdot E_{CAL} + 0.001022 \cdot E_{CAL}^2 \quad \text{for } E_{CAL} < 20 \text{ GeV} \\ &1.0 \quad \text{for } E_{CAL} \geq 20 \text{ GeV} \end{aligned}$$

which had been obtained in an earlier study. This function is used here in order to stay consistent with the ZEUS SVTX analysis.

No efficiency correction needs to be applied in the NVTX or ISR analyses, as for these the energy dependent probability cut is used.

## 5.4.4 Positron Position Measurement

### 5.4.4.1 SRTD Region

In addition to the event vertex the impact point of the scattered electron in the calorimeter provides the second space point, from which the electron scattering angle is reconstructed.

In the SRTD region ( $-34.0 < x_{el} < 32.0 \text{ cm}$ ;  $-33.3 < y_{el} < 32.7 \text{ cm}$ ;  $z_{el} < -140.0 \text{ cm}$ ) the electron position reconstruction is entirely based on the SRTD, events without any SRTD information are discarded. With respect to calorimeter cracks, where the electron position can be determined to less than 1 mm, the SRTD position reconstruction has been shown to have a resolution of  $\sim 3 \text{ mm}$ . This and further details concerning the electron position reconstruction using the SRTD are described in [68].

### SRTD alignment

Due to the large and rapidly varying cross section at low- $Q^2$ , misalignments of the SRTD and RCAL give rise to substantial systematic effects in different detector regions. Since the two L-shaped SRTD halves are physically mounted on the face of the RCAL, their position relative to the latter is fixed and measured precisely. Therefore, although only the SRTD is mentioned in the following, the results also apply to the RCAL. In order to determine the relative and absolute position of the two SRTD halves, an alignment study based on the event rate symmetry has been performed [69].

Assuming the rate of DIS events to be completely  $\phi$ -symmetric with respect to the  $ep$ -interaction point, a comparison of the rates in different detector regions should reveal possible detector misalignments. For this study the runs 9362 - 9766 were analysed. In these runs all considered calorimeter cells and relevant trigger modules were fully functioning, no systematic effects of calorimeter energy mismeasurements are known.

The set of Monte Carlo events has been generated with the structure function MRSD<sub>L</sub> [134] and the detector simulation MOZART, version NUM12V1.

Figure ( 5.11) shows the four regions used in the event rate measurement. The event rates as a function of distance to the (x,y) interaction point were determined using events satisfying:

- The electron finder SINISTRA with a probability cut at 0.9;
- $E - P_z > 35 \text{ GeV}$  for photoproduction background rejection;
- $E_e > 20 \text{ GeV}$  in order to minimize systematic effects due to inactive material and corresponding energy loss ( $E_e$  is the electron energy after SRTD correction);
- The study is restricted to the SRTD, CAL-only events are ignored;
- region 1  $\rightarrow (x_e + 1.0) \leq -13.0 \text{ cm}$  and  $|y_e + 0.3| \leq 7.0 \text{ cm}$  ( $x_e$  and  $y_e$  are the electron position as reconstructed by the SRTD); see figure 5.11;
- region 2  $\rightarrow (x_e + 1.0) \geq 13.0 \text{ cm}$  and  $|y_e + 0.3| \leq 7.0 \text{ cm}$
- region 3  $\rightarrow |x_e| \leq 5.0 \text{ cm}$  and  $(y_e + 0.3) \geq 13.0 \text{ cm}$  (the  $x_e$ -cut is tighter in order to stay away from the SRTD cracks and a masked-off SRTD strip);
- region 4  $\rightarrow |x_e| \leq 5.0 \text{ cm}$  and  $(y_e + 0.3) \leq -13.0 \text{ cm}$ .

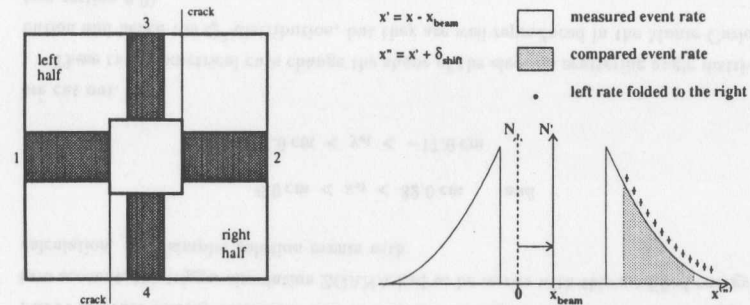


Figure 5.11: Left: The SRTD as seen from the interaction point. The grey shaded areas indicate the regions 1 to 4 used for this rate study. The two L-shaped SRTD/RCAL halves are separated by cracks. Right: Schematic diagram of the alignment algorithm based on event rate symmetry with respect to the beam.

The comparison of the different halves is done in the following way:

- According to the detector survey the relative distance of the two L-shaped detector halves is 2 mm larger than assumed in the position reconstruction and the Monte Carlo simulation. This is taken into account by moving the right SRTD half in the data by +2 mm in the positive  $x$ -direction;
- A transformation into a coordinate system, in which the  $(x, y)$ -vertex lies at the origin (primed system), is performed. Event rates are expected to be a function of the radial distance to the origin only;
- Plot the event rates versus:
  - $x$  in region 1
  - + $x$  in region 2
  - + $y$  in region 3
  - $y$  in region 4
  - in the new coordinate system;
- Assuming a possible shift of the SRTD by  $\delta_x$  or  $\delta_y$ , which are varied over a range of several millimeters, a set of event rate distributions is obtained. A  $\chi^2/ndf$  is calculated for every  $\delta$  value by comparing the rate distributions in regions 1 and 2 and regions 3 and 4 respectively;

Example plots for the  $x$ -shift determination in data and Monte Carlo are shown in figures 5.12 and 5.13. The behaviour of  $\chi^2/ndf$  as a function of  $\delta$  reveals possible shifts of the SRTD, which is shown in figure 5.14.

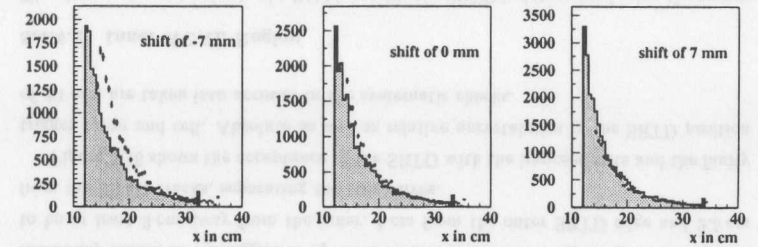


Figure 5.12: SRTD alignment in data. The histograms represent the event rate in the right SRTD half (region 2), the dots the one in the left half (region 1).

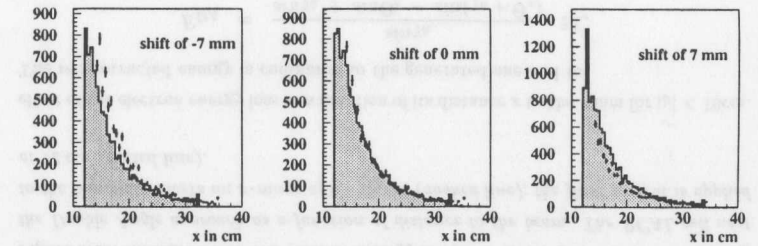


Figure 5.13: SRTD alignment in MC. The histogram represents the event rate in the right SRTD half (region 2), the dots the one in the left half (region 1).

As can be seen the  $\chi^2/ndf$  in the Monte Carlo reaches a minimum of  $\sim 1$  without any shifts in  $x$  and  $y$ . This result demonstrates that the rate symmetry method works, since the Monte Carlo geometry is consistent in the event generation and reconstruction by construction. However in the data a clear shift of  $\sim 4$  mm in  $x$  is found, while a possible shift in  $y$  as small as  $\sim -1$  mm might be seen.

As a result of this study in the event reconstruction the left SRTD half is shifted in  $x$ -direction by 4 mm, the right by 6 mm, which is consistent with other studies [70].

However a later alignment study based on the tracking detectors [124] showed, that the relative shift of the two SRTD halves is  $-2$  mm rather than the assumed  $+2$  mm. This results in a total correction of 5 mm for the left and 3 mm for the right SRTD half, which is used in the SVTX, NVTX and the ISR analyses.

For a large fraction of the 94 data (run 9767 - 10263) a TEC-card of the calorimeter first-level trigger was not functioning, resulting in a depletion of detected electrons in that region. In principle this effect can be reproduced in the trigger simulation ZGAN, but for some of the Monte Carlo files used the necessary information is missing. In order to take possible edge effects in adjacent trigger towers into account, events with

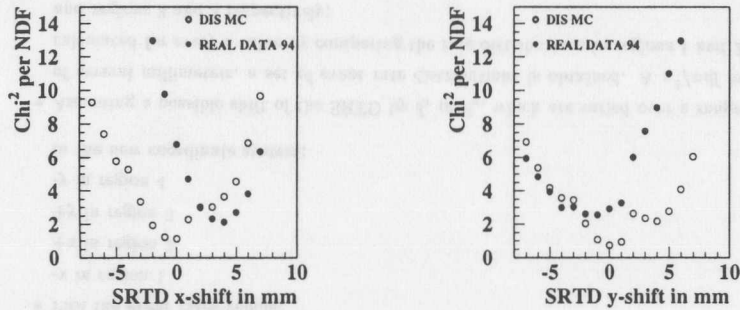


Figure 5.14:  $\chi^2$  per ndf as a function of the shift  $\delta_x$  (left) and  $\delta_y$  (right) for Monte Carlo (open circles) and data (full circles).

$$-37.0 \text{ cm} < x_{el} < -5.0 \text{ cm} \quad \text{and}$$

$$-37.0 \text{ cm} < y_{el} < -7.0 \text{ cm}$$

are therefore cut out in the Monte Carlo and data. As a systematic check the Monte Carlo events in the affected TEC region are reweighted according to the fraction of data luminosity, for which the TEC was fully functioning. No significant effect on the final  $F_2$  has been found.

For almost all 1994 runs considered, one of the two photomultiplier tubes (PMT) in an electromagnetic cell in the RCAL was not functioning. In the offline reconstruction this PMT information could be ignored and the cell energy be reconstructed by doubling the energy of the remaining PMT, the procedure usually applied in cases of a 'dead' PMT. In order to stay consistent and to take the corresponding effects on the trigger into account, the trigger simulation ZGANa had to be re-run with this modified energy calculation. As a simpler solution events with

$$6.0 \text{ cm} < x_{el} < 32.0 \text{ cm} \quad \text{and}$$

$$-33.0 \text{ cm} < y_{el} < -17.0 \text{ cm}$$

are cut out.

These two geometrical cuts change the shape of the electron scattering angle distribution and hence the  $Q^2$ -distribution, but they are well reproduced in the Monte Carlo (see section 6.9).

In the region close to the beampipe the reconstruction of the electron impact position and energy is poor, due to energy leakage into the beam hole. Figure 5.15 shows the

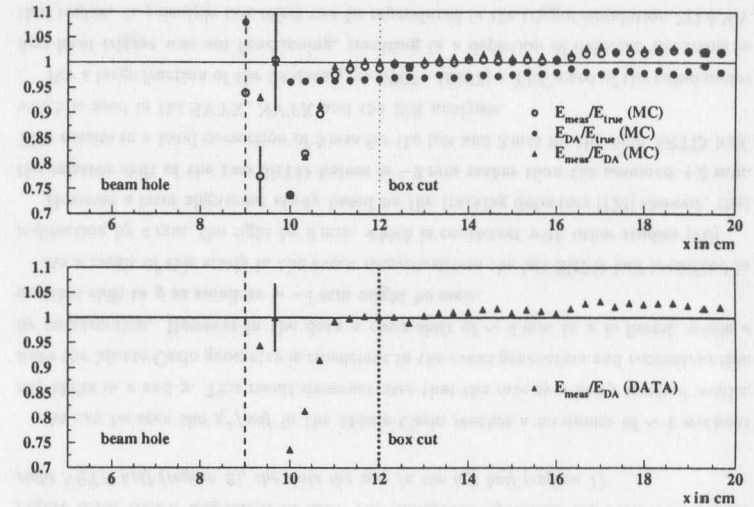


Figure 5.15: Measured and true electron energy compared to the one reconstructed using the Double Angle approach as a function of distance to the beam. The RCAL cell next to the beamhole covers an  $x$ -range of 9–29 cm (dashed line), the final box-cut is applied at 12 cm (dotted line).

effect of the electron energy loss as a function of its distance  $x$  to the beam for  $|y| < 10$  cm. The reconstructed energy is compared to the generated one and to

$$E_{DA} = \frac{\sin \gamma_h}{\sin \gamma_h + \sin \Theta_e - \sin(\gamma_h + \Theta_e)} \cdot 2E_e$$

which is the electron energy as reconstructed from the angles of the scattered electron and the hadronic final state <sup>2</sup>. The effect in the other regions around the beam hole is essentially identical. As suggested by these results the electron impact point is required to be at least 3 cm away from the inner, 1 cm from the outer SRTD edge and 2.5 cm from the SRTD cracks, separating the two halves.

Figure 5.16 shows the acceptance of the SRTD with the imposed cuts and the faulty trigger tower and cell. Absolute as well as relative uncertainties in the SRTD position of  $\pm 1$  mm are taken into account in the systematic checks.

#### 5.4.4.2 Inner RCAL Region

The electron impact point in the RCAL outside the SRTD is determined using the energy sharing between the two sides ( $E_{left}$  and  $E_{right}$ ) of a calorimeter cell, as implemented

<sup>2</sup>A reconstruction prescription for the hadronic angle  $\gamma_h$  from measured quantities is given in 6.5.

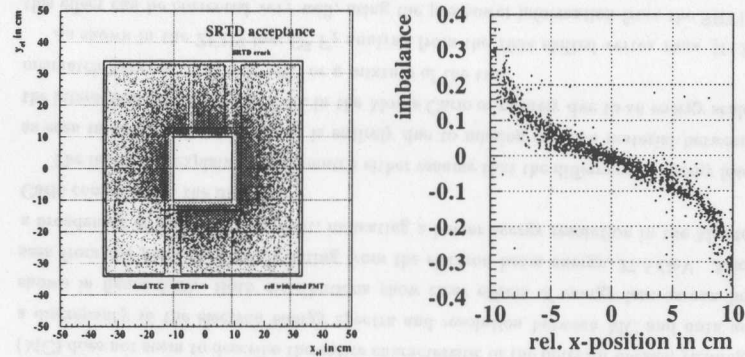


Figure 5.16: *Left: Scatter plot of the electron impact position in the SRTD region. The two 'L'-shaped regions indicate the nominal acceptance for the two SRTD halves. The cells affected by the dead trigger tower and the dead PMT are indicated by dashed lines. Right: Energy imbalance as a function of the relative  $x$ -position in a calorimeter cell.*

in the routine ELECPO [71]. The imbalance, defined as

$$imbalance = \frac{E_{left} - E_{right}}{E_{left} + E_{right}} \quad (5.1)$$

is strongly correlated with the relative electron position in the calorimeter cell (see figure 5.16). Since ELECPO was tuned to HES information, where the HES position in the data was shifted by  $\approx 3$  cm in  $z$ -direction with respect to the one assumed in the reconstruction, a systematic check with and without this shift was done. Possible systematic shifts of the reconstructed radius value of the electron impact point by up to 2 mm are hence accounted for.

#### 5.4.4.3 Outer RCAL and BCAL Region

In the entire BCAL and FCAL and RCAL outside a radial distance of 70 cm from the  $z$ -axis, the electron position is determined from the extrapolation of a matched track to the electron  $z$  (in F/RCAL) or radius-position (in BCAL), if available. A track is matched if the extrapolated position is within 5 cm of the electron position as reconstructed by ELECPO.

Figure 5.17 shows the distributions of the electron scattering angle  $\Theta_{el}$  for all events and for events with a matched track in Monte Carlo and data. Although they are consistent within errors the resulting track matching efficiency as a function of  $\Theta_{el}$  is systematically higher in Monte Carlo than in data. Since this effect is not investigated any further a matched track is not required for an electron in these calorimeter regions, but only used for a precise position reconstruction.

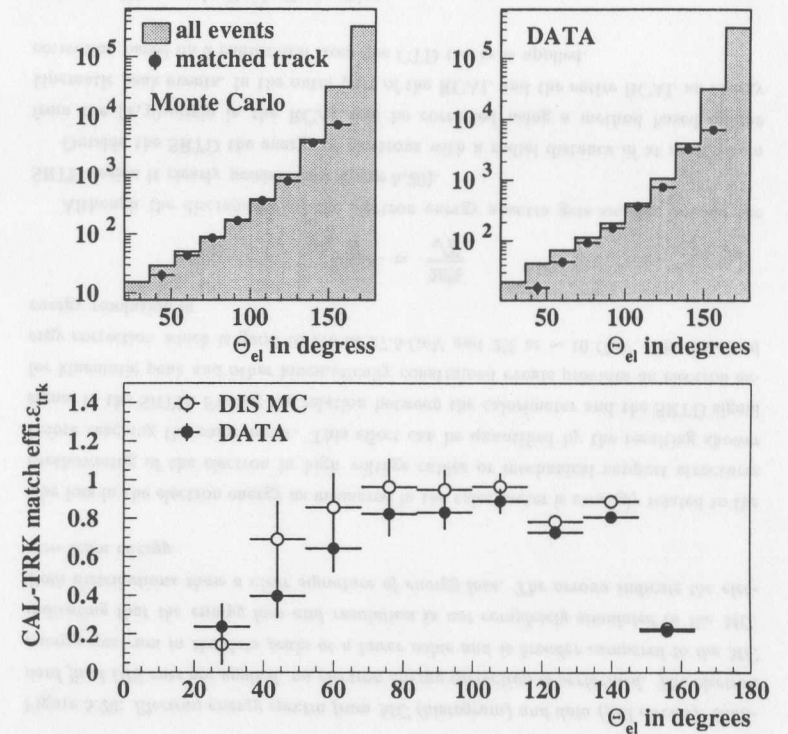


Figure 5.17: *Upper left: Distribution of the electron scattering angle  $\Theta_{el}$  for all events (histogram) and for events with a matched track (dots) in Monte Carlo. Upper right: corresponding distributions for data. Lower: Track matching efficiency as a function of  $\Theta_{el}$  for data (closed circles) and Monte Carlo (open circles).*

Using these techniques the resolution obtained in the electron scattering angle  $\Theta_e$  varies between  $0.1^\circ$  and  $0.2^\circ$  (see figure 5.18). Figure 5.19 shows the scattering angle distributions for all three analyses. Good agreement between Monte Carlo and data is found. The kinks in the NVTX and ISR distributions are due to the geometrical cut on the trigger tower and one additional RCAL cell.

#### 5.4.5 Positron Energy Measurement

The measurement of the scattered electron energy plays a crucial role for the kinematic reconstruction of DIS events, especially for the 'electron only' reconstruction method. This method has a better intrinsic resolution than the 'double angle' or purely hadronic

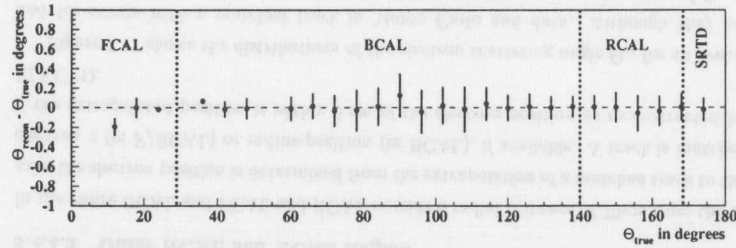


Figure 5.18: Electron scattering angle resolution in the different detector regions.

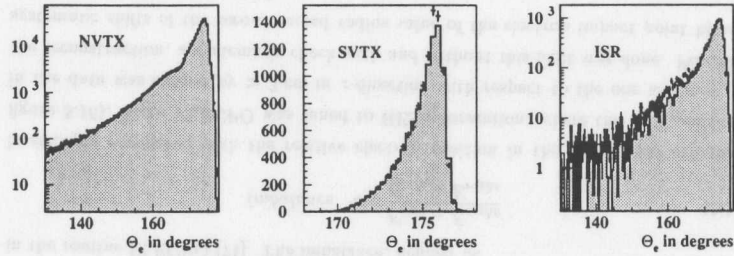


Figure 5.19: Electron scattering angle distributions after final cuts for the NVTX, SVTX and ISR analysis.

methods and is therefore of vital importance for 1994 DIS analyses which reach down to  $Q^2 \approx 3.5 \text{ GeV}^2$ . As shown in many analyses the ZEUS detector Monte Carlo (MC) does not seem to describe the entire characteristic of the detector details, yielding a discrepancy in the electron energy spectra and resolution between MC and data as shown in figure 5.20. Both distributions show clear effects of energy loss as can be seen from the peak position deviating from the electron beam energy, 27.5 GeV. Also a broadening of the peak is evident, indicating a better energy resolution in the Monte Carlo compared to the data.

The models to explain this mismatch either assume that the difference in energy loss as seen in the calorimeter (CAL) is entirely due to missing inactive material between the interaction point and the CAL in the Monte Carlo or entirely due to an energy scale mismatch between data and MC, or a mixture of the two.

As shown in the ZEUS low  $Q^2$   $F_2$  analysis from the 1994 shifted vertex runs [112] this effect can be corrected very well, using the preshower information from the SRTD [68]. Figure 5.21 shows a summary of this correction method. In kinematic peak events (a definition of these is given in the following subsection) the scattered electron has approximately the electron beam energy (27.5 GeV), hence providing test beam conditions.

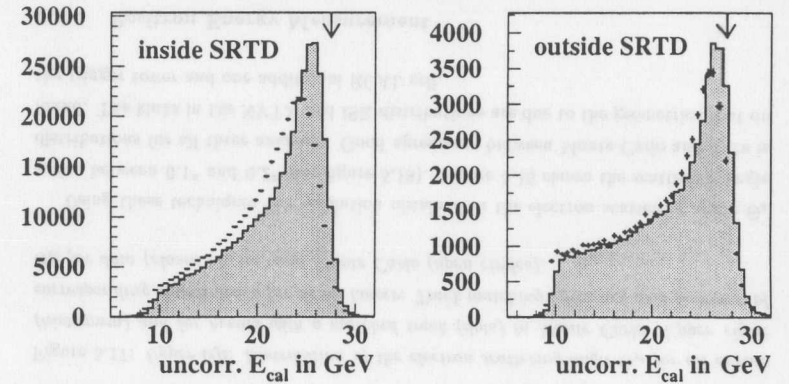


Figure 5.20: Electron energy spectra from MC (histogram) and data (full circles). Standard final DIS cuts are applied, no electron energy correction is performed. The electron energy spectrum in the data peaks at a lower value and is broader compared to the MC indicating that the energy loss and resolution is not completely simulated in the MC. Both distributions show a clear signature of energy loss. The arrows indicate the electron beam energy.

The loss in the electron energy as measured in the calorimeter is strongly related to the preshowering of the electron in high voltage cables or mechanical support structures before reaching the calorimeter. This effect can be quantified by the resulting shower signal in the SRTD. Fitting the relation between the calorimeter and the SRTD signal for kinematic peak and other kinematically constrained events provides an electron energy correction which is good to 1% at 27.5 GeV and 2% at  $\sim 10 \text{ GeV}$ . The obtained energy resolution is

$$\frac{\sigma(E)}{E} = \frac{26\%}{\sqrt{E}}$$

Although the discrepancy of the electron energy spectra gets smaller outside the SRTD region it clearly persists (see figure 5.20).

Outside the SRTD the energy of electrons with a radial distance of at most 70 cm from the  $(x, y)$ -origin in the RCAL can be corrected using a method based on the kinematic peak events. In the outer part of the RCAL and the entire BCAL an energy correction based on a calibration from the CTD tracks is applied.

#### 5.4.5.1 Kinematic Peak Correction

As shown in earlier studies [80, 81] the discrepancy in the energy loss between data and MC can be corrected based on kinematic peak (KP) events.

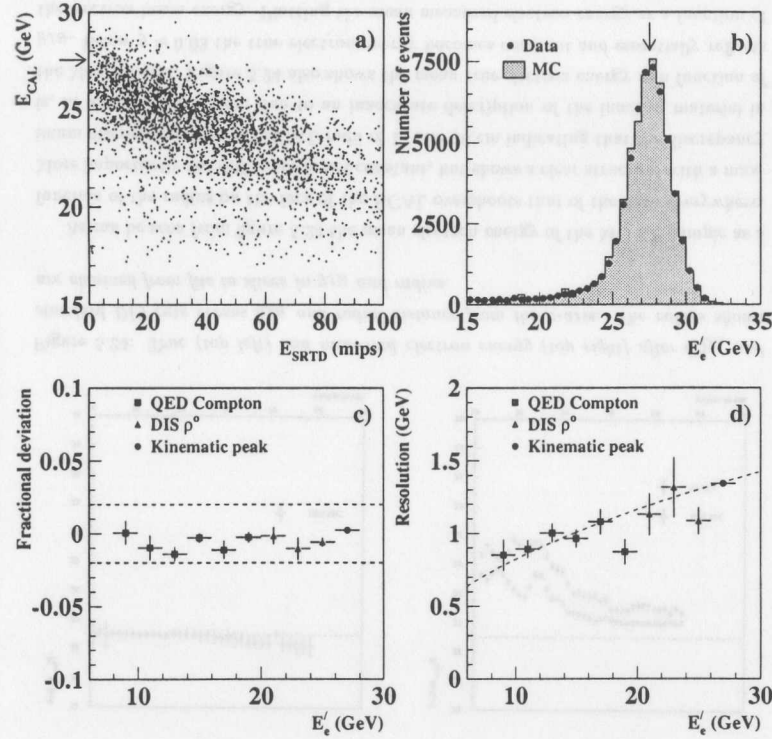


Figure 5.21: For kinematic peak events the strong correlation between the electron energy loss and the SRTD signal (top left) is used to correct the electron energy. The result is good to 1 – 2% (top right and bottom left). The lower right plot shows the energy resolution as a function of the energy.

At low  $y$ , the electron energy exhibits the so-called kinematic peak behaviour. In this region, the electron energy is essentially at the electron beam energy, 27.52 GeV, independent of  $x$  and  $Q^2$  (see figure 5.22). Appropriate cuts can isolate this region.

All standard DIS cuts are applied to reject background:

- $E - P_z \geq 35$  GeV
- 16 cm box cut (only RCAL is used)
- $E_e \geq 10$  GeV

Cuts are then made in  $Q^2$ , measured with the double angle method ( $Q_{DA}^2$ ) in order

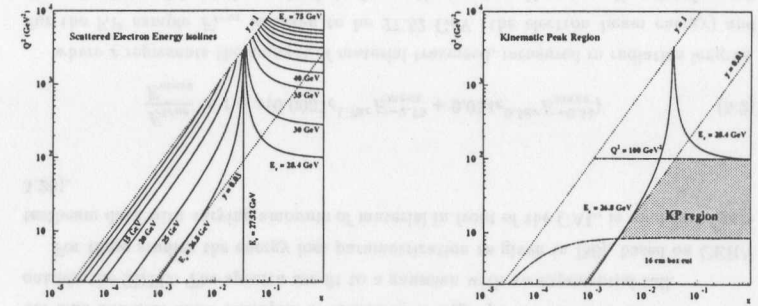


Figure 5.22:  $(z, Q^2)$  plane. left: The electron isolines from 5 to 25 GeV, from 30 to 75 GeV and at 26.8 GeV, 27.5 GeV and 28.4 GeV are shown. right: Events in the kinematic peak region (grey area) are selected using the cuts  $Q^2 = 100$  GeV<sup>2</sup> and 16 cm box cut (dashed-dotted line) and  $y = 0.03$  (dotted line).

not to be too sensitive to the electron energy scale. Events are rejected if  $Q_{DA}^2 \geq 100$  GeV<sup>2</sup>, hence removing the higher electron energy tail in the energy distributions.

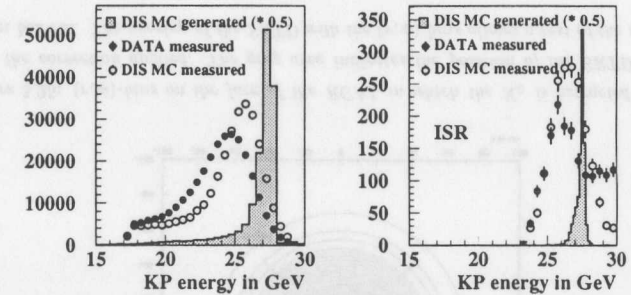


Figure 5.23: Electron energy distribution of the kinematic peak sample. Compared to the true Monte Carlo (histogram) and the measured Monte Carlo (open circles) the data distribution (closed circles) is considerably shifted to lower energies and is broader, indicating a degraded resolution.

The distributions of the true electron energies from the Monte Carlo after cuts shows a sharp peak at the electron beam energy 27.52 GeV (see figure 5.23). Events with initial state radiation give rise to the low energy tail while most of the photons from final state radiation are included in the electron cluster by the electron finder. The measured energy distributions for the kinematic peak sample are shown as open circles for the Monte Carlo and closed circles for the data. The peak in the data is below the MC peak by 4.6% while the data spectrum is significantly broader indicating a distorted

energy resolution.

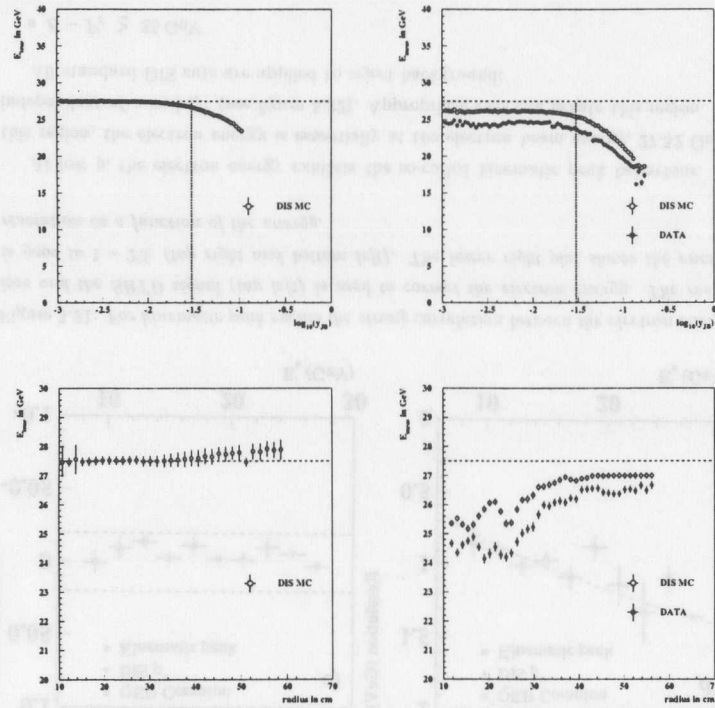


Figure 5.24: True (top left) and measured electron energy (top right) after  $Q_{DA}^2$  and standard DIS cuts versus  $y_{JB}$  and radial distance from the  $z$ -axis. The values shown are obtained from fits to slices in  $y_{JB}$  and radius.

As can be seen from figure 5.24 the mean electron energy of the MC KP sample as a function of the radius on the face of the RCAL overshoots that of the data everywhere. More importantly the difference is not constant, but shows a clear structure with a maximum discrepancy between RCAL radii of 16 and 26 cm indicating that the discrepancy is, at least in this region, due to an inaccurate description of the inactive material in the Monte Carlo. Figure 5.24 also shows the mean true electron energy as a function of  $y_{JB}$ . Below  $y \approx 0.03$  the true electron energy becomes constant and essentially reflects the electron beam energy. Plotting the mean measured electron energy as a function of  $y_{JB}$  shows that below  $y_{JB} \approx 0.03$  the electron energy becomes independent of  $y$ . Also the true electron energy as a function of radius on the face of the RCAL is depicted. Evidently there is no significant dependence on the electron impact point. Therefore

the kinematic peak sample provides an almost monoenergetic set of events giving the opportunity to investigate the spatial dependence of the energy loss by the CAL.

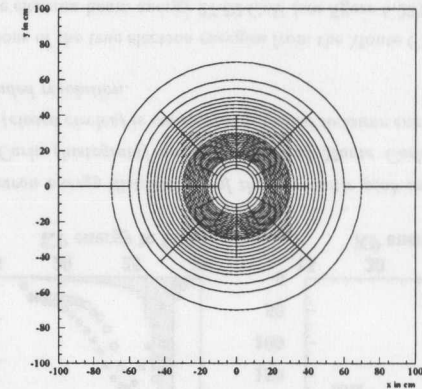


Figure 5.25:  $(r, \phi)$ -bins on the face of the RCAL in which the  $X_0$  is extracted and in turn the correction applied. The grey area indicates the position of the SRTD with a 13 cm box cut. The overlap of the SRTD with the  $(r, \phi)$  bins allows a test of the method.

By construction the KP sample provides a ‘test beam’ at 27.52 GeV. Using small  $(r, \phi)$  bins on the face of the RCAL the sample is binned such that the amount of material traversed by the electron before reaching the RCAL in each bin is approximately constant (figure 5.25). The energy loss as determined from the peak of the measured energy spectrum in each bin in combination with results from CERN test beam measurements on energy loss characteristics allows one to correct the electron energy.

The innermost bins overlap with the SRTD, allowing a test of the method. Figure 5.26 and 5.27 show examples of measured energy spectra for data and MC in bins outside the SRTD. The spectra are fit to a gaussian with an exponential tail.

For these studies the energy loss parametrization as given in [80], based on CERN testbeam data with varying amounts of material in front of the CAL, is used (see figure 5.28).

$$\frac{E_{true}}{E_{meas}} = 1 + x(0.0037e^{1.79x}E_{meas}^{-2.75} + 0.054e^{0.58x}E_{meas}^{-0.51}) \quad (5.2)$$

where  $x$  represents the amount of material traversed, measured in radiation lengths. For the KP sample  $E_{true}$  is taken to be 27.52 GeV (the electron beam energy) and  $E_{meas}$  is obtained from the peak of the fits to the spectra. Hence an  $X_0$  value for each bin in data and MC can be obtained. In turn the true electron energy can be evaluated for all measured electron energies in the KP bins.

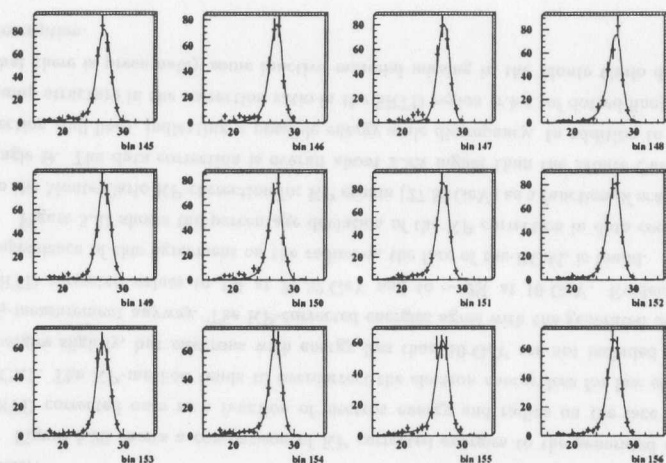


Figure 5.26: Example of data KP sample electron energy spectra in GeV in correction bins. The distributions are fitted to a gaussian with an exponential tail.

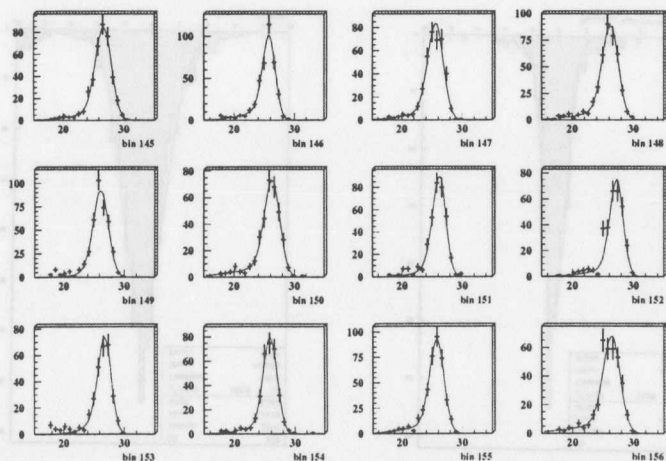


Figure 5.27: Example of Monte Carlo KP sample electron energy spectra in GeV in correction bins. The distributions are fitted to a gaussian with an exponential tail.

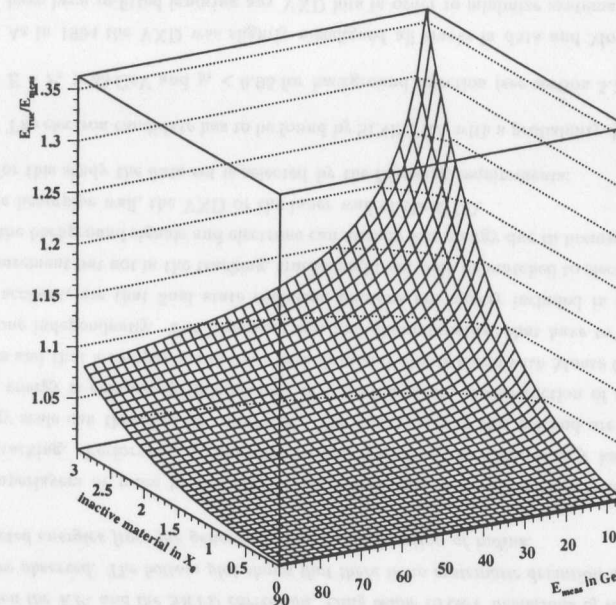


Figure 5.28: Parametrisation of the ratio between the true electron energy  $E_{true}$  and measured electron energy  $E_{meas}$  as a function of  $E_{meas}$  and the amount of penetrated inactive material  $X_0$ .

In order to obtain good agreement between data and MC a correction based on the measured  $X_0$  values is not sufficient. The MC has to be smeared, bin by bin, such that the energy resolution is modelled as well as the energy loss. From the widths of the gaussian fits to the measured energy spectra in data and MC a bin-by-bin smearing is calculated assuming the percentage increase of the energy resolution from MC to data to be energy independent.

The kinematic peak correction can be tested with kinematically constrained events like QED-Compton events and elastically produced DIS  $\rho$ 's. The correction, which is only sensitive to the energy loss in a small RCAL-bin averaged over many events, can also be compared to the SRTD energy correction, which corrects electron energies on an event-by-event basis exploiting the presampler effect.

Figure 5.29 shows the comparison of electron energies reconstructed using the kinematic constraint of the QED-Compton events with the KP corrected energy. The KP correction tends to give a slightly higher energy value, but this effect gets smaller for electrons outside the SRTD, where the energy resolution of the KP correction gets

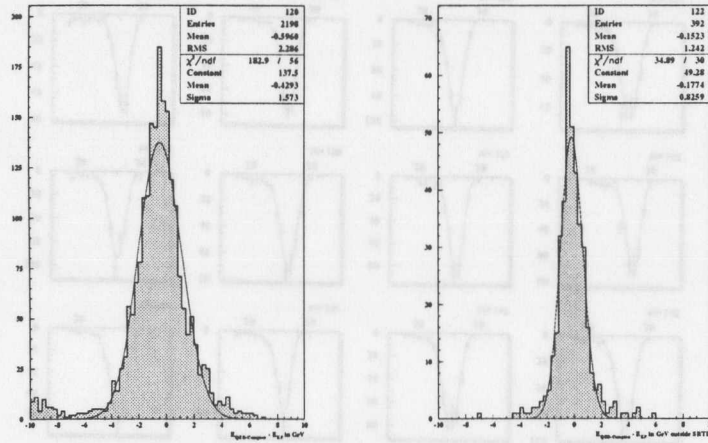


Figure 5.29: Comparison of KP energy correction with energies constrained by kinematics for all QED-Compton events (left) and only the ones with electrons outside the SRTD (right).

better.

Figure 5.30 shows a comparison of KP corrected energies to the generated or the SRTD corrected ones as a function of electron energy and radius on the face of the RCAL. The KP-method tends to overcorrect the electron energy loss for low electron energies slightly, but electrons with energy less than 10 GeV are not included in the  $F_2$ -measurement anyway. The KP-corrected energies agree with the generated and the SRTD corrected values to 1% at 27.52 GeV and to  $\sim 2\%$  at 10 GeV. Evidently no dependence of this agreement on the radius on the face of the RCAL is found.

Figure 5.31 shows the percentage deviation of the KP correction in data compared to the Monte Carlo KP correction for KP events (27.52 GeV) as a function of scattering angle  $\Theta$ . The data correction is overall about 2.5% higher than the Monte Carlo correction (full line), indicating a possible energy scale discrepancy. In addition to that a bump structure in the correction ratio in the SRTD region (r.h.s. of dotted line) shows that there is presumably some inactive material missing in the Monte Carlo detector description.

#### 5.4.5.2 Energy Calibration based on Tracking

Due to the  $Q_{DA}^2 < 100 \text{ GeV}^2$  cut the KP sample runs out of statistics at an RCAL radius of  $\approx 70 \text{ cm}$ . Therefore, outside this region the KP energy correction cannot be applied anymore. However, as particles that hit the outer RCAL or BCAL traverse

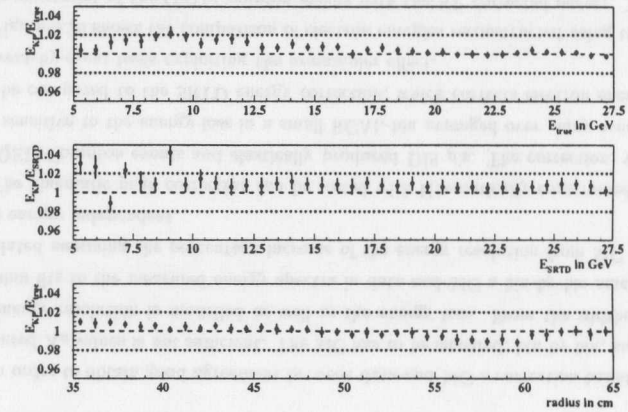


Figure 5.30: KP correction as a function of electron energy: The top plot shows the ratio of KP corrected over generated electron energy. The correction is good to  $\pm 2\%$  (dotted line), at higher energies even better. The middle plot demonstrates the good agreement between the KP- and the SRTD correction. Only below 10 GeV deviations of more than 2% are observed. The bottom plot shows that there is no systematic deviation of the KP corrected energies from the generated values as a function of radius.

six superlayers or more in the CTD their momentum is very well determined from the tracking. Performing a calorimeter-track matching the CAL energy loss or the energy scale can therefore be calibrated. The advantages of this method are that the CAL energy is completely independent of the momentum reconstruction of the CTD tracks and that a comparison of data with data and Monte Carlo with Monte Carlo can be done independently. The disadvantages and characteristics, that have to be taken into account, are that final state radiation photons are mostly included in the CAL measurement but not in the tracking, tracks might not only be matched to electrons but also the background signals and electrons can already lose energy due to bremsstrahlung in the beampipe wall, the VXD or the inner wall of the CTD.

For this study the data set is selected by the following requirements:

- The electron candidate has to be found by SINISTRA with a probability  $P_{SI} > 0.9$ ;
- $E - P_z > 35 \text{ GeV}$  and  $y_e < 0.95$  for background rejection (see section 5.7);
- As in 1994 the VXD was slightly misaligned all tracks in data and Monte Carlo have been re-fitted ignoring any VXD hits in order to minimize systematic effects on the momentum reconstruction;
- Extrapolating tracks via a helix fit to the end of the magnetic field map in the

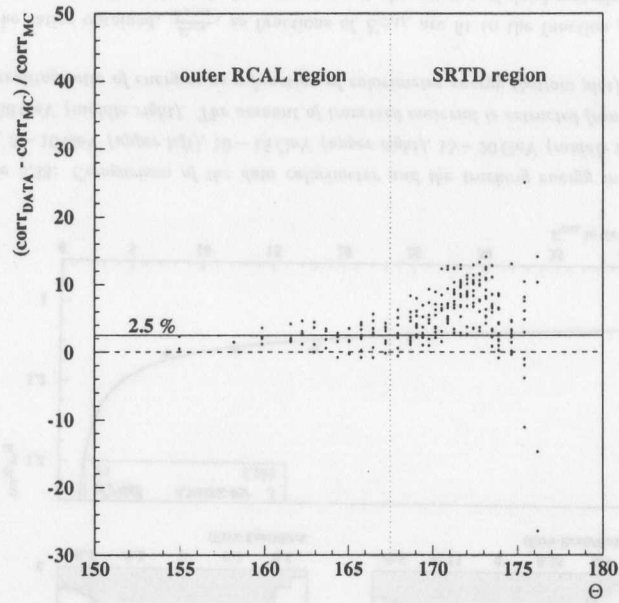


Figure 5.31: Percentage deviation of the KP correction in data compared to the Monte Carlo KP correction for KP events (27.52 GeV) as a function of scattering angle  $\Theta$ . The data correction is overall about 2.5% higher than the Monte Carlo correction (full line), indicating a possible energy scale discrepancy. In addition to that a bump structure in the correction ratio in the SRTD region (r.h.s. of dotted line) shows that there is presumably some inactive material missing in the Monte Carlo detector description.

inner part of the detector and using a tangential straight line for the following at most 10 cm to the face of the CAL one and only one track must match the electron candidate within 5 cm. For systematic checks the track was also required to originate from the event vertex, but no significant effect on the final result has been observed.

In order to perform the calibration study in detector regions with approximately constant amount of material, the data set is subdivided according to the electron impact point to be at a radius of 70–100 cm, 100–120 cm or greater than 120 cm in the RCAL or the electron to be in the BCAL.

For each of these spatial bins electron energy bins of 5–10 GeV, 10–15 GeV, 15–20 GeV and 20–30 GeV are defined. In each bin the percentage deviation of the electron energy measured in the calorimeter,  $E_{CAL}$ , with respect to the tracking determination,

$E_{trk}$ , is sampled. Examples of the resulting distributions for  $100 < \text{radius} \leq 120$  cm in the data and Monte Carlo are shown in figure 5.32 and 5.33 respectively. The central peak positions are determined by fits to gaussian with exponential tails to account for the final state radiation effects.

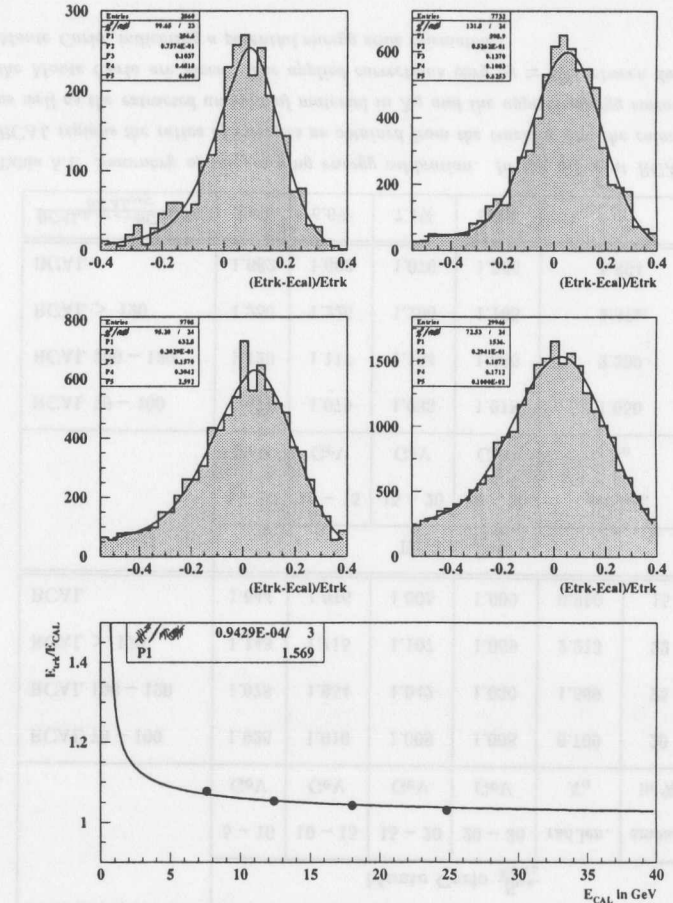


Figure 5.32: Comparison of the Monte Carlo calorimeter and the tracking energy in bins of  $E_{CAL}$  5–10 GeV (upper left), 10–15 GeV (upper right), 15–20 GeV (middle left) and 20–30 GeV (middle right). The amount of traversed material is extracted from a fit to the resulting ratio of energies as a function of calorimeter energy (bottom plot).

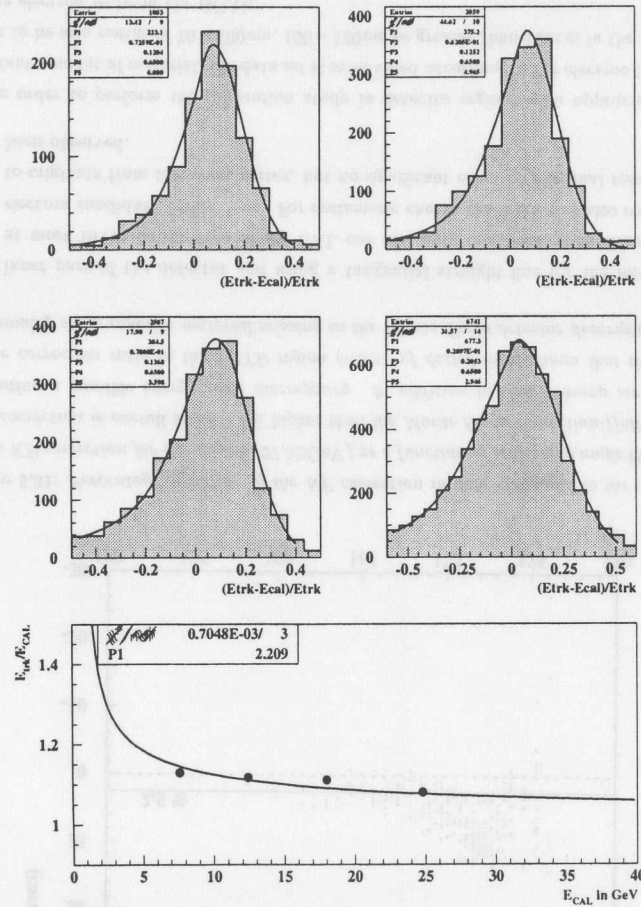


Figure 5.33: Comparison of the data calorimeter and the tracking energy in bins of  $E_{CAL}$  5 – 10 GeV (upper left), 10 – 15 GeV (upper right), 15 – 20 GeV (middle left) and 20 – 30 GeV (middle right). The amount of traversed material is extracted from a fit to the resulting ratio of energies as a function of calorimeter energy (bottom plot).

The ratios obtained,  $\frac{E_{trk}}{E_{CAL}}$ , as functions of  $E_{CAL}$  are fit to the function given in equation ( 5.2), where the only free parameter is the amount of dead material, which causes the observed energy loss. As in the KP-correction this quantity for a given detector region allows one to determine the correction of the measured to the true electron

energies. However, the correction has to be supplemented by additional smearing of the Monte Carlo energies.

	Monte Carlo $\frac{E_{trk}}{E_{CAL}}$					
	5 – 10 GeV	10 – 15 GeV	15 – 20 GeV	20 – 30 GeV	rad.len. $X_0$	smear. in %
RCAL 70 – 100	1.028	1.010	1.008	1.008	0.700	20
RCAL 100 – 120	1.078	1.054	1.042	1.030	1.569	25
RCAL > 120	1.143	1.115	1.107	1.069	2.213	22
BCAL	1.044	1.016	1.005	1.009	0.950	15
	DATA $\frac{E_{trk}}{E_{CAL}}$					
	5 – 10 GeV	10 – 15 GeV	15 – 20 GeV	20 – 30 GeV	rad.len. $X_0$	
RCAL 70 – 100	1.071	1.079	1.033	1.018	1.650	
RCAL 100 – 120	1.129	1.117	1.154	1.080	2.209	
RCAL > 120	1.250	1.226	1.200	1.165	2.871	
BCAL	1.082	1.083	1.076	1.066	1.894	
$\frac{BCAL_{DATA} - BCAL_{MC}}{BCAL_{MC}}$	3.6%	6.6%	7.1%	5.6%		

Table 5.1: Summary of the tracking energy calibration. In the different RCAL and BCAL regions the ratios of energies as obtained from the tracking and the calorimeter as well as the extracted amount of material in  $X_0$  and the applied energy smearing in the Monte Carlo are given. The applied corrections vary by  $\approx 6\%$  between data and Monte Carlo, indicating a potential energy scale mismatch.

A summary of the results from the tracking calibration is given in table 5.1. the general tendency of increasing energy loss with increasing RCAL radius due to cryotubes, cabling and mechanical support structures in the data is well reproduced by the Monte Carlo. The obtained correction factors vary between  $\sim 1 - 14\%$  in the Monte Carlo and  $2 - 25\%$  in the data. The extracted amount of traversed radiation lengths in the data is about  $0.4 - 0.9X_0$  larger than in the Monte Carlo. But more importantly the energy corrections in the BCAL, where the amount of material in front of the

calorimeter is relatively small and its geometrical distributions is well defined (mostly the superconducting coil), are overall about 6% larger in the data than in the Monte Carlo, indicating an energy scale mismatch.

1 – 1.5% energy loss effects due to the electron traversing the beampipe and the inner detector walls are not corrected for. Similar results have been found in [86].

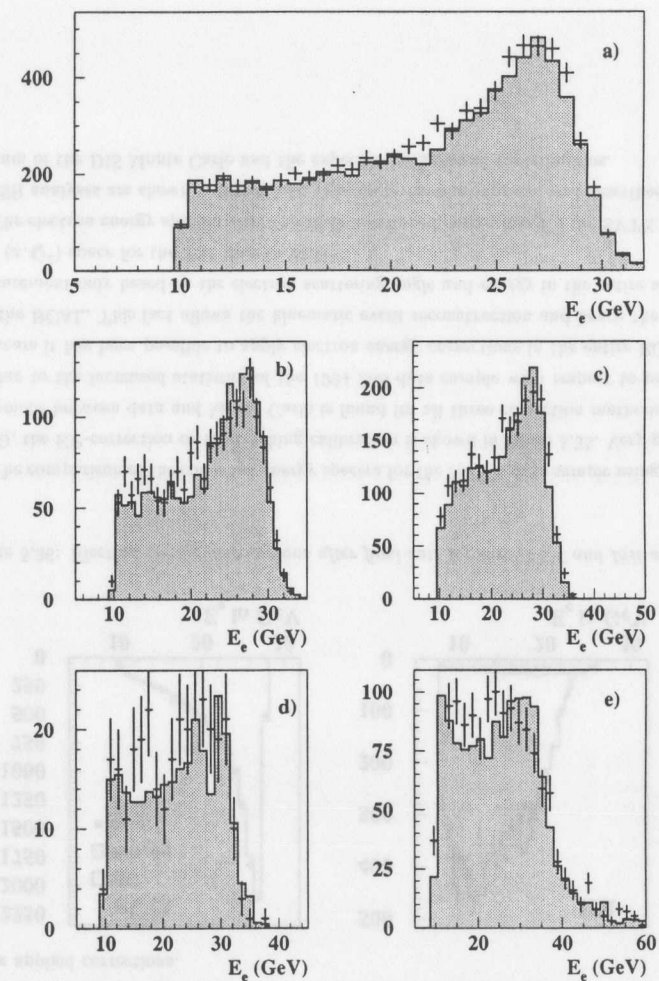
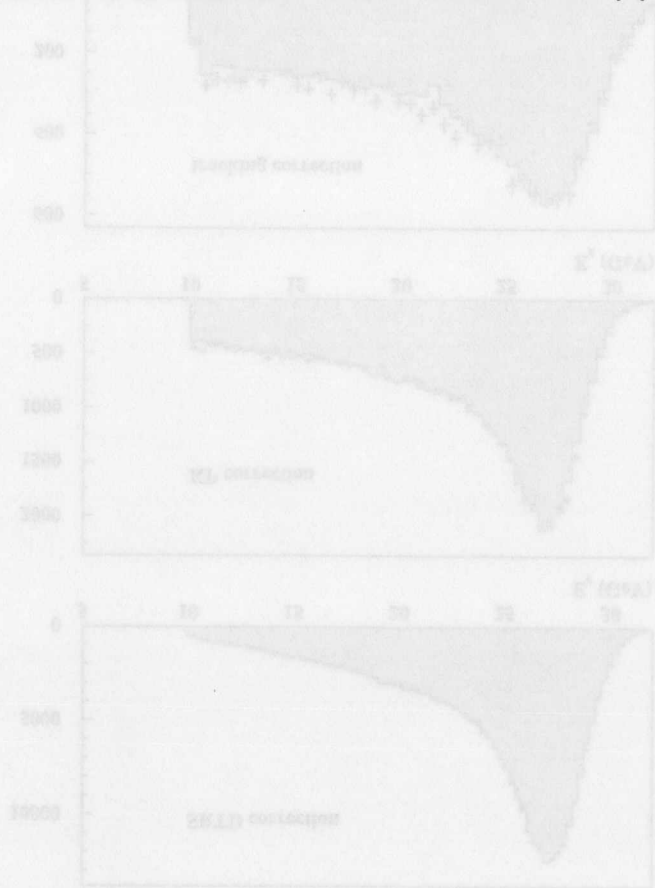


Figure 5.34: Electron energy spectrum for data (dots) and Monte Carlo (histogram) after calibration using the tracking correction for different regions in the RCAL and BCAL. a) RCAL radius 70 – 100 cm, b) RCAL radius 100 – 120 cm, c) RCAL radius > 120 cm, d) BCAL edge  $z < -90$  cm and e) rest of the BCAL.

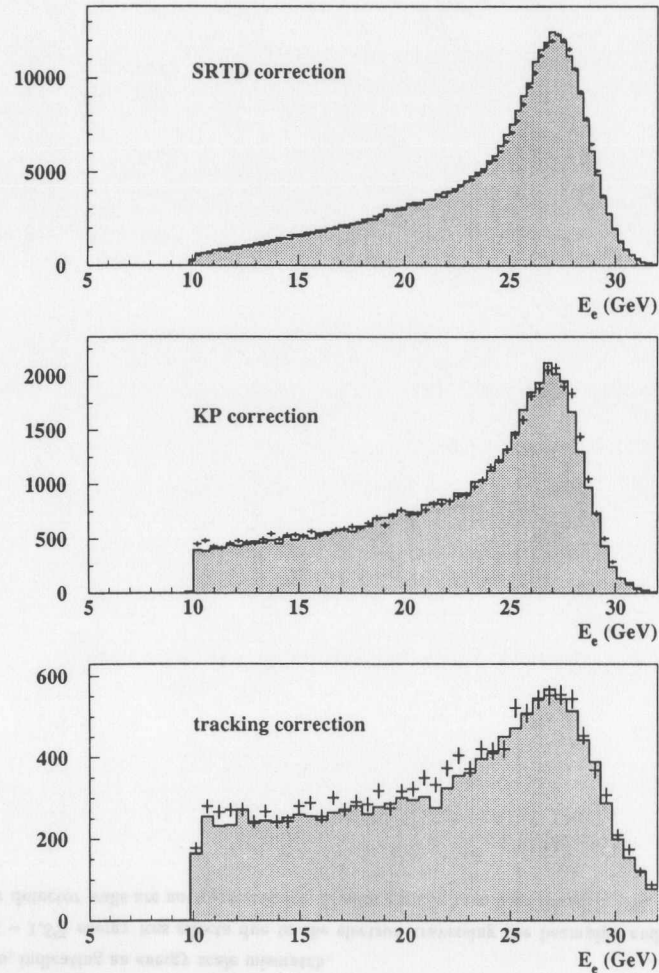


Figure 5.35: Electron energy spectrum for data (dots) and Monte Carlo (histogram) after correction using the SRTD (top), the KP correction (middle) or the tracking correction (bottom).

Figure 5.34 shows a comparison of the electron energy spectra in the different detector regions after the tracking energy calibration. In all regions very good agreement in peak position and width between data and Monte Carlo is found, providing confidence in the applied corrections.

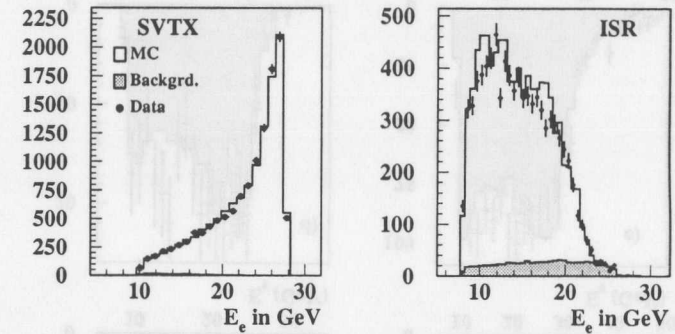


Figure 5.36: Electron energy distributions after final cuts for the SVTX and ISR analyses.

The comparison of the corrected energy spectra for the NVTX data sample using the SRTD, the KP-correction or the tracking calibration is shown in figure 5.35. Very good agreement between data and Monte Carlo is found for all three correction methods.

Due to the increased statistics of the 1994 DIS data sample with respect to previous years it has been possible to apply electron energy corrections in the entire RCAL and the BCAL. This fact allows the kinematic event reconstruction and hence the  $F_2$ -measurement only based on the electron scattering angle and energy in the entire accessible  $(x, Q^2)$  space for the first time in ZEUS.

The electron energy spectra after the afore mentioned corrections for the SVTX and the ISR analyses are shown in figure 5.36. The data distributions are well described by the sum of the DIS Monte Carlo and the expected background contributions.

### 5.5 Luminosity Calorimeters.

The position and energy reconstruction of the emitted photon plays a crucial role in the ISR analysis. No special photon finder is run on the data of the luminosity calorimeter, but rather its total energy is determined. The position and hence angle reconstruction is based on a centre of gravity algorithm, which determines  $x$ - and  $y$ -coordinate of the photon separately from hits in the grid of the scintillator fingers in the calorimeter.

However, the simulation of this detector component is complicated. The usual simulation of calorimeter showers is, mainly for processing time and particle multiplicity reasons, terminated according to parametrisations, which are tuned to test-beam data. In order to shield the luminosity photon calorimeter against synchrotron radiation, a carbon-lead filter ( $\sim 3.5 X_0$ ) is placed about 1 m in front of it. Particle showers, that start in this filter, can therefore be terminated before a full development in the actual calorimeter is simulated. Therefore the energy measurement in the photon calorimeter is simulated separately from the standard ZEUS detector simulation, according to parameters obtained from the data [74].

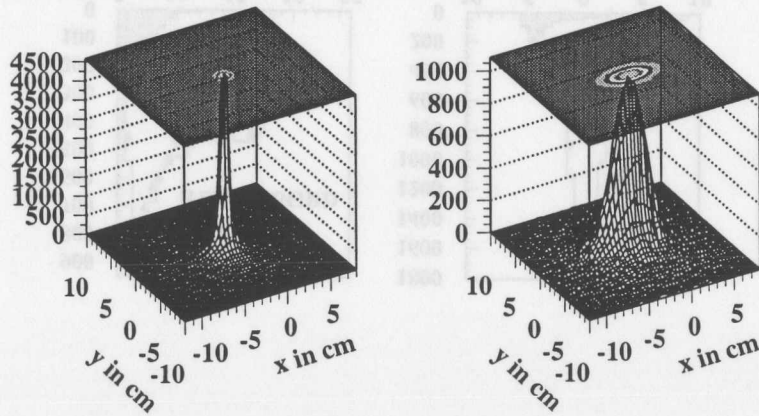


Figure 5.37: Distribution of the photon impact points in  $x$  and  $y$  in the photon luminosity calorimeter for Monte Carlo events before (left) and after reweighting (right).

Due to the rather small geometrical acceptance of the luminosity photon calorimeter and its long distance from the interaction, it is particularly sensitive to the beam tilt and divergence. As the standard simulation has been done using average values, an adequate description of the beam divergence in  $x$  and  $y$  is obtained only after reweighting the Monte Carlo events to the distributions found in the data (see figure 5.37).

The resulting distributions of the reconstructed  $x$ - and  $y$ -photon positions in the

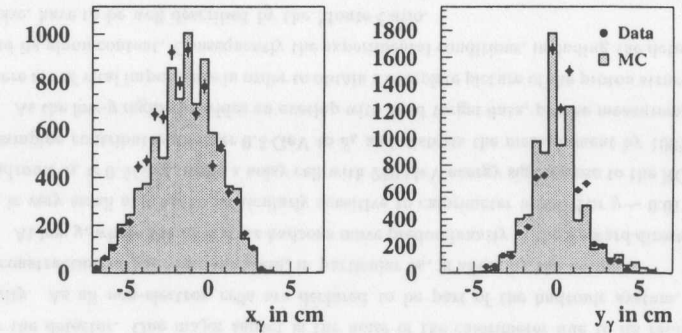


Figure 5.38: Distributions of the photon impact point in  $x$  and  $y$  comparing data (full circles) and Monte Carlo (histogram).

luminosity calorimeter are shown in figure 5.38. Adequate agreement between data and Monte Carlo can be seen. However, the small discrepancies and fluctuations are due to the shower terminators in the Monte Carlo and of no particular importance for the present analysis, as the photon position is not explicitly used in the reconstruction.

The photon energy can be directly measured in the luminosity calorimeter, but it can also be estimated from quantities reconstructed in the main calorimeter as

$$E_{\gamma}^{CAL} = E_e \cdot \left(1 - \frac{1 - y_e}{1 - y_{DA}}\right) \quad (5.3)$$

The photon energy spectrum from the direct measurement and a comparison to this estimate from the main calorimeter, after all selection cuts, are shown in figure 5.39.

The shaded histograms represent bremsstrahlung background (see section 5.7). Very good agreement between data and Monte Carlo obtained after adding the bremsstrahlung background is evident.

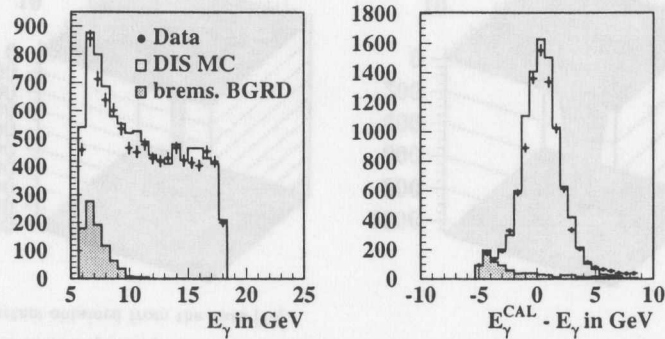


Figure 5.39: Left: Spectrum of photon energies as reconstructed by the lumi-photon calorimeter after final event selection. The sum of the bremsstrahlung background (shaded histogram) and the DIS Monte Carlo is displayed as open histogram and describes the data (full circles) very well. Right: Difference in photon energy as reconstructed from the main detector and measured in the photon-lumi calorimeter. Again the data are well described by the sum of the bremsstrahlung background and the DIS Monte Carlo.

## 5.6 Hadronic Event Parameters.

### 5.6.1 Introduction.

Since ZEUS is essentially a  $4\pi$ -detector, not only the scattered electron, but also the hadronic products in the final state are detected. Their energies as well as their angles can be reconstructed in the calorimeter. These together with the energy and angle of the scattered electron provide an overconstrained system for the reconstruction of the kinematic variables  $x$ ,  $y$  and  $Q^2$ , of which only two are independent.

This fact is exploited in the NVTX analysis (see section 6.6), whereas the SVTX and the ISR analyses are almost entirely based on the reconstruction of the electron.

The hadronic final state reconstruction is performed using the calorimeter and the event vertex. All calorimeter cells, which are not assigned to the scattered electron, are interpreted to be part of the hadronic system. The following three quantities are reconstructed from these cells:

$$\begin{aligned}\delta_h &= \sum_h E_h - P_{z,h} \\ P_{T,h} &= \sqrt{\left(\sum_h p_{x,h}\right)^2 + \left(\sum_h p_{y,h}\right)^2} \\ \cos \gamma_h &= \frac{P_{T,h}^2 - \delta_h^2}{P_{T,h}^2 + \delta_h^2}\end{aligned}$$

The angle  $\gamma_h$  characterises the hadronic energy flow. In the naive parton model  $\gamma_h$  is the polar angle of the struck quark.

### 5.6.2 Noise Simulation.

The reconstruction of kinematical variables suffers from measurement errors introduced by the detector. One major aspect is the noise of the calorimeter due to its radioactivity. As all non-electron cells are declared to be part of the hadronic system, the reconstruction of hadronic variables, in particular  $\delta_h$ , is affected by the noise.

At low  $y$ , where the final state hadrons move predominantly in the forward direction,  $\delta_h$  is very small and hence particularly sensitive to calorimeter noise. For  $y \sim 0.01$  the hadronic  $\delta_h \approx 0.5$  GeV, while a noisy cell with 250 MeV energy signal close to the RCAL beam pipe contributes another 0.5 GeV to  $\delta_h$  and distorts the measurement by 100%.

As the low- $y$  region provides an overlap with fixed target data, precise measurements there are of vital importance in order to obtain a complete picture of the proton structure and its gluon content. Consequently the experimental conditions, including the detector noise, have to be well described by the Monte Carlo.

Since it was found that the noise description in the BEMC, FEMC, FHAC1 and FHAC0 sections of the calorimeter is not adequate in the simulation, the following procedure has been proposed in [76]:

In the run range considered for the NVTX analysis, random trigger and passthrough events, which are essentially empty as far as  $ep$ -scattering or beam-gas events are concerned, are selected. This sample provides a representative picture of the calorimeter noise, taking run-by-run variations into account. For this sample the number of noisy cells per event and the cell energy versus the imbalance of the two PMTs in a cell (figure 5.40) are sampled for the ten different calorimeter regions (R/B/FEMC, R/FHAC0, R/B/FHAC1 and B/FHAC2).

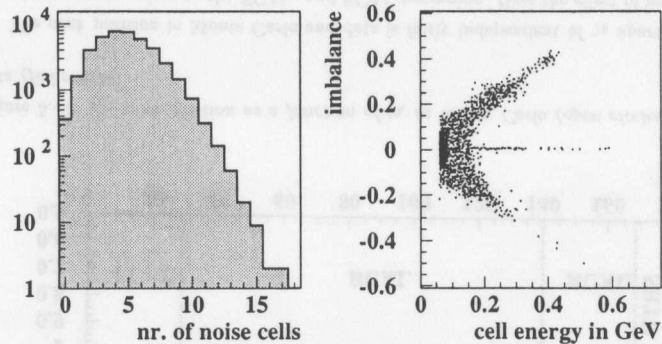


Figure 5.40: Calorimeter noise in the BEMC section. Left: Number of noise cells per event. Right: Energy versus imbalance for these cells.

The noise in Monte Carlo events is finally replaced by calorimeter entries randomly generated according to the distributions measured in the data.

This procedure has been followed in essence. In order to investigate effects due to noise variations with cell position, for example for cells close to or far away from the beampipe, the number of noisy cells has been sampled as a function of their position in the calorimeter. However, the improvement in description compared to the position independent procedure has been found to be small.

### 5.6.3 Noise Cuts.

Calorimeter noise originates from several sources, for example the radioactivity of the uranium or noise in the PMTs or readout electronic. Certain cells also tend to produce mini-sparks, where one of the two cell PMTs frequently gives a large signal.

The latter can be identified via their hit frequency. The uranium and electronic noise produce cell energy distributions, that peak at low values. Nevertheless high energy tails overlap with an energy region populated by deposits originating from  $ep$ -interactions. Different cut combinations have been studied [77, 78].

In order to reduce the contamination of the data sample by this noise, affected cells

are removed according to criteria identifying calorimeter noise. These criteria, used in the analyses presented here, are

$$\begin{aligned}
 E_{\text{cell}} &< 100 \text{ (150) MeV for isolated EMC (HAC) cells} \\
 \text{relative imbalance} &> 0.8 \text{ for isolated cell with energy} < 0.7 \text{ GeV} \\
 \text{and} &\text{ particularly noisy cells are removed explicitly}
 \end{aligned}$$

In the SVTX analysis the FCAL modules 7 and 8 are exceptionally noisy. As this analysis is almost entirely based on the electron reconstruction and focusses on the kinematic region, where the final state electrons as well as the hadrons move predominantly in the rear direction, these modules are cut out completely and ignored in the reconstruction of hadronic event variables. The effect on  $\delta$ , the only quantity where hadronic energy enters the analysis, has been found to be negligible in a Monte Carlo study.

### 5.6.4 Hadronic Energy Scale.

In the determination of hadronic event parameters the hadronic energy measurement and its reproducibility in the Monte Carlo play a crucial role. Because of the collimation of hadronic energy into jets and the unknown distribution over charged and neutral particles it is not possible to select well defined hadrons for energy correction studies. Instead the hadronic energy scale is studied using global event quantities, such as the transverse momentum of the hadronic final state ( $p_{T,h}$ ) and of the scattered electron ( $p_{T,e}$ ) or  $\delta_h$ . As the latter can be reconstructed or, if necessary, be corrected very precisely (see section 5.4) it serves here as a reference scale.

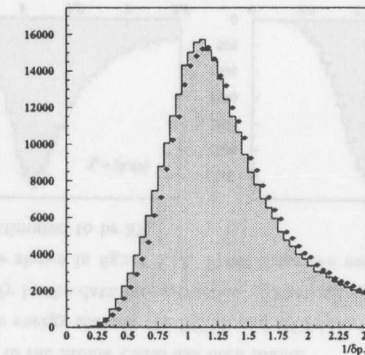


Figure 5.41:  $\frac{p_{T,e}}{p_{T,h}}$ -distribution in Monte Carlo (histogram) and data (full circles). The peak in the data is clearly shifted to larger values of  $\frac{1}{\delta_{pT}}$ , indicating an energy mismatch.

In an ideal measurement  $p_{T,h}$  must equal  $p_{T,e}$  as a consequence of energy and momentum conservation. Particle losses in the forward or rear beamhole are expected to

affect the measurement of  $p_{T,h}$  only little as their transverse momentum is relatively small. However,  $\delta_h$  is reduced which in turn can also affect the reconstruction of the hadronic angle  $\gamma_h$ . Particle losses are also simulated in the Monte Carlo, so that these effects should be reproducible.

Figure 5.41 shows the distribution of  $\frac{1}{\delta p_T} = \frac{p_{T,e}}{p_{T,h}}$  for events, which pass the final selection cuts. The overall characteristics such as shape and width, are in good agreement between Monte Carlo and data.

But the data distribution appears to be slightly shifted to higher values of  $\frac{1}{\delta p_T}$ , indicating a possible scale mismatch. In order to investigate, whether this effect is to be attributed to the energy scale, missing material in the detector simulation or other effects, the peak position of the  $\frac{1}{\delta p_T}$ -distribution, as obtained from a gaussian fit, has been studied as a function of the hadronic angle  $\gamma_h$ . The results are shown in figure 5.42.

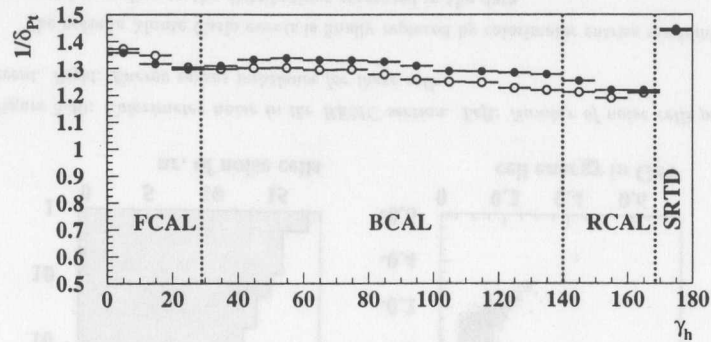


Figure 5.42:  $\frac{1}{\delta p_T}$  peak position as a function of  $\gamma_h$  in Monte Carlo (open circles) and data (full circles).

The peak position in Monte Carlo and data is fairly independent of  $\gamma_h$  apart from the extreme region close to the FCAL- and RCAL-beampipe. Here the effect of particle losses in the beamhole is clearly visible. But more importantly  $\frac{1}{\delta p_T}$  in the data tends to be larger than in the Monte Carlo in certain detector regions. In the FCAL, i.e. at small  $\gamma_h$ ,  $\frac{1}{\delta p_T}$  is well reproduced by the simulation, but in the RCAL a mismatch can be seen, which becomes a significant discrepancy in the BCAL. As there is only very little inactive material in front of the calorimeter in the BCAL, i.e. the beampipe, inner and outer wall of the CTD and the solenoid, the scenario of inadequate description of material can be excluded. The discrepancy in  $\frac{1}{\delta p_T}$  between data and Monte Carlo amounts to  $\sim 4 - 6\%$  in the BCAL and  $\sim 1 - 3\%$  in the RCAL. These figures are consistent with the size of the overall electron energy correction in the corresponding calorimeter sections.

In [82], where the calorimeter energy has been compared to the track momentum for hadronic particles isolated in phase space, a deviation of up to 9% in the measured energy with respect to the Monte Carlo has been found.

Consequently the energy scale in the BCAL and RCAL have been corrected by 6% and 2.5% respectively in the data reconstruction of hadronic quantities. The resulting  $\frac{1}{\delta p_T}$  distributions are shown in figure 5.43. From these the uncertainty on the energy scale correction is estimated to be 3%.

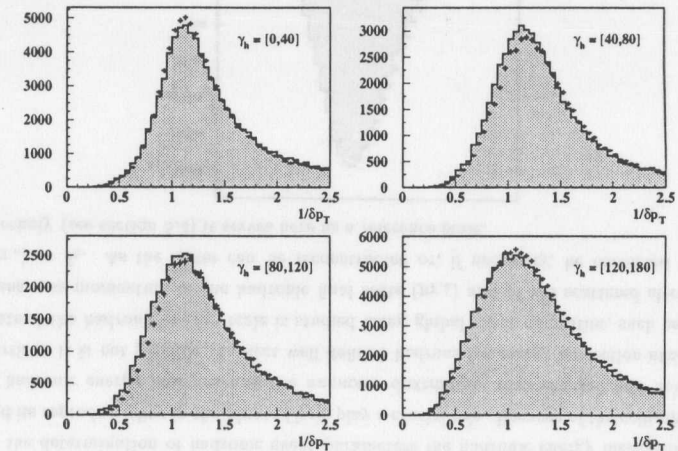


Figure 5.43:  $\frac{1}{\delta p_T}$  distribution in different  $\gamma_h$  region for Monte Carlo (histogram) and data (full circles).

Following the same approach, corrections for the hadronic angle  $\gamma_h$  and  $y_{JB} = \frac{\delta_h}{2E_c}$  where  $\delta_h = (E - P_z)_h$  have been determined. The resulting distributions are depicted in figure 5.44.

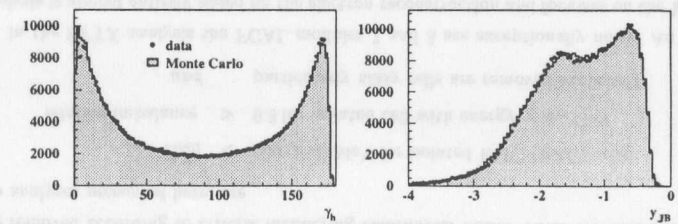


Figure 5.44:  $\gamma_h$ - and  $y_{JB}$ -distributions for Monte Carlo (histogram) and data (full circles).

Both hadronic quantities are well described by the simulation. Only the difference of the longitudinal hadronic energy and momentum, i.e.  $y_{JB} \sim (E - P_z)_h$ , shows a small discrepancy between data and Monte Carlo in the  $y_{JB}$ -range  $10^{-3} - 10^{-1}$ . The possible effect on  $F_2$  is covered by the systematic errors.

5.6.5 Large Rapidity Gap Events.

Studies of the first HERA data, recorded in 1992, revealed the presence of a new class of events in DIS [119]. These events, which contribute about 10% of the DIS sample, are characterised by the absence of energy deposits in the forward direction. An example event in figure 5.45, recorded in 1994, demonstrates the topology.

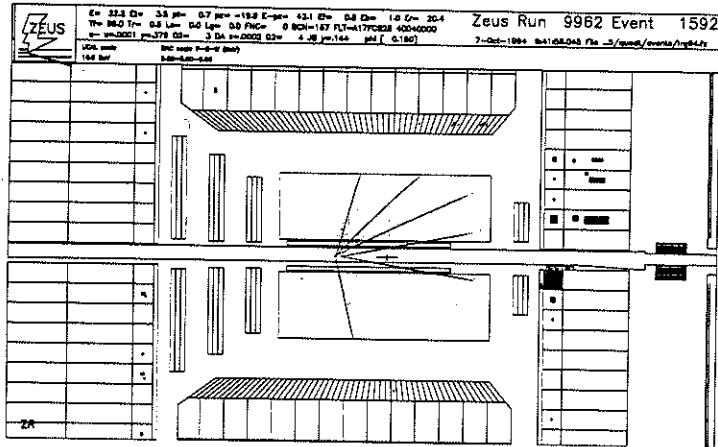


Figure 5.45: A typical 1994 LRG event in the ZEUS detector. The absence of energy deposits around the FCAL beamhole, originating from the proton remnant, contrasts the topology of usual DIS events.

In regular DIS events the proton breaks up, its remnant moves in the forward direction and deposits energy in the inner ring of the FCAL close to the beampipe. The region between the remnant and the current jet, which originates from the struck quark, is filled with hadrons resulting from the colour flow between the two. Gaps without particle flow between the current jet and the proton remnant are exponentially suppressed.

The direction of the outgoing final state hadrons is described using the pseudorapidity

$$\eta = -\ln \left[ \tan \frac{\Theta}{2} \right]$$

where  $\Theta$  is the polar angle of the particle. A selection method for this new class of events is based on the quantity  $\eta_{max}$ , where  $\eta_{max}$  is the largest  $\eta$ -value for any calorimeter cell with at least 400 MeV energy, i.e. for the cell closest to the outgoing proton direction.

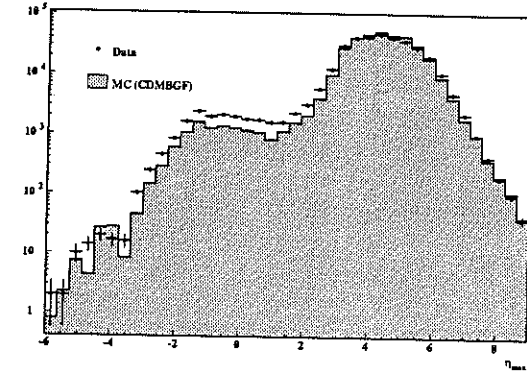


Figure 5.46:  $\eta_{max}$ -distribution for data (full circles) compared to the Ariadne 4.06 Monte Carlo (histogram).

Values of  $\eta_{max} \simeq 4.3$  are observed for energy deposits at the edge of the FCAL. Larger rapidity values can be obtained when a few calorimeter cells around the FCAL beam hole are combined to form a cluster with reconstructed position in the beam hole.

The new event class with essentially no energy in the forward direction yields very small or even negative  $\eta_{max}$ -values. They have an unpopulated region in their rapidity distribution and hence are called 'large rapidity gap (LRG)'-events.

The events are interpreted as diffractive<sup>3</sup> dissociative scattering, which is mediated via the exchange of a colourless object, usually called the pomeron.

Figure 5.47 shows schematic diagrams contrasting the regular and the large rapidity gap DIS events. IP denotes the colourless object in the proton, off which the virtual photon scatters.  $Q^2$  is the usual squared 4-momentum transfer of the electron, whereas  $t$  describes the 4-momentum transfer at the proton vertex.

In this picture the outgoing proton should stay intact for a considerable fraction of LRG events. This has been confirmed by tagging the final state proton and reconstructing its momentum in the leading proton spectrometer [120, 121].

As the fraction of large rapidity gap events in the sample of DIS events has been shown to be almost independent of  $Q^2$  [122], the process is considered to be leading twist.

Large rapidity gap events have been observed in all three analyses.

<sup>3</sup>The expression 'diffractive' indicates the analogy between the final state particle flow in hadron scattering and the phenomena of diffraction patterns in optics.

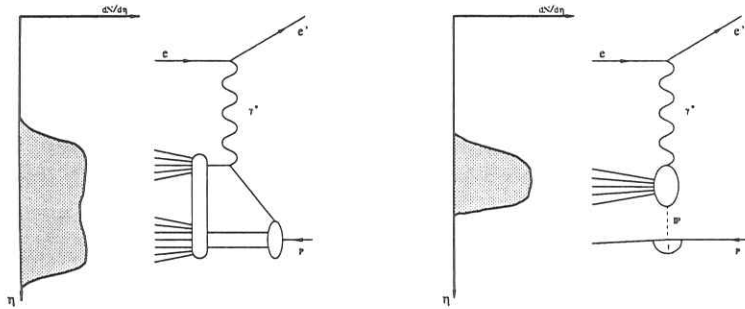


Figure 5.47: Final state particle flow as a function of the pseudorapidity  $\eta$  for regular DIS events (left) and for large-rapidity gap events (right).

$F_2$  is defined to be the inclusive structure function. Therefore the LRG events are included in the analysed event sample. As shown in figure 5.46 the LRG events have been added to the Monte Carlo description of the  $ep$ -scattering process using the colour dipole model, as implemented in the ARIADNE 4.06 Monte Carlo [59].

## 5.7 Backgrounds.

The selected DIS data sample is contaminated by two classes of background events. The one class can be identified on event by event basis as background and hence be removed from the sample. The other class gives rise to events that are essentially indistinguishable from DIS events and must therefore be subtracted statistically.

The largest and most important background source in the NVTX and the SVTX analyses are photoproduction events. In the ISR analysis the background originating from bremsstrahlung processes dominates.

### 5.7.1 Photoproduction Background.

Photoproduction events are characterised by  $Q^2$ -values close to zero. Even though the electron is scattered through a very small angle and lost down the rear beampipe, isolated hadrons or photons from  $\pi^0$ -decays can be misidentified as an electron.

The majority of photoproduction background events can be suppressed using the quantity  $\delta$  (section 5.2) by requiring

$$\delta > 38 \text{ GeV}$$

This cut also removes hard initial state photon radiation events from the sample, where the loss in  $\delta$  due to the photon escaping down the beampipe is  $2 \cdot E_{Lumi}^\gamma$ . If these events are not rejected they can cause large migrations in the reconstruction of the kinematic variables.

Since the ISR analysis focusses particularly on these events, the  $\delta$  calculation has to include the final state photon. Therefore the quantity  $\delta' = \delta + 2 \cdot E_{Lumi}^\gamma$  is determined. All selection cuts are imposed on this variable instead of  $\delta$ .

Also an upper cut is imposed, in order to remove background events from electron beam gas interactions or cosmic muons, which can leave large energy deposits only in the rear calorimeter

$$\delta < 65 \text{ GeV}$$

Nevertheless, some photoproduction events pass these selection cuts. Their contribution to the measured cross section has to be subtracted statistically. Several methods have been used in order to estimate this remaining background:

- Tagged photoproduction
- Photoproduction Monte Carlo

### 5.7.1.1 Tagged Photoproduction.

A subsample of the photoproduction background events can be identified as such and tagged due to the detection of the scattered electron in the luminosity electron calorimeter. In order to exclude bremsstrahlung events no signal should be seen in the luminosity photon calorimeter. Hence a cut on  $E_{lumi}^\gamma < 3$  GeV is imposed. Due to the very restricted geometrical acceptance of the electron luminosity calorimeter, the efficiency of tagging such events depends on the scattered electron energy and angle, and hence on  $\delta$ . In order to get a good energy response from the luminosity calorimeter a cut of  $7.5 < E_{lumi}^e < 20$  GeV is applied. Hence 15–40 GeV of the events'  $\delta$  is lost, which leaves a  $\delta$ -range of about 15–40 GeV for this method to give a reasonable estimate of the photoproduction background from the tagged data.

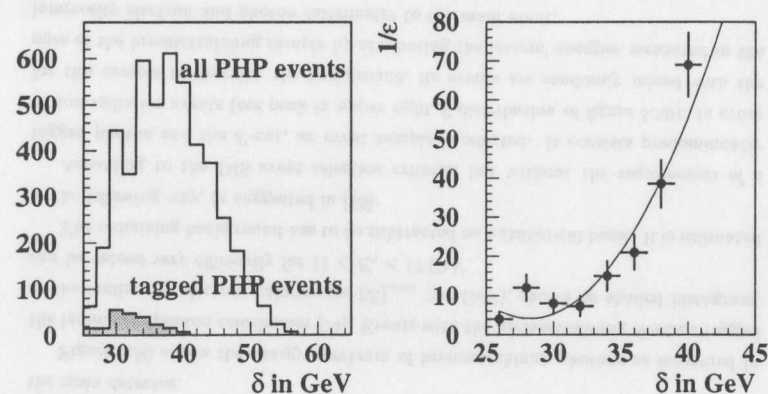


Figure 5.48: Left:  $\delta$ -distribution for all (open histogram) and the tagged (shaded histogram) photoproduction Monte Carlo events, that pass the DIS selection. Right: Resulting inverse tagging efficiency as a function of  $\delta$ .

The electron tagging efficiency, however, is extracted from a photoproduction Monte Carlo 4.5. Figure 5.48 shows the  $\delta$ -distribution for all and the tagged photoproduction events in the Monte Carlo. The ratio of the distributions is the inverse efficiency, to which a second order polynomial plus a constant term is fitted.

### 5.7.1.2 Photoproduction Monte Carlo.

Samples of 346301 and 87861 minimum bias non-diffractive photoproduction events have been generated using the PYTHIA 5.7 [72] event generator and the ALLM [139] parametrisation. The samples correspond to a cross section of 1148 nb.

As hadrons usually have to enter the rear part of the calorimeter in order to fake an

electron, the photoproduction events were generated in the kinematic region  $y_{gen} > 0.6$ , which corresponds to a photon-proton centre of mass energy of  $W \gtrsim 190$  GeV. Only events which have some chance to give rise to background are considered at all. As a consequence of the  $y$ -cut, which effectively sets an upper limit on the scattered and lost electron energy, this method can only be applied above  $\delta \approx 30$  GeV as seen in the main calorimeter.

In order to reduce the size of data storage and the corresponding processing time for the photoproduction Monte Carlo sample, only events that satisfy the trigger preselection and have the DIS DST bit set are written out. These events are then analysed following the same reconstruction chain and selection criteria as DIS events.

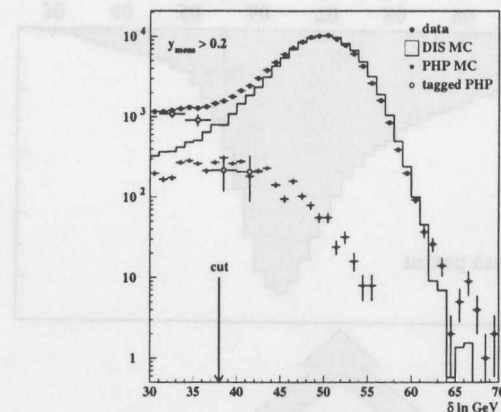


Figure 5.49:  $\delta$ -distribution at high- $y$ . Good agreement between the tagged photoproduction and the photoproduction Monte Carlo is observed, which allows the background estimation in the data compared to the DIS Monte Carlo.

Figure 5.49 shows the  $\delta$  distribution at  $y_{meas} > 0.2$  for data (closed circles), DIS Monte Carlo (open histogram), photoproduction Monte Carlo (stars) and the tagged photoproduction events (open circles). At  $\delta$ -values larger than  $\sim 50$  GeV the DIS-Monte Carlo agrees well with the data, while it undershoots at low  $\delta$  due to the background contamination in the data. The flattening of the photoproduction Monte Carlo at  $\delta < 38$  GeV is a consequence of the  $y_{true} > 0.6$  cut on the generator level. In the  $\delta$ -distribution between 32 and 43 GeV the background estimates from the tagging method can be used as a cross check. Good agreement with the photoproduction Monte Carlo is found for  $\delta > 38$  GeV. At  $\delta \approx 35$  GeV the sum of DIS Monte Carlo and tagged photoproduction amount to the number of events measured in the data.

The different methods give consistent results. But due to the limited statistics of

tagged events the photoproduction Monte Carlos are used in the background determination of the NVTX as well as the SVTX analysis.

From the comparison of the different methods the uncertainty on the photoproduction background determination is estimated to be +100% and -50%. The resulting uncertainty in  $F_2$  is accounted for by the systematic errors.

### 5.7.2 Bremsstrahlung Background.

In the ISR analysis the main source of background is the accidental coincidence of a DIS or photoproduction event with bremsstrahlung events of the Bethe-Heitler process  $ep \rightarrow ep\gamma$ . Unless the bremsstrahlung electron is seen in the luminosity electron calorimeter, the origin of the photon can not be identified, so that it is attributed to the event in the main detector.

Figure 5.50 shows the energy spectrum of bremsstrahlung photons as measured in the luminosity photon calorimeter [74]. Events with the bremsstrahlung electron tagged in the luminosity electron calorimeter ( $E_{Lumi}^e > 3$  GeV), shown as shaded histogram, can be vetoed very efficiently for  $11 < E_\gamma < 17$  GeV.

The remaining background has to be subtracted on a statistical basis. It is estimated in the following way, as suggested in [75]:

According to the DIS event selection criteria, but without the requirement of a tagged photon and the  $\delta'$ -cut, an event sample is selected. It consists predominantly of non-radiative events (see peak in upper right  $\delta'$ -distribution of figure 5.50). In order for this sample to describe the background, its events are randomly mixed with the ones of the bremsstrahlung sample by attributing the latter's energies measured in the luminosity electron and photon calorimeter to the main event.

The  $\delta'$ -distribution of the resulting sample (bottom plot in figure 5.50) peaks at  $\approx 64$  GeV and extends from 10 GeV to 120 GeV.

This background sample is normalised by a fit to the  $\delta'$ -distribution of the data after all cuts but the  $\delta'$ -cut are applied, in the range 67 to 94 GeV (figure 5.51). No DIS events are possible here, taking energy and momentum conservation and the detector resolution into consideration. Using this sample the bremsstrahlung background in any distribution can be subtracted.

After correcting the energy of the scattered electron and hadronic final state the event quantity  $\delta$  is extracted. Figure 5.52 shows the resulting distributions for the three analyses. Adding the background estimates to the DIS-Monte Carlo a very good description of the data is obtained.

### 5.7.3 Beam Induced Background.

Another considerable source of background arises from the proton or electron interactions with residual beam gas, where the cross section for protons is larger than that for

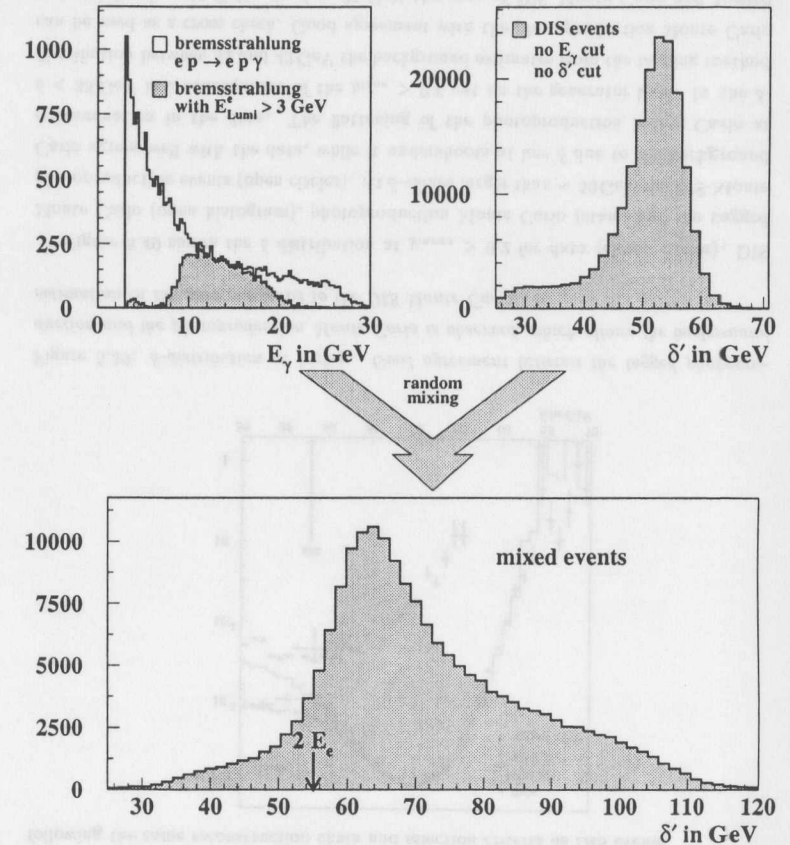


Figure 5.50: Upper left:  $E_{Lumi}^e$  spectrum for all and for electron tagged bremsstrahlung events. Upper right:  $\delta'$  distribution for a sample of events passing all DIS cuts, but no requirements on the final state photon are made (no  $E_{Lumi}^e$  cut and no  $\delta'$  cut). Bottom:  $\delta'$  distribution for the sample resulting from the random mixing of bremsstrahlung and DIS events.

electrons. In these events, which are characterised by a large track multiplicity and a high activity in the calorimeter, an isolated low-energetic deposit close to the RCAL beampipe can be misidentified as an electron.

Proton beam gas events that originate upstream of the detector (in the negative  $z$ -direction) can be identified using the calorimeter timing. The calorimeter times for

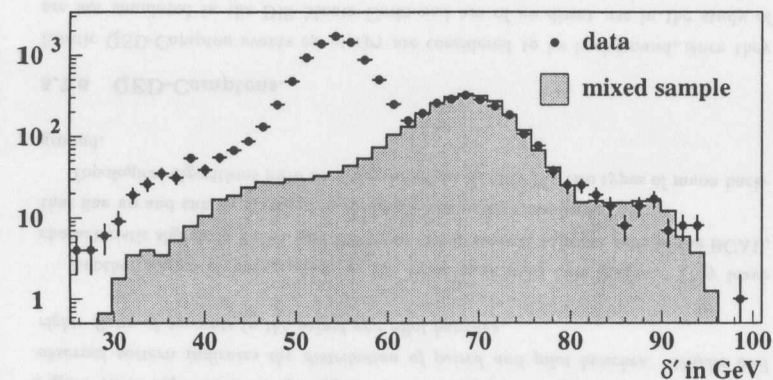


Figure 5.51:  $\delta'$  distribution for the data in comparison to the bremsstrahlung background sample. The latter is normalised to the data in the  $\delta'$ -range 67 to 94 GeV.

FCAL, BCAL and RCAL are the energy weighted time, when the PMTs give a signal for cells with energy deposits larger than 200 MeV. These times are corrected for the final state particles' time-of-flight. Therefore, for nominal  $ep$  interactions,  $t_{FCAL}$ ,  $t_{RCAL}$  and their difference  $t_{FCAL} - t_{RCAL}$  peak at zero (figure 5.53). However, for a proton beam gas interaction that occurs upstream of the detector, the final state particles reach the RCAL earlier and the FCAL later than for events originating from  $z = 0$ .

For electron beam gas events the situation is very similar, but the RCAL plays the role of the FCAL and vice versa.

If the calorimeter energy deposits are large enough to determine the corresponding times, they are required to be

$$\begin{aligned} |t_{FCAL} - t_{RCAL}| &< 8 \text{ nsec} \\ |t_{FCAL}| &< 8 \text{ nsec} \\ |t_{RCAL}| &< 8 \text{ nsec} \end{aligned}$$

in order to reduce the beam gas background.

Remaining background from proton or electron beam-gas interactions around  $z = 0$  has to be subtracted statistically. For this purpose the number of events, that pass the final DIS selection and originate from unpaired proton or electron (pilot) bunches is determined and scaled with the ratio of the currents in the paired and unpaired bunches.

Figure 5.54 shows the number of triggered DIS events as a function of their bunch-crossing number. The combination of paired and pilot bunches results in the observed pattern. Also shown is the ratio of currents for paired and pilot bunches.

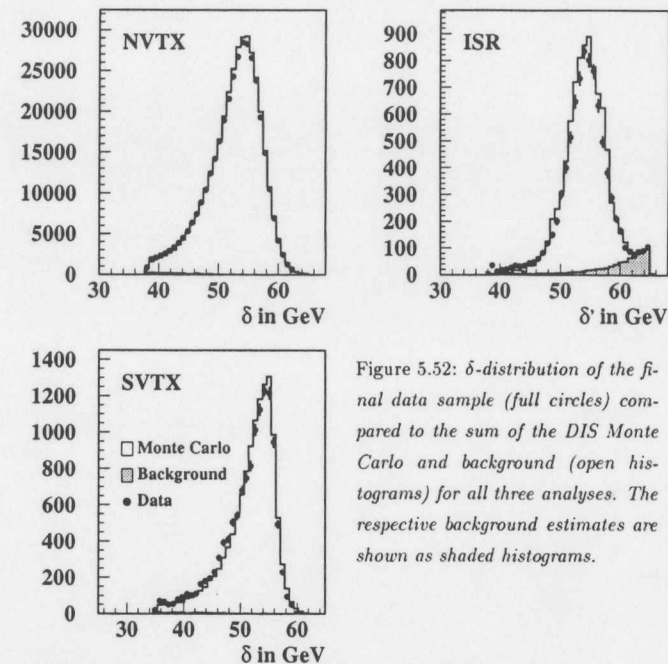


Figure 5.52:  $\delta$ -distribution of the final data sample (full circles) compared to the sum of the DIS Monte Carlo and background (open histograms) for all three analyses. The respective background estimates are shown as shaded histograms.

#### 5.7.4 Fake FCAL Electrons.

In photoproduction events isolated objects in the FCAL can be misidentified as the scattered electron. However, the available phase space for low energy electrons at high  $Q^2$  is very small in DIS events. Hence most of these events, which are all characterised by a large  $y$ -value as reconstructed from the electron only, are background and have to be removed from the sample. This is achieved by the requirement

$$y_{elec} < 0.95$$

#### 5.7.5 Cosmic and Halo Muons.

Cosmic radiation is another background source to be considered. Muons as products of interactions in the upper atmosphere penetrate the ZEUS detector almost vertically and deposit very little energy in the calorimeter. However, in some cases the muon interacts in the calorimeter and produces a shower, which mimics a scattered electron. These cosmic events are characterised by a large EMC energy deposit, while the number of active cells and hence the total calorimeter energy are very small. Usually only two tracks are reconstructed in the CTD.

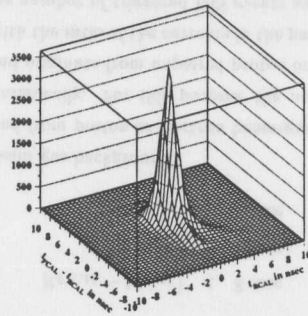


Figure 5.53: Difference of average FCAL and RCAL time versus RCAL time. No contribution from beam-gas events can be seen anymore after final selection cuts are applied.

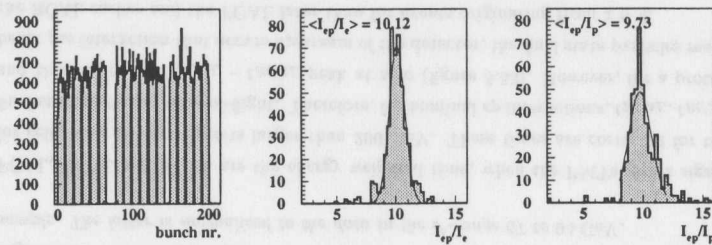


Figure 5.54: Left: Number of triggered events as a function of bunch number. The observed pattern indicates the distribution of paired and pilot bunches. Middle and right: Ratio of currents in the paired and pilot bunches.

Another source of background are the beam-associated halo muons. They leave characteristic signals in FCAL and RCAL or hits in several adjacent cells in the BCAL, that line up and can be matched to entries in the muon chambers.

Topological algorithms have been developed to identify the two types of muon background.

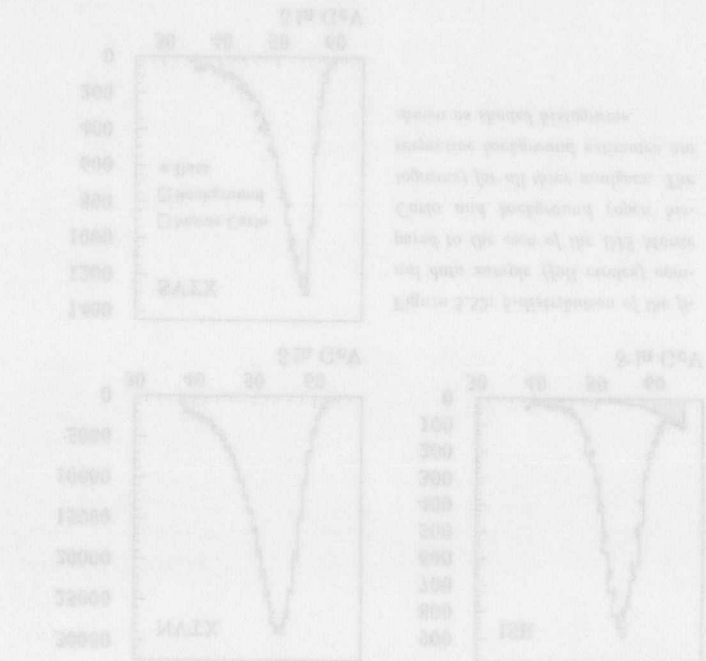
### 5.7.6 QED-Comptons.

Elastic QED-Compton events  $e p \rightarrow e p \gamma$  are considered to be background, since they are not simulated in the DIS Monte Carlo and are of no direct use in the study of the proton structure. These events are characterised by two electromagnetic clusters in the calorimeter with  $15 \text{ GeV} < E_1 + E_2 < 30 \text{ GeV}$ , at most one track in the CTD and essentially no energy deposit in the FCAL. Based on these criteria the events are

identified and removed from the sample.

### 5.7.7 Sparks.

In the BCAL sudden discharges of the static charge between a photomultiplier and its shielding ('sparks'), which occur randomly, can yield 'hot' calorimeter cells, which fake high- $Q^2$  electrons. Spark events are characterised by a large imbalance of the 'electron' calorimeter cell, as only one of the two PMTs produces a signal. Therefore these events can easily be identified and removed from the sample.



## Chapter 6

# Reconstruction of Event Kinematics.

### 6.1 Introduction.

An accurate reconstruction of the Lorentz-invariant kinematic variables  $x$ ,  $y$  and  $Q^2$  is of crucial importance for the description of DIS events, in particular for the measurement of proton structure functions. The kinematic reconstruction based on quantities measurable in the ZEUS detector using several methods is described in this chapter.

A new reconstruction method, the ' $P_T$ '-method, is introduced. It exploits the redundancy of the electron and hadron system and incorporates the advantages of the conventional methods in different kinematic regions.

The accessible kinematic range has been extended to low- $Q^2$  using ISR events. Their reconstruction also depends on the measurement of the emitted photon and is described in a separate section ( 6.7).

The Monte Carlo is used to study the resolution and migration functions of the kinematic reconstruction. The resulting distributions of the kinematic variables are finally compared to those of the data.

### 6.2 Observables in DIS.

Figure 6.1 illustrates the basic neutral current electron-proton scattering process, where  $k$  and  $k'$  denote the four-momentum of the incoming and the scattered electron respectively. The four-momentum of the initial state proton is given by  $P$ , that of the hadronic final state by  $P'$ . The latter includes the so-called 'current jet', into which the struck quark fragments, and the proton remnant, which goes in the direction of the incoming proton.

In the ZEUS coordinate system, where the initial proton moves in the positive  $z$ -

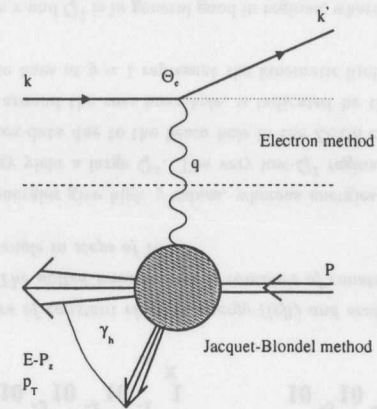


Figure 6.1: Basic ep scattering process leaving signatures from the electron and the hadron flow in the detector.

direction, and ignoring the particles' rest mass these four-momenta can be written as:

$$k = \begin{pmatrix} E_e \\ 0 \\ 0 \\ -E_e \end{pmatrix}, k' = \begin{pmatrix} E' \\ E' \sin \Theta \cos \phi \\ E' \sin \Theta \sin \phi \\ E' \cos \Theta \end{pmatrix}, P = \begin{pmatrix} E_p \\ 0 \\ 0 \\ E_p \end{pmatrix}, P' = \begin{pmatrix} E_h \\ P_{x,h} \\ P_{y,h} \\ P_{z,h} \end{pmatrix} \quad (6.1)$$

$E_e$  and  $E_p$  are the energies of the initial electron and proton respectively,  $E'$ ,  $\Theta$  and  $\phi$  are the energy, polar and azimuthal angle of the scattered electron and  $E_h$  and  $P_{x,h}$ ,  $P_{y,h}$  and  $P_{z,h}$  are the energy and momentum of the hadronic final state  $X$ , where a summation over the final state particles is assumed.

When hadronic event parameters are used in the kinematic reconstruction it has to be ensured, that any influence on it from the final state fragmentation, i.e. the rapidity distribution or the number of jets, is negligible. Furthermore the loss of final state particles, predominantly in the forward direction due to the centre of mass movement in the ZEUS laboratory frame, must not distort the determination of event kinematics. Therefore the difference of energy and longitudinal momentum  $\delta_h = (E - P_z)_h$  and the transverse momentum  $p_{T,h} = \sqrt{p_{x,h}^2 + p_{y,h}^2}$ , which satisfy these requirements, are used.

It can then be assumed that the hadronic flow, i.e. the current jet, can be described by a massless object of energy  $E_j$  and angle  $\gamma$ , which can be calculated from  $\delta_h$  and  $p_{T,h}$ . In the naive quark parton model,  $E_j$  and  $\gamma$  are the energy and polar angle of the outgoing struck quark.

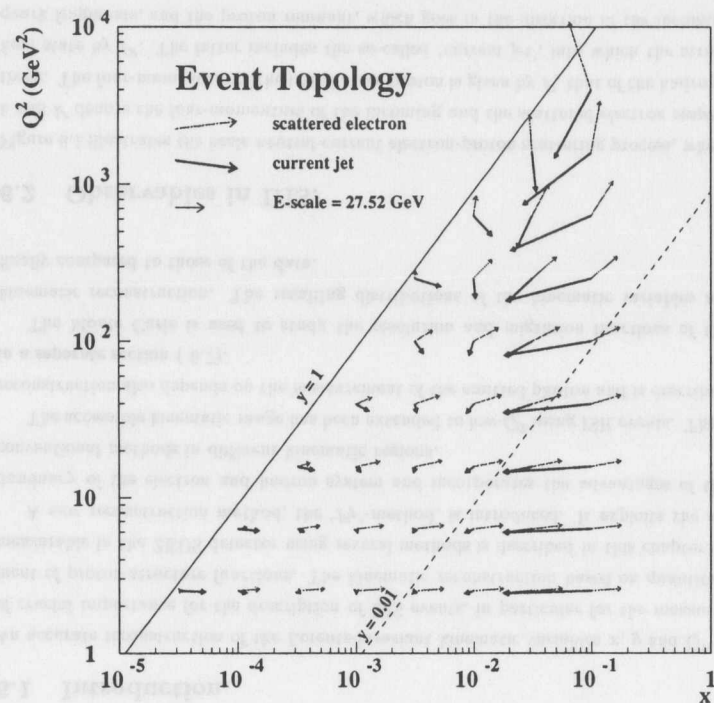


Figure 6.2: Topology of DIS events as a function of  $x$  and  $Q^2$  showing the direction of the scattered electron (thin line) and the struck quark (thick line). The length of the arrow is proportional to the particle's energy.

The event topology of the outgoing particles, i.e. the scattered electron and the current jet, in this quark parton picture, representing the lowest order QCD calculation, is displayed in figure 6.2 for different values of  $x$  and  $Q^2$ . The electron scattering angle can be seen to increase with  $Q^2$ . At high- $x$  the outgoing current jet is very energetic, indicated by the length of the arrow.

### 6.3 Electron Method.

The most straight forward method to reconstruct  $x$  and  $Q^2$  or alternatively  $y$  and  $Q^2$  uses the energy  $E'$  and angle  $\Theta$  of the scattered electron only. This method, called 'electron method', is used in all fixed target experiments. Using the definitions of the

variables  $x$ ,  $y$ ,  $Q^2$  and  $s$  (section 2.2), the following expressions are obtained:

$$Q_{el}^2 = 2E_e E' (1 + \cos \Theta) = 4E_e E' \cos^2 \frac{\Theta}{2}$$

$$y_{el} = 1 - \frac{E'}{2E_e} (1 - \cos \Theta) = 1 - \frac{E'}{E_e} \sin^2 \frac{\Theta}{2}$$

$$x_{el} = \frac{Q_{el}^2}{s y_{el}} = \frac{E' \cos^2 \frac{\Theta}{2}}{E_p (1 - \frac{E'}{E_e} \sin^2 \frac{\Theta}{2})}$$

It is to be noted that the relation

$$Q_{el}^2 = \frac{p_{T,el}^2}{1 - y_{el}} \quad (6.2)$$

holds. The contours of constant energy or scattering angle in the  $(x, Q^2)$  plane, accessible at HERA, are displayed in figure 6.3.

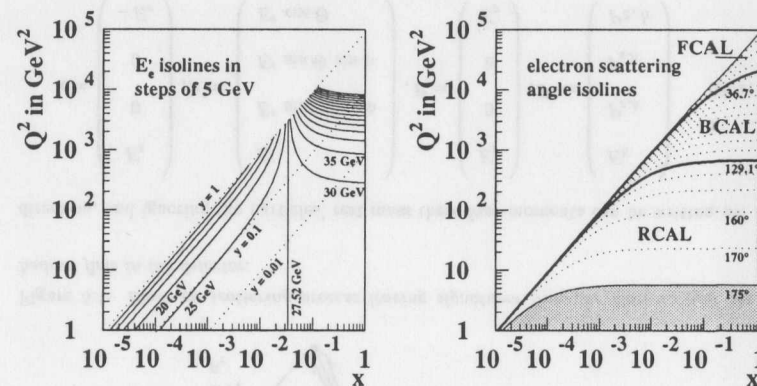


Figure 6.3: Contours of constant electron energy (left) and scattering angle (right) in the  $(x, Q^2)$  plane. The dotted lines represent contours of constant  $y$  (1, 0.1, 0.01) or constant scattering angle in steps of  $10^\circ$ .

Small electron energies give high  $y$ -values, whereas energies much larger than the electron beam energy yield a large  $Q^2$ . The very low- $Q^2$  region, which is not covered by the nominal vertex data due to the beam hole in the ZEUS calorimeter, specifically a box cut of 13 cm around the rear beamhole, is indicated by the grey-shading in the right hand plot. The lines at  $y = 1$  represent the kinematic limit, given by the HERA beam energies.

The resolution in  $x$  and  $Q^2$  is in general good in regions, where the  $E'$ - and  $\Theta$ -isolines are close together. However, for isolines far apart small variations in  $E$  or  $\Theta$  result in large shifts in  $x$  or  $Q^2$ .

The errors of the reconstructed  $x$  and  $Q^2$  due to measurement errors of the outgoing electron energy  $E'$  and scattering angle  $\Theta$  are given by:

$$\frac{\Delta x_{el}}{x_{el}} = \sqrt{\left(\frac{1}{y}\right)^2 \left(\frac{\Delta E'}{E'}\right)^2 + \left[-\tan \frac{\Theta}{2} + \left(\frac{1}{y} - 1\right) \cot \frac{\Theta}{2}\right]^2 (\Delta\Theta)^2}$$

$$\frac{\Delta Q_{el}^2}{Q_{el}^2} = \sqrt{\left(\frac{\Delta E'}{E'}\right)^2 + \tan^2 \frac{\Theta}{2} (\Delta\Theta)^2}$$

The  $x$ -resolution is good for  $y$ -values close to one. However, it deteriorates with decreasing  $y$  due to the  $\frac{1}{y}$  amplification of the errors in the measured energy. This behaviour restricts analyses based on the electron method to the high- $y$  region  $y > 0.01$ , as the electron energy scale is understood to  $\sim 1\%$  at the electron beam energy 27.5 GeV.

The resolution in  $Q^2$  is very good as long as the electron is far away from the RCAL beamhole, i.e. at medium and high  $Q^2$ . But at large  $\Theta$ -values the divergence of the tan-function at  $90^\circ$  amplifies the error on the  $\Theta$  measurement.

#### 6.4 Jacquet-Blondel Method.

As both ZEUS and H1 are essentially  $4\pi$ -detectors, in contrast to most fixed target experiments, the event kinematics can also be determined from the hadronic final state alone. This method, which is based on  $\delta_h$  and  $p_{T,h}$ , can also be used for the kinematic reconstruction of charged current events and was developed by Jacquet and Blondel [83].

As the proton remnant is mostly lost in the forward beam-pipe, the hadronic quantities  $p_{T,h}$  and  $\delta_h$  of the hadron flow in the event are a good approximation to those of the current jet,  $p_{T,j}$  and  $(E - P_z)_j$ . Hence the four-momentum of the hadronic final state can be written as

$$P' = \begin{pmatrix} E_j \\ E_j \sin \gamma \cos \phi_j \\ E_j \sin \gamma \sin \phi_j \\ E_j \cos \gamma \end{pmatrix} \quad (6.3)$$

With  $q = k - k' = -P + P'$  and using the definition of  $y$  from equation 2.4, one obtains:

$$y_{JB} = \frac{E_j - P_{z,j}}{2E_e} = \frac{\delta_h}{2E_e} \quad (6.4)$$

Transverse momentum conservation, i.e.  $p_{T,el} = p_{T,h}$ , and equation 6.2 imply:

$$Q_{JB}^2 = \frac{p_{T,h}^2}{1 - y_{JB}} \quad (6.5)$$

Finally,  $x_{JB}$  is given by:

$$x_{JB} = \frac{Q_{JB}^2}{s \cdot y_{JB}} \quad (6.6)$$

The contours of constant current jet energy and angle in the  $(x, Q^2)$ -plane are shown in figure 6.4.

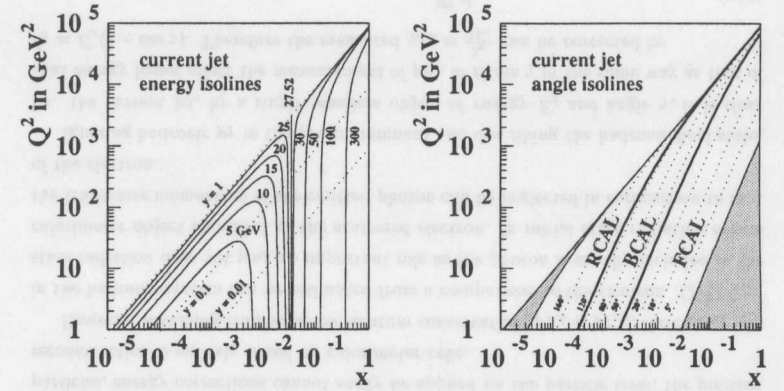


Figure 6.4: Contours of constant jet energy (left) or hadronic angle (right). The shaded regions are not accessible to ZEUS due to particle losses in the FCAL and RCAL beamhole.

In contrast to the electron method, the effect on the resolution in  $x$  from measurement errors of the jet energy is small at high  $x$ . The resolution there is good and deteriorates with decreasing  $x$ . However the FCAL beam hole at  $\gamma \sim 2.2^\circ$  limits the reach of this reconstruction method to  $y \gtrsim 10^{-3}$ . At very low  $x$  and high  $y$  a similar limit is set by the RCAL beamhole (see grey shaded regions in right hand plot).

The resolution in  $x$  and  $Q^2$ , using the current jet information, diverges at  $y \sim 1$ , as can be seen from the following expressions:

$$\frac{\Delta x_{JB}}{x_{JB}} = \sqrt{\left(\frac{1}{1-y}\right)^2 \left(\frac{\Delta E_j}{E_j}\right)^2 + \left[-\tan \frac{\gamma}{2} + \frac{y}{1-y} \cot \frac{\gamma}{2}\right]^2 (\Delta y)^2} \quad (6.7)$$

$$\frac{\Delta Q_{JB}^2}{Q_{JB}^2} = \sqrt{\left(\frac{2-y}{1-y}\right)^2 \left(\frac{\Delta E_j}{E_j}\right)^2 + \left[2 \cot \gamma + \frac{y}{1-y} \cot \frac{\gamma}{2}\right]^2 (\Delta \gamma)^2} \quad (6.8)$$

At low  $y$  the  $x$  resolution is mainly determined by the energy measurement uncertainty.

The Jacquet-Blondel method does not make any assumptions, either on the internal structure of the proton or on the jet topology of the final state. It is therefore independent of jet definition conventions.

However, the sum over the final state particles is approximated by summing over the energy deposits in the calorimeter cells not assigned to the scattered electron. Not only geometrical effects, such as the calorimeter granularity and cell size, but also the presence of uranium noise in the detector distort the measurement of  $\delta_h$  and  $p_{T,h}$ , in

particular at low  $y$ . These effects can introduce large migrations in the kinematic reconstruction and require a very good understanding of the noise in the entire calorimeter (see section 5.6.2).

## 6.5 Double Angle Method.

In the Double Angle method [84]  $x$ ,  $y$  and  $Q^2$  are reconstructed using the scattering angles  $\Theta$  and  $\gamma$  of the final state electron and current jet, respectively. It is motivated by the observation that angles are usually more accurately measured than energies and is, to first order, independent of the calorimeter energy scale.

Solving equation 6.5 for  $\sin \gamma = \frac{p_{T,h}}{E_j}$  and equation 6.4 for  $1 - \cos \gamma = \frac{\delta_h}{E_j}$ , one obtains

$$\cos \gamma = \frac{Q_{JB}^2(1 - y_{JB}) - 4E_e^2 y_{JB}}{Q_{JB}^2(1 - y_{JB}) + 4E_e^2 y_{JB}} \quad (6.9)$$

$$= \frac{p_{T,h}^2 - \delta_h^2}{p_{T,h}^2 + \delta_h^2} \quad (6.10)$$

In the naive quark parton picture and neglecting particle masses, energy and momentum conservation of the scattering process yield:

$$xP + E_e = E' + E_j$$

$$xP - E_e = E' \cos \Theta + E_j \cos \gamma \quad (6.11)$$

$$E' \sin \Theta = E_j \sin \gamma$$

The energy of the scattered electron  $E'$  can now be expressed in terms of the angles  $\Theta$  and  $\gamma$  and the electron beam energy  $E_e$ , by solving equation 6.11 for  $E'$ :

$$E'_{DA} = 2E_e \frac{\sin \gamma}{\sin \Theta + \sin \gamma - \sin(\Theta + \gamma)} \quad (6.12)$$

Substituting the electron energy  $E'$  in the formulae of the electron method by this expression results in the Double Angle reconstruction of  $x$ ,  $y$  and  $Q^2$ :

$$Q_{DA}^2 = 4E_e^2 \frac{\sin \gamma (1 + \cos \Theta)}{\sin \gamma + \sin \Theta - \sin(\Theta + \gamma)} \quad (6.13)$$

$$y_{DA} = \frac{\sin \Theta (1 - \cos \gamma)}{\sin \gamma + \sin \Theta - \sin(\Theta + \gamma)} \quad (6.14)$$

$$x_{DA} = \frac{E_e \sin \gamma + \sin \Theta + \sin(\Theta + \gamma)}{E_p \sin \gamma + \sin \Theta - \sin(\Theta + \gamma)} \quad (6.15)$$

## 6.6 'P<sub>T</sub>'-Method.

### 6.6.1 Introduction.

The 'P<sub>T</sub>'-method is a new way of reconstructing the kinematic variables, combining all information on the scattered electron and the hadronic final state. It is the first attempt

to exploit the overconstraint on the event kinematics from all quantities measured in the hermetic detector and incorporates the advantages of the conventional reconstruction methods in the different kinematic regions, resulting in the improved measurement of  $y$  and  $Q^2$  in the entire  $(x, Q^2)$  plane. Due to the stability of the method the accessible kinematic range has been extended to low  $y$ , where an overlap with the fixed target data can be achieved.

The P<sub>T</sub>-method was proposed in [85] and is used in the measurement of  $F_2$  from the 1994 ZEUS data for the first time.

The P<sub>T</sub>-method is based on a three-step correction, assuming energy and momentum conservation, followed by the final reconstruction of  $x$ ,  $y$  and  $Q^2$ .

### 6.6.2 P<sub>T</sub>-Balancing.

As described in section 5.4 the energy and position, and hence the scattering angle of the final state electron can be measured very precisely. Since one only deals with a single, charged particle, several methods based on tracking, kinematic constraints or the presampler effect in the SRTD allow the correction for energy loss in the passive detector material. If the electron or a large fraction of its shower in the calorimeter is not detected, the event is not analysed any further.

The particles in the hadronic final state also suffer from energy loss while penetrating passive detector material, which distorts the measurement of the event kinematics. As the hadronic final state is usually a multi-particle system, which can also contain neutral particles, energy corrections cannot easily be applied on the particle level; the position reconstruction is entirely based on calorimeter cells.

However, assuming transverse momentum conservation,  $p_{T,h} = p_{T,e}$ , the energy loss in the hadronic system can be estimated from a comparison to the electron. QED final state radiation does not play an important role as the photon is usually included in the calorimeter object identified as the scattered electron. In initial state radiation events the transverse momentum of the emitted photon can be neglected in comparison to that of the electron.

Ignoring hadronic  $p_T$  in the proton remnant and describing the hadronic final state, i.e. the current jet, by a single massless object of energy  $E_j$  and angle  $\gamma$ , it is clear that energy losses affect the measurement of  $p_{T,h} = E_j \sin \gamma$  in the same way as that of  $\delta_h = E_j(1 - \cos \gamma)$ . Therefore the measured  $y_{JB} = \frac{\delta_h}{2E_e}$  can be corrected by

$$y_{(1)} = y_{JB} \frac{p_{T,e}}{p_{T,h}} \quad (6.16)$$

This is the P<sub>T</sub>-correction.

This correction, which is applied on an event-by-event basis, is extracted from the data.

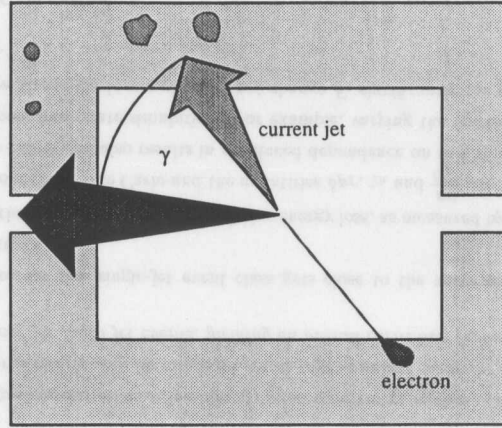


Figure 6.5: Schematic diagram of the DIS event topology. The electron  $p_T$  is balanced by the current jet. The colour flow between the current and the remnant jet also implies a particle flow in this region.

However, this picture is too naive. The colour flow between the struck quark and the di-quark results in a hadron flow between the current jet and the proton remnant. Consequently the hadronic system is not a well-collimated jet. Also effects from different detector regions contribute to the overall energy loss. Therefore the event topology has to be taken into account in the  $p_T$ -correction. Equation 6.16 is hence generalised to

$$y_{(1)} = y_{JB}/\mathcal{C} \quad (6.17)$$

where the correction function  $\mathcal{C}$  is extracted from the Monte Carlo. In contrast to [85] where the correction function was chosen to be a function of  $\frac{p_{T,h}}{p_{T,el}}$ ,  $p_{T,h}$  and  $\gamma_h$ , the correction function is here chosen to be a function of the quantities  $\frac{p_{T,h}}{p_{T,el}}$ ,  $\gamma_h$  and  $\frac{E_{T,el}}{E_{T,tot}}$ , where  $E_{T,el}$  and  $E_{T,tot}$  are the electron and event transverse energy.

Figure 6.6 shows the ratio  $\frac{y_{JB}}{y_{true}}$  as a function of  $\delta p_T = \frac{p_{T,h}}{p_{T,el}}$  in bins of  $\gamma$ , as extracted from the Monte Carlo. Almost all events lie in the region  $0.5 \leq \delta p_T \leq 1.5$ . At low  $\gamma$ ,  $\frac{y_{JB}}{y_{true}}$  rises almost linearly with  $\delta p_T$  as expected from equation 6.16. The current jet moves very close to the proton remnant in the forward direction, so that the rapidity interval between the two, that could be filled with an additional hadron flow, is rather small. Particle losses in the forward beamhole affect neither  $p_{T,h}$  nor  $\delta_h$ . However, at low  $\gamma$  the calorimeter noise contributes considerably to  $\delta_h$  and can even dominate. This explains, why the correction is here larger than 1. With decreasing  $\gamma$  the noise contribution to  $y_{JB}$  decreases and the effect of energy loss in passive material becomes dominant, so that the correction falls below unity. The fact that with increasing  $\gamma$

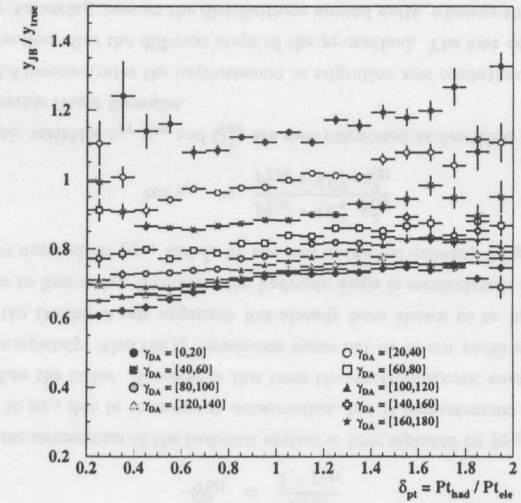


Figure 6.6: ' $p_T$ '-correction function as a function of  $\delta p_T$  for different regions of  $\gamma_h$ .

a larger fraction of the  $p_{T,h}$  gets carried by particles between the current jet and the proton remnant while its contribution to  $\delta_h$  decreases leads to a deviation from the linear behaviour of the correction as a function of  $\delta p_T$ .

The naive interpretation of  $\gamma$  as the angle between the current jet and the proton remnant is only applicable in single-jet events. In case of multi-jet events energy loss characteristics from many detector regions are mixed and average out the correction. The ratio  $\frac{E_{T,el}^c}{E_{T,tot}^c}$  is used to estimate the jet-structure in an event (see figure 6.7)

In events with  $\frac{E_{T,el}^c}{E_{T,tot}^c} > 0.4$  the transverse momentum and energy is shared between the electron and the current jet, the hadronic final state is identified to have a single jet. However, in events with  $\frac{E_{T,el}^c}{E_{T,tot}^c} \leq 0.4$  the hadronic energy must have been deposited in the calorimeter in the form of several separate jets, that partially cancel their transverse momentum in order to balance that of the electron. These events have multi-jet final states.

For these two event classes the  $p_T$ -correction has been extracted separately. As shown in figure 6.7 for multi-jet events the correction on  $\delta_h \sim y_{JB}$  is only weakly dependent on  $\delta p_T$ , the expected linear rise is averaged out. Nevertheless the overall characteristics of the correction to be larger than 1 at low- $\gamma$  and to be decreasing with increasing  $\gamma$  can still be seen clearly.

For single-jet events, however, a much stronger rise of  $\mathcal{C}$  with increasing  $\delta p_T$  is found, which increases in slope with increasing  $\gamma$ . Due to the cleaner event topology

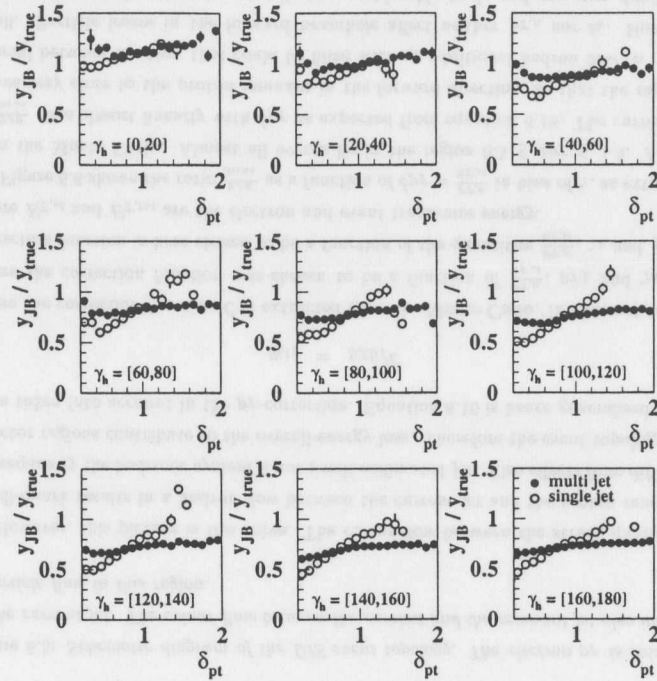


Figure 6.7: ‘ $p_T$ ’-correction as a function of  $\delta p_T$  in different  $\gamma_h$  regions. The expected linear behaviour is clearly seen for single jet events (open circles), while the  $\delta p_T$ -dependence is averaged out for multi jet events, yielding an overall correction factor.

the correction for this single-jet event class gets close to the naive expectation from equation 6.16.

As only the functional form of the relative energy loss, as measured by  $\delta p_T$ , on  $\frac{y_{JB}}{y_{true}}$  is extracted from the Monte Carlo and the quantities  $\delta p_T$ ,  $\gamma_h$  and  $\frac{E_{el}^1}{E_{tot}^1}$  are measured in the data, the  $p_T$ -correction also results in a reduced dependence on the Monte Carlo model of the hadronic final state simulation. For example, varying the fraction of diffractive events in the Monte Carlo sample does not change  $F_2$  significantly (as will be shown in section 7.8).

### 6.6.3 $\Sigma$ -Correction.

At high  $y$  the current jet moves in the rear direction. Here particle losses in the RCAL beamhole do not change  $p_{T,h}$  considerably in contrast to  $\delta_h$ , which is essentially reduced

by twice their energy. The requirement of the event balancing in transverse momentum can not correct for this effect.

But the  $y$ -reconstruction of the electron method provides a very good resolution at high- $y$ . This fact is exploited in the  $\Sigma$ -correction, which is the second correction step of the  $p_T$ -method. The  $\Sigma$ -correction, first presented in [87] and used by H1 [115, 116], combines  $y_{el}$  and  $y_{JB}$ .

$$y_{\Sigma} = y_{JB} \frac{2E_e}{\delta} = y_{JB} \frac{1}{y_{JB} + 1 - y_{el}} \quad (6.18)$$

The general idea is to replace the scale  $2E_e$  in the calculation of  $y_{JB}$  by  $\delta$ . For fully contained events  $\delta \simeq 2E_e$ , but in case of particle losses down the rear beamhole  $\delta_h$  and  $\delta$  are both reduced by the same amount, so that  $y_{\Sigma} = \frac{\delta_h}{\delta}$  is only weakly affected. In the context of the  $p_T$ -method the corresponding correction is:

$$y_{(2)} = y_{(1)} \frac{1}{y_{(1)} + 1 - y_{el}} \quad (6.19)$$

This correction is applied on an event-by-event basis and improves the  $y$ -resolution particularly at high- $y$ .

### 6.6.4 Kinematic Reconstruction of the $p_T$ -Method.

According to equation 6.2 one could now calculate  $Q^2$  as

$$Q_{(2)}^2 = \frac{p_{T,el}^2}{1 - y_{(2)}} \quad (6.20)$$

The transverse momentum of the hadronic system is here replaced by  $p_{T,el}$ , which must be identical to  $p_{T,h}$  due to momentum conservation, but is reconstructed with a better resolution than the latter. However in this term the electromagnetic energy scale does not cancel completely. Also the  $Q^2$ -resolution turns out to be not particularly good.

Instead the Double Angle approach has already been shown to be independent of energy scales to first order. Therefore the hadronic angle is recalculated, replacing  $p_{T,h}$  by the better determined  $p_{T,el}$  and  $\delta_h$  by the now corrected quantity  $2E_e \cdot y_{(2)}$ :

$$\cos \gamma_{p_T} = \frac{p_{T,el}^2 - 4E_e^2 \cdot y_{(2)}^2}{p_{T,el}^2 + 4E_e^2 \cdot y_{(2)}^2} \quad (6.21)$$

The kinematic variables  $x_{p_T, y_{p_T}}$  and  $Q_{p_T}^2$  are then calculated as described in section 6.5, using the Double Angle formulae.

Figure 6.8 demonstrates the improvement in migration and resolution of the  $y$ - and  $Q^2$ -reconstruction after the different steps of the  $p_T$ -method. The first correction step, imposing  $p_T$ -balancing, centres the distributions around unity, whereas the second step, the  $\Sigma$ -correction, improves their  $y$ -resolution particularly at high  $\gamma$ , which corresponds to high  $y$ . The  $Q^2$ -resolution of the  $p_T$ -method is significantly better than using  $Q_{(2)}^2$ .

The  $p_T$ -method is used for the kinematic reconstruction in the NVTX analysis.

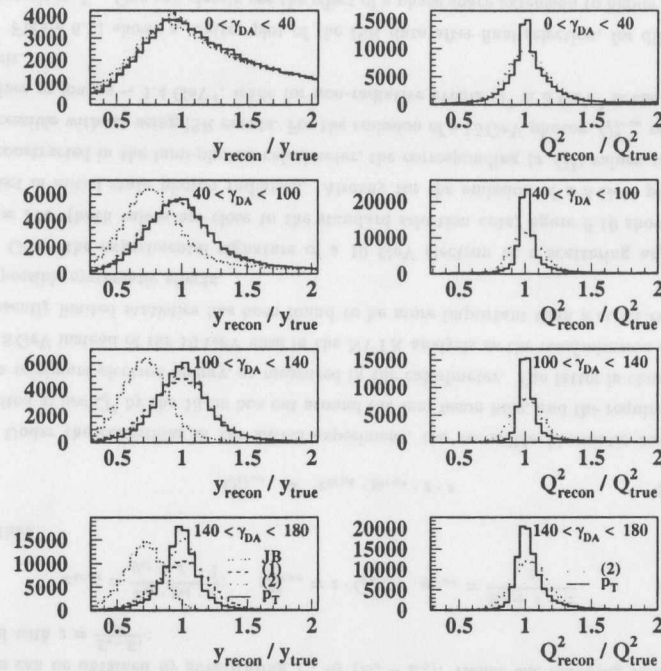


Figure 6.8: Resolution in  $y$  and  $Q^2$  after the different steps of the  $p_T$ -method. The first correction centres the distributions around unity, whereas the second correction improves the  $y$ -resolution particularly at high  $y$ . The final step to using the kinematic variables  $x_{p_T}$ ,  $y_{p_T}$  and  $Q^2_{p_T}$  provides the best resolution in  $y$  and  $Q^2$ .

## 6.7 Radiative Events.

The kinematic reconstruction methods presented so far assume the incoming electron to have the electron beam energy and the scattered electron to have the energy measured in the calorimeter (apart from detector resolution effects). However, because of QED radiative processes (see figure 4.1) these assumptions are not fulfilled, resulting in two effects: Firstly the reconstructed kinematic variables are systematically shifted. The incoming or outgoing electron energy at the electron-photon<sup>1</sup> vertex, which are relevant for the reconstructed  $Q^2$  of the photon probing the proton structure, differ from the assumed values. Secondly the cross section calculation has to be modified with respect

<sup>1</sup>The same is true for  $Z^0$ -exchange. For simplicity it is only referred to the photon as exchanged boson.

to the Born level. The latter is particularly important for the Monte Carlo simulation of DIS events and has been discussed in section 4.2.

In Final State Radiation (FSR), a real photon is emitted from the final state electron. In most cases the final state photon is emitted at very small angles with respect to the scattered electron. Due to the finite granularity of the calorimeter and the electron and photon preshowering in inactive material before reaching the calorimeter, the measured electron energy effectively includes that of the photon. Hence the effects of FSR on the kinematic reconstruction are relatively small.

In Initial State Radiation (ISR), a real photon of energy  $E_\gamma$  is emitted from the initial state electron. If the photon is emitted collinearly ( $\Theta_\gamma \leq 0.5$  mrad) with respect to the incident electron and escapes the main detector through the rear beamhole, the electron energy becomes  $(E_e - E_\gamma)$ , where  $E_e$  is the electron beam energy. The event can be interpreted as a scattering process with reduced centre of mass energy. This can also be seen in the event characteristics such as transverse energy ( $E_T$ ) or track multiplicity (figure 6.9).

Due to the limited geometrical acceptance of the lumi-photon calorimeter only  $\sim 40\%$  of the ISR photons are lumi-tagged.

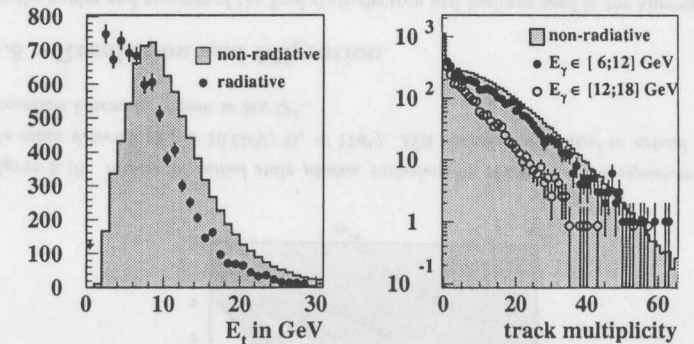


Figure 6.9: Distribution of transverse energy (left) and track multiplicity (right) for radiative and non-radiative events. The  $E_T$  distribution is normalised to the number of events, the track multiplicity to the number of events without tracks.

The following part of this section refers specifically to the ISR analysis, unless noted otherwise.

ISR events can in principle be identified from measurements in the main calorimeter without requiring a photon in the luminosity photon calorimeter. The photon energy can be reconstructed as

$$E_\gamma^{CAL} = E_e - \frac{1}{2}(E - P_z) \quad (6.22)$$

In order to reduce the effect of possible energy scale mismatches, the expression can be transformed, using transverse momentum conservation, to

$$E_{\gamma}^{CAL} = E_e \left( 1 - \frac{1 - y_{el}}{1 - y_{DA}} \right) \quad (6.23)$$

However the photon emission is not guaranteed to be collinear, so that the event kinematics cannot be determined from the main detector alone. Therefore a tagged photon in the lumi-photon calorimeter is required in the ISR analysis. The measured energy,  $E_{\gamma}$ , rather than its estimation  $E_{\gamma}^{CAL}$ , is used in the determination of the event kinematics.

Here the electron method has been chosen for the kinematic reconstruction as it suffers less from migrations at low  $Q^2$ , the main focus of the ISR analysis, than the Double Angle method.

Reconstructing  $x$ ,  $y$  and  $Q^2$  mistakenly assuming the incoming electron energy to be the beam energy  $E_e$ , results in the so-called 'apparent variables'. From these the true ones can be obtained by substituting  $E_e$  by  $(E_e - E_{\gamma})$ . Hence the following relations hold with  $z = \frac{E_e - E_{\gamma}}{E_e}$ :

$$x_{true} = \frac{x_{el} \cdot y_{el} \cdot z}{y_{el} + z - 1}; \quad Q_{true}^2 = z \cdot Q_{el}^2; \quad y_{true} = \frac{y_{el} + z - 1}{z} \quad (6.24)$$

so that

$$Q_{true}^2 = x_{true} \cdot y_{true} \cdot z \cdot s \quad (6.25)$$

Under the conditions of the ZEUS experiment, the accessible kinematic range is limited at low  $Q^2$  by the 13 cm box cut around the rear beam hole, and the requirement of a minimum electron energy, as measured in the calorimeter. The latter is chosen to be 8 GeV instead of the 10 GeV used in the NVTX analysis as the maximisation of the presently limited statistics has been found to be more important than a strict control of possible systematic effects.

Given the experimental signature of a 10 GeV electron at a scattering angle of  $\Theta = 174^\circ$  (both values are close to the standard selection cuts) figure 6.10 shows the effect of initial state photon radiation. Already for the emission of a 5 GeV photon, reconstructed in the lumi-photon calorimeter, the corresponding  $(x, Q^2)$  values are not accessible without using ISR events. For the emission of a 15 GeV photon,  $Q_{true}^2$  reaches values as low as  $\sim 1.4 \text{ GeV}^2$ , while for non-radiative events  $Q^2 \simeq 3 \text{ GeV}^2$  is the lower limit.

Figure 6.11 shows a scatter plot of the ISR data after final selection, for different intervals in  $E_{\gamma}$ . One can clearly see the effect of a phase space extension to higher  $x$  and lower  $Q^2$  the larger the energy of the emitted photon. This effect is the main motivation for performing the ISR analysis. It is complementary to the SVTX analysis as two different methods have been applied to two statistically independent data samples.

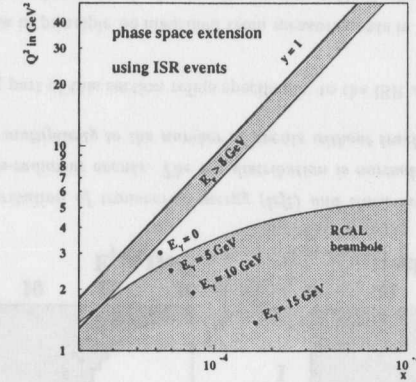


Figure 6.10: Impact of initial state photon emission for constant event signature in the main detector ( $E_e^i = 10 \text{ GeV}$ ;  $\Theta_e = 174^\circ$ ). ISR events can be used to extend the accessible kinematic region to low  $Q^2$ .

## 6.8 Resolution and Migration.

As the angles and energies of the final state electron and hadrons used in the kinematic reconstruction have to be measured with the detector, which only has a finite granularity and resolution, the kinematic variables  $x$ ,  $y$  and  $Q^2$  can only be determined with finite resolution. In addition in some regions of the  $(x, Q^2)$  plane systematic shifts are introduced, i.e. events migrate from one  $(x, Q^2)$  region to another. Even though these effects, which can distort the cross section measurement in a particular  $(x, Q^2)$  bin, are corrected for using the Monte Carlo, the uncertainty on this correction can become an important factor in the analysis. Hence resolution and migration have to be controlled and kept as small as possible.

As already mentioned, the different reconstruction methods show different sensitivity to measurement errors in the leptonic or hadronic event variables. These differences are investigated by comparing the reconstructed  $x$ ,  $y$  and  $Q^2$  to the true values in the Monte Carlo. Figure 6.12 shows the comparison of reconstructed and true variables for the four reconstruction methods considered.

The electron method yields a remarkable resolution in  $Q^2$ , while its  $y$ -resolution deteriorates quickly below  $y \simeq 0.1$  due to the increased sensitivity to the energy at small  $y$ . This is also reflected in the  $x$ -resolution, which is good at low  $x$ , but rather poor and systematically shifted to lower values at high  $x$ . The electron method is suitable for measurements at low  $x$  and low  $Q^2$  and is hence used in the SVTX and ISR analyses. However the low- $y$  region is not accessible for precise measurements using the electron only.

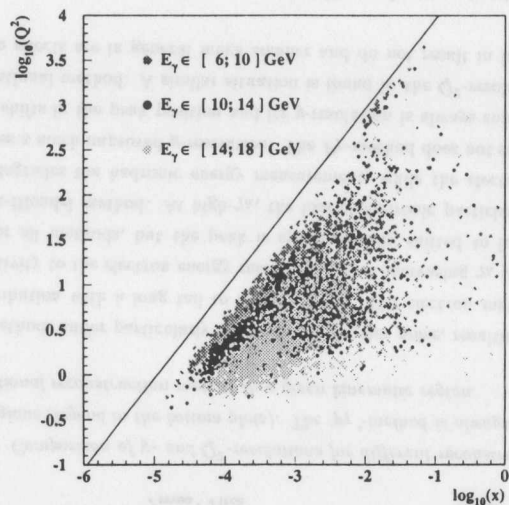


Figure 6.11: ISR data sample after final selection cuts. The more energetic the emitted photon, the lower the effective centre of mass energy and hence the reached  $Q^2$ .

The Jacquet-Blondel method shows a rather poor  $Q^2$ -resolution. The reconstructed  $Q^2$  is also shifted to lower values, which introduces large migrations. However the  $y$ -reconstruction is good down to  $y \simeq 0.04$ . Below this value the hadronic activity in the detector becomes very small and the uranium noise in the calorimeter becomes an important factor. True low- $y$  events are reconstructed at higher  $y$ . This effect can also be seen as a systematic shift to lower values of  $x$  at high- $x$ . Even though the Jacquet-Blondel method is not favourable for general reconstruction of neutral current events, its good  $y$ -resolution at medium and low  $y$  makes it superior to the electron method in this particular region of phase space.

The Double Angle method, which was used in the  $F_2$  measurement from the 93 ZEUS data [109], yields a reasonably good resolution in  $Q^2$ . Its  $y$ -resolution at high  $y$  is not as good as that of the electron method. But in contrast to the latter it stays acceptable down to  $y \sim 0.04$ . At lower  $y$ -values the calorimeter noise dominates again and distorts the  $y$ - and  $x$ -measurement. This method is suitable for measurements in the entire accessible  $(x, Q^2)$  region, but its reach down to low  $y$ , i.e. the region of the fixed target data, is limited.

Finally the  $P_T$ -method combines the advantages of the three conventional reconstruction methods. Its  $Q^2$ -resolution is as good as that of the electron method. Its  $y$ -resolution at high  $y$  is comparable to that of the electron method. But in contrast to

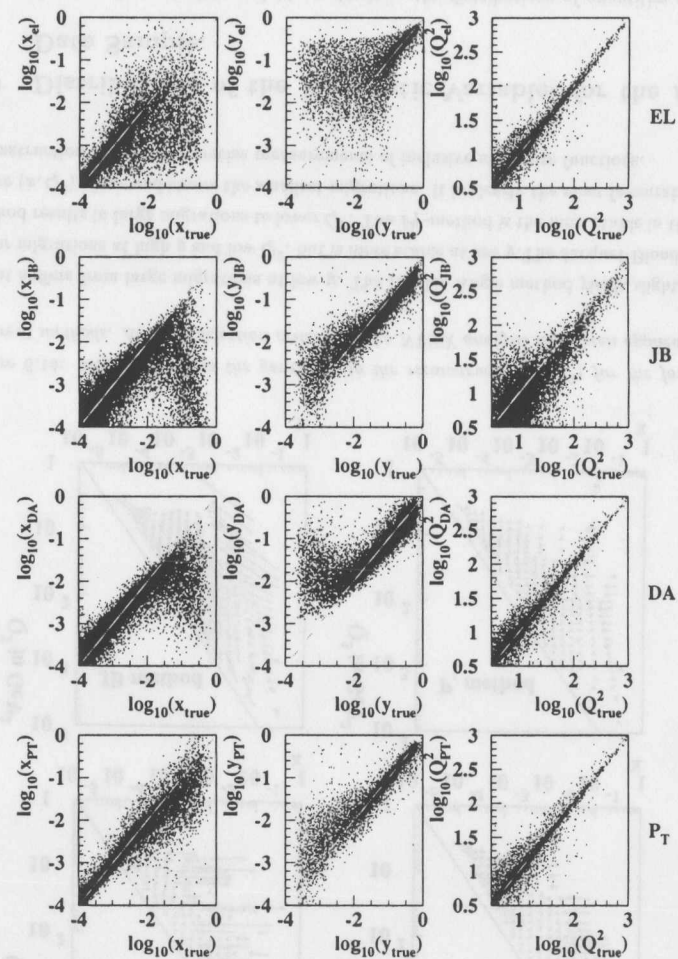


Figure 6.12: Comparison of the kinematic reconstruction in  $x$ ,  $y$  and  $Q^2$  using different methods. The final selection cuts of the NVTX analysis have been applied.

the latter it stays good at medium  $y$  and adopts the stable behaviour of the Jacquet-Blondel method at low  $y$ . Consequently this method yields the best resolution in  $x$ ,  $y$  and  $Q^2$  and is chosen in the NVTX analysis.

A more quantitative picture of the resolution is provided in figure 6.13. The  $y$ -resolution at low  $\gamma_h$  is relatively large for all reconstruction methods. The hadronic

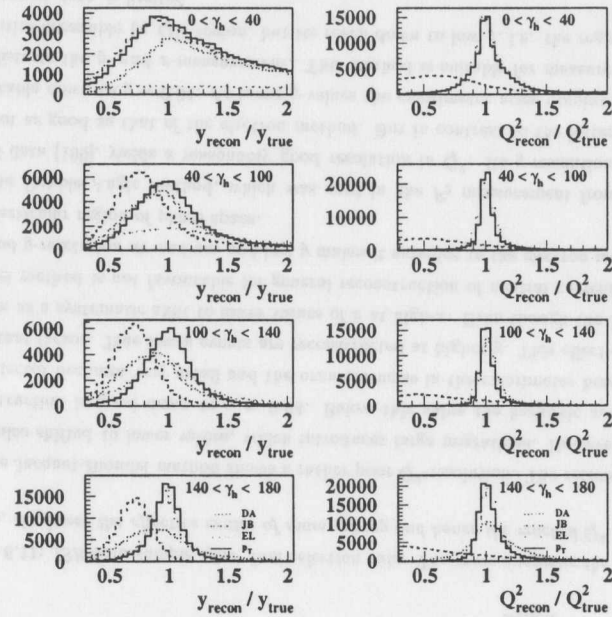


Figure 6.13: Comparison of  $y$ - and  $Q^2$ -resolutions for different reconstruction methods in four  $\gamma$ -regions (legend in the bottom plots). The ' $P_T$ '-method is always as good as the best conventional reconstruction method in a given kinematic region.

or mixed methods suffer particularly from the calorimeter noise, resulting in an asymmetric distribution with a long tail to higher values. The electron method is limited by its sensitivity to the electron energy resolution. With increasing  $\gamma_h$  the  $y$ -resolution improves for all methods, but the peak is systematically shifted to lower values for the Jacquet-Blondel method. At high- $\gamma_h$ , the loss of hadronic particles in the RCAL beamhole degrades the hadronic energy measurement, while the electron reconstruction provides a much improved  $y$ -resolution. The  $P_T$ -method does not suffer from large systematic shifts in the peak position and its  $y$ -resolution is always comparable to the best conventional method. A similar situation is found in the  $Q^2$ -resolution, although degradation effects are in general much smaller and do not result in large systematic shifts.

The migration of events due to systematic shifts in the reconstruction of  $x$ ,  $y$  and  $Q^2$  is shown in figure 6.14. The tail of the arrow is the average value of the true  $(x, Q^2)$  in a bin (for the binning see section 7.2) and the head indicates the average value of the reconstructed  $(x, Q^2)$ . It can again be seen that the electron method is good at high

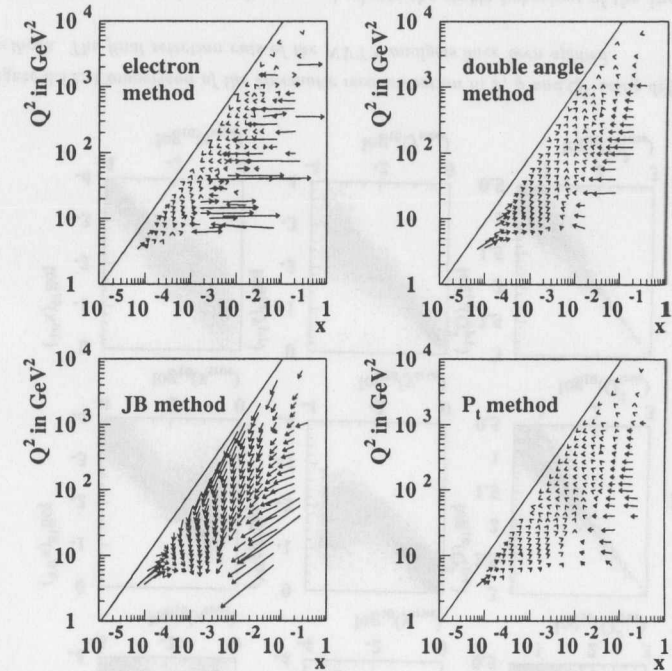


Figure 6.14: Migrations from the generated to the reconstructed  $(x, Q^2)$  for the four different methods. All final selection criteria of the NVTX analysis have been applied.

$y$ , but suffers from large migrations at low  $y$ . The Double Angle method yields slightly larger migrations at high  $y$  and low  $Q^2$ , but is more stable at low  $y$ . The Jacquet-Blondel method results in large migrations to lower  $Q^2$ . The  $P_T$ -method is the most stable in the entire  $(x, Q^2)$  plane and shows the smallest migrations. It is clearly the most favourable reconstruction method for precise measurements of inclusive structure functions.

## 6.9 Distributions of the Kinematic Variables for the $F_2$ Data Sample.

Good agreement between data and Monte Carlo in the distributions of quantities directly measured in the detector, such as energies and angles, has already been shown in chapter 5. The resulting distributions of the kinematic variables, which are used in the

$F_2$  measurement, are presented here. The distributions of the data, shown as full circles, are compared to the sum of the DIS Monte Carlo and the background (open histogram), which is the estimate from the photoproduction Monte Carlo for the NVTX and the SVTX analyses and the bremsstrahlung background in the case of the ISR analysis. The respective background estimates are shown separately as shaded histograms.

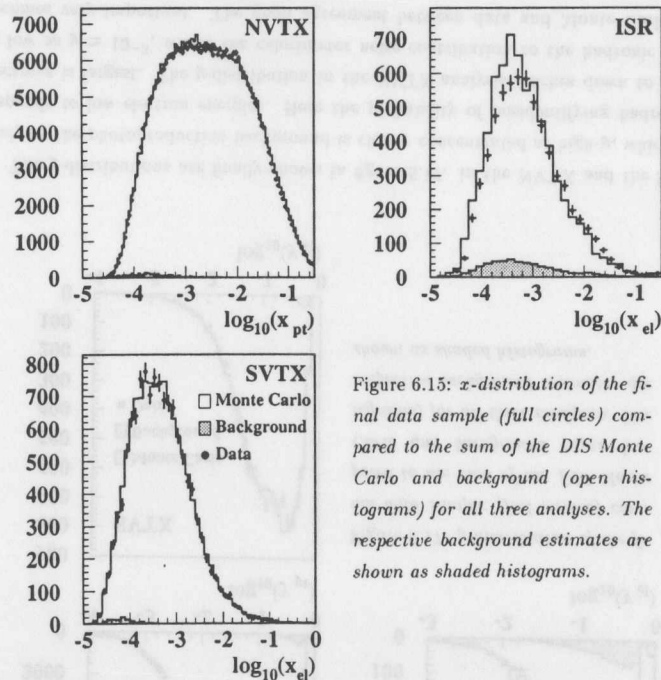


Figure 6.15:  $x$ -distribution of the final data sample (full circles) compared to the sum of the DIS Monte Carlo and background (open histograms) for all three analyses. The respective background estimates are shown as shaded histograms.

The  $x$ -distributions are shown in figure 6.15. The overall agreement between data and Monte Carlo in the NVTX analysis is very good over the entire  $x$ -range covered. At  $\sim 10^{-3}$  the Monte Carlo overshoots the data slightly and small peak in the data at  $\sim 10^{-2}$  is not reproduced by the simulation. The estimated photoproduction background is very small and concentrates around  $x \approx 10^{-4}$ , as this corresponds to the affected low- $Q^2$  region.

In the ISR analysis the Monte Carlo describes the data fairly well for  $x > 10^{-3}$ . However at lower  $x$  the simulation tends to overshoot the data. The background, here originating from bremsstrahlung overlay events, is larger than for the non-radiative analyses and shows up mainly at  $10^{-4} - 10^{-3}$ . The overall description of the data is adequate.

The SVTX analysis covers a much smaller range in  $x$  than the NVTX one. The small background from photoproduction events is found below  $x \approx 10^{-4}$ . Adding it to the DIS Monte Carlo results in a very good description of the data over the full accessible  $x$ -range.

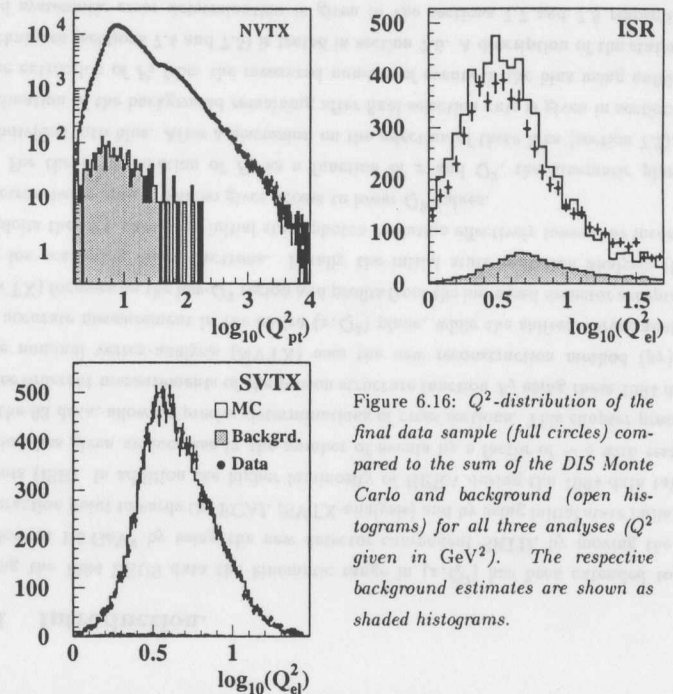


Figure 6.16:  $Q^2$ -distribution of the final data sample (full circles) compared to the sum of the DIS Monte Carlo and background (open histograms) for all three analyses ( $Q^2$  given in  $\text{GeV}^2$ ). The respective background estimates are shown as shaded histograms.

Figure 6.16 shows the  $Q^2$ -distributions. The simulation of the NVTX data is again very good. The small photoproduction background is found at  $Q^2$  below  $10 \text{ GeV}^2$ , as expected. The kink in the  $Q^2$ -distribution at  $\sim 30 \text{ GeV}^2$  is fully reproduced by the Monte Carlo and is the result of the extended box cut, removing events in the region of the malfunctioning calorimeter trigger card.

The Monte Carlo in the ISR analysis overshoots the data slightly at low- $Q^2$ , while it provides a good description of the data above  $Q^2 \approx 5 \text{ GeV}^2$ . Since bremsstrahlung background is not due to misidentification of the scattered electron but results from random overlays in the lumi-photon calorimeter, it covers the entire  $Q^2$ -range.

The Monte Carlo description of the  $Q^2$ -distribution in the SVTX analysis is very good over the whole accessible range, while the photoproduction background is ex-

tremely small.

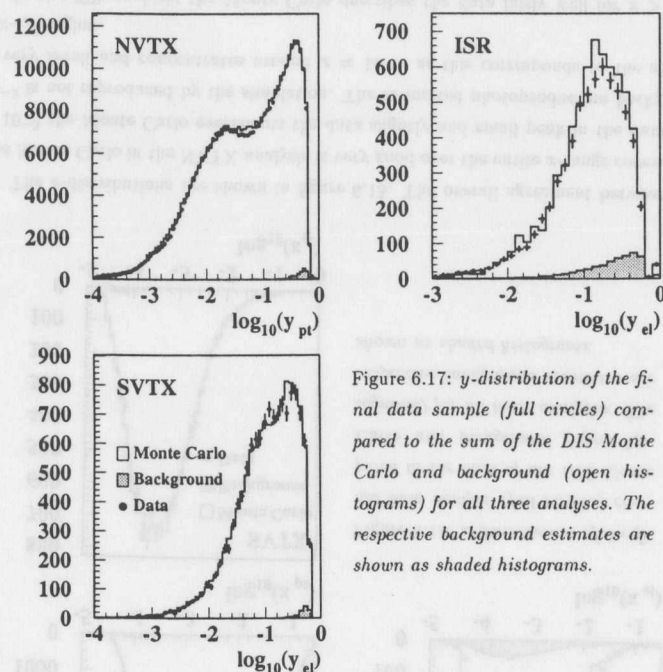


Figure 6.17:  $y$ -distribution of the final data sample (full circles) compared to the sum of the DIS Monte Carlo and background (open histograms) for all three analyses. The respective background estimates are shown as shaded histograms.

The  $y$ -distributions are finally shown in figure 6.17. In the NVTX and the SVTX analyses the photoproduction background is clearly concentrated at high- $y$ , which corresponds to low electron energies. Here the probability of misidentifying hadrons as electrons is largest. The  $y$ -distribution in the NVTX analysis reaches down to values as low as  $y \simeq 10^{-3}$ , where the calorimeter noise contribution to the hadronic signal becomes very important. The good agreement between data and Monte Carlo provides confidence in the simulation of these detector effects. As lower electron energies can also result from a larger energy range of emitted photons in the final state, the bremsstrahlung background in the ISR analysis contributes most at high  $y$ , too. Apart from a small region below  $y \simeq 0.1$  the NVTX data are very well reproduced by the simulation, while the Monte Carlo overshoots the data in the ISR analysis slightly at high  $y$ . The Monte Carlo description of the SVTX data is again very good.

The effects of the small mismatches between data and Monte Carlo distributions on the final  $F_2$  values are taken into account in the determination of the systematic errors (section 7.8).

## Chapter 7

### Extraction of $F_2$ .

#### 7.1 Introduction.

Using the 1994 ZEUS data the kinematic range in  $(x, Q^2)$  has been extended to  $Q^2$  as low as  $1.5 \text{ GeV}^2$  by using the new detector component SRTD, by moving the  $ep$ -interaction point towards the FCAL (SVTX-analysis) and by using initial state radiation events (ISR). In addition the higher luminosity of HERA during the 1994 data taking period has given an increase in the number of events by a factor of  $\sim 5$  with respect to the 93 data, allowing precise determinations of cross sections. This chapter presents three different measurements of the proton structure function  $F_2$  using these 1994 data. The nominal vertex-analysis (NVTX) uses the new reconstruction method ( $p_T$ ) for an accurate measurement in the entire  $(x, Q^2)$  plane, while the shifted vertex analysis (SVTX) focusses on the low- $Q^2$  region and profits from the increased detector acceptance for low-scattering angle electrons. Finally the initial state radiation analysis (ISR) exploits the fact, that hard initial state photon radiation effectively lowers the incoming electron beam energy and so gives access to lower  $Q^2$ -values.

For the determination of  $F_2$  as a function of  $x$  and  $Q^2$ , the kinematic plane is subdivided into bins. After a discussion on the selection of these bins (section 7.2), the estimation of the background remaining after final selection cuts is given in section 7.3. The extraction of  $F_2$  from the measured number of events in the bins using unfolding techniques (sections 7.4 and 7.5) is tested in section 7.6. A description of the statistical and systematic error determination is given in the sections 7.7 and 7.8 respectively. The results are presented, described and compared to other measurements in the next chapter.

## 7.2 Bin Selection.

In order to obtain the most precise picture of the proton structure the number of analysis bins should be as large as possible. However, this choice is limited due to the following requirements:

- The bins must have enough events so that statistical fluctuations are not important. Also the size of the statistical errors has to be reasonably small ( $\lesssim 10\%$ , but in a few bins of the NVTX analysis  $\sim 20\%$ ) for a meaningful measurement. Due to the  $\frac{1}{Q^2}$ -dependence of the neutral current  $\epsilon p$ -cross section the rapidly falling event statistics is the limiting factor at high- $Q^2$ . Large migration effects can result in an event depletion of a particular region in the  $(x, Q^2)$  plane. This effect limits the event statistics at high- $x$ . The selection cuts allow only certain  $(x, Q^2)$ -values to be reconstructed. The requirement of a minimum electron energy of  $E'_e > 10$  GeV (8 GeV in the ISR analysis) sets a limit at low  $x$  for medium and low  $Q^2$  values. The geometrical acceptance of the detector, in particular the box-cut, limits the event statistics at low  $Q^2$ .
- The resolution in the reconstructed  $x$  and  $Q^2$  as well as systematic migrations in these variables due to particle losses, photon radiation or the finite detector resolution and granularity (see chapter 7) require a minimum bin size for a reliable and statistically independent measurement of  $F_2$  in the bins. An adequate fraction of events produced in a certain bin must be reconstructed in the same bin. This can be achieved by requiring, that the bin widths,  $S(x)$  and  $S(Q^2)$ , satisfy

$$S(x) \gtrsim \sigma(x) \quad (7.1)$$

$$S(Q^2) \gtrsim \sigma(Q^2) \quad (7.2)$$

where  $\sigma(x)$  and  $\sigma(Q^2)$  are the resolutions of the kinematic variables  $x$  and  $Q^2$ , as shown in the previous chapter.

The quality of the bins can be quantified using the following definitions of acceptance and purity:

$$\begin{aligned} \text{acceptance}(i) &= \frac{\# \text{ events, generated in bin } i \text{ and passing the final event selection}}{\# \text{ events generated in bin } i} \\ \text{purity}(i) &= \frac{\# \text{ events, generated and reconstructed in bin } i}{\# \text{ events reconstructed in bin } i} \end{aligned} \quad (7.3)$$

Both quantities are determined using the DIS-Monte Carlo and take values between 0 and 1. The acceptance is mainly a measure of the effect of event selection and detector acceptance on the data sample, whereas the purity indicates if the events measured in a bin are contaminated with event migration from adjacent bins. It is therefore

sensitive to the resolution and systematic shifts in the reconstruction of  $x$  and  $Q^2$ . In the analyses presented here the acceptance is required to be  $\geq 30\%$ . However, for most bins the acceptance is  $> 50\%$ . Good bins are required to have a purity of  $\gtrsim 30\%$ . A few exceptional bins in the ISR analysis, which are nevertheless very stable against systematic checks, can have a purity of  $\sim 18\%$ .

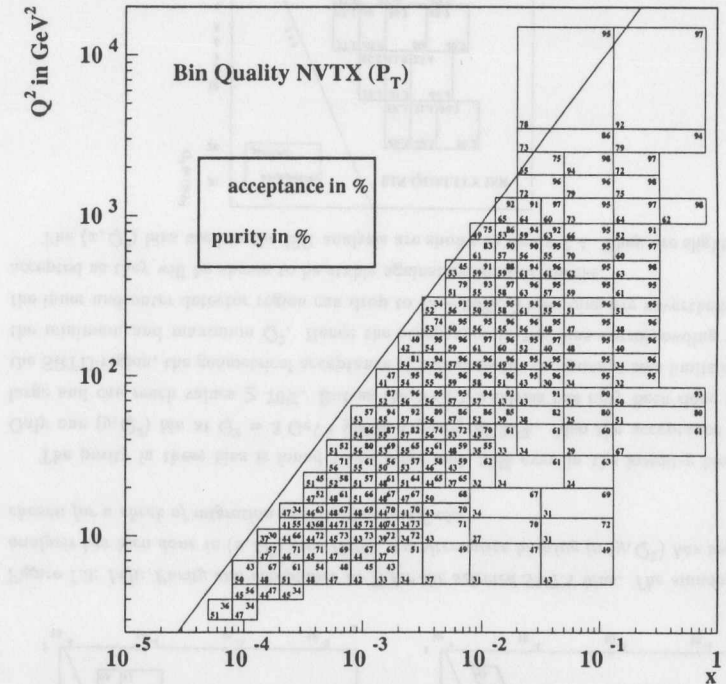


Figure 7.1: Purity and acceptance in % for the selected NVTX ( $p_T$ ) bins. The deteriorating vertex- and hence  $Q^2$ -resolution at low  $y$  requires a larger  $Q^2$ -binning.

Figure 7.1 shows the  $(x, Q^2)$  bins in the NVTX analysis, selected according to the above quality criteria. As can be seen the acceptance is generally larger than 40%, only in the lowest  $Q^2$  bins it does drop to  $\sim 34\%$ . Also the purity is very high, in most bins  $\geq 40\%$ . Only at low  $y$  does it fall below 40%, in two bins even below 30%. But since these bins are stable against systematic checks, they are included in the set of accepted bins. This choice of bins has been made using the  $p_T$ -method. The fact that at low  $y$  a coarser binning, in particular in  $Q^2$ , is chosen is mainly due to the deteriorating  $z$ -vertex resolution in this region (see section 5.3).

In section 5.4.5 several methods of correcting the scattered electron energy have been presented. As a consequence  $F_2$  can be measured from the 1994 ZEUS data, using the electron method for the first time in the entire  $(x, Q^2)$  plane. As the electron method shows characteristics significantly different from that of the  $p_T$ -method, in particular at low  $y$ , a special binning has been chosen here.

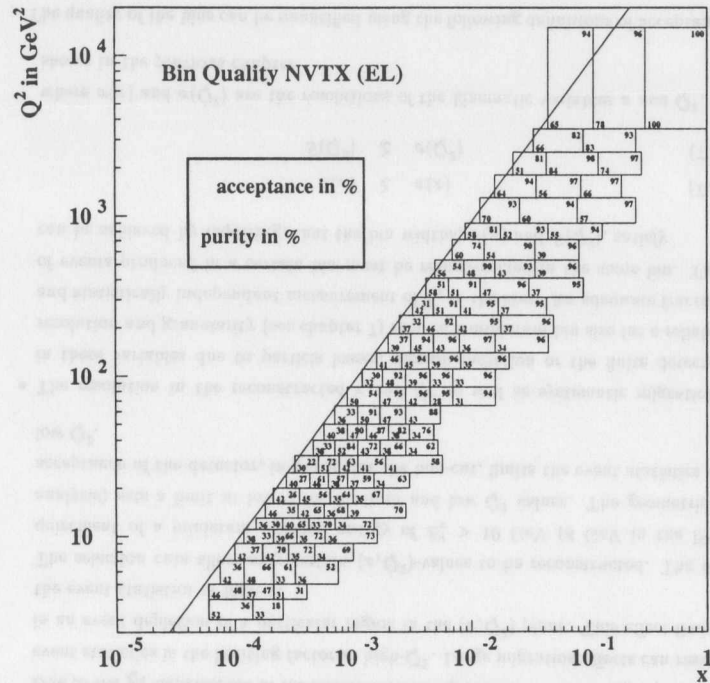


Figure 7.2: Purity and acceptance in % for the selected NVTX (el)-bins. The deteriorating  $x$ -resolution at high  $x$  limits the el-measurement to the high- $y$  region.

The bins only populate the medium- and high- $y$  region, as shown in figure 7.2. Both the acceptance and the purity are again rather large. But due to the deteriorating  $x$ -resolution towards high- $x$  the bin width in  $x$  is here larger than for the  $p_T$ -bins.

The good bins for the SVTX analysis are presented in figure 7.3. The main analysis here has also been done in  $(x, Q^2)$ -bins. But in order to test the analysis procedure for its dependence on the simulation, in particular the electron energy corrections and general migrations in the electron method, an alternative binning in  $(y, Q^2)$  has also been chosen (see right hand side of figure 7.3).

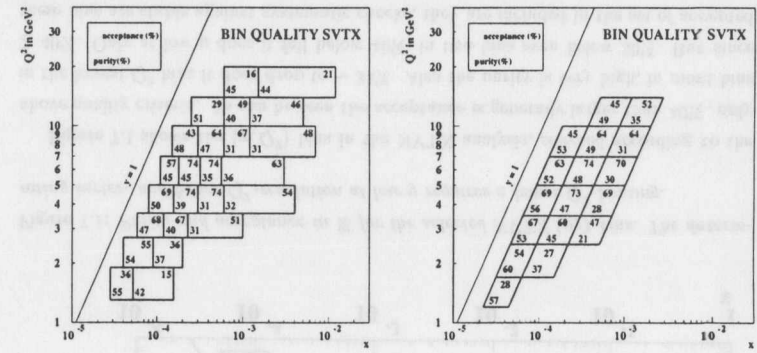


Figure 7.3: Left: Purity and acceptance in % for the selected SVTX bins. The standard analysis has been done in  $(x, Q^2)$  bins (left). An alternative binning in  $(y, Q^2)$  has been chosen for a check of migration and resolution effects.

The purity in these bins is found to be large and 30% even in the lowest- $y$  bins. Only one  $(y, Q^2)$  bin at  $Q^2 = 3 \text{ GeV}^2$  yields a purity of 21%. Also the acceptance is large and can reach values  $\geq 70\%$ . But as the SVTX analysis has only been done in the SRTD-region, the geometrical acceptance of this detector component sets limits on the minimum and maximum  $Q^2$ . Hence the acceptance in the bins corresponding to the inner and outer detector region can drop to 15 – 20%. These bins are nevertheless accepted as they will be shown to be stable against systematic checks.

The  $(x, Q^2)$  bins used in the ISR analysis are shown in figure 7.4. They are slightly

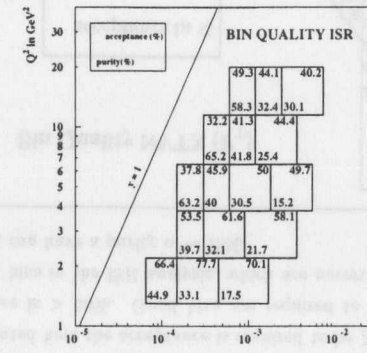


Figure 7.4: Purity and acceptance in % for the selected ISR bins. Due to the reduced centre of mass energy a lower  $y$ -region is accessible than using non-radiative events.

larger than the ones in the SVTX analysis, mainly due to the limited event statistics and additional resolution effects from the lumi-photon calorimeter. In comparison to the SVTX bins it can also clearly be seen that the ISR bins cover a lower- $y$  region, despite using the electron method. This is a consequence of the effective reduction in the centre of mass energy resulting from the photon emission. The acceptance in all but one ISR bins is  $> 40\%$ . The purity is generally larger than 30% and only drops in exceptional bins at low- $y$  to 15–20%.

The  $x$ - or  $Q^2$ -value at which the measured  $F_2$  is finally quoted are chosen for convenience and can differ slightly from the mean measured values in the bins. This is taken into account in the extraction of  $F_2$ .

### 7.3 Remaining Backgrounds.

After the final event selection the samples contain a small number of background events which are not due to deep inelastic neutral current scattering:

- The amount of background not associated with  $ep$ -collisions is determined from pilot or empty bunches, as described in section 5.7. It amounts to less than  $\sim 1.5\%$  in all bins of the NVTX analysis. No such background is found in the SVTX analysis, it is estimated to be less than 1%.

Due to the additional requirement of a reconstructed photon in the lumi-photon calorimeter, the non- $ep$  background in the ISR analysis is negligible, except for the lowest  $Q^2$  bins, where it amounts to 5–7%.

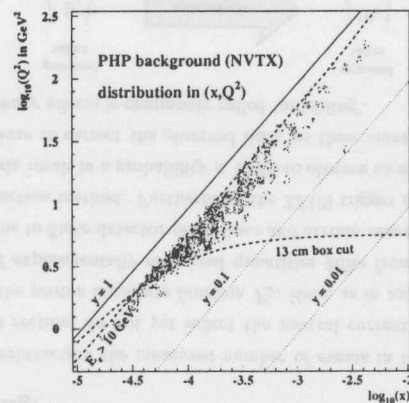


Figure 7.5: Photoproduction Monte Carlo background events passing the final selection cuts. They populate only the high- $y$  region, mainly at low- $Q^2$ .

- The contamination of the final event samples from photoproduction background is estimated from the photoproduction Monte Carlo. The number of events passing the selection cuts is determined in every bin, so that the background can be subtracted statistically.

The distribution of the estimated photoproduction background in the  $(x, Q^2)$  plane is shown in figure 7.5 for the NVTX analysis. In the SVTX analysis a similar distribution is obtained. The background clearly concentrates at high- $y$  and low- $Q^2$ , as expected. In these bins its contribution relative to the number of measured events is found to be at most 6% in the SVTX and the NVTX analyses. Potential photoproduction background is included in the bremsstrahlung sample used in the ISR analysis for background subtraction. Based on the  $\delta$ -distribution its contribution to the finally selected event sample is estimated to be negligible.

- In the ISR analysis the bremsstrahlung background, selected and normalised as described in section 5.7, is subtracted statistically in each  $(x, Q^2)$  bin separately. Its relative contribution to the measured events is below 10%, except the lowest  $x$  bins, where it can be up to 24%.

The total background contribution to each bin is given with the final results on  $F_2$  in tables 13.1 to 13.11.

## 7.4 Unfolding.

After background subtraction the measured number of events in the  $(x, Q^2)$  bins, i.e. the measured cross section, do not yet reflect the neutral current  $ep$ -scattering cross section and hence the proton structure function  $F_2$ . Here, as in any other experiment, the distributions of experimentally measured quantities differ from the corresponding real distributions due to finite detector resolutions and certain assumptions made in the kinematic reconstruction method. Furthermore the ZEUS trigger system and the final data selection criteria result in a probability  $< 100\%$  to observe an event in the detector. The general procedure to correct the observed data for these smearing, migration and acceptance or efficiency effects is commonly called 'unfolding'.

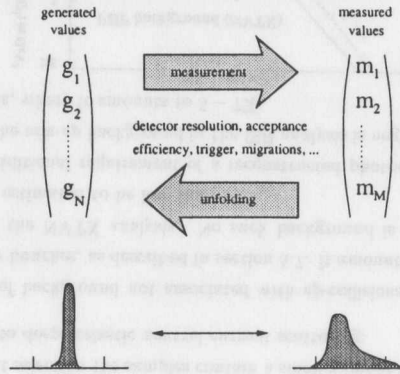


Figure 7.6: Schematic diagram of the unfolding technique. Measured quantities, distorted by detector resolution and acceptance, are corrected for these effects.

The relation between the true quantities  $g(x_1, x_2, \dots, x_n)$  and the measured quantities  $m(x_1, x_2, \dots, x_n)$  is

$$m(x_1, x_2, \dots, x_n) = \int dx'_1 dx'_2 \dots dx'_n T(x_1, x_2, \dots, x_n; x'_1, x'_2, \dots, x'_n) g(x_1, x_2, \dots, x_n) \quad (7.4)$$

where  $x_1, x_2, \dots, x_n$  are the characteristic event parameters and the expression  $T(x_1, x_2, \dots, x_n; x'_1, x'_2, \dots, x'_n)$  is the so-called transfer-function. This very general description can be simplified by considering  $g_i$  and  $m_j$  to be the generated and measured number of events in bin  $i$  and  $j$  respectively. The transfer function is then described by a matrix  $T_{ij}$ , so that

$$m_i^{MC} = \sum_j (T_{ij}^{MC}) g_j^{MC} \quad (7.5)$$

The aim of the unfolding procedure is to find the correct values for the true or generated number of events,  $g_j$ , if the measured event numbers,  $m_i$ , are given and the transfer matrix  $T_{ij}$  is known from Monte Carlo studies.

There are several approaches to unfolding, a subset is discussed in the following.

### 7.4.1 Bin-by-Bin Unfolding.

Only considering net event migrations from or into a bin, the transfer matrix is simplified to a diagonal matrix. The bins are no longer correlated and can be treated separately. With the correction factor

$$\frac{1}{T_{i,i}^{MC}} = c_i^{MC} = \frac{\# \text{ events generated in bin } i}{\# \text{ events measured in bin } i} \quad (7.6)$$

which is obtained from the Monte Carlo, the number of generated events,  $g_i$ , can be approximated by the unfolded event number

$$u_i^{Data} = c_i^{MC} \cdot m_i^{Data} \quad (7.7)$$

Due to varying contributions in different kinematic regions, the correction factors can vary considerably between different  $(x, Q^2)$  bins.

The method is straight forward and fast. However, small differences in the resolution, migration or acceptance between the Monte Carlo and the data can result in significant fluctuations of the unfolded number of events around the generated value.

As only net migrations are considered, this method requires the Monte Carlo simulation to describe the data very well in all phase space regions from which the measured events originate. In order to reduce the dependence of the method on the structure function, used in the generation of the Monte Carlo events, the algorithm can be extended iteratively. Given that the initial structure function in the simulation describes the data adequately, the unfolded event numbers after the first iteration,  $u_i^{(1)}$ , are good approximations to the generated ones,  $g_i$ . Based on the former,  $F_2$  can be extracted and used as input data to a next-to-leading order QCD fit program [118, 123]. After reweighting the Monte Carlo to the structure function resulting from this fit, the correction factors  $c_i^{(2)}$  are determined again, yielding an improved estimate of the generated number of events:

$$u_i^{(2)} = c_i^{(2)} \cdot m_i \quad (7.8)$$

The iteration procedure can be repeated until a stable result is obtained.

In the case of the  $F_2$  measurements presented here, for which the Monte Carlo events have been generated according to the MRSA structure function, the second iteration results differ from the first iteration ones by less than 2%. Any further iteration does not change the unfolded number of events significantly, so the result is stable.

#### 7.4.2 Matrix Inversion.

Let  $m$  and  $g$  be the column vectors, representing the measured and generated number of events,  $m_i$  and  $g_i$ , and  $T$  be the transfer matrix  $T_{ij}$ . The generated number of events can be obtained by inverting equation 7.5.

$$u = (T^{MC})^{-1} m^{Data} \quad (7.9)$$

This method is mathematically precise. However, the matrix inversion does not always yield physically meaningful results as the transfer matrix is not necessarily regular. Small differences in resolution, migration or acceptance between Monte Carlo and data can produce large fluctuations in the unfolded event numbers. Due to these numerical instabilities this method is not considered any further.

#### 7.4.3 Matrix Unfolding.

In contrast to the matrix inversion, where the transfer matrix is determined from the Monte Carlo and then inverted, a matrix that describes the relation from the measured to the generated event numbers directly can be constructed from the Monte Carlo simulation. This approach avoids the numerically unstable matrix inversion. But as in the bin-by-bin unfolding this method relies on the Monte Carlo representing approximately the actual proton structure function  $F_2$ , since contributions from all bins are taken into account in the unfolding of the event number in a particular bin.

Let  $M$  be the matrix

$$M_{ij}^{MC} = \frac{\# \text{ events (generated in bin } i \text{ \& measured in bin } j), \text{ before cuts}}{\# \text{ events (measured in bin } j), \text{ after cuts}} \quad (7.10)$$

An estimate for the number of events, generated in bin  $i$  and measured in any bin, is then given by

$$\hat{u}_i^{Data} = \sum_j M_{ij}^{MC} \cdot m_j^{Data} \quad (7.11)$$

where  $m_j^{Data}$  is again the number of events measured in bin  $j$  after cuts. But a second step in the unfolding is required as events may be generated in bin  $i$  but not measured anywhere (because the trigger might not have accepted them, the scattered electron might not have been identified etc.). This additional correction for the efficiency of identifying DIS events at all has to be applied to every bin separately

$$\delta_i^{MC,eff} = \frac{\# \text{ events (generated in bin } i), \text{ before cuts}}{\# \text{ events (generated in bin } i), \text{ before cuts \& electron found}} \quad (7.12)$$

The number of events, generated in bin  $i$ , can therefore be estimated by

$$\begin{aligned} u_i^{Data} &= \delta_i^{MC,eff} \cdot \hat{u}_i^{Data} \\ &= \delta_i^{MC,eff} \cdot \sum_j M_{ij}^{MC} \cdot m_j^{Data} \end{aligned} \quad (7.13)$$

As the unfolded number of events now depends on the measured event number in several bins, small differences in resolution, migration and acceptance between Monte Carlo and data do not yield large fluctuations. The resulting cross section and hence the  $F_2$  values tend to be smooth. But the unfolded event numbers and  $F_2$  values are now correlated between bins.

In order not to smooth the extracted  $F_2$  too much and bias the result to the shape of  $F_2$  as described by the Monte Carlo (see section 7.6), this method is only used for general cross checks for consistency of the different methods.

#### 7.4.4 Bayes Unfolding.

Another unfolding method is based on the Bayes probability theorem and has been published in [88]. In contrast to the afore described matrix unfolding, which describes the relation from the measured to the generated event numbers, the Bayes unfolding describes the relation from the generated to the measured event numbers. Now the matrix elements are defined as

$$B_{ij}^{MC} = \frac{\# \text{ events (generated in bin } j \text{ \& measured in bin } i)}{\# \text{ events (generated in bin } j)} \quad (7.14)$$

and interpreted as the conditional probability for an event, being generated in bin  $j$ , to be measured in bin  $i$ . Also the total probability,  $\alpha_i$ , of an event, which is generated anywhere, to remain in the final sample of events measured in bin  $i$  is determined equivalently to equation 7.12.

$$m_i^{MC} = \frac{1}{\alpha_i} \sum_j B_{ij}^{MC} \cdot g_j^{MC} \quad (7.15)$$

Exploiting Bayes' theorem the generated events  $g_j$  are reweighted iteratively until the resulting measured events in the Monte Carlo,  $m_i^{MC}$ , give a good description of the measured events in the data,  $m_i^{Data}$ . The reweighted generated events are then taken as the unfolded true event distribution in the bins.

This unfolding method was also used in the ZEUS- $F_2$  measurement from the 1993 data. As it takes correlations between bins due to resolution or migration into account by using a matrix, the finally unfolded event numbers are correlated, too. The corresponding  $F_2$  again tends to be smooth and slightly biased in shape to the input Monte Carlo structure function. However after several iterations this bias disappears.

The Bayes unfolding is used to estimate the systematic uncertainties on  $F_2$  due to the choice of the unfolding method.

The central  $F_2$  values in all three analyses have been obtained using the iterated bin-by-bin unfolding.

A simple test of the three unfolding algorithms considered here is presented in section 7.6.

### 7.5 From the Cross Section to $F_2$ .

In the single-photon-exchange approximation of deep inelastic scattering the double differential cross section for inclusive neutral current  $ep$  scattering is given in terms of the structure functions  $F_i$ :

$$\frac{d^2\sigma(e^\pm p)}{dx dQ^2} = \frac{2\pi\alpha^2}{xQ^4} \left[ Y_+ F_2(x, Q^2) - y^2 F_L(x, Q^2) \mp Y_- xF_3(x, Q^2) \right] \cdot (1 + \delta_r(x, Q^2)) \quad (7.16)$$

where  $Y_\pm = 1 \pm (1-y)^2$  and  $\delta_r(x, Q^2)$  is the electroweak radiative correction to the Born level cross section. Since  $y^2 F_L$  and  $F_3$ , which also include contributions from  $Z^0$ -exchange, and  $\delta_r$  are expected to be small in the kinematic range of the present measurements, this equation can be rewritten as

$$\frac{d^2\sigma(e^\pm p)}{dx dQ^2} = \frac{2\pi\alpha^2 Y_+}{xQ^4} F_2(x, Q^2) \cdot (1 - \delta_L \mp \delta_3) \cdot (1 + \delta_r) \quad (7.17)$$

The  $\delta_i(x, Q^2)$  are corrections which separate the contributions from  $F_L$ ,  $Z^0$ -exchange and QED-radiation.

Neglecting the  $Z^0$ -exchange the corresponding expression for deep inelastic  $ep$  scattering with photon radiation in the initial state is

$$\frac{d^3\sigma}{dx dQ^2 dz} = \alpha^3 P(z) \frac{1 + (1 - \frac{Q^2}{szz})^2}{xQ^4} \left[ F_2(x, Q^2) - (1 - \epsilon) F_L(x, Q^2) \right] \quad (7.18)$$

where  $\epsilon = \frac{2(1-y)}{1+(1-y)^2}$  is the relative polarisation of the exchanged virtual photon, and  $z = \frac{E_e - E_\gamma}{E_e}$  is the fraction remaining of the incoming electron's energy after the photon radiation. Integrated over the photon emission angle  $\Theta_\gamma < \Theta_0$ , where the collinear approximation is valid, this probability can be written as

$$P(z) = \frac{1+z^2}{1-z} \ln \frac{E_e^2 \Theta_0^2}{m_e^2} - \frac{z}{1-z} \quad (7.19)$$

where  $E_e$  is the energy of the incoming electron,  $m_e$  is its mass. Integrating over  $z$ , the accepted range of photon energies, yields

$$\frac{d^2\sigma}{dx dQ^2} \sim F_2(x, Q^2) \cdot (1 + \delta_L) \quad (7.20)$$

In all three analyses the produced or unfolded number of events,  $N_i$ , in bin  $i$  is proportional to this cross section and the Luminosity  $\mathcal{L}$  of the data sample

$$\begin{aligned} N_i &= \mathcal{L} \cdot \int \frac{d^2\sigma}{dx dQ^2} dx_i dQ_i^2 \\ &= \mathcal{L} \cdot \sigma_i \end{aligned} \quad (7.21)$$

where the integration is performed over the bin boundaries.

Assuming that the structure function dependence on  $x$  and  $Q^2$  in the Monte Carlo resembles that of the data, which has been achieved with the iterative reweighting

procedure, the values of the different structure functions (here data and Monte Carlo) can be related to the ratio of events produced in the bin:

$$\begin{aligned} \frac{N_i^{Data}/\mathcal{L}^{Data}}{\sigma_{i,generated}^{MC}} &= \frac{\sigma_i^{Data}}{\sigma_i^{MC}} \\ &= \frac{F_2^{Data}(x, Q^2) \frac{2\pi\alpha^2}{xQ^4} \cdot (1 - \delta_L^{Data} \mp \delta_3^{Data})(1 + \delta_r^{Data})}{F_2^{MC}(x, Q^2) \frac{2\pi\alpha^2}{xQ^4} \cdot (1 - \delta_L^{MC} \mp \delta_3^{MC})(1 + \delta_r^{MC})} \\ &= \frac{F_2^{Data}(x, Q^2)}{F_2^{MC}(x, Q^2)} \end{aligned} \quad (7.22)$$

The last step, cancelling out all correction factors, assumes that the Monte Carlo simulation describes the relative contribution to the cross section from  $F_L$ ,  $Z^0$  and QED radiation correction correctly. The first two assumptions have to be made as neither  $F_L$  nor  $F_3$  have been measured in the HERA range so far and are therefore based on QCD and the electroweak force in the standard model.

Higher order QED radiative effects, not included in HERACLES, were estimated to be 0.2 – 0.5% using the program HECTOR [93]. These corrections are not included in the presented analyses.

As the NVTX and SVTX Monte Carlo samples were generated including  $F_L$ ,  $Z^0$ -exchange and  $\mathcal{O}(\alpha)$  photon radiation, the respective corrections are applied implicitly. Only in the ISR analysis, where the contribution from  $F_L$  has not been included in the generated Monte Carlo sample, an explicit correction for it has to be applied.

$$F_2^{Data} = F_2^{MC} \frac{N_i^{Data}/\mathcal{L}}{\sigma_{generated}^{MC}} \cdot (1 + \delta_L) \text{ with } \delta_L = \frac{\sigma_{F_L=0}}{\sigma_{F_L^{QCD}}} - 1 \quad (7.23)$$

As  $F_L$  is reduced by  $y^2$  its contribution is largest at high- $y$ . The corrections in the corresponding bins are less than 7%.

### 7.6 Test of the $F_2$ -Extraction.

In order to test and compare the unfolding methods the Monte Carlo event sample has been divided into two statistically independent samples. One is treated as data and unfolded with corrections obtained from analysing the other sample. This has been carried out four times, reweighting the samples independently to the structure function parametrisations MRSD0' or MRSD'. The results obtained are shown with statistical errors in comparison to the structure function curves in figure 7.7.

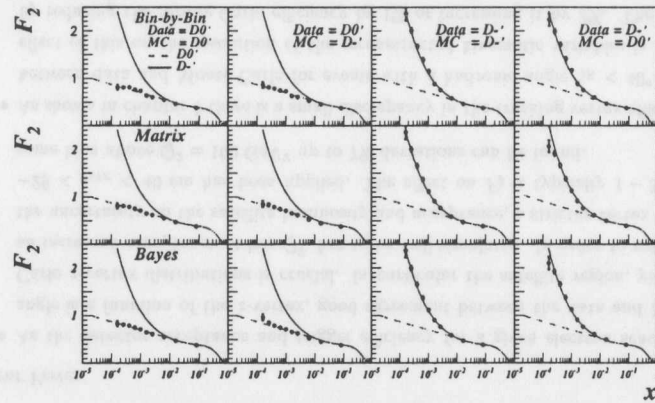


Figure 7.7: Test of the unfolding methods. Monte Carlo event samples, reweighted to the structure functions MRSD0' (two last columns) or MRSD' have been unfolded using corrections from other Monte Carlo samples, which have been reweighted to different structure functions. The resulting  $F_2$  is shown at  $Q^2 = 10 \text{ GeV}^2$ .

The four top plots depict the unfolded  $F_2$ , using the bin-by-bin correction method. The points scatter slightly around the curve. But no bias towards the structure function used in the correction sample can be seen.

The four middle plots show the  $F_2$  as extracted by the matrix unfolding. Apart from the lowest- $x$  point in the rightmost plot, which suffers from a statistical fluctuation, all points are exactly on the line and yield a smooth  $F_2$ .

The four plots at the bottom display the  $F_2$  after the first step of the Bayes unfolding. A small deviation from the input structure function can be seen in the second plot, where the MRSD0' parametrisation has nevertheless been clearly recovered.

The results for all three unfolding methods are in very good agreement with the input structure function. Even if very different data and correction samples are chosen, there is essentially negligible bias, providing confidence in the  $F_2$  results obtained from the 1994 ZEUS data.

### 7.7 Statistical Error.

The statistical error of  $F_2$  in a particular bin is calculated taking three contributions into account, the real data, the DIS-Monte Carlo and the photoproduction or bremsstrahlung background with:

$N^{obs}$  = number of observed events in the bin  
including background

$N^{DATA}$  = number of data events measured in the bin

$$= N^{obs} - N_{eff}^{PHP}$$

$N^{MC}$  = number of Monte Carlo events contributing to the measurement in the bin (every event counted as 1)

$\alpha_i$  = cross section weights for DIS-Monte Carlo events

$N_{eff}^{MC}$  = effective number of DIS-Monte Carlo events in the bin

$$= \frac{(\sum_{i=1}^{N^{MC}} \alpha_i)^2}{\sum_{i=1}^{N^{MC}} (\alpha_i^2)}$$

$N^{PHP}$  = number of PHP-MC or bremsstrahlung events in bin

$\beta_i$  = cross section weights for PHP-Monte Carlo or bremsstrahlung events

$N_{eff}^{PHP}$  = effective number of PHP-Monte Carlo or bremsstrahlung events in the bin

$$= \frac{(\sum_{i=1}^{N^{PHP}} \beta_i)^2}{\sum_{i=1}^{N^{PHP}} (\beta_i^2)}$$

The resulting error on  $F_2$  is calculated from these as:

$$\begin{aligned} \frac{\Delta F_2}{F_2} &= \sqrt{\left(\frac{\delta N^{DATA}}{N^{DATA}}\right)^2 + \left(\frac{\delta N_{eff}^{MC}}{N_{eff}^{MC}}\right)^2} \\ &= \sqrt{\frac{N^{obs} + N_{eff}^{PHP}}{(N^{obs} - N_{eff}^{PHP})^2} + \frac{1}{N_{eff}^{MC}}} \\ &= \sqrt{\frac{\left(N^{obs} + \frac{(\sum_{i=1}^{N^{PHP}} \beta_i)^2}{\sum_{i=1}^{N^{PHP}} (\beta_i^2)}\right)^2}{\left(N^{obs} - \frac{(\sum_{i=1}^{N^{PHP}} \beta_i)^2}{\sum_{i=1}^{N^{PHP}} (\beta_i^2)}\right)^2} + \frac{\sum_{i=1}^{N^{MC}} (\alpha_i^2)}{(\sum_{i=1}^{N^{MC}} \alpha_i)^2}} \end{aligned} \quad (7.24)$$

For increasing Monte Carlo statistics  $\lim_{N^{MC} \rightarrow \infty} (N_{eff}) \rightarrow \infty$ , so that the Monte Carlo contribution gets negligible in this case, as intuitively expected. This procedure is also described in [95].

## 7.8 Systematic Uncertainties.

A crucial aspect of the  $F_2$  analyses is a realistic estimation of the systematic errors entering from different sources. Numerous checks have been performed in order to test the stability of  $F_2$ . For each case in turn a quantity entering the analysis, such as calibrations, correction functions, alignment etc., is varied within errors and the full event selection and  $F_2$  extraction is repeated. Also the background estimation is repeated and subtracted consistently.

The bin-by-bin variations in  $F_2$  from the central value, added in quadrature separately for the positive and negative deviations, have been used to estimate the systematic errors. In the following these systematic checks are described for the three analyses in turn.

### 7.8.1 Systematic Checks in the NVTX Analysis.

In the NVTX analysis the systematic checks are subdivided into seven categories.

#### *Event Vertex*

- As the detector acceptance and trigger efficiency for a given electron scattering angle is a function of the  $z$ -vertex, good agreement between the data and Monte Carlo  $z$ -vertex distributions is crucial. In particular the satellite region, yielding an increased acceptance at low- $Q^2$ , has to be well simulated. In order to estimate the uncertainty on the satellite luminosity and acceptance, a stricter vertex cut of  $-28 < z_{vtx} < 40$  cm has been applied. The effect on  $F_2$  is typically 1 – 3%, in some bins above  $Q^2 = 100$  GeV<sup>2</sup> up to 7% deviations can be found.
- As shown in chapter 5 there is a small discrepancy in the tracking vertex efficiency between data and Monte Carlo for events with a hadronic angle  $\gamma_h < 40^\circ$ . The effect of this on the resolution of the reconstructed kinematic variables is tested by reducing the Monte Carlo efficiency by 1% or increasing it by 3%. The effect is about 0.5% and hence negligible.
- The event  $z$ -vertex as reconstructed in the Monte Carlo is shifted by  $\pm 4$  mm, representing the tracking vertex resolution for the inclusive DIS data sample. This has the effect of  $\leq 0.8\%$  changes in  $F_2$ .

#### *Detector Alignment*

- The fiducial cut at the inner edge of the rear calorimeter and SRTD (box cut), which guarantees good containment of the electron shower in the detector, is increased from 3 to 4 cm for data and Monte Carlo. The results in the lowest  $Q^2$ -bins change by 3.5%, while all other bins are essentially unaffected.

- To account for an uncertainty in the relative position of the two halves of the rear calorimeter and the SRTD, their position in the data is varied by  $\pm 1$  mm each, representing a smaller and larger gap between the two halves. At  $Q^2 < 20$  GeV<sup>2</sup> the resulting  $F_2$  varies typically by 1.5%, higher  $Q^2$  bins are stable.
- The radius value of the electron impact point in the calorimeter is varied by  $\pm 2$  mm. These checks also account for a possible systematic shift in the  $z$ -position of the electron in the rear calorimeter as determined by ELECPO. For bins at  $Q^2 > 20$  GeV<sup>2</sup> the effect is 1 – 1.5%, the lower  $Q^2$  results do not change as they are based on the SRTD.
- For events with a matched track the resulting electron scattering angle is varied by  $\pm 0.2^\circ$ , which is the effective resolution of the electron scattering angle as reconstructed from tracks. The variations in  $F_2$  are negligible.
- The absolute position of the SRTD in the data with respect to the Monte Carlo position is shifted by  $\pm 2$  mm. At  $Q^2 = 6.5$  GeV<sup>2</sup> the effect on  $F_2$  is  $\sim 2\%$  and  $\sim 0.5\%$  in all other bins at  $Q^2 < 20$  GeV<sup>2</sup>. The higher  $Q^2$  bins are stable.

#### *Positron Finding Efficiency and Energy Scale*

- In the Monte Carlo simulation the reconstructed electron energy in the RCAL is increased and decreased by a linear function (2% at 5 GeV and 1% at 27.5 GeV). The BCAL scale is varied by  $\pm 3\%$ . These numbers represent the current understanding of the CAL energy scale. The observed variations in  $F_2$  are 1 – 2%.
- The electron energy correction in the RCAL is obtained from a mixture of a 2.5% energy scaling in the data followed by a subsequent kinematic peak correction. At  $20 \leq Q^2 \leq 120$  GeV<sup>2</sup> the effect is less than 1%, the other  $Q^2$  regions are not affected at all, since they rely on different correction methods.
- Although the anti-correlation of electron energy loss in the calorimeter and the probability as given by SINISTRA is taken into account, yielding consistent electron finding efficiencies for data and Monte Carlo, a systematic check with the Monte Carlo efficiency reduced by 1% above 15 GeV and about 3% at 10 GeV is performed. No effect is seen at  $Q^2 \geq 35$  GeV<sup>2</sup>. At lower  $Q^2$  variations of  $\sim 1\%$  are found, except for the low- $x$  bins, where they increase to  $\sim 3\%$ .

#### *Hadronic Energy Scale*

- The energy scale of all entries in the calorimeter, which are not assigned to the scattered electron, is varied by  $\pm 3\%$ . This variation is applied as a global scale as

well as for the different calorimeter parts (FCAL/BCAL/RCAL) separately. The value of 3% is obtained from comparisons of  $\frac{P^H}{P_T}$  between data and Monte Carlo after electron energy and hadronic scale correction. The change in  $F_2$  is typically  $\sim 4\%$  at very high and low  $y$ , while bins at medium  $y$  are stable to within  $\pm 1\%$ .

#### Hadronic Energy Flow

- The cut on  $\delta_{pt} = \frac{P^H}{P_T}$  is removed, allowing for events in which most of the hadrons are lost in the forward beampipe ('non-contained events'). This has a negligible effect on  $F_2$ .
- The hadronic correction function in the 'PT'-method shows a significantly different behaviour for 'single-jet events' ( $\frac{E_T^c}{E_T^{tot}} > 0.4$ ) and 'multi-jet events' ( $\frac{E_T^c}{E_T^{tot}} < 0.4$ ), which is accounted for in the standard correction. As a systematic check this dependence is ignored, relying more strongly on the Monte Carlo simulation of the hadronic final state. This check results in 1%-variations of  $F_2$ .
- In order to check the dependence of the  $F_2$ -results on the simulation of the hadronic final state and in particular of diffractive events their contribution is reweighted to 20% and 0%, while keeping the cross section unchanged as a function of  $x$  and  $Q^2$  constant. For the latter additional reweighting is required, since the fraction of diffractive events in the Monte Carlo depends slightly on  $x$  and  $Q^2$ . The results are in general stable to within  $\pm 1\%$ , only the low- $x$  bins at  $Q^2 \leq 4.5 \text{ GeV}^2$  show variations of 5%.
- The hadronic correction function in the 'PT'-method is not taken from sampling the  $E - P_z$  loss as a function of  $P_T$  loss etc., but a polynomial fit to this function is performed and applied, smoothing the correction. The effect on  $F_2$  is less than 1%.

#### Photoproduction Background Subtraction

- Although the determination of the photoproduction background contamination of the data sample using the PYTHIA Monte Carlo gives consistent results with the  $\delta$ -fit method, a comparison with tagged photoproduction events yields an uncertainty of +100% and -50%. The subtracted photoproduction background is varied by this amount.  $F_2$  is affected by  $\pm 3\%$  at high  $y$  and  $Q^2 \leq 20 \text{ GeV}^2$  and stable elsewhere.

#### Miscellaneous

- As small differences in the resolution and migration of kinematic variables can lead to large fluctuations of  $F_2$ , in particular at  $y \sim 10^{-2}$ , where the  $y$ -distribution is

rapidly falling, the  $F_2$ -measurement has been repeated using the Bayes unfolding method. Resulting variations are typically below 1%, only some  $F_2$ -values at low- $y$  change by up to 10%.

Even though hadronic event parameters enter the NVTX electron analysis only via the  $\delta$ -cut, identical checks have been performed in this analysis and added in quadrature to obtain the systematic errors.

Figure 7.8 shows the relative deviation from the central  $F_2$ -value as a function of  $y$  for the first six categories and  $Q^2 < 100 \text{ GeV}^2$ . In the diagram of the total systematic error the  $\pm 5\%$  range is indicated by horizontal lines.

The statistical errors amount to 2 - 4% for most bins and can grow to 8% at high  $y$ . For the majority of bins at  $5 \cdot 10^{-2} \leq y \leq 5 \cdot 10^{-1}$  the total systematic error is below 5%. For larger values of  $y$  it increases to  $\approx 10\%$ . At low values of  $y$  the total systematic error can get as large as 8 - 10%, mainly due to the contribution from electromagnetic and hadronic energy scale uncertainties.

A similar plot for  $Q^2 > 100 \text{ GeV}^2$  is shown in figure 7.9.

The systematic errors shown do not include the uncertainty in the measurement of the integrated luminosity ( $\pm 1.5\%$ ), the overall trigger efficiency ( $\pm 1.0\%$ ) or the uncertainty due to higher order electroweak radiative corrections ( $\pm 0.5\%$ ). These effects result in a combined normalisation uncertainty of 2% in  $F_2$ , which is also not included in the quoted errors in table 13.1 and 13.6

group	$a^+$	$b^+$	$c^+$	$a^-$	$b^-$	$c^-$
1	0.1111	0.0225	-0.7531	-0.2399	-0.1166	1.7702
2	-1.5631	0.0024	—	1.3691	-0.1024	—
3	0.4737	-0.3952	—	-0.6364	0.5158	—
4	0.7555	-0.5623	—	-0.7374	0.6382	—
5	-1.4477	-0.2003	—	0.6239	-0.4781	—
6	0.6807	—	—	0.6807	—	—

Table 7.1: Parameters describing the envelopes of positive and negative deviations of  $F_2$  by the six categories of systematic checks.

Since the systematic errors on  $F_2$  in the NVTX analysis are strongly  $y$ -dependent, this behaviour has been investigated and parametrised. These parametrisations do not only allow the consideration of correlated systematic errors in phenomenological or

QCD-analyses of the data, but they can also be used for case studies of future high-luminosity measurements with ZEUS, where systematic errors will play a crucial role.

For the six different categories of systematic checks the following functional forms have been fitted to the percentage errors  $\frac{\Delta F_2}{F_2}$  [%]

$$\text{group 1 (vertex)} : a_1/(\log_{10} y) + b_1 \cdot (\log_{10} y)^3 + c_1$$

$$\text{group 2 (alignment)} : a_2 + b_2 \cdot (\log_{10} y)$$

$$\text{group 3 (EM scale)} : a_3/(\log_{10} y) + b_3 \cdot (\log_{10} y)^2$$

$$\text{group 4 (HAD scale)} : a_4/(\log_{10} y) + b_4 \cdot (\log_{10} y)^2$$

$$\text{group 5 (HAD flow)} : a_5 + b_5 \cdot (\log_{10} y)$$

$$\text{group 6 (PHP)} : a_6/(\log_{10} y)$$

The envelope of positive and negative deviations are parametrised by  $a^+$ ,  $b^+$ ,  $c^+$  and  $a^-$ ,  $b^-$ ,  $c^-$  respectively. Their values obtained from a fit to the NVTX data are given in table 7.1.

Due to their nature systematic errors do not shift  $F_2$  in the same direction for each bin or have the same effect in every region of the  $(x, Q^2)$  plane. In order to provide a deeper insight into the effect of systematic checks in different  $(x, Q^2)$  and their contribution to the total error, a different way of displaying the effect of these checks has been chosen. Figures 7.10 and 7.11 show the selected  $(x, Q^2)$  bins 32-times, once for every systematic check. Bins in which the  $F_2$  obtained for a particular check is stable to within  $\pm 1.5\%$  are left white, while bins in which  $F_2$  increases by more than 1.5% are shown in light shading. Bins yielding an  $F_2$ , which is reduced by more than 1.5% compared to the central value are shown in dark shading.

For example reducing the electron energy increases  $F_2$  by more than 1.5% in the low- $y$  bins and decreases  $F_2$  at high  $y$ , while a positive change in the energy scale has the opposite effect (see check 15 and 16 in figure 7.10). Increasing the photoproduction background estimate reduces  $F_2$  at high  $y$  and medium or low  $Q^2$  while decreasing the background effects essentially the same bins in the opposite way.

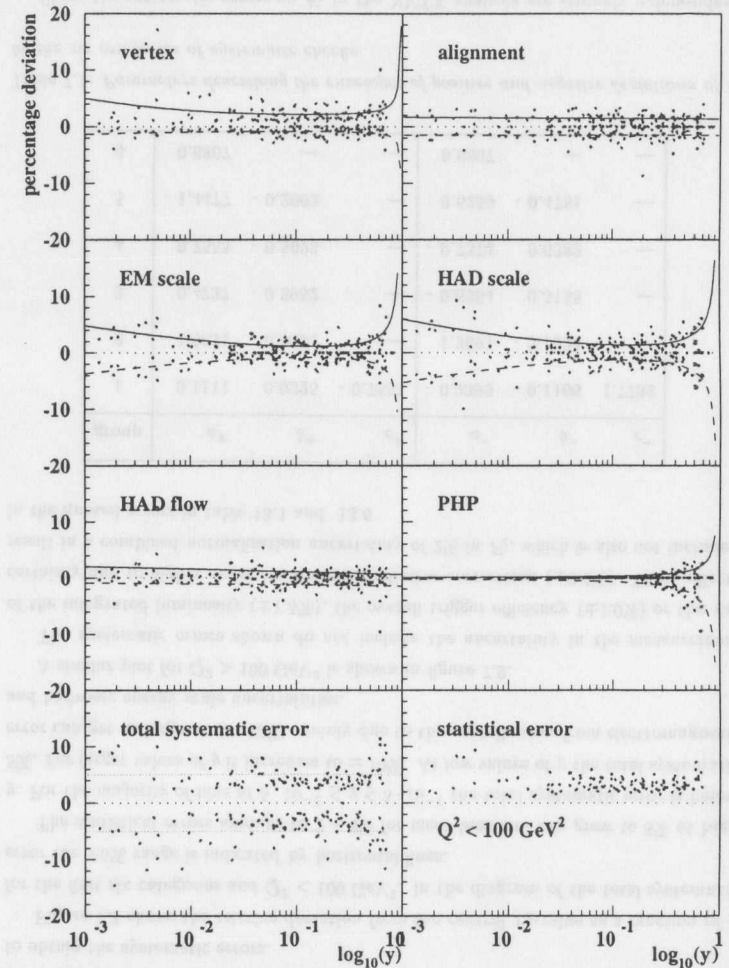


Figure 7.8: Relative systematic error of the NVTX  $F_2$ , determined with the  $p_T$ -method, for different categories of systematic uncertainties for bins with  $Q^2 < 100 \text{ GeV}^2$ .

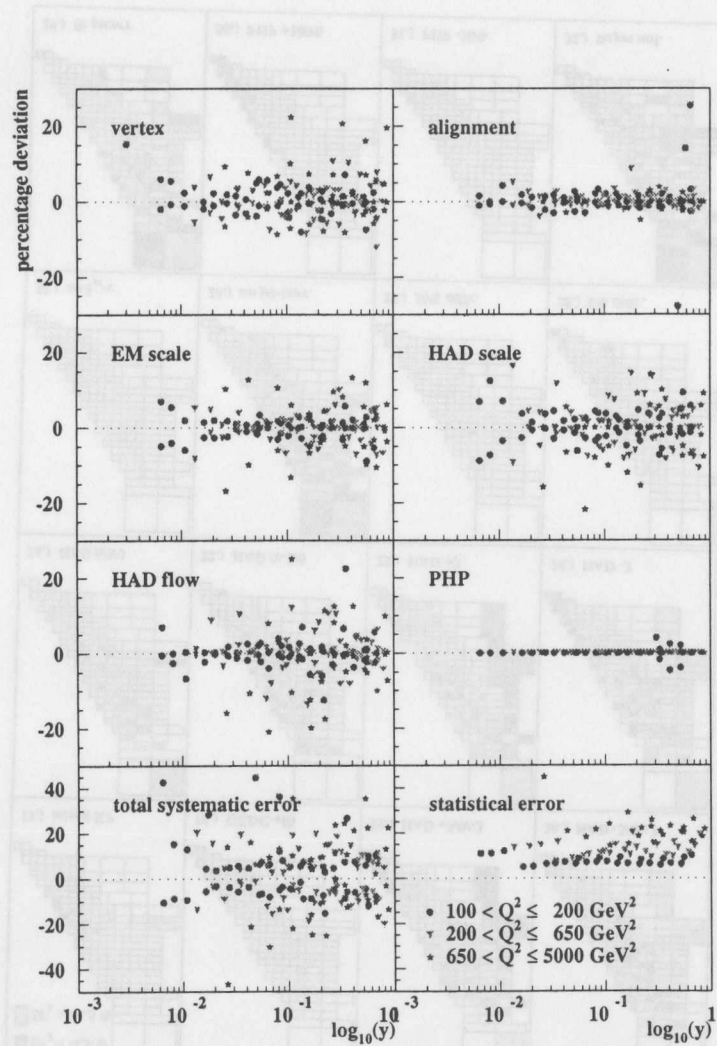


Figure 7.9: Relative systematic error of the NVTX  $F_2$ , determined with the  $p_T$ -method, for different categories of systematic uncertainties for bins with  $Q^2 > 100 \text{ GeV}^2$ .

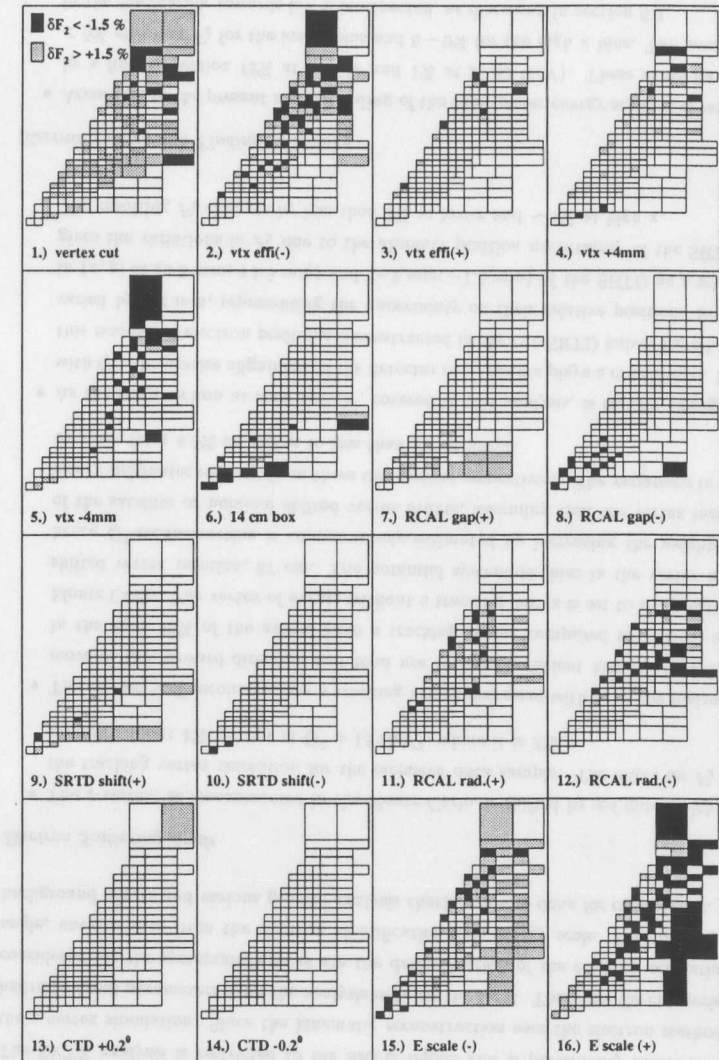


Figure 7.10: Systematic checks of the NVTX  $F_2$  ( $p_T$ ). For every check the selected ( $x, Q^2$ ) bins are drawn. The fill colour indicates if the corresponding  $F_2$ -value is stable to within  $\pm 1.5\%$  (white), increases (light shading) or decreases (dark shading) by more than 1.5%.

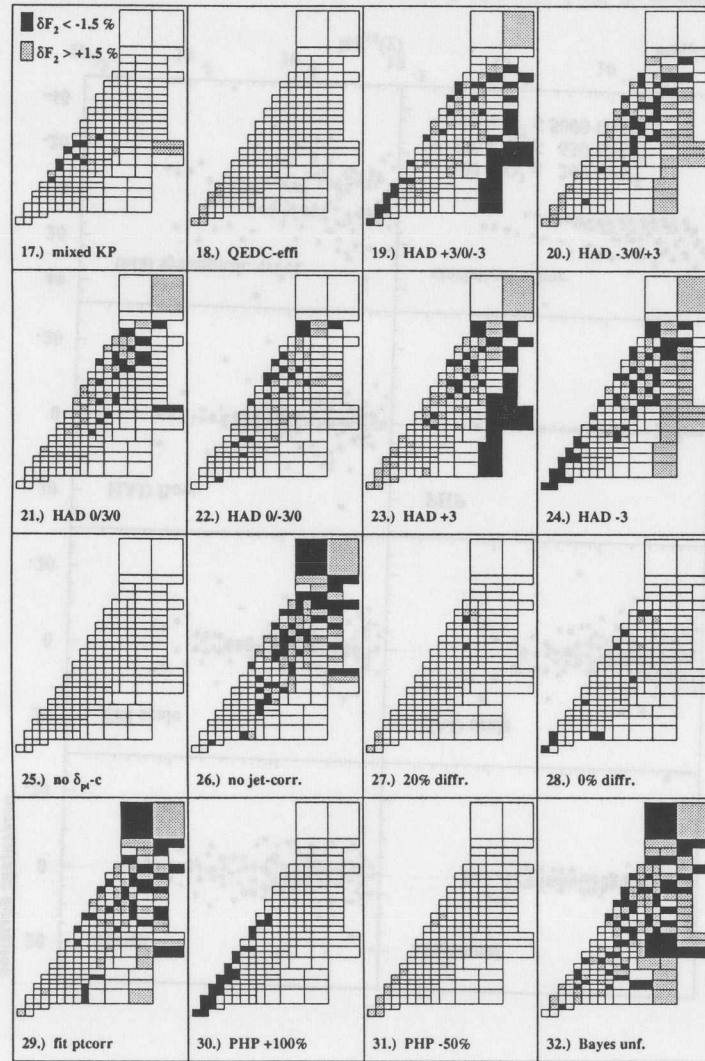


Figure 7.11: Systematic checks of the NVTX  $F_2$  ( $p_T$ ). For every check the selected ( $x, Q^2$ ) bins are drawn. The fill colour indicates if the corresponding  $F_2$ -value is stable to within  $\pm 1.5\%$  (white), increases (light shading) or decreases (dark shading) by more than  $1.5\%$ .

### 7.8.2 Systematic Checks in the SVTX Analysis.

The SVTX analysis is restricted to the SRTD region and is particularly sensitive to the  $z$ -vertex simulation. Since the kinematic reconstruction uses the electron method, hadronic event parameters enter the analysis only via the  $\delta$ -cut. Therefore the categories considered for the systematic checks are the determination of the electron scattering angle, uncertainties from the electron identification and energy scale. Hadronic and background effects and various general analysis checks are also done for consistency.

#### Electron Scattering Angle

- The  $z$ -vertex, as reconstructed in the Monte Carlo, is shifted by  $\pm 4$  mm, which is the tracking vertex resolution for the inclusive data sample. The effect on  $F_2$  is typically about  $1\%$ , except at  $Q^2 = 15 \text{ GeV}^2$ , where it is  $3\%$ .
- The efficiency of reconstructing a tracking vertex decreases with  $y$ , as the hadrons move in the forward direction and tend not to leave sufficient hits in the CTD. In the data  $70\%$  of the events have a tracking vertex compared to  $73\%$  in the Monte Carlo. The vertex of events without a tracking vertex is set to the nominal shifted vertex position,  $67$  cm. The potential systematic bias in the vertex and hence  $Q^2$ -reconstruction is conservatively estimated by increasing the weighting of the satellite or nominal shifted vertex events, assuming that the vertex inefficiency originates entirely from these two regions respectively. The variations in  $F_2$  decrease from  $4.5\%$  at high  $x$  to less than  $1\%$  at low- $x$ .
- As the cross section at such low- $Q^2$ , covered in this analysis, is rapidly changing with  $Q^2$ , the precise alignment of the detector components plays a crucial role. For this reason the electron positions reconstructed in the two SRTD halves have been varied by  $\pm 2$  mm, representing the uncertainty on their relative position. Shifts in  $(x, y)$  of  $(+2 \text{ mm}; +1.5 \text{ mm})$  and  $(-2 \text{ mm}; -1.5 \text{ mm})$  of the SRTD as a whole gives the variations in  $F_2$  due to the absolute position uncertainty of the SRTD. The resulting  $F_2$  changes by less than  $5\%$  at low- $x$  and  $\sim 1\%$  at high  $x$ .

#### Electron Energy and Finding Efficiency

- According to the present understanding of the calorimeter energy scale, it is varied by a linear function ( $2\%$  at  $5 \text{ GeV}$  and  $1\%$  at  $27.52 \text{ GeV}$ ). These shifts have a  $< 5\%$  effect on  $F_2$  for the low- $x$  bins and  $6 - 9\%$  for the high  $x$  bins. The increase in the fluctuation towards low- $y$  is expected, as discussed in section 6.3.
- The minimum probability for an object to be identified as an electron by the neural network has been lowered from  $0.9$  to  $0.8$ . This variation results in changes of  $F_2$  by  $\leq 2.5\%$ , except a  $4\%$  effect at the lowest  $x$ , lowest  $Q^2$  bin.

- In addition, an independent electron finder (EEXOTIC, [96]), which had been used in the ZEUS- $F_2$  measurement from 1993 data, has been used as a check of the neural network SINISTRA. Consistent results have been obtained in the region, where the efficiencies of both finders are reasonably high. However, the variation of  $F_2$  can be up to 20 and 16% in the low- $x$  bins of the two lowest  $Q^2$ -rows and is by far the dominating source of uncertainties in this region.
- The electron finding efficiency is varied within the errors of its determination based on the QED Compton study (section 5.4.3). The effect is negligible, apart from the low- $x$  bins, where it can be as much as 3%. Possible energy dependent variations of the trigger efficiency are also accounted for by this check.

#### Background and Hadronic Final State

- The fiducial cut on the electron position at the inner edge of the calorimeter to discard events, where the scattered electron is not fully contained in the detector, has been increased from 3 to 4 cm. This results in a 3% change in  $F_2$  for the lowest  $y$ -bins and the lowest  $Q^2$ -bins.
- The photoproduction background estimate has been changed by +100% and -50%. The effect in  $F_2$  is 2 - 6% for the low- $x$  bins and negligible in all other bins.
- As the  $\delta$ -cut also tests to some extent the simulation of particle losses in the beam-pipes, i.e. the hadronic particle flow, the contribution of diffractive scattering events to the total cross section has been increased from 9% to 15%, yielding at most a 3% effect in  $F_2$ .  
Varying the  $\delta$ -cut from 35 GeV to 32 or 38 GeV checks the estimate of photoproduction background contamination, QED radiative effects and the hadronic energy flow. It results in 3% effects on  $F_2$  at low  $x$  and low  $Q^2$ .

#### Miscellaneous

- The agreement between data and Monte Carlo in the  $z$ -vertex distribution and effects from possible discrepancies have been tested by setting all  $z$ -vertices in data and Monte Carlo to the primary interaction point,  $z = 67$  cm. The effect is  $\sim 15\%$  at high  $Q^2$  and  $< 5\%$  for all other bins except one at  $Q^2 = 1.5$  GeV<sup>2</sup>.
- The electron energy scale and photoproduction background contamination have been checked by varying the electron cut from 10 to 8 and 12 GeV. The resulting change in  $F_2$  is up to 3% at high  $y$  and negligible elsewhere.

- The tracking reconstruction in the data, which uses a slightly older version than in the Monte Carlo, has been repeated with the code used in the latter in order to obtain consistent data sets. The effect on  $F_2$  is  $\sim 3\%$ .
- Effects of possible differences in smearing and migration between data and Monte Carlo have been checked by using the Bayes unfolding. The variations of  $F_2$  can be as large as  $\sim 10\%$  in the low  $x$  bins.
- As the bin-by-bin unfolding assumes the structure function in the Monte Carlo to give a good description of the data, the sensitivity of the results to it is checked by reweighting the Monte Carlo to the GRV(94) structure function. This changes  $F_2$  by  $\sim 2\%$  in the low  $x$  bins, the other bins are stable to within  $\pm 0.5\%$ .

In this last category only the Bayes unfolding check has been included in the systematic error determination, in order not to obtain strongly correlated errors. The underlying effects are nevertheless covered by the other checks.

Figure 7.12 shows the deviation from the central  $F_2$  values in the analysed  $(x, Q^2)$  bins for the different systematic checks. The  $\pm\sigma_{stat}$  range is indicated by dashed lines, the  $\pm 15\%$  range by dotted lines. Checks resulting in a deviation of more than  $\pm\sigma_{stat}$  are labelled.

Identical checks have been performed for the SVTX analysis in  $(y, Q^2)$  bins. The final systematic errors are given in tables 13.9 and 13.10.

In addition to the above errors, there is an overall normalisation uncertainty of 3% due to the uncertainty in the trigger efficiency and the measurement of the luminosity. These errors are not included in the tables 13.9 and 13.10.

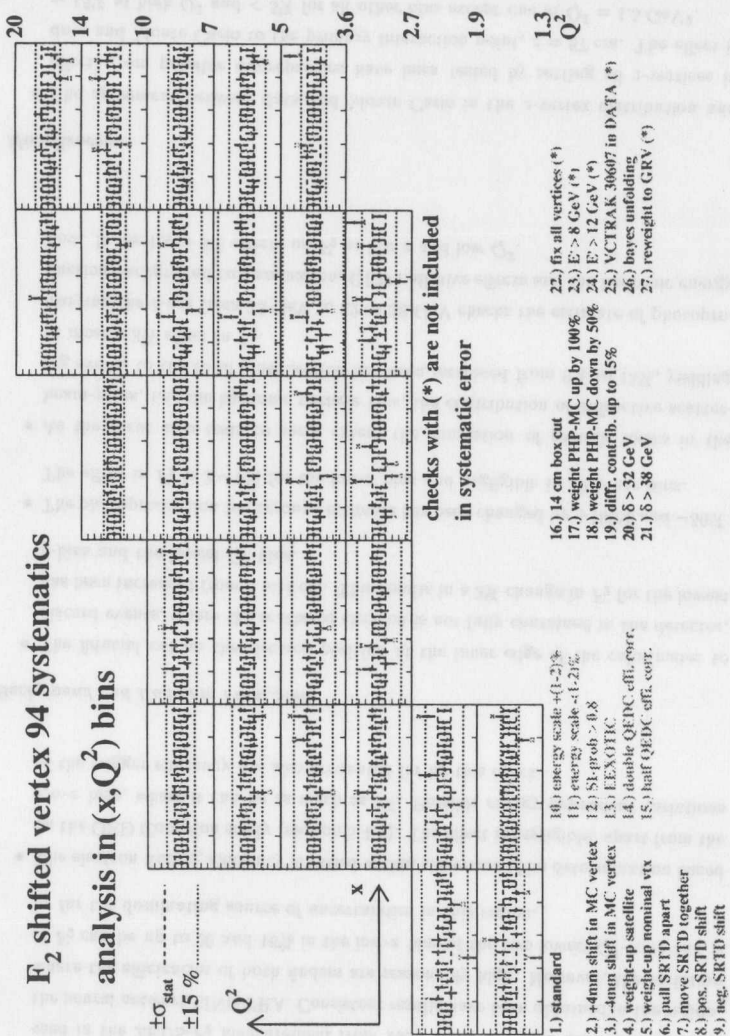


Figure 7.12: Systematic errors of the SVTX  $F_2$ , determined in  $(x, Q^2)$  bins, for several checks in different categories of systematic uncertainties. Checks yielding a deviation of more than  $\pm\sigma_{stat}$  are labelled.

7.8.3 Systematic Checks in the ISR Analysis.

In addition to the electron scattering angle and energy, the  $F_2$  results of the ISR analysis also depend on the correct simulation of the luminosity photon calorimeter. Therefore one further category of systematic checks, focussing on the impact of the photon reconstruction in the analysis, has been included.

Electron Energy and Identification

- In order to test the dependence of the  $F_2$ -results on the chosen cut on the neural network output probability, which is energy dependent in the standard analysis, this selection criterium has been replaced by the requirement

$$P_{SI} > 0.9$$

where an efficiency correction based on the QED-Compton studies has to be applied. The effect on  $F_2$  is largest in the lowest  $Q^2$  bins and even there at most 2%.

- The calorimeter energy scale is varied by a linear function (2% at 5 GeV and 1% at 27.52 GeV). At high  $y$   $F_2$  can vary by up to 15%, but the lower  $y$  bins are stable to within 2%.
- The required minimum electron energy is increased from 8 to 10 GeV, testing the bremsstrahlung simulation and the electron finding efficiency simulation. In the lowest  $Q^2$  bins  $F_2$  drops by  $\sim 10\%$ . The effect in all other bins is less than 2%.

Electron Scattering Angle

- The uncertainty of the relative and absolute position of the two SRTD-halves plays a crucial role in the ISR analysis due to the rapid cross section variations at low  $Q^2$ . The effect on  $F_2$  is estimated by shifting the two SRTD-halves by  $\pm 2$  mm in  $x$ -direction apart or together. Also positive and negative shifts of the entire SRTD by (2 mm; 1.5 mm) in  $(x, y)$  have been performed. These checks introduce a 1–4% uncertainty in  $F_2$ .
- The reconstructed  $z$ -vertex in the Monte Carlo has been shifted by  $\pm 4$  mm. The effect on  $F_2$  is less than 1% and hence negligible.
- The impact of detector alignment and the simulation of the electron energy losses in the RCAL beampipe on  $F_2$  are estimated by changing the box-cut from 13 to 14 cm. The resulting changes in  $F_2$  are typically 1–3%.

*Photon Reconstruction*

- According to the uncertainty in the lumi-photon calorimeter calibration, its scale is varied linearly (3% at 5 GeV to 0.4 % at 27.52 GeV). The effect on  $F_2$  is 5 – 15%.
- The resolutions of the reconstructed kinematic variables are also dependent on the resolution of the lumi-photon calorimeter and in particular the latter's simulation. The photon energy resolution in the Monte Carlo is degraded from  $26.5\%/\sqrt{E(\text{GeV})}$  to  $28.5\%/\sqrt{E(\text{GeV})}$ , resulting in typically 4% variations of  $F_2$ .
- The Monte Carlo description of the lumi-photon calorimeter acceptance is mainly limited by geometrical shadowing from magnets. In the Monte Carlo a contour cut, extracted from bremsstrahlung data [99], is applied on the projected generated impact point of the photon in the lumi-calorimeter. This independent determination of the geometrical acceptance of the lumi photon calorimeter has a 5 – 8% effect on  $F_2$ .
- The description of the bremsstrahlung background and the photon energy scale are tested by increasing the required minimum photon energy from 6 to 7 GeV. The effect on  $F_2$  is 3% at low  $y$  and grows to 11% at high  $y$ .

*Background and Miscellaneous*

- The  $\delta'$ -cut has been varied, testing the description of the hadronic final state and the impact of higher order corrections in the Monte Carlo. This check is also sensitive to the photoproduction background contamination of the data sample and has a negligible effect on  $F_2$ .
- The tagging efficiency and the bremsstrahlung background description are tested by dropping the requirement that the lumi electron energy be less than 3 GeV. Variations in  $F_2$  are up to 7% at high  $y$  and decrease to 3% at low  $y$ .
- In the standard analysis the Monte Carlo is reweighted to a NLO-QCD fit, obtained from the 1993 ZEUS- $F_2$  and the iterated ISR  $F_2$  data. The dependence of the structure function, represented by the Monte Carlo, is tested by reweighting it to the NLO-QCD fit to the 1994 ZEUS- $F_2$  data. The resulting  $F_2$  is stable to within  $\pm 2\%$ .
- The determination and normalisation of the bremsstrahlung background is of crucial importance as it contributes considerably to the measured number of events. A conservative estimate of the effects from potential normalisation uncertainties is obtained by varying the bremsstrahlung background by  $\pm 10\%$ . The effect on  $F_2$  is negligible at low  $y$  and at most 3% at high  $y$ .

- The dependence of the  $F_2$ -result on the Monte Carlo structure function and the simulation of resolution and migration effects is tested by using the Bayes unfolding technique. The variation in  $F_2$  can be as large as 10%, but is typically  $\sim 5\%$ .

Figure 7.13 shows the deviation from the central  $F_2$  values for the different systematic checks. The  $\pm\sigma_{stat}$  range is indicated by dashed lines, the  $\pm 15\%$  range by dotted lines. Checks resulting in deviations larger than  $\pm\sigma_{stat}$  are labelled.

The total systematic errors are listed in table 13.11. The overall normalisation uncertainty of 3% due to the uncertainty in the luminosity measurement (2.5%), the trigger efficiency (1%) and the Monte Carlo normalisation (1%) are not included in the systematic errors. The effect of additional QED radiative corrections not included in the HERACLES Monte Carlo generator is small compared to the experimental errors [100].

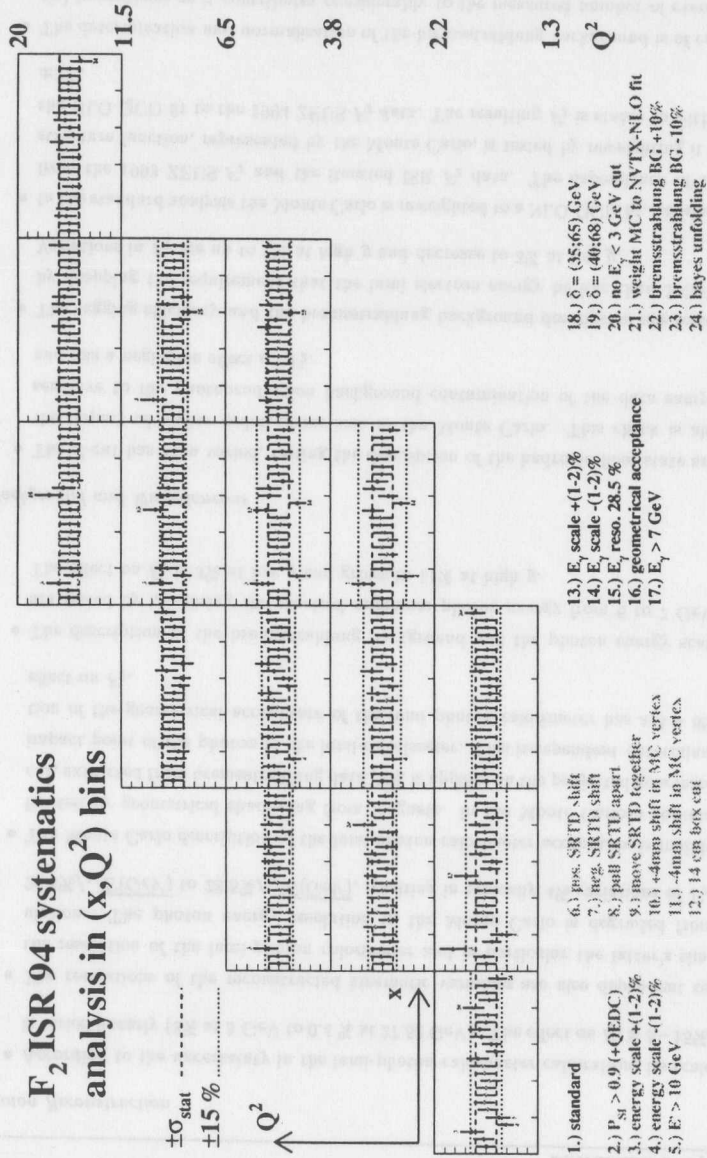


Figure 7.13: Systematic errors of the ISR  $F_2$ , determined in  $(x, Q^2)$  bins, for several checks in different categories of systematic uncertainties. Checks yielding a deviation of more than  $\pm\sigma_{stat}$  are labelled.

## Chapter 8

# Final Results on $F_2$ .

### 8.1 Introduction.

This chapter presents the results of the  $F_2$  structure function measurement. The  $F_2$  values including statistical and total systematic errors as well as bin ranges in  $x$  and  $Q^2$  or  $y$  and  $Q^2$ , the measured number of events, the estimated number of background events and the values of  $x$  and  $Q^2$ , where  $F_2$  is quoted, are listed in tables 13.1 to 13.11 for the different analyses. Not included are the overall normalisation uncertainties, resulting from the estimate of the ZEUS trigger efficiency and the luminosity measurement.

$F_2$  is plotted versus  $x$  for fixed  $Q^2$  and compared to the published ZEUS results and recent parton distribution functions separately for the three analyses. The results of the NVTX analysis are also compared to fixed target measurements from BCDMS, E665, NMC and SLAC. The scaling violations, as shown in plots of  $F_2$  versus  $Q^2$  for fixed  $x$  are also demonstrated. Finally an alternative way of looking at the data in terms of the total virtual photon-proton scattering cross section is presented.

## 8.2 Shifted Vertex $F_2$ .

The measured  $F_2$  values from the SVTX analysis are listed in tables 13.9 and 13.10. The analysis of this data set allows  $F_2$  measurements at  $Q^2$ -values as low as  $1.5 \text{ GeV}^2$  and  $x = 3.5 \cdot 10^{-5}$  and therefore significantly increases the measured kinematic region. Figure 8.1 shows  $F_2$  versus  $x$  for fixed  $Q^2$  obtained using the  $(x, Q^2)$ - (red circles) and  $(y, Q^2)$ -binning (green triangles) in comparison to the published ZEUS results [112]. The statistical errors are shown as inner error bars, the total errors, which are the quadratic sum of statistical and systematic errors, are shown as the outer error bars. Apart from the highest  $x$  points at  $Q^2 = 4.5 \text{ GeV}^2$  and  $6 \text{ GeV}^2$ , where  $F_2$  is quoted at slightly different  $x$ -values, the results of the  $(x, Q^2)$ -analysis are in very good agreement with the ZEUS measurement.

Even though statistically correlated the good agreement between the  $(x, Q^2)$ - and the  $(y, Q^2)$ -analysis serves as an independent systematic check and confirms the results obtained.

The rise of  $F_2$  towards low  $x$ , as first reported in [108, 114] and confirmed in [109, 115] is observed to persist down to  $Q^2 = 1.5 \text{ GeV}^2$ . However, the slope of this rise decreases with decreasing  $Q^2$  as expected, since  $F_2$  has to vanish at  $Q^2 \simeq 0$ .

The measured  $F_2$  values are compared to the predictions of GRV(94) [102] which are based on perturbative QCD using the DGLAP evolution equations. This model, starting the evolution at a scale  $Q_0^2 = 0.34 \text{ GeV}^2$  with valence-like spectra for the gluon and sea distributions, describes the changing rise of the data well, even down to the lowest  $x$  and lowest  $Q^2$  point. But the GRV prediction generally tends to overshoot the data slightly, in particular the low- $x$  points.

In contrast to this the parametrisation of Donnachie and Landshoff [103] is the extrapolation of a fit to  $Q^2 \simeq 0$  and hadron scattering data and inspired by Regge phenomenology. This model is clearly ruled out for  $Q^2 \geq 2 \text{ GeV}^2$  and disfavoured at  $Q^2 = 1.5 \text{ GeV}^2$ .

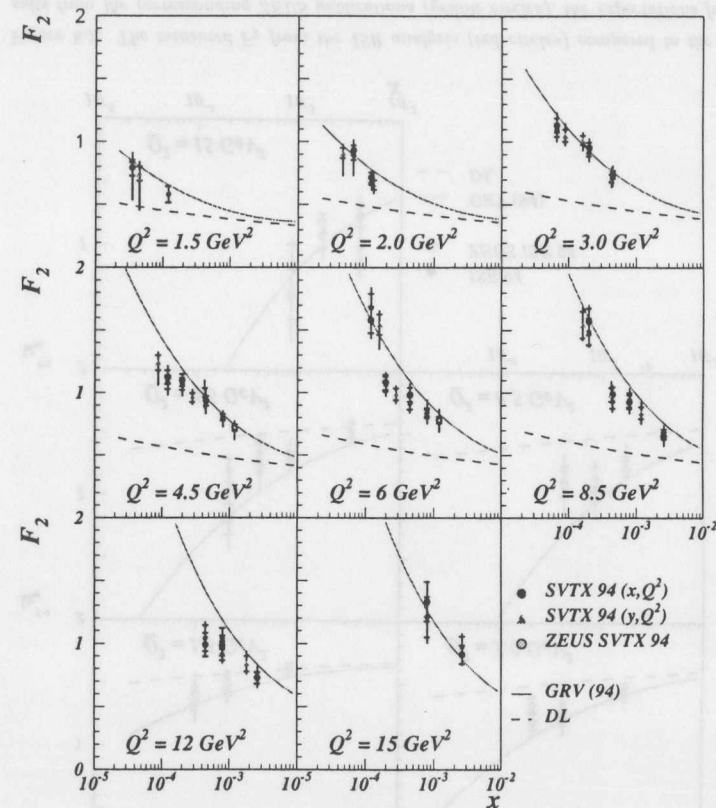


Figure 8.1: The measured  $F_2$  from the SVTX analysis in  $(x, Q^2)$  bins (red circles) and in  $(y, Q^2)$  bins (green triangles) compared to the results from the corresponding ZEUS publications (yellow circles), the expectations from GRV(94) (steep red line) and Donnachie and Landshoff (DL - flat black line). An overall normalisation uncertainty of 3% is not shown.

### 8.3 Initial State Radiation- $F_2$ .

The  $F_2$  results from the ISR analysis are listed in table 13.11. Figure 8.2 shows the ISR measurement in comparison to the ZEUS publication [112] versus  $x$  for fixed  $Q^2$ . The inner error bars show the statistical errors and the outer the total errors. The two measurements are in good agreement. Only at  $Q^2$  of 3.0 and 4.5  $\text{GeV}^2$  a discrepancy shows up, but the points are nevertheless consistent within errors.

The ISR  $F_2$  also shows the rise towards low- $x$  down to  $Q^2 = 1.5 \text{ GeV}^2$ . Due to the effective reduction in the centre of mass energy the ISR analysis reaches to higher  $x$  than the SVTX analysis, hence providing a complementary measurement to the latter. However, due to the limited statistics, which also implies a limited control over the systematic effects, the errors of the ISR  $F_2$  are slightly larger than in the SVTX analysis. This fact results in a reduced power of discrimination between the different models. Nevertheless comparison with the curves shows that the Donnachie-Landshoff parametrisation is excluded at  $Q^2 \geq 3 \text{ GeV}^2$  while the GRV prediction describes the overall behaviour of  $F_2$  rather well. As mentioned before, however, GRV tends to overshoot the data slightly. Due to the size of the errors at low  $x$  the ISR  $F_2$  measurement does not allow any discrimination between the two models at  $Q^2 \leq 3.0 \text{ GeV}^2$  as it is spanned by them and consistent with both.

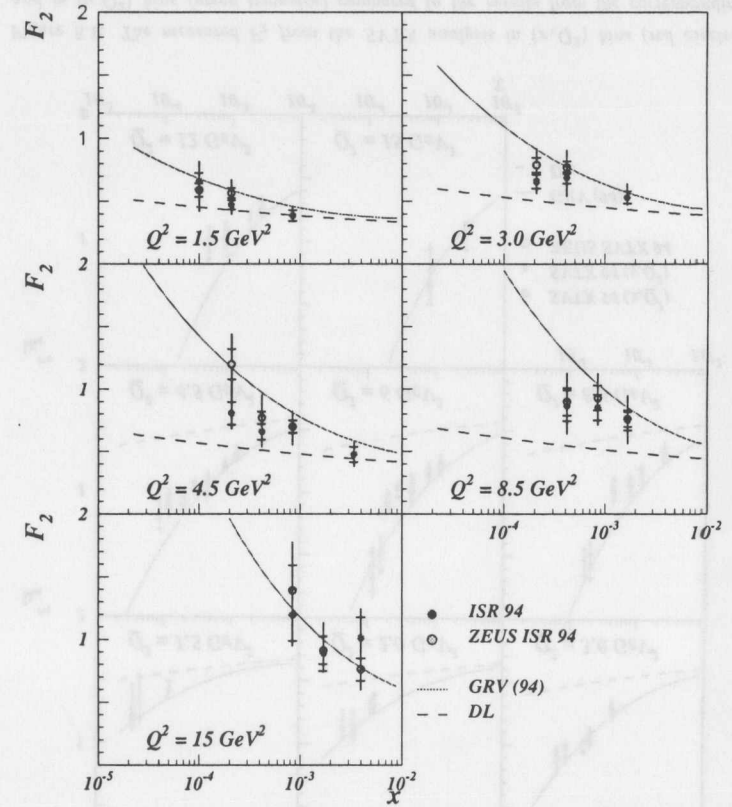


Figure 8.2: The measured  $F_2$  from the ISR analysis (red circles) compared to the results from the corresponding ZEUS publications (yellow circles), the expectations from GRV(94) (steep red line) and Donnachie and Landshoff (DL - flat black line). An overall normalisation uncertainty of 3% is not shown.

### 8.4 Nominal Vertex $F_2$ .

The results of the NVTX analyses, using the  $p_T$ - or the  $EL$ -reconstruction methods are listed in tables 13.1 to 13.8. Figures 8.3 to 8.5 show the results from both measurements versus  $x$  for fixed  $Q^2$ . The rise of  $F_2$  towards low  $x$  has been measured with much increased precision. Both analyses are in very good agreement. But the  $EL$ -analysis covers a smaller  $(x, Q^2)$ -range and yields larger errors. Nevertheless this systematic check provides confidence in the  $p_T$ -results.

At  $Q^2 > 100 \text{ GeV}^2$  the errors can be seen to be dominated by the event statistics, also resulting in larger fluctuations than observed in the low- $Q^2$  region. Despite the very large event statistics some  $F_2$ -points at low  $y$  deviate by one or more  $\sigma$  of the total error from the curve, which is well determined by the precise fixed target data in this region. These effects play an important role in QCD-analyses of the  $F_2$  data, the corresponding extraction of the gluon momentum density and phenomenological fits, as will be shown in chapter 10.

The ZEUS NLO QCD-fit, used for the reweighting of the Monte Carlo in the extraction of correction factors, describes the data very well down to  $Q^2$  as low as  $3.5 \text{ GeV}^2$ , providing strong confidence in the applied efficiency and acceptance corrections and the entire unfolding procedure (see also section 7.6).

Figures 8.6 and show 8.7 show the NVTX  $F_2$  from  $Q^2 = 3.5 \text{ GeV}^2$  to  $1200 \text{ GeV}^2$  in comparison to the corresponding data from the ZEUS publication [110] and the 1993 ZEUS data [109]. As can be seen the covered  $x$ -range has been extended between 1993 and 1994 to high  $x$ , while the improved  $Q^2$ -resolution and increased statistics allowed a finer binning in  $Q^2$ . Due to the installation of the detector component, SRTD, the reach of the NVTX data to low  $Q^2$  has been extended from  $8.5 \text{ GeV}^2$  to  $3.5 \text{ GeV}^2$ . In addition the total errors could be typically reduced by a factor of 2–3 compared to the 1993 data.

Apart from a few fluctuating points the agreement between data from the NVTX analysis and the ZEUS publication is very good over the entire  $(x, Q^2)$  plane. This is particularly pleasing as all major aspects of the analyses, such as energy corrections etc., have been done independently, sometimes using alternative methods.

The NVTX  $F_2$  is displayed in figures 8.8 and 8.9 together with the fixed target data from BCDMS [128], NMC [129], E665 [130] and SLAC [131]. Several structure function parametrisations are shown for comparison. The fixed target data has been interpolated to the displayed  $Q^2$ -values using the combined fit of NMC given in [132]. Thanks to the  $p_T$ -method the extension of the covered kinematic range towards low  $y$  provides an overlap between the NVTX and the fixed target data in several  $Q^2$ -bins. Filling the gap between the fixed target and the HERA range is particularly important as a direct check on the relative normalisation of the fixed target and collider experiments. This is of further relevance as the normalisation uncertainty was found to play an important

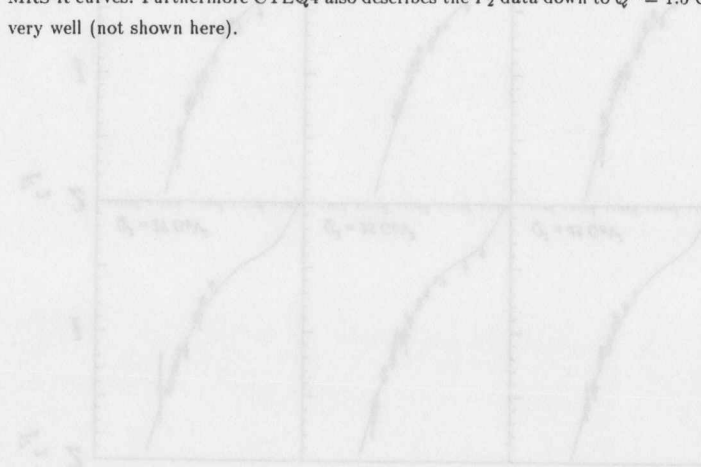
role [118, 123] between experiments in the extraction of the gluon density from 1993 ZEUS data. In the overlap region the NVTX and fixed target data can be seen to yield reasonable agreement (see also figure 8.10).

The depicted structure function parametrisations of the MRS- [137] and the CTEQ-groups [138] include preliminary or final 1994  $F_2$ -data from ZEUS [110, 112] and H1 [116].

The GRV(94) prediction describes the data very well for  $Q^2 \geq 70 \text{ GeV}^2$ . But at lower  $Q^2$  it tends to overshoot the data, in particular at low  $x$ . Nevertheless the general characteristics, i.e. the shape of  $F_2$ , are also adequately described in this region, indicating that perturbative QCD using conventional DGLAP evolution equations can describe the current data and its low- $x$  dynamics very well.

The MRS-R2 parametrisation fits the data very well in the entire NVTX region and provides a good overall picture of the proton structure. It tends to be slightly lower than the data below  $Q^2$  of  $3 \text{ GeV}^2$ . This effect is discussed further in chapter 10.

The CTEQ4 parametrisation describes the NVTX data in shape and normalisation very well all the way down to  $Q^2 = 3.5 \text{ GeV}^2$  and is essentially indistinguishable from the MRS-R curves. Furthermore CTEQ4 also describes the  $F_2$  data down to  $Q^2 = 1.5 \text{ GeV}^2$  very well (not shown here).



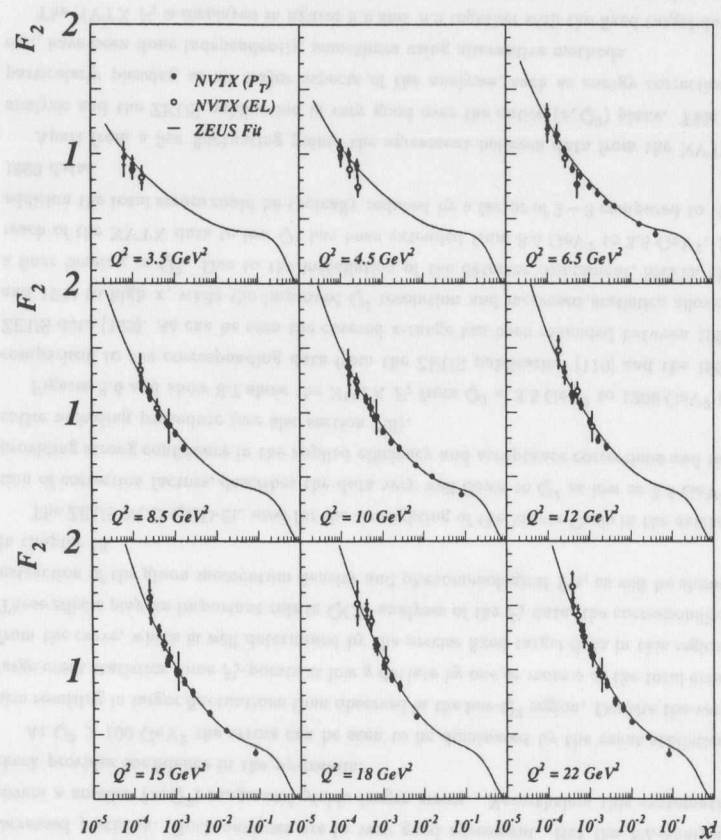


Figure 8.3: The  $F_2$  from the NVTX analysis in  $(x, Q^2)$  bins using the  $p_T$ - (full circles) or the EL-reconstruction method (open circles). The structure function of the Monte Carlo, which has been used for acceptance corrections, is shown as solid line.

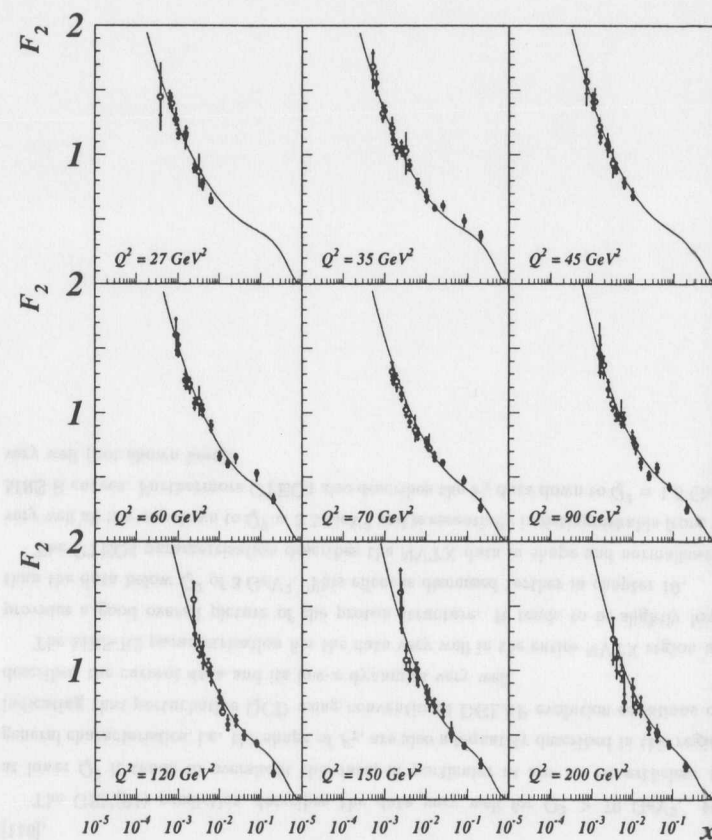


Figure 8.4: The  $F_2$  from the NVTX analysis in  $(x, Q^2)$  bins using the  $p_T$ - (full circles) or the EL-reconstruction method (open circles). The structure function of the Monte Carlo, which has been used for acceptance corrections, is shown as solid line.

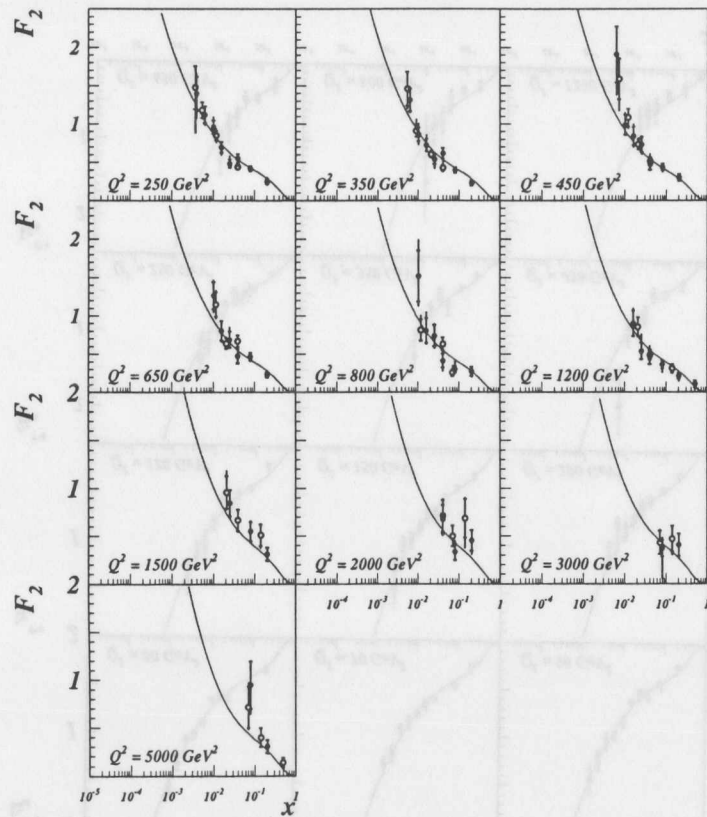


Figure 8.5: The  $F_2$  from the NVTX analysis in  $(x, Q^2)$  bins using the  $p_T$ - (full circles) or the EL-reconstruction method (open circles). The structure function of the Monte Carlo, which has been used for acceptance corrections, is shown as solid line.

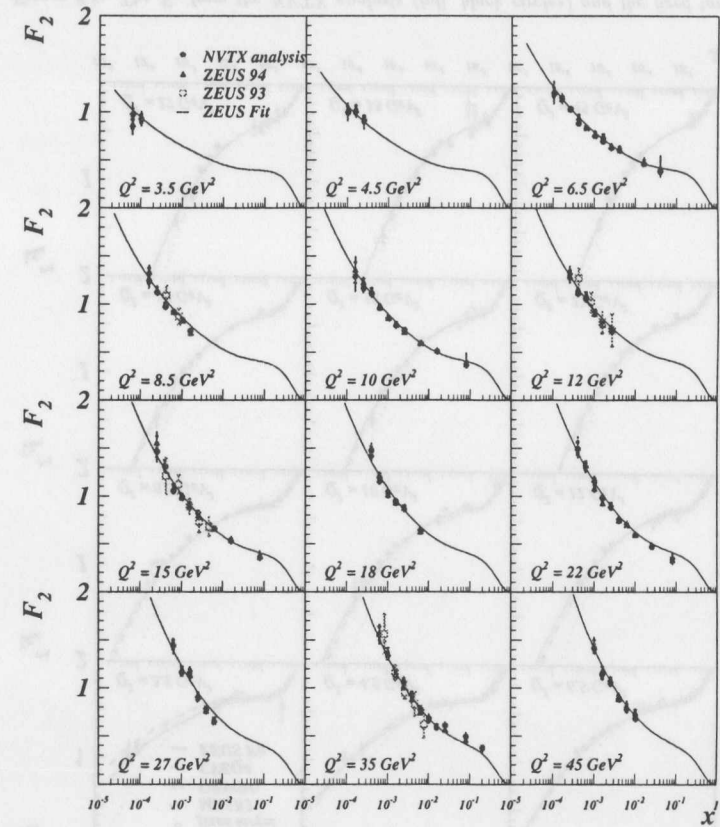


Figure 8.6: The  $F_2$  from the NVTX analysis (red circles) in comparison to the corresponding ZEUS publication from 94 data (black triangles) and the 93 ZEUS- $F_2$  (green rectangles). For the extraction of acceptance corrections the Monte Carlo has been reweighted to the solid blue line, representing an early ZEUS NLO-QCD fit.

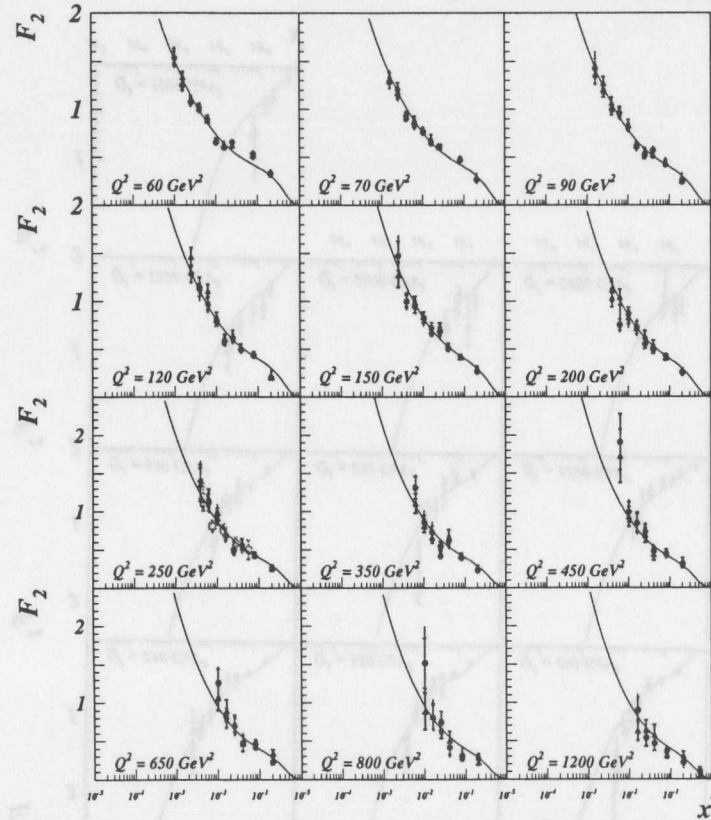


Figure 8.7: The  $F_2$  from the NVTX analysis (red circles) in comparison to the corresponding ZEUS publication from 94 data (black triangles) and the 93 ZEUS- $F_2$  (green rectangles). For the extraction of acceptance corrections the Monte Carlo has been reweighted to the solid blue line, representing an early ZEUS NLO-QCD fit.

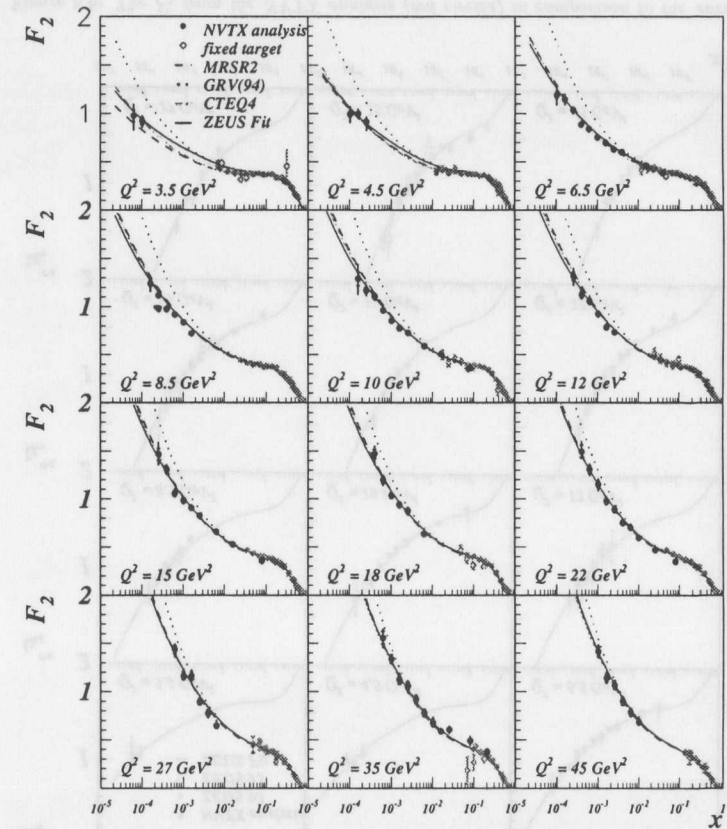


Figure 8.8: The  $F_2$  from the NVTX analysis (full, black circles) and the fixed target data from BCDMS, NMC, E665 and SLAC (open green circles) in comparison to several structure function parametrisations.

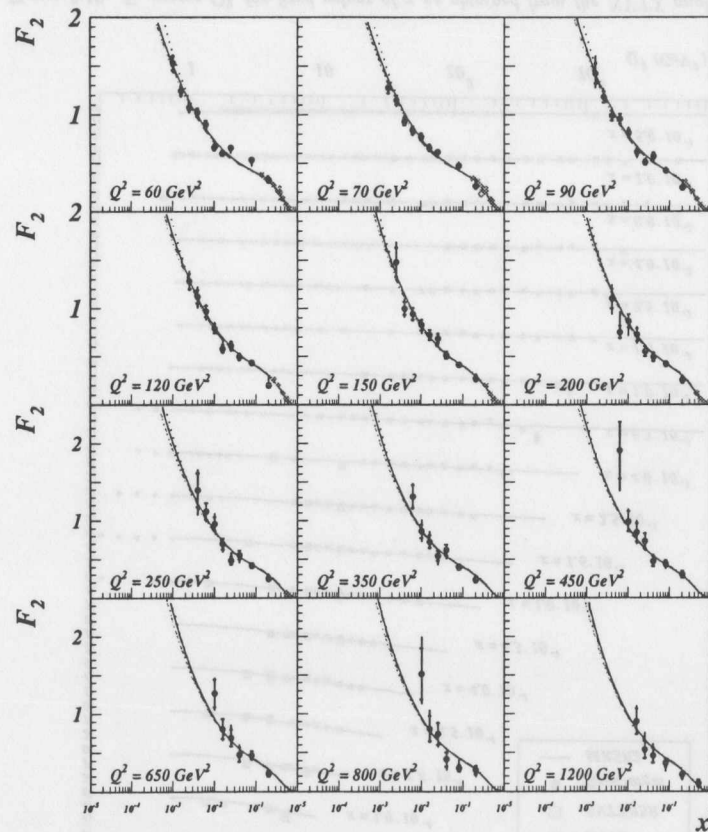


Figure 8.9: The  $F_2$  from the NVTX analysis (full, black circles) and the fixed target data from BCDMS, NMC, E665 and SLAC (open green circles) in comparison to several structure function parametrisations.

### 8.5 Scaling Behaviour.

The scaling of the proton structure function  $F_2$ , i.e. the independence of  $Q^2$ , is valid only in the naive Quark-Parton Model. In QCD, the quark densities in the proton and hence also the proton structure functions, evolve with  $Q^2$ , as a result of the gluon bremsstrahlung from quarks and gluons and the quark pair production from gluons.

Figure 8.10 shows the  $F_2$  versus  $Q^2$  for fixed  $x$  as obtained in the NVTX analysis (red rectangles) and earlier measurements at fixed target experiments (green circles). For comparison the proton structure function parametrisation MRS-R2 is also depicted. The scaling of  $F_2$  can be clearly seen at  $x = 0.2$ , where it was initially found at SLAC. However, towards lower  $x$  the scaling violation due to the increasing importance of the gluon and its rising density in the proton becomes more and more apparent.

At medium and high  $x$  the good agreement between the fixed target data and the ZEUS data can be seen in the overlap region, indicating the small size of normalisation uncertainties.

The evolution of the parton densities and hence  $F_2$  in  $Q^2$  will be used in chapter 10 to extract the gluon density in the proton.

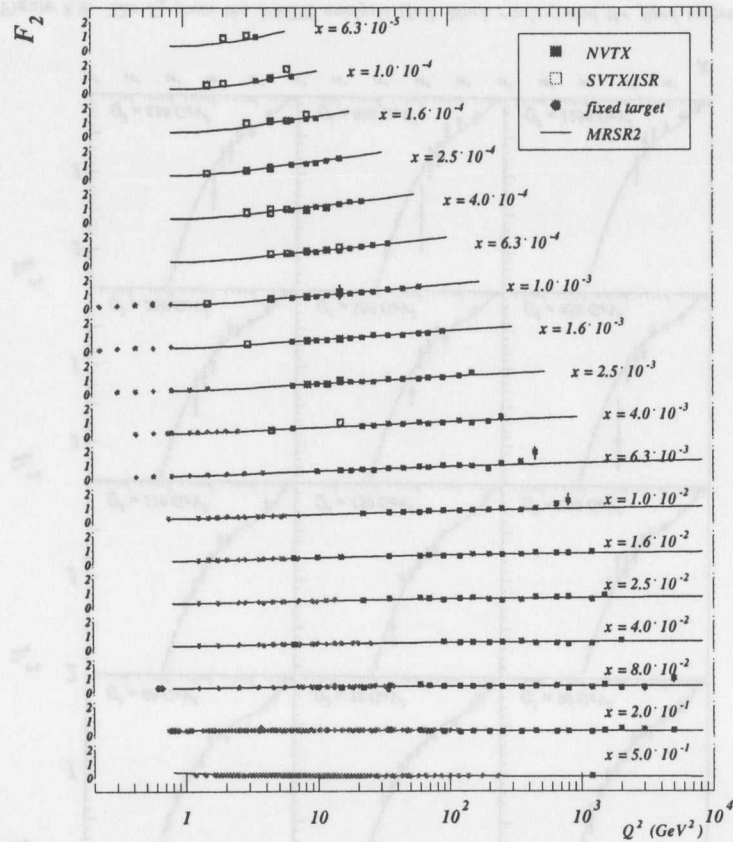


Figure 8.10:  $F_2$  versus  $Q^2$  for fixed values of  $x$  as obtained from the NVTX analysis (red full rectangles), the SVTX and ISR analysis (red open rectangles) and the fixed target experiments (green circles). The exhibited scaling behaviour of  $F_2$  at  $x = 0.2$  is contrasted by scaling violations at low  $x$ , where the rising gluon density dominates the evolution.

## 8.6 Total Cross Section.

The persistent rise of  $F_2$  at low  $x$  for small  $Q^2$  indicates that the photoproduction-like regime has not yet been reached. A different way of looking at the data emphasizing this fact is to express the DIS cross section as the product of the flux of virtual photons and the total cross section  $\sigma_{tot}^{\gamma^*p}$  for the scattering of virtual photons on protons [140].  $\sigma_{tot}^{\gamma^*p}$  is defined in terms of the cross section for the absorption of transverse and longitudinal photons,  $\sigma_T$  and  $\sigma_L$  respectively, by

$$\sigma_{tot}^{\gamma^*p} = \sigma_T(x, Q^2) + \sigma_L(x, Q^2) \quad (8.1)$$

The expression for  $F_2$  in terms of  $\sigma_T$  and  $\sigma_L$  is

$$F_2(x, Q^2) = \frac{Q^2(1-x)}{4\pi^2\alpha} \frac{Q^2}{Q^2 + 4M_p^2x^2} [\sigma_T(x, Q^2) + \sigma_L(x, Q^2)] \quad (8.2)$$

where  $M_p$  is the mass of the proton. The separation into the photon flux and cross section can be interpreted in a way similar to the interaction of real particles provided that the lifetime of the virtual photon is large compared to the interaction time, or  $x \ll 1/(2M_p R_p)$  where  $R_p \approx 4 \text{ GeV}^{-1}$  is the proton radius (see appendix 12). At small  $x$  the expression can be written in terms of the total virtual photon-proton centre of mass energy  $W$  with  $W^2 = M_p^2 + Q^2(1-x)/x \approx Q^2/x$

$$\sigma_{tot}^{\gamma^*p}(W^2, Q^2) \approx \frac{4\pi^2\alpha}{Q^2} F_2(x, Q^2) \quad \text{for } x \ll 1/(2M_p R_p) \quad (8.3)$$

The measured  $F_2$  data from the present analyses are converted to the total virtual photon-proton cross section and displayed in figure 8.11 for  $Q^2 \leq 120 \text{ GeV}^2$  along with low energy data and real photoproduction cross section measurements [142, 143]. In order to guide the eye the recent parametrisation by ALLM [139] is shown.

The steep rise of  $F_2$  at low- $x$  for fixed  $Q^2$  is now seen as the rise in  $\sigma_{tot}^{\gamma^*p}$  with  $W^2$  even at  $Q^2$ -values as low as  $1.5 \text{ GeV}^2$  in contrast to the cross section for real photons, which exhibits only a slow rise similar to that seen in hadron-hadron total cross sections.

The slope of the rise of  $F_2$  at low  $x$ , or alternatively of  $\sigma_{tot}^{\gamma^*p}$  at high  $W^2$  is expected to increase with  $Q^2$  in perturbative QCD. The NVTX, SVTX and ISR data are fitted to the functional form  $F_2(x, Q^2) = a(Q^2) + b(Q^2) \cdot x^{-\lambda(Q^2)}$  in every  $Q^2$  bin<sup>1</sup> and  $x < 0.02$ , in order to quantify the  $Q^2$ -dependence of the slope. A fit of the form  $F_2 \sim \ln \frac{1}{x}$  is also performed and discussed further in section 9.2. In the fit the statistical and systematic errors have been added in quadrature.

Figure 8.12 shows the result. The measure of the  $F_2$  slope with  $x$ ,  $\lambda(Q^2)$ , is indeed found to increase with  $Q^2$ . With the current precision the rise of  $\lambda$  with  $Q^2$  is consistent with a logarithmic rise. The full line indicates the best fit of the form

$$\lambda = a_0 + a_1 \cdot \log_{10}(Q^2)$$

<sup>1</sup>This is done in order to quantify the rise even though the rise itself is expected to be slower than any power of  $\frac{1}{x}$  and faster than any power of  $\ln \frac{1}{x}$

For total cross sections in hadron-hadron scattering and real photoproduction the value of  $\lambda$  has been determined to be  $\approx 0.08$  [104]. Therefore the  $Q^2$ -dependence of  $\lambda(Q^2)$  at  $Q^2 \lesssim 1 \text{ GeV}^2$  is expected to be weaker than logarithmic.

Despite the extension of the accessible kinematic range to low- $Q^2$ , the exact extend of the transition region from photoproduction-like behaviour to behaviour described by perturbative QCD cannot be determined from the 1994 ZEUS data, presented here, alone. However, in order to study this transition region in more detail ZEUS has installed a beam-pipe calorimeter (BPC) in 1995<sup>2</sup> which covers the range  $0.1 \text{ GeV}^2 \leq Q^2 \leq 0.65 \text{ GeV}^2$ . Preliminary results have been shown in [126, 127].

Using the shifted vertex data sets from 1995  $F_2$  can be measured in the region  $0.4 \lesssim Q^2 \lesssim 3 \text{ GeV}^2$ . Preliminary results of these measurements have been shown in [111, 117].

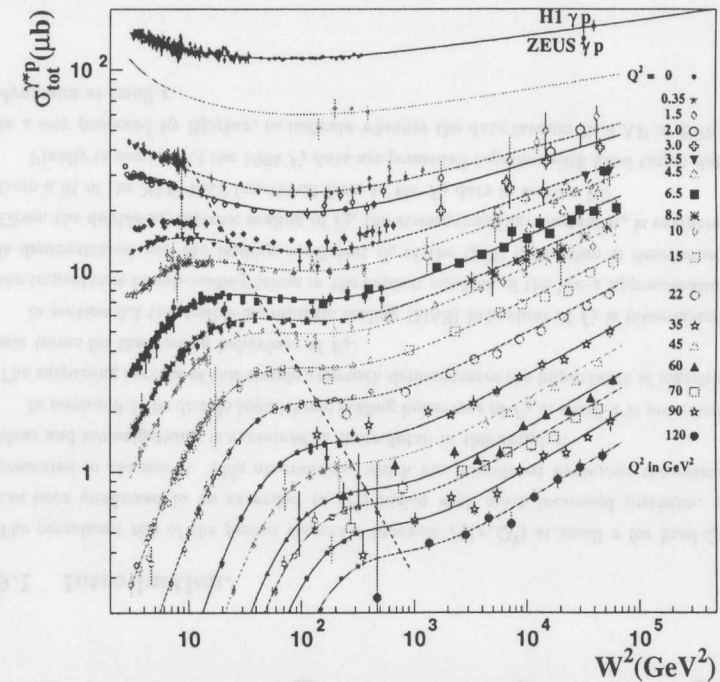
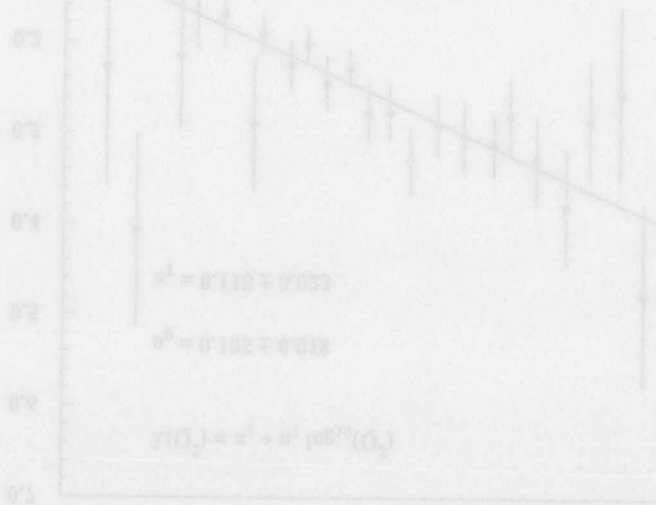


Figure 8.11: The total virtual photon-proton cross section versus  $Q^2$  for different  $Q^2$  values. The cross section values obtained from the  $F_2$  values of the analyses described in this thesis (big symbols) are shown in addition to data from fixed target experiments (small symbols). The region to the right of the dashed line corresponds to  $x < 1/(2 \cdot M_p \cdot R_p)$ . Also shown is the  $Q^2$  behaviour of the measured cross section for real photoproduction. The solid lines correspond to a recent parametrisation by ALLM.

<sup>2</sup>Studies were done with a prototype in 1994 [125].

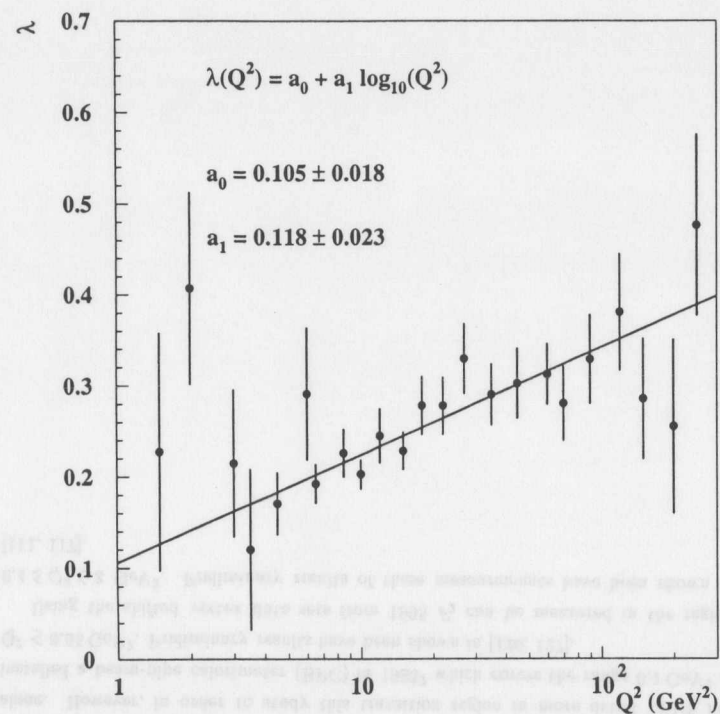


Figure 8.12:  $Q^2$ -dependence of the exponent  $\lambda(Q^2)$  as obtained in fits for the form  $F_2 \sim x^{-\lambda(Q^2)}$  at fixed  $Q^2$  and  $x < 0.02$ .

## Chapter 9

# Phenomenological Analysis of $F_2$ .

### 9.1 Introduction.

The prominent rise of the proton structure function  $F_2(x, Q^2)$  at small  $x$  for fixed  $Q^2$  has been confirmed in an extended  $(x, Q^2)$  region with much increased precision, as presented in chapter 8. This observation, which has stimulated numerous theoretical ideas and investigations, is examined in more detail in this chapter.

In section 9.2 the double-logarithmic scaling behaviour of  $F_2$  at small- $x$  is presented. The surprising success of this simple approach demonstrates the importance of logarithmic terms for the leading behaviour of  $F_2$ .

In section 9.3 the double-asymptotic scaling (DAS) behaviour of  $F_2$  is investigated, the importance of sub-leading terms in the explicit solution of the low- $x$  approximation is demonstrated and the leading coefficient  $\beta_0$  of the QCD  $\beta$ -function is determined. Given the double-asymptotic scaling of  $F_2$ , the strong coupling constant  $\alpha_s$  is extracted from a fit of the NLO-DAS functional form to the  $F_2$  data in section 9.3.

Finally in section 9.4 the 1994  $F_2$  data are presented together with fixed target data in a way proposed by Bjorken, to indicate whether the data favours DGLAP or BFKL dynamics at small  $x$ .

## 9.2 Double-Logarithmic Scaling.

### 9.2.1 The Scaling of the $F_2$ Data.

The rise of  $F_2$  versus  $Q^2$  for fixed  $x$  and versus  $x$  for fixed  $Q^2$  is shown in the top plots of figure 9.1 for the three  $F_2$  measurements at three example values of  $x$  and  $Q^2$  respectively. The  $Q^2$ -dependence of  $F_2$  exhibits a logarithmic behaviour. The slope of this rise vanishes at  $x \approx 0.08$  and increases with decreasing  $x$ . Also the  $x$ -dependence of  $F_2$  shows a logarithmic rise, where the slope increases with  $Q^2$ .

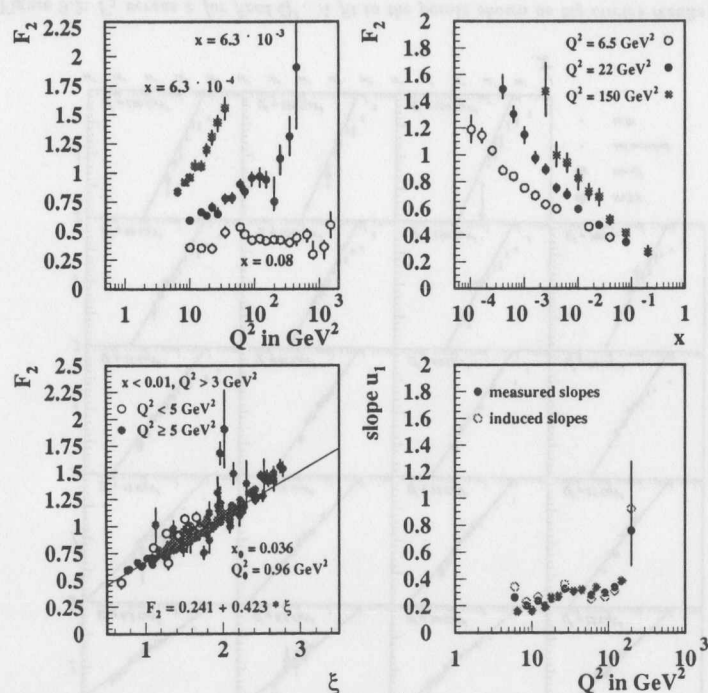


Figure 9.1:  $F_2$  exhibits a logarithmic rise in  $Q^2$  for fixed  $x$  (top left) and in  $x$  for fixed  $Q^2$ . The suggested double logarithmic scaling is shown as a linear rise of  $F_2$  versus the scaling variable  $\xi$  (bottom left). The good agreement in the direct and the induced measurement of the  $x$ -slope can be seen in the bottom right plot.

As the rise in  $F_2$  is the main focus of this study, only the limited phase space

$$x < 10^{-2}; \quad Q^2 > 5 \text{ GeV}^2$$

is considered.

The following considerations have been proposed in [145].

The observed rise of  $F_2$  in  $x$  for fixed  $Q^2$  is reflected in the fact that the data can be well described by the function

$$F_2(x, Q^2) = u_0(Q^2) + u_1(Q^2) \cdot \log \frac{v(Q^2)}{x} \quad (9.1)$$

Given the current precision of the data higher order terms in  $\log \frac{1}{x}$  are not necessary to obtain a good fit to the data. The offset  $u_0$  and the slope  $u_1$  as well as  $v$ , which is defined as the weighted average ( $\ln \frac{1}{x}$ ) and reflects the available  $x$ -range for a given  $Q^2$ , are functions of  $Q^2$  and represent the functional form of  $F_2$ .

The data exhibits a linear rise in  $\log Q^2$  and  $\log \frac{1}{x}$ . As the extrapolation of this rise to lower  $Q^2$  or larger  $x$  suggests the existence of a common fix point  $(x_0, Q_0^2)$  the following ansatz is made

$$F_2(x, Q^2) = a + m \cdot \xi \quad (9.2)$$

with the double-logarithmic scaling variable

$$\xi = \log \frac{Q^2}{Q_0^2} \cdot \log \frac{x_0}{x} \quad (9.3)$$

The comparison of this form with equation 9.1 for  $x = x_0$  and  $x = v(Q^2)$  yields

$$u_1(Q^2) = \frac{u_0(Q^2) - a}{\log(\frac{x_0}{v(Q^2)})} \quad (9.4)$$

This relation allows the comparison of the direct measured slope  $u_1$  in equation 9.1 with the induced one (equation 9.4) in the scaling approach.

110 out of 231  $F_2$  points from the three measurements lie in the considered phase space region. A fit to the function, given in equation 9.2, yields

$$\chi^2 = 336.10/110 \quad \text{using statistical errors only}$$

$$\chi^2 = 100.77/110 \quad \text{using statistical } \oplus \text{ systematic errors}$$

The symbol  $\oplus$  indicates the quadratic sum of the two error contributions.

The resulting parameters are

$$a = 0.241 \pm 0.030$$

$$m = 0.423 \pm 0.023$$

$$x_0 = 0.036 \pm 0.005$$

$$Q_0^2 = 0.960 \pm 0.130$$

The good quality of the fit can be seen from the  $\chi^2$ , and is also depicted in the bottom left plot of figure 9.1. The scaling behaviour of  $F_2$  in  $\xi$  is clearly established. It also gives a good description of the data at lower  $Q^2$  down to  $3 \text{ GeV}^2$ . In the bottom

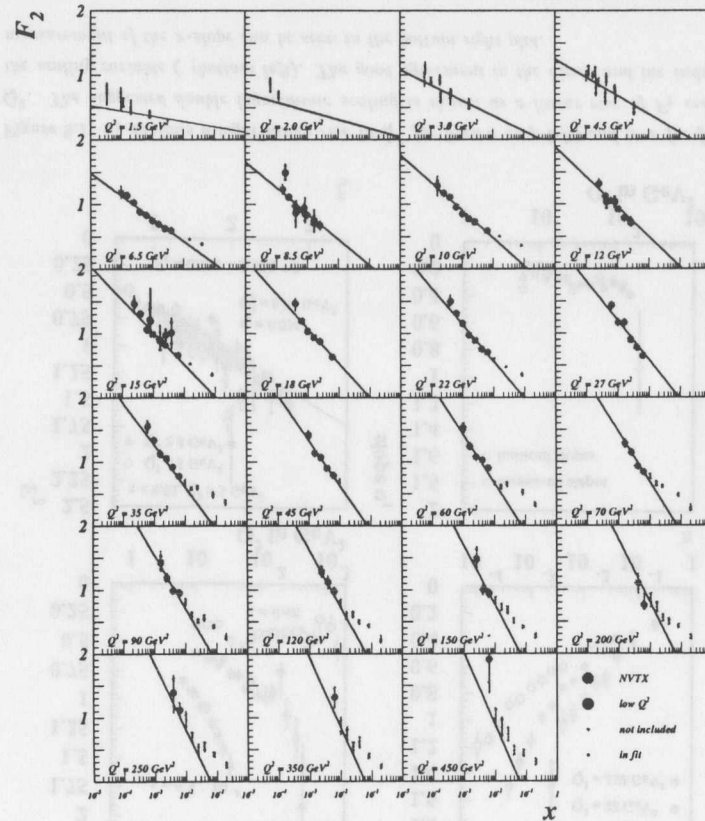


Figure 9.2:  $F_2$  versus  $x$  for fixed  $Q^2$ . A fit to the points shown as big circles results in the double-logarithmic scaling description, shown as full line. The low- $Q^2$  and high- $x$  points (small symbols) are not included in the fit.

right plot of figure 9.1 the directly measured slope  $u_1$  is compared to the induced one. Good agreement between the two determinations is found, confirming that equation 9.1 and 9.2 provide a consistent picture. The scaling behaviour of  $F_2$  is shown in the more familiar way versus  $x$  for fixed  $Q^2$  in figure 9.2. Given the simplicity of the approach the double-logarithmic scaling behaviour of  $F_2$  is surprisingly well established and provides a good picture of the proton structure at low  $x$ .

### 9.2.2 Interpretation and Unitarity Constraints.

The success of the simple double logarithmic scaling approach raises the question whether it can be understood in terms of physics and what its implications are.

Unitarity places a limit on the total proton-proton cross section at large energies, known as the Froissart bound [146]

$$\sigma_{tot}^{pp} \leq \frac{\pi}{m_\pi^2} \left( \ln \frac{s}{s_0} \right)^2 \quad (9.5)$$

where  $m_\pi$  is the pion mass,  $s$  is the centre of mass energy squared and  $s_0$  is some constant. However, since the numerical value of  $s_0$  is not known the practical use of equation 9.5 is limited as for every cross section behaviour, measured in a restricted energy range, a value  $s_0$  can always be found such that the equation 9.5 is satisfied. Nevertheless, at asymptotically large energies,  $s \rightarrow \infty$ , the Froissart bound limits the growth of the parton densities, and hence, the growth of  $F_2$  at small  $x$ . As discussed in [145, 37] the elastic gluon-gluon scattering cross section  $\Delta\sigma_{gg}$  provides the dominant contribution to the perturbative part of  $\sigma_{tot}$  and must clearly also satisfy the Froissart bound. If the gluon density at fixed  $Q^2$  rises such that

$$x \cdot g(x, Q^2) \leq B \cdot \ln \frac{1}{x} \quad (9.6)$$

where  $B$  is a constant, the resulting cross section  $\Delta\sigma_{gg}$  rises with the centre of mass energy square,  $s$ , such that  $\Delta\sigma_{gg} \lesssim \left( \ln \frac{Q^2}{x} \right)^2 \sim (\ln s)^2$ . Thus, this rise does not violate the Froissart bound but could saturate it if the gluon density equalled the bound in equation 9.6.

Such a behaviour of the gluon density at small  $x$  is given by the following contribution to  $F_2$  via the photon-gluon fusion process (BGF) [147]

$$\Delta F_2^{qg} = A + \frac{\alpha_s}{3\pi} \sum_q e_q^2 B \ln \frac{Q^2}{Q_0^2} \ln \frac{x_0}{x} \quad (9.7)$$

where  $A$  is a constant and the sum is carried out over all quarks with masses small compared to  $Q$ . The BGF process gives the dominant contribution to  $F_2$  at low  $x$  via the strongly rising gluon density. This is reflected in the good description of the data by the double-logarithmic scaling approach (equation 9.2) which has been chosen to exhibit the same functional form as the BGF term (equation 9.7). A continuing good description of the rise in  $F_2$  towards asymptotically small  $x$  by the double-logarithmic scaling would therefore indicate a saturation of equation 9.6 by the gluon density, resulting, in turn, in a saturation of the Froissart bound.

Based on a calculation by Gribov [148]  $F_2$  is found to behave [149] like

$$F_2 \propto Q^2 \ln \frac{1}{x} \quad (9.8)$$

This result not only implies strong scaling violations but also saturation of the condition 9.6 by the gluon density.

However, in order to investigate further whether the rise of  $F_2(x, Q^2)$  is adequately described by a functional form  $\sim \ln \frac{1}{x}$ , which saturates the unitarity bound, or if the data prefer a stronger rise like  $x^{-\lambda}$ , which would violate unitarity asymptotically, or to see whether the rise in  $F_2$  becomes 'softened' by gluon recombination and screening effects, measurements with much increased precision or at lower values of  $x$  will be necessary.

### 9.3 Double-Asymptotic Scaling.

#### 9.3.1 Introduction.

The behaviour of the proton structure function at small  $x$  is related to the singularities of the operator product expansion matrix elements. As a consequence of this relation there are two specific predictions of NLO QCD as embedded in the DGLAP equations. These predictions depend on whether the above mentioned singularities lie to the left or the right of those of the anomalous dimensions<sup>1</sup>.

- One of these predictions has been considered and incorporated into parametrisations and fits to HERA data in [28]. If at a given starting scale  $Q_0^2$ , sufficiently large for perturbative QCD to be valid, structure functions behave like a power of  $x$  for  $x \rightarrow 0$

$$F_i(x, Q_0^2) = f_i(Q_0^2) x^{-\lambda_i(Q_0^2)} + \mathcal{O}(x^{-\mu_i}), \quad \mu_i < \lambda_i(Q_0^2)$$

for  $i = S, G$ , then this behaviour is preserved by the evolution to all larger  $Q^2$  so that

$$F_i(x, Q^2) \stackrel{x \rightarrow 0}{\sim} f_i(Q^2) x^{-\lambda_i} \quad \text{for all } Q^2 \geq Q_0^2$$

Separating the proton structure function  $F_2$  into a singlet and a non-singlet contribution,  $F_2 = F_S + F_{NS}$ , the small  $x$  behaviour is at leading order dominated by the singlet term which is predicted to be

$$F_2(x, Q^2) = B_S \cdot [\alpha_s(Q^2)]^{d_+(1+\lambda)} \cdot x^{-\lambda}$$

with the free parameters  $B_S$ ,  $\Lambda_{QCD}$  and  $\lambda$ ;  $d_+$  is a function of  $\lambda$ . The parameter  $\lambda$  depends on the starting scale  $Q_0^2$ . However, it does not have a direct *perturbative* dependence on  $Q^2$ . However,  $\lambda$  might indirectly depend on  $Q^2$  via the number of excited flavours. The non-singlet contribution to  $F_2$  was also parametrised and sub-dominant terms included. This was found to be important when fitting data in the increased  $Q^2$  range and the improved precision attainable in 1994 HERA runs. This more sophisticated approach, extended to next to leading order, has been shown to give a good fit to the data [29]. The dominant term has been found to behave like  $x^{-\lambda}$  with  $\lambda_s \sim 0.34 \pm 0.03$  independent of  $Q^2$ .

- The other prediction is based on the assumption that at a low starting scale  $Q_0^2$ , which might be close to the non perturbative regime, the singlet and gluon distributions are soft, i.e.

$$F_i(x, Q_0^2) \sim \mathcal{O}(x^0)$$

<sup>1</sup>Under a transformation from  $x$  space to moment space the splitting functions, which describe the gluon radiation or splitting and hence the QCD evolution, transform into terms called anomalous dimensions.

for  $i = S, G$ . Already in 1974 DeRújula et al. [150] found that under these conditions perturbative QCD predicts a universal growth in the structure function at large  $Q^2$  and small  $x$ , faster than any power of  $\ln \frac{1}{x}$  and slower than any power of  $\frac{1}{x}$ . This result, which is a consequence of QCD being an asymptotically free field theory, has been revived recently by Ball and Forte [151] in the investigation of double asymptotic scaling.

In the following the second prediction and its implications are studied in more detail. This choice should not be interpreted as a prejudice against the first prediction. At present it cannot be decided which of the two alternatives is valid on the basis of perturbative QCD alone. This has to be investigated in comparison to the data.

### 9.3.2 The Leading-Order Case.

Taking the low  $x$  approximation of the splitting function the leading-order Altarelli-Parisi evolution equations [160] can be written as a two-dimensional wave equation which propagates the gluon distribution from its boundaries into the asymptotic region.

Defining the two scaling variables

$$\sigma = \sqrt{\ln \frac{x_0}{x} \ln \frac{t}{t_0}}, \quad \rho = \sqrt{\ln \frac{x_0}{x} / \ln \frac{t}{t_0}} \quad (9.9)$$

with  $t = \ln \frac{Q^2}{\Lambda^2}$  and  $x_0$  and  $Q_0^2$  as starting values explicit solutions of the gluon density  $G(\sigma, \rho) = xg(x, Q^2)$  in the limit  $\sigma \rightarrow \infty$  are found. Apart from subasymptotic correction factors the asymptotic growth of the gluon distribution drives a similar growth of the structure function  $F_2$ :

$$F_2^p(\sigma, \rho) \sim N f\left(\frac{\gamma}{\rho}\right) \frac{\gamma}{\rho} \frac{1}{\sqrt{\gamma\sigma}} \exp\left[2\gamma\sigma - \delta \cdot \left(\frac{\sigma}{\rho}\right)\right] \quad (9.10)$$

where  $\gamma = 2\sqrt{N_c/\beta_0}$ , the leading coefficient  $\beta_0$  of the QCD  $\beta$ -function  $\beta_0 = \frac{11}{3}N_c - \frac{2}{3}n_f$ ,  $\delta = (1 + \frac{2n_f}{11N_c})/(1 - \frac{2n_f}{11N_c})$  and the function  $f(\frac{\gamma}{\rho})$ , which depends on the details of the starting distribution and tends to unity for sufficiently large  $\rho$ . Provided the small- $x$  behaviour of the starting distribution of the gluon at  $t_0$  is sufficiently soft  $G(\sigma, \rho)$  increases exponentially with  $\sigma$  for fixed  $\rho$  and is independent of  $\rho$  for fixed  $\sigma$ .

In order to compare the  $F_2$  data with the correspondingly expected behaviour for  $F_2(\sigma, \rho)$  the rescaling function

$$R'_F(\sigma, \rho) = R \cdot \exp\left[\delta \cdot \left(\frac{\sigma}{\rho}\right) + \frac{1}{2} \ln \sigma + \ln \frac{\rho}{\gamma}\right] \quad (9.11)$$

is defined, where  $R$  is an arbitrary normalisation factor. Then  $\ln(R'_F \cdot F_2)$  is predicted to rise linearly with  $\sigma$ , independently of  $\rho$  (in order to reduce the dependence of the function  $f$  the cut  $\rho^2 \geq 2$  is imposed). The slope of the rise is given by

$$2\gamma = \frac{12}{\sqrt{33 - 6n_f/N_c}} = 2.4$$

for  $N_c = 3$  colours and  $n_f = 4$  flavours. Except for the initial assumption that the input distributions are soft this slope is a parameter-free prediction of perturbative QCD.

Defining the rescaling function

$$R_F(\sigma, \rho) = R'_F \cdot \exp[-2\gamma\sigma] \quad (9.12)$$

the leading behaviour in 9.10 is removed completely, so that  $R_F \cdot F_2 = \text{constant}$ ,  $R_F \cdot F_2$  exhibits scaling in both  $\sigma$  and  $\rho$  (double asymptotic scaling 'DAS').

However, if the initial assumption on a flat input gluon distribution is not satisfied the predictions change drastically and no universal scaling can be found. The slope of  $\ln(R'_F \cdot F_2)$  would not be constant but rise with  $\rho$  and  $\ln(R_F \cdot F_2)$  would not scale with  $\rho$  and  $\sigma$  but would rise with  $\rho$  and, strongly vary with  $\sigma$ .

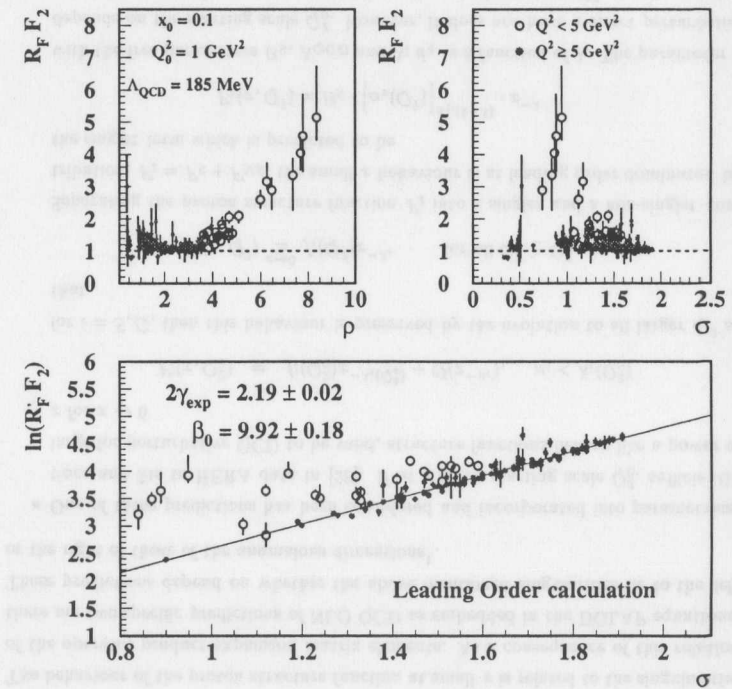


Figure 9.3: The double asymptotic scaling of  $R_F \cdot F_2$  versus  $\rho$  and  $\sigma$  in leading order is shown in the top plots.  $R'_F \cdot F_2$  exhibits an exponential rise with  $\sigma$  and slope  $2\gamma$  (bottom plot).

Figure 9.3 shows  $R_F \cdot F_2$  versus  $\rho$  and  $\sigma$  for all three  $F_2$  measurements. The values  $x_0 = 0.1$  and  $Q_0^2 = 1 \text{ GeV}^2$  are chosen according to the initial suggestion in [151]. For

data with  $Q^2 \geq 5 \text{ GeV}^2$ , shown as full circles, the double asymptotic scaling behaviour for a soft gluon input is found to be a dominant feature of the data. However, large scaling violations are found for the low  $Q^2$  points, indicating the importance of higher order terms in this region and the short evolution path for DAS. The slope of  $\ln(R_F \cdot F_2)$  from a fit to data with  $Q^2 \geq 5 \text{ GeV}^2$  and  $x < x_0 < 0.1$ , is  $2\gamma_{exp} = 2.19 \pm 0.02$ , which is slightly smaller than the expected value,  $2\gamma_{QCD} = 2.4$ .

The good quality of the fit is reflected in the  $\chi^2$ :

$$\begin{aligned}\chi^2 &= 468/94 && \text{for statistical errors only} \\ \chi^2 &= 117/94 && \text{for statistical } \oplus \text{ systematic errors}\end{aligned}$$

Despite the slight deviation from the QCD prediction in  $2\gamma$  the double asymptotic scaling behaviour of  $F_2$  has been established. Assuming a soft gluon input at a low starting scale  $Q_0^2$  and using the Altarelli-Parisi evolution equation in perturbative QCD the explicit functional form of the double asymptotic scaling approach provides a very economical description of the data. Only three parameters  $x_0$ ,  $Q_0^2$  and  $\Lambda_{QCD}$  have to be given or fitted.

### 9.3.3 The Next-to-Leading-Order Case.

With the increased precision of the 1994  $F_2$  data it becomes apparent that leading order DAS does not describe the data perfectly as scaling violations are observed (figure 9.3). Therefore the DAS formalism has been extended to a two-loop calculation which has been presented by Ball and Forte in [152]. The scaling variables are now defined as

$$\begin{aligned}\sigma &= \sqrt{\xi\zeta}, & \rho &= \sqrt{\xi/\zeta} \\ \text{with } \xi &= \ln \frac{x_0}{x}, & \zeta &= \ln \left( \frac{\alpha_s(t_0)}{\alpha_s(t)} \right)\end{aligned}$$

Where  $\alpha_s$  is calculated at second order. In leading order  $\zeta$  reduces to  $\ln \left( \frac{t}{t_0} \right)$ .

The structure function  $F_2$  takes the asymptotic form

$$F_2^p \sim \frac{5 n_f \gamma}{162 \rho} \frac{1}{\sqrt{4\pi\gamma\sigma}} \exp \left[ 2\gamma\sigma - \delta_+ \cdot \left( \frac{\sigma}{\gamma} \right) \right] \cdot \left[ 1 - \left( \epsilon_+ (\alpha_s(t_0) - \alpha_s(t)) - \frac{9 \epsilon_-}{n_f \gamma^2} \alpha_s(t) \right) \frac{\rho}{\gamma} \right] \quad (9.13)$$

with

$$\begin{aligned}\delta_+ &= \frac{11 + \frac{2n_f}{27}}{\beta_0}, & \epsilon_+ &= \left( \frac{103}{27} n_f + 3 \frac{\beta_1}{\beta_0} \right) / \pi \beta_0 \\ \gamma &= \sqrt{\frac{12}{\beta_0}}, & \epsilon_- &= \frac{26 n_f}{3\pi\beta_0}\end{aligned}$$

The rescaling functions also receive small corrections:

$$\begin{aligned}R_F^{(2)}(\sigma, \rho) &= R_F(\sigma, \rho) \cdot \left[ 1 - \alpha_s(t_0) \left( \epsilon_- \left( \epsilon_+ + \frac{9 \epsilon_-}{n_f \gamma^2} \right) \right) e^{-\sigma/\rho} \right]^{-1} \\ R_F^{(2)'}(\sigma, \rho) &= R_F^{(2)}(\sigma, \rho) \cdot \exp[2\gamma\sigma]\end{aligned}$$

The top plots of figure 9.4 show  $R_F \cdot F_2$  versus  $\rho$  and  $\sigma$  in NLO. The double asymptotic scaling behaviour is clearly established. But in contrast to the leading order case the scaling in next-to-leading order works even down to  $Q^2$  as low as  $1.5 \text{ GeV}^2$ . Including higher order terms obviously reduces the subasymptotic region. The straight line fit to  $\ln(R_F \cdot F_2)$  versus  $\sigma$  has been done for  $5 < Q^2 < 35 \text{ GeV}^2$  and  $Q^2 > 35 \text{ GeV}^2$  separately, as the number of active flavours is 4 and 5 respectively. Also a cut on  $x < x_0$  has been imposed.  $\Lambda_{QCD}^{(n_f=4)}$  is fixed to 263 MeV while  $x_0$  and  $Q_0^2$  are free parameters. Points included in the fit are shown as full circles, other points are shown as open circles or rectangles for completeness.

In the region of  $n_f = 4$  the fit yields

$$\begin{aligned}\chi^2 &= 158/56 && \text{for statistical errors only} \\ \chi^2 &= 46/58 && \text{for statistical } \oplus \text{ systematic errors}\end{aligned}$$

and the slope

$$2\gamma_{exp} = 2.39 \pm 0.07$$

which is in very good agreement with the value  $2\gamma_{QCD} = 2.4$ , that is expected from QCD. Therefore the measured value of the leading coefficient  $\beta_0$  of the QCD  $\beta$ -function,  $\beta_{0,exp} = 8.35 \pm 0.48$ , is also in very good agreement with the QCD prediction  $\beta_{0,QCD} = 8.33$ .

In the region  $n_f = 5$  a similar picture is observed, although fewer points are available, which in addition span a smaller range in  $\sigma$ . The values of  $x_0$  and  $Q_0^2$  are very close to the ones for  $n_f = 4$ . The fit yields

$$\begin{aligned}\text{no convergence} &&& \text{for statistical errors only} \\ \chi^2 &= 13/18 && \text{for statistical } \oplus \text{ systematic errors}\end{aligned}$$

and the slope

$$2\gamma_{exp} = 2.48 \pm 0.13$$

while QCD predicts a value of  $2\gamma_{QCD} = 2.50$ . These results imply  $\beta_{0,exp} = 7.79 \pm 0.81$  while  $\beta_{0,QCD} = 7.67$  is expected from QCD. Again very good agreement between the measurement and the QCD prediction is obtained. However, the relatively large experimental error, which reflects the small  $\sigma$ -range covered, does not allow a precise test of  $\beta_0^{(n_f=5)}$ . Nevertheless the double asymptotic scaling behaviour of  $F_2$  has been confirmed in next-to-leading order and the measurements of  $\beta_0$  are in very good agreement with the parameter-free QCD prediction.

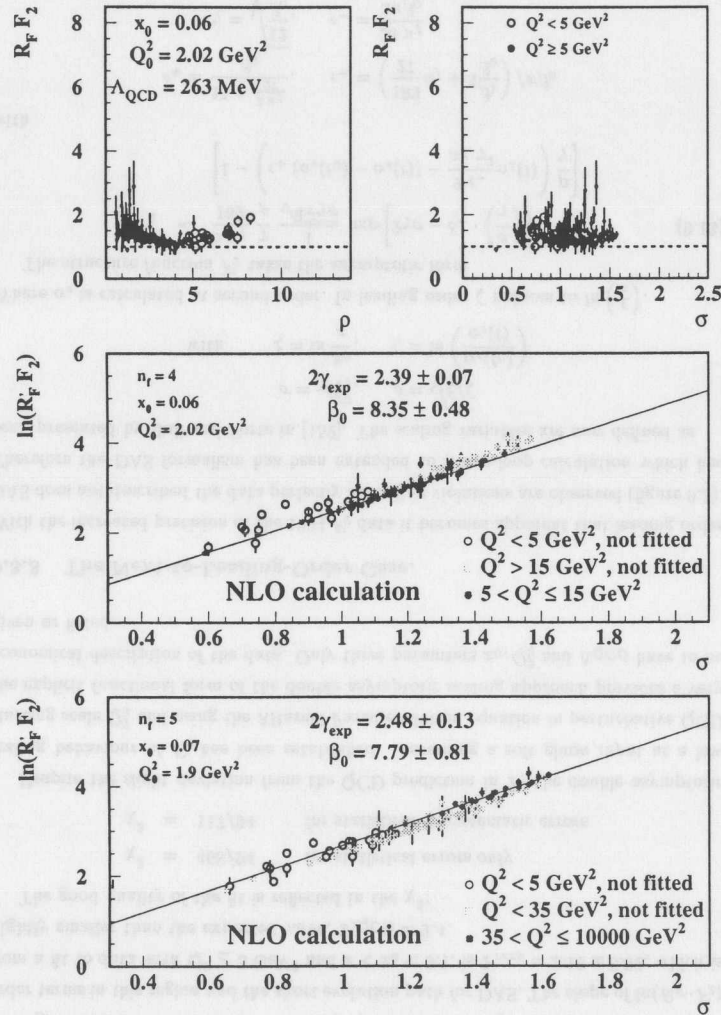


Figure 9.4: The double asymptotic scaling of  $R_F \cdot F_2$  versus  $\rho$  and  $\sigma$  in next-to-leading order is shown in the top plots.  $R_F \cdot F_2$  exhibits an exponential rise with  $\sigma$  and slope  $2\gamma$  for 4 (middle plot) as well as 5 active flavours (bottom plot). Points included in the fit are shown as full circles, others points as open circles or open rectangles.

### 9.3.4 $\alpha_s$ -Extraction from $F_2$ using NLO-DAS.

The observation that the  $F_2$  data exhibit double-asymptotic scaling and the functional form of  $F_2$  at small  $x$ , predicted by next-to-leading order perturbative QCD, describes the data well implies that the assumption of a soft input gluon distribution at the starting scale  $Q_0^2$  is consistent with the data.

The rise in  $F_2$  at small  $x$  is mainly driven by the three gluon vertex, which is proportional to the strong coupling constant  $\alpha_s$  and the gluon density. As DAS has been shown to work reasonably well, the working assumption of a soft gluon distribution at  $Q_0^2$  is made. Hence it should be possible to measure  $\alpha_s$  using the HERA low  $x$   $F_2$  data, as stated in [153, 152].

This approach has been followed by fitting the functional form 9.13 to the  $F_2$  data. The free parameters in the fit are the starting scales  $x_0$  and  $Q_0^2$ , a normalisation factor  $b$  and  $\Lambda_{\overline{MS}}^{(n_f=4)}$  in the  $\overline{MS}$  renormalisation scheme.  $\alpha_s$  is calculated iteratively in NLO, ensuring the continuity of  $\alpha_s$  at the quark mass thresholds as done in NLO evolution programs by the MRS group and R.K. Ellis [106, 107]. Details of this procedure are described in section 10.2.5.

The perturbative and asymptotic region in phase space is defined by the requirements

$$Q_{\min}^2 = 5 \text{ GeV}^2, \quad x < \min(x_0, 0.1) \\ \xi \cdot \zeta > 2$$

In the fit the quadratic sum of statistical and systematic errors is used. The central fit gives

$$b = 3.511 \pm 0.08 \\ x_0 = 0.127 \pm 0.009 \\ Q_0^2 = 2.150 \pm 0.170 \\ \Lambda_{\overline{MS}}^{(n_f=4)} = 278 \pm 29 \text{ MeV} \\ \text{with } \chi^2 = 252/177.$$

where  $b$  is the normalisation constant in equation 9.13.

Figure 9.5 shows the resulting running coupling  $\alpha_s$  as a function of  $Q^2$ . The central fit is shown as full line, the error band, originating from the experimental errors in  $F_2$ , as dashed lines.

Figure 9.6 shows the resulting fit to  $F_2$  together with the measured data points. The low- $Q^2$  measurements from the SVTX and the ISR analyses are depicted as open circles, the NVTX analysis as full circles. The fit gives a good description of the data in the  $Q^2$ -range from 6 – 5000  $\text{GeV}^2$ . However, the onset of a slight undershooting of the low- $x$  points at  $Q^2 = 6 \text{ GeV}^2$  becomes more drastic at  $Q^2$  of 4.5 or 3  $\text{GeV}^2$ . In this region higher order terms clearly need to be included in the calculations. Below  $Q^2 = 2.15 \text{ GeV}^2$  no curve can be shown as this is the starting scale  $Q_0^2$ .

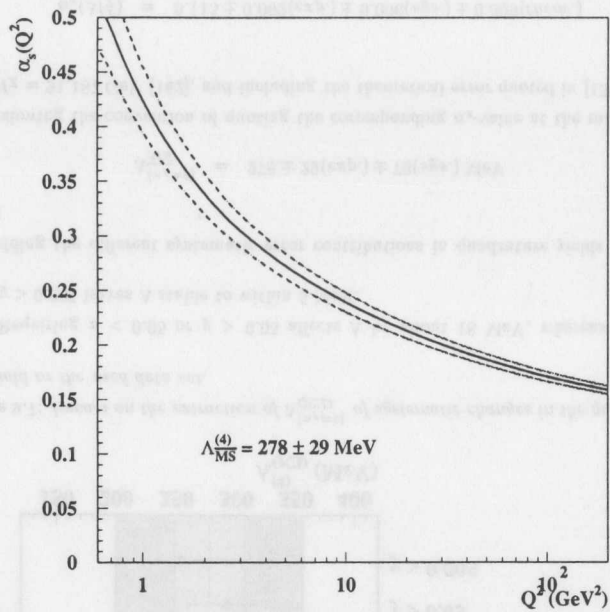


Figure 9.5: The running strong coupling  $\alpha_s$  as a function of  $Q^2$ . The full line shows the coupling corresponding to the central  $\Lambda$  value obtained in the NLO DAS-fit, the dashed lines indicate the uncertainty from the experimental errors on  $F_2$ .

From figure 9.6 it can also be seen that the somewhat large  $\chi^2$  is dominated by a few points at low  $y$  and  $Q^2$  of 35, 60 and 70  $\text{GeV}^2$ . Removing these points from the data set by the requirement  $y > 0.05$  yields

$$\chi^2 = 182/146$$

where the obtained  $\Lambda_{\overline{MS}}^{(n_f=4)} = 293 \pm 33 \text{ MeV}$  is in good agreement with the central value.

Only considering statistical errors yields  $\delta\Lambda_{stat} = 16 \text{ MeV}$ , while  $\delta\Lambda_{exp} = 29 \text{ MeV}$  includes all experimental effects on the  $F_2$  measurement. However, in order to estimate the systematic error on  $\Lambda_{\overline{MS}}^{(4)}$  the sensitivity of the fit to the selection of the data set and parameters of the fitting procedure, such as quark mass thresholds, have to be taken into account. The following systematic checks on the fitting procedure have been performed (see figure 9.7):

- The mass of the  $b$ -quark, which enters in the threshold treatment of  $\alpha_s$ , has been varied from 4.74  $\text{GeV}$  to 4.2 and 5.0  $\text{GeV}$ . The average effect on  $\Lambda$  is about 10  $\text{MeV}$ .

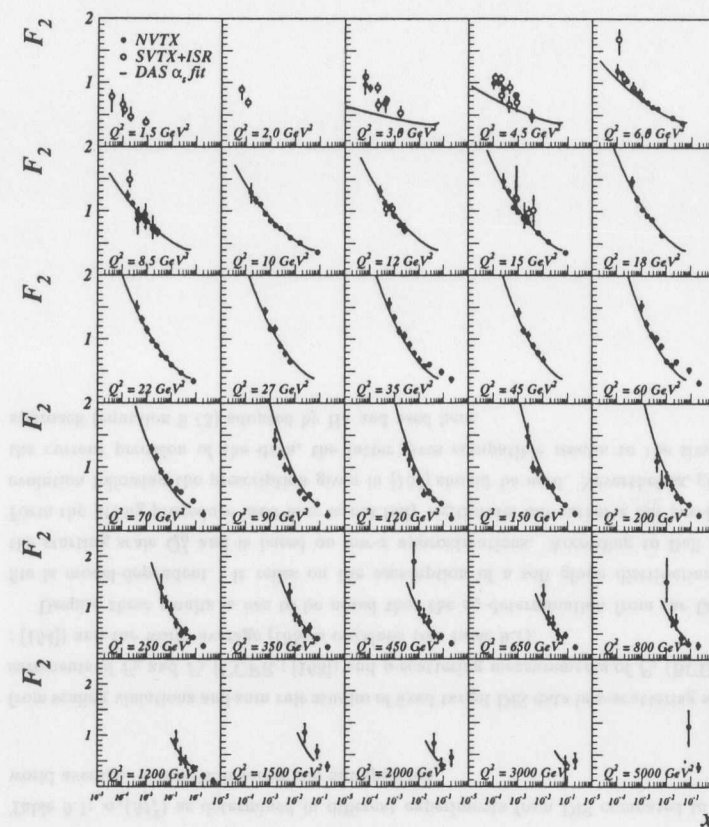


Figure 9.6:  $F_2$  versus  $x$  for fixed  $Q^2$  together with the DAS- $\alpha_s$  fit. The NVTX data are shown as full circles, the low- $Q^2$  data as open circles.

- The  $Q^2$ -range has been restricted to  $5 < Q^2 < 120 \text{ GeV}^2$  and  $x < 0.5 x_0$  has been required. The average deviation from the central  $\Lambda$ -value is 28  $\text{MeV}$ .
- Varying the minimum  $Q^2$  in the data set from 5 to 4 or 7  $\text{GeV}^2$  results in  $\Lambda$ -variations of  $\pm 70 \text{ MeV}$ . This behaviour is not surprising as deviations of the central fit to the data have been observed to show up in the low- $Q^2$  region. But this region is expected to dominate  $\alpha_s$  determinations as the  $\log(Q^2)$  terms vary most rapidly there. Also the precision of the present  $F_2$  data is highest around  $Q^2 \simeq 6 \text{ GeV}^2$ .

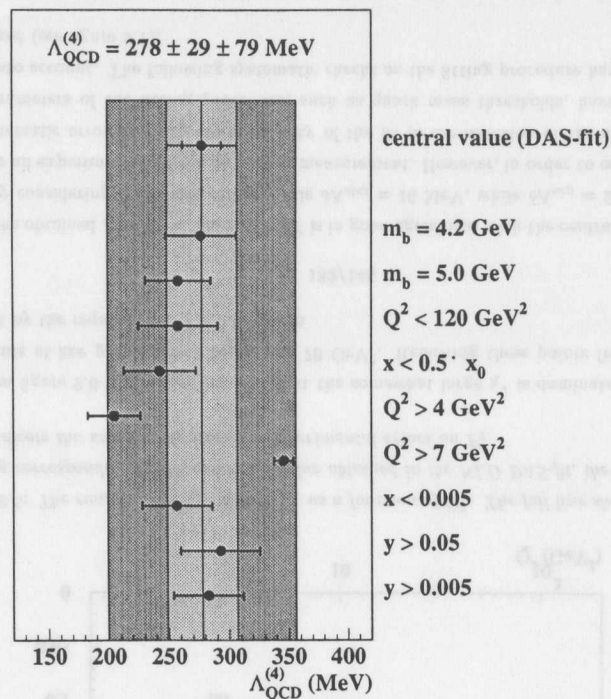


Figure 9.7: Impact on the extraction of  $\Lambda_{\text{QCD}}^{(n_f=4)}$  of systematic changes in the quark mass threshold or the used data set.

- Requiring  $x < 0.05$  or  $y > 0.05$  affects  $\Lambda$  by about 18 MeV, whereas a cut of  $y > 0.005$  leaves  $\Lambda$  stable to within 5 MeV.

Adding the different systematic error contributions in quadrature yields the final result

$$\Lambda_{\overline{MS}}^{(n_f=4)} = 278 \pm 29(\text{exp.}) \pm 79(\text{sys.}) \text{ MeV} \quad (9.14)$$

Following the convention of quoting the corresponding  $\alpha_s$ -value at the mass of the  $Z^0$ ,  $M_Z = 91.187 \text{ GeV}$  [162], and including the theoretical error quoted in [153] results in

$$\alpha_s(M_Z^2) = 0.115 \pm 0.002(\text{exp.}) \pm 0.006(\text{sys.}) \pm 0.009(\text{theor.}) \quad (9.15)$$

This result is in good agreement with the  $\alpha_s$ -extraction from DAS fits to H1 data [166],  $\alpha_s(M_Z^2) = 0.113 \pm 0.002(\text{stat}) \pm 0.007(\text{sys.})$ . Also good agreement with the  $\alpha_s$ -value

determination	$\alpha_s(M_Z^2)$
DAS fit	$0.115 \pm 0.007$
BCDMS	$0.113 \pm 0.005$
CCFR <sup>2</sup>	$0.111 \pm 0.006$
Ball-Forte	$0.122 \pm 0.004$
world average	$0.118 \pm 0.006$

Table 9.1:  $\alpha_s(M_Z^2)$  as determined in different experiments from DIS compared to the world average. Theoretical errors are not specified.

from scaling violations and sum rule studies of fixed target DIS data in  $\nu$ -scattering measurements of  $F_2$  and  $F_3$  (CCFR : [163]) and  $\mu$ -scattering measurements of  $F_2$  (BCDMS : [164]) and the world average [165] is obtained (see table 9.1).

Despite these results it has to be noted that the  $\alpha_s$ -determination from the DAS-fits is model-dependent. It relies on the assumption of a soft gluon distribution at the starting scale  $Q_0^2$  and is based on low- $x$  approximations. According to Ball and Forte the fitting procedure used here is not fully legitimate, but rather a full two-loop evolution following the prescription given in [153] should be used. Nevertheless, given the current precision of the data, the latter gives compatible results to the simpler approach (equation 9.13) adopted by H1 and used here.

<sup>2</sup>The CCFR collaboration announced recently [163] that mainly due to neutrino beam energy corrections their result changes to  $\alpha_s(M_Z^2) = 0.119 \pm 0.004$

### 9.4 The Bjorken Plot.

An important open question concerning the mechanism for the small- $x$  dynamics at HERA is whether the rise in  $F_2$  towards low  $x$  can be entirely described by the DGLAP [160, 161] evolution equations or if the onset of BFKL dynamics can be seen. The latter is expected to yield a strong rise of  $F_2$  at low  $x$  of  $F_2 \sim x^{-\lambda}$  with  $\lambda \simeq 0.3 - 0.5$ , provided there is enough phase space for building up the power-law behaviour. Such an observation would be of fundamental importance as it had a qualitative impact on the understanding and description of the data in terms of perturbative QCD.

In order to observe tendencies towards BFKL dynamics more clearly, Bjorken suggested [149] plotting  $\log(F_2)$ , or equivalently  $\log(Q^2) \cdot \sigma_{tot}^{\gamma^*p}$ , versus  $\log(Q^2)$  for fixed  $W^2$ , as shown in figure 9.8. The fixed target data, shown as small symbols, as well as the 1994  $F_2$  data presented in this thesis (large symbols) on this plot form curves concave down. However, if any part of the curve at high  $W^2$  changed its curvature and went up, this would be a signal of BFKL behaviour, as that is the only way to approach the Gribov bound. The photoproduction cross section as measured by ZEUS [142] is shown as full line for guidance.

In the presently available data no such tendency is visible, and there seems to be no need yet for BFKL dynamics in the evolution of the inclusive structure function  $F_2$ . However, other studies have shown the data to be compatible with a  $x^{-\lambda}$  rise of the gluon density and the proton structure function  $F_2$  at low  $x$  [30, 24] or obtain an improved description of the data when also including leading  $\log \frac{1}{x}$  terms [32]. More exclusive measurements might be more successful in revealing the presence of BFKL dynamics at the  $x$ -values accessible at HERA [31].

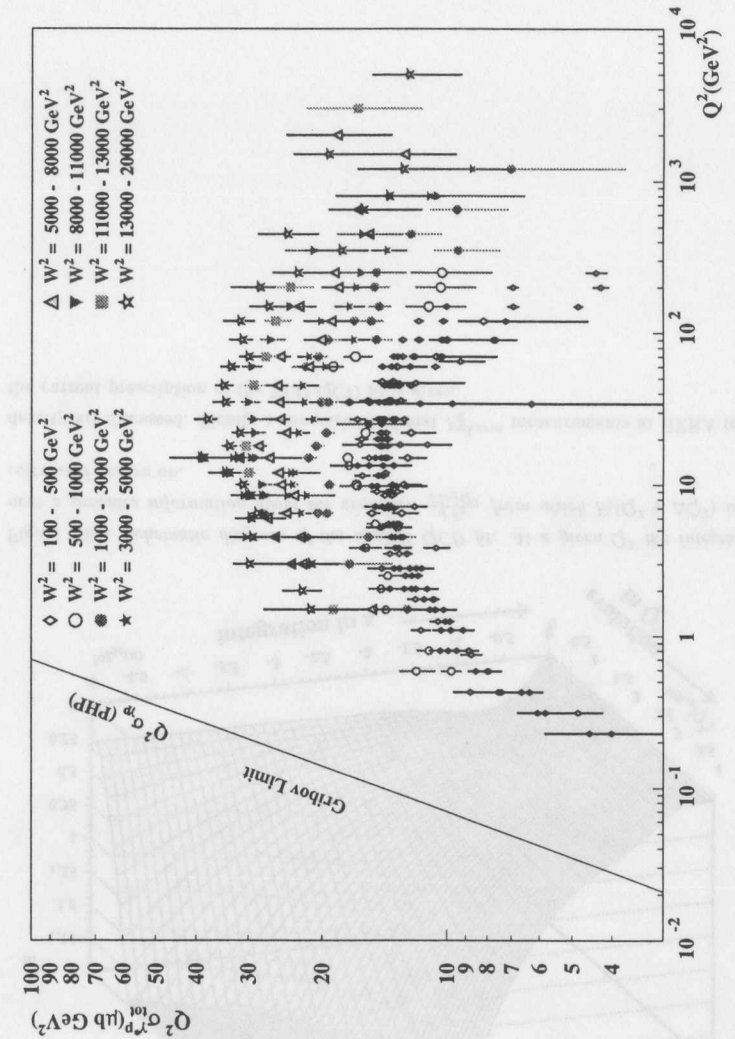


Figure 9.8: Bjorken plot: The fixed target data (small symbols) as well as the 94  $F_2$  data, presented in this thesis, show a concave down curved behaviour. The photoproduction cross section is shown as full line for guidance. A change of this curvature at high  $W^2$  can be interpreted as a signal for BFKL dynamics.

## Chapter 10

# QCD-Analysis of the $F_2$ -Data.

### 10.1 Introduction.

The precise measurement of the proton structure function  $F_2$  in a wide  $(x, Q^2)$  region using the ZEUS detector (see chapters 4 to 8) in combination with a wealth of accurate measurements of the proton and deuteron structure function  $F_2^p$  and  $F_2^d$  in fixed target experiments provide a detailed picture of the structure of hadronic matter. The study of these data offers the opportunity to perform tests of QCD to unprecedented precision.

This chapter presents a QCD analysis aiming at the determination of the next-to-leading order (NLO) gluon momentum distribution in the proton. The method applied is the following (figure 10.1):

- A set of parton distribution functions (PDFs) is parametrised as a function of  $x$  at a starting scale  $Q_0^2$ . One of these PDFs describes the gluon momentum distribution in the proton.
- Starting at  $Q_0^2$  the PDFs are evolved upwards in  $\log Q^2$  using the NLO DGLAP equations [160, 161]. As a result of this procedure the PDFs are stored on a grid in  $x$  and  $Q^2$ .
- For all  $F_2$  data points considered the corresponding theoretical value is constructed from the grid. Their comparison is quantified in a  $\chi^2$  value.
- This procedure is iterated until a set of PDF parametrisations at  $Q_0^2$  is found that minimises the total  $\chi^2$ .

Section 10.2 describes the details of the NLO evolution program and the data sets used.

The results of the fits are presented in section 10.3. Comparisons to the data as well as to global QCD fits are given. The contribution from different experimental errors, as well as the uncertainty in  $\alpha_s$ , to the error of  $F_2$  and in particular to the gluon momentum

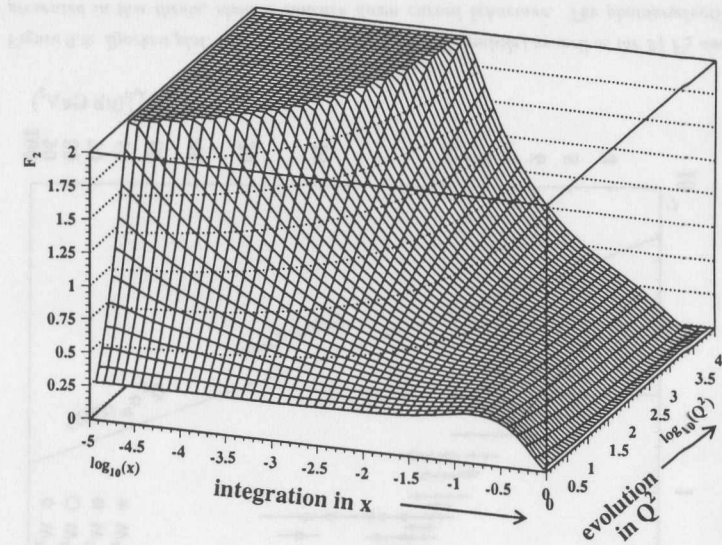


Figure 10.1: Schematic diagram of the applied QCD fit: At a given  $Q^2$  the integral over  $x$  provides information about the evolution  $\frac{dF_2}{d \log Q^2}$  from which  $F_2(Q^2 + \Delta Q^2)$  is calculated and so on.

density are discussed. Finally a comparison of first  $F_2^{charm}$  measurements at HERA to the current prescription of the NLO QCD fit is given.

## 10.2 The NLO-Evolution.

This study uses the NLO evolution program of the MRS group, which has been kindly provided by R.G. Roberts. Only minor modifications have been performed, mainly in order to reduce the processing time of the evolution, namely a different way of taking experimental normalisation uncertainties into account and a change in the internal book-keeping structures.

### 10.2.1 The Data Sets.

The following data sets are used:

- $F_2^p$  from the 1994 ZEUS data as presented in this thesis. Data points of all three analyses (NVTX, SVTX and ISR) are included in the fit. The data set covers a range of  $1.5 - 5000 \text{ GeV}^2$  in  $Q^2$  and  $3.5 \cdot 10^{-5} - 5.1 \cdot 10^{-1}$  in  $x$ . The normalisation uncertainty of the three subsets are 2% for the NVTX, 3% for the SVTX and 3% for the ISR data. The point by point variations of  $F_2^p$  for each systematic check, as discussed in section 7.8, are taken into account for the NVTX data. Statistical and total systematic errors are considered for the SVTX and the ISR data.
- $F_2^p$  and  $F_2^d$  as measured by NMC [133]. The measurements, obtained from 90, 120, 200 and 280 GeV muon beam energy runs, cover a kinematic range of  $0.8 - 62.3 \text{ GeV}^2$  in  $Q^2$  and  $0.0035 - 0.479$  in  $x$ . The normalisation uncertainty is 2.5%. Point by point variations for 10 systematic checks have been provided by NMC and are taken into account.
- $F_2^p$  and  $F_2^d$  from BCDMS [128]. The data cover the kinematic region  $7.5 - 230 \text{ GeV}^2$  in  $Q^2$  and  $0.07 - 0.75$  in  $x$ . The normalisation uncertainty is 3%. Only statistical and total systematic errors are provided, error correlations for different systematic checks are not given. The BCDMS data tend to dominate the QCD fit due to its high precision (total errors  $\lesssim 2\%$ ) and is therefore only included in systematic checks, but not in the central fit.
- $F_2^p$  and  $F_2^d$  from E665 [130]. This data set covers the range  $0.23 - 64.3 \text{ GeV}^2$  in  $Q^2$  and  $8.9 \cdot 10^{-4} - 0.39$  in  $x$ , where its normalisation is known to within 1.8% ( $F_2^p$ ) and 1.9% ( $F_2^d$ ). As only statistical and total systematic errors are available the data are only included in order to investigate systematic effects in the fit.

In order to minimise possible higher twist effects, which would be expected to be relevant at low  $Q^2$  and high  $x$ , a minimum  $Q^2$  of  $2 \text{ GeV}^2$  is required for the fixed target data.

### 10.2.2 The Quality of the Fit.

In order to quantify the quality of the NLO fit the following definition of  $\chi^2$  has been chosen:

$$\chi^2 = \sum_{i=1}^{n_{\text{points}}} \left( \frac{F_2^{\text{data}}(x_i, Q_i^2) - f(\text{set}_i) \cdot F_2^{\text{fit}}(x_i, Q_i^2)}{\sigma_i^{\text{point}}} \right)^2 + \sum_{j=1}^{n_{\text{sets}}} \left( \frac{1 - f(j)}{\sigma_j^{\text{norm}}} \right)^2 \quad (10.1)$$

where  $F_2^{\text{data}}$  and  $F_2^{\text{fit}}$  are the measured and calculated structure function values respectively;  $\sigma_i^{\text{point}}$  is the statistical error or a combination of statistical and systematic errors of a particular data point  $i$ ;  $\sigma_j^{\text{norm}}$  is the normalisation uncertainty of the data set  $j$ ;  $\text{set}_i$  is a function uniquely specifying the data set that a particular data point  $i$  belongs to and  $f(j)$  defines the normalisation of the data set  $j$ . The second term in equation 10.1 guarantees that the normalisation factor, if left as a free parameter, stays around unity within reasonable bounds as specified by the normalisation uncertainty. The first sum runs over all data points, the second sum over all data sets included in the fit. The best fit is specified by a set of parameters, that define the parametrisations of the parton distribution functions (PDF) at  $Q_0^2$ , and that set of normalisations, that minimise the total  $\chi^2$ .

### 10.2.3 Parametrisations of the Parton Distribution Functions.

The universal parton distributions  $f_i(x, Q^2)$  have to be parametrised at a sufficiently large  $Q_0^2$ , from where they can be evolved to higher  $Q^2$  using the next-to-leading order Altarelli-Parisi equations in perturbative QCD. As the dynamical parton model of GRV [102] has been found to describe the  $F_2$  data rather well down to  $Q^2 = 1.5 \text{ GeV}^2$  the starting scale for this study is chosen to be  $Q_0^2 = 1 \text{ GeV}^2$ . Here the parton distributions are parametrised as

$$x u_v = A_u x^{\eta_1} (1-x)^{\eta_2} (1 + \epsilon_u \sqrt{x} + \gamma_u x) \quad (10.2)$$

$$x d_v = A_d x^{\eta_3} (1-x)^{\eta_4} (1 + \epsilon_d \sqrt{x} + \gamma_d x) \quad (10.3)$$

$$x S = A_s x^{-\lambda_s} (1-x)^{\eta_s} (1 + \epsilon_s \sqrt{x} + \gamma_s x) \quad (10.4)$$

$$x g = A_g x^{-\lambda_g} (1-x)^{\eta_g} (1 + \epsilon_g \sqrt{x} + \gamma_g x) \quad (10.5)$$

where the valence distributions  $u_v = u - \bar{u}$  and  $d_v = d - \bar{d}$  and the total quark sea  $S = 2(\bar{u} + \bar{d} + \bar{s} + \bar{c})$ . Despite the fact that the sea  $S$  and the gluon  $g$  are both singlet quantities they evolve slightly differently as  $\frac{\partial g}{\partial \ln Q^2} = P_{gg} \otimes g + \dots \neq \frac{\partial S^{\text{singlet}}}{\partial \ln Q^2} = P_{qg} \otimes g + \dots$  in general. Therefore  $\lambda_s$  and  $\lambda_g$  are allowed to vary independently.

Three of the four  $A_i$  coefficients are determined by sum rules:

$$\left. \begin{aligned} A_u &: \int_0^1 dx u_v(x) = 2 \\ A_d &: \int_0^1 dx d_v(x) = 1 \end{aligned} \right\} \text{flavour sum rule}$$

$$A_g : \int_0^1 dx [x \cdot S(x) + x \cdot u_v(x) + x \cdot d_v(x) + x \cdot g(x)] = 1 \quad \text{momentum sum rule}$$

$A_s$  is a free parameter in the fit.

At  $Q_0^2$  the quark sea is distributed onto the three light flavours as

$$\begin{aligned} 2\bar{u} &= 0.4S - \Delta \\ 2\bar{d} &= 0.4S + \Delta \\ 2\bar{s} &= 0.2S \end{aligned} \quad (10.6)$$

with the general parametrisation  $x \cdot \Delta = x(\bar{d} - \bar{u}) = A_\Delta x^{\eta_\Delta} (1-x)^{\epsilon_\Delta} (1 + \gamma_\Delta x + \delta_\Delta x^2)$ .

The suppression of the strange distribution to 20% of the quark sea is motivated by a next-to-leading order analysis on dimuon production by the CCFR collaboration [155], which places limits on the strange content of the proton.

Evidence for  $\bar{d} > \bar{u}$  (on average) comes from the NA51 Drell-Yan asymmetry in  $pp/pn$  [156] and the measurements of the Gottfried sum by NMC [157]. The  $u, d$  flavour symmetry breaking term  $x \cdot \Delta$  is introduced, accounting for these results. Here  $\delta$  is chosen to be zero for the time being as the precision of the currently available data does not yet require this term.

The normalisation  $A_\Delta$  is determined from the requirement

$$\int_0^1 dx (\bar{d} - \bar{u}) = \frac{1}{2} - \frac{3}{2} \cdot S_G$$

where  $S_G = \int_0^1 \frac{dx}{x} (F_2^p - F_2^n)$  is the 'Gottfried sum' as measured by NMC.

The charm distribution is currently evolved as a massless parton from zero at  $Q^2 = Q_0^2$ . As  $Q_0^2 < m_c^2$  this prescription would overestimate  $F_2^{\text{charm}}$ . Instead the suppression factors

$$\begin{aligned} S_{HQ}(Q^2) &= \left[ 1 - N \left( \frac{m_0^2}{Q^2} \right) \right] \\ \text{with } N(z) &= 6z \left[ 1 - \frac{2z}{\sqrt{1+4z}} \ln \left( \frac{\sqrt{4z+1}+1}{\sqrt{4z+1}-1} \right) \right] \\ S_{HQ}(x) &= (1-x)^3 \end{aligned}$$

and  $m_0^2 = 3.5 \text{ GeV}^2$  (charm mass) are introduced to account for the threshold behaviour of massive quarks (see figure 10.2).

#### 10.2.4 $Q^2$ -Evolution of Singlet and Non-Singlet Quantities.

The DGLAP evolution equations can be written separately for the gluon density  $g$  and the singlet quantities  $q_i^S$ , whose  $Q^2$  evolution depend on the gluon density, and the non-singlet quantities  $q_i^{NS}$ , that are independent of the gluon density:

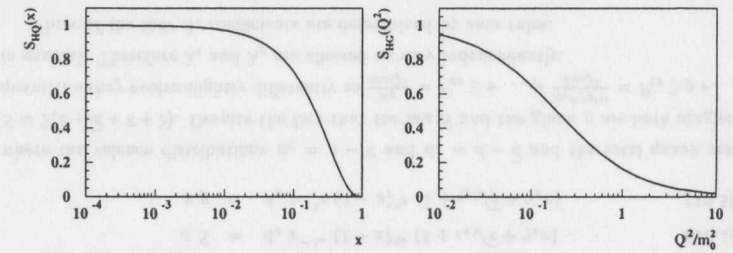


Figure 10.2: The charm quark mass threshold behaviour is modelled via suppression factors  $S_{HQ}(x)$  (left) and  $S_{HQ}(Q^2)$  (right).

	$q^s$	$= S(x, Q^2) + V(x, Q^2)$
singlet		$= 2(\bar{u} + \bar{d} + \bar{s} + \bar{c}) + u_v + d_v$
	$g$	
	$(u_v + d_v)$	
	$d_v$	
non-singlet	$f_c^{NS}$	$= \frac{1}{N_f} q^s - (c + \bar{c})$
	$f_s^{NS}$	$= \frac{1}{N_f} q^s - (s + \bar{s})$
	$f_u^{NS}$	$= -\frac{1}{N_f} q^s + (u + \bar{u})$

Table 10.1: Singlet and non-singlet quantities as evolved and stored on the  $(x, Q^2)$  grid.

singlet

$$\begin{aligned} \frac{d q_i^S(x, Q^2)}{d \log Q^2} &= \frac{\alpha_s(Q^2)}{2\pi} \int_x^1 \frac{dz}{z} \left[ q_i^S(z, Q^2) \cdot P_{qq} \left( \frac{x}{z} \right) + 2N_f \cdot g(z, Q^2) \cdot P_{qg} \left( \frac{x}{z} \right) \right] \\ \frac{d g(x, Q^2)}{d \log Q^2} &= \frac{\alpha_s(Q^2)}{2\pi} \int_x^1 \frac{dz}{z} \left[ q^s(z, Q^2) \cdot P_{gq} \left( \frac{x}{z} \right) + g(z, Q^2) \cdot P_{gg} \left( \frac{x}{z} \right) \right] \end{aligned} \quad (10.7)$$

non-singlet

$$\frac{d q_i^{NS}(x, Q^2)}{d \log Q^2} = \frac{\alpha_s(Q^2)}{2\pi} \int_x^1 \frac{dz}{z} q_i^{NS}(z, Q^2) \cdot P_{NS} \left( \frac{x}{z} \right) \quad (10.8)$$

with the NLO splitting function as given in [158].

Therefore the parton distributions are separated into singlet and non-singlet quantities, which are actually evolved and stored on the  $(x, Q^2)$  grid (table 10.1).

$c^{grid}$	$= -f_x^{NS} + \frac{1}{N_f} q^S$	$= c + \bar{c}$
$\delta^{charm}$	$= S_{HQ}(x) \cdot S_{HQ}(Q^2) \cdot c^{grid}$	
$c^{flavour}$	$= c^{grid} - \delta^{charm}$	$= c + \bar{c} - 1.0 \cdot \delta^{charm}$
$s^{flavour}$	$= \frac{1}{N_f} q^s - f_s^{NS} + 0.2 \cdot \delta^{charm}$	$= s + \bar{s} + 0.2 \cdot \delta^{charm}$
$u^{flavour}$	$= f_u^{NS} + \frac{1}{N_f} q^s + 0.4 \cdot \delta^{charm}$	$= u + \bar{u} + 0.4 \cdot \delta^{charm}$
$d^{flavour}$	$= q^s - u^{flavour} - s^{flavour} - c^{flavour}$	$= d + \bar{d} + 0.4 \cdot \delta^{charm}$

Table 10.2: Flavour parton distributions as constructed from grid quantities.

The parton distribution functions of the different quark flavours in the  $\overline{MS}$  scheme can be constructed from these quantities as shown in table 10.2

The additional quark sea contribution  $\delta^{charm}$ , which is made available by the charm suppression at  $Q^2 \approx m_c^2$ , is distributed onto the three light flavours  $u$ ,  $d$  and  $s$  in the ratio 40 : 40 : 20 (compare to equation 10.6).

The integrals in equation 10.7 and 10.8 are solved numerically using gaussian integration. The resulting slope  $\frac{d f_i}{d \log Q^2}$  in combination with a given starting value of the PDF  $f_i(Q^2)$  allows the determination of the value  $f_i(Q^2 + \Delta Q^2)$ , the PDF can be evolved up to the highest  $Q^2$  covered by data points. In principle the same procedure could also be used for the evolution of the PDF to smaller  $Q^2$  values. However, this is neither necessary nor practical given the starting scale  $Q_0^2 = 1 \text{ GeV}^2$  and the data set considered.

### 10.2.5 Calculation of $\alpha_s$ .

The precise calculation of the strong coupling constant  $\alpha_s$  in the entire  $Q^2$ -range, i.e. also across quark mass thresholds, is of vital importance for the evolution of the PDFs. Formally integrating the  $Q^2$  scale dependence of  $\alpha_s$ , given by the renormalisation group equation, to next-to-leading order yields

$$\ln \frac{Q^2}{\Lambda_{(4)}^2} = \frac{4\pi}{\beta_0 \alpha_s} - \frac{\beta_1}{\beta_0^2} \ln \left[ \frac{4\pi}{\beta_0 \alpha_s} + \frac{\beta_1}{\beta_0} \right] \quad (10.9)$$

with  $\beta_0 = 11 - \frac{2}{3} N_f$ ,  $\beta_1 = 102 - \frac{38}{3} N_f$  the first two coefficients of the QCD  $\beta$ -function. Solving this equation iteratively, using Newton's method, yields  $\alpha_s(Q^2, n_f = 4)$  for four active flavours. To ensure the continuity of  $\alpha_s$  at the quark mass thresholds [37], essentially following the prescription of Marciano [159],  $\alpha_s$  is calculated as

$$\alpha_{s(4)}(Q^2) = \alpha_s(Q^2, 4) \quad 3.5 \text{ GeV}^2 \leq Q^2 \leq 30 \text{ GeV}^2$$

$$\frac{1}{\alpha_{s(3)}(Q^2)} = \frac{1}{\alpha_s(Q^2, 3)} + \frac{1}{\alpha_s(m_c^2, 4)} - \frac{1}{\alpha_s(m_c^2, 3)} \quad Q^2 < 3.5 \text{ GeV}^2$$

$$\frac{1}{\alpha_{s(5)}(Q^2)} = \frac{1}{\alpha_s(Q^2, 5)} + \frac{1}{\alpha_s(m_b^2, 4)} - \frac{1}{\alpha_s(m_b^2, 5)} \quad Q^2 > 30 \text{ GeV}^2$$

with  $m_c^2 = 3.5 \text{ GeV}^2$  and  $m_b^2 = 30 \text{ GeV}^2$  the squares of the charm and the beauty masses respectively.

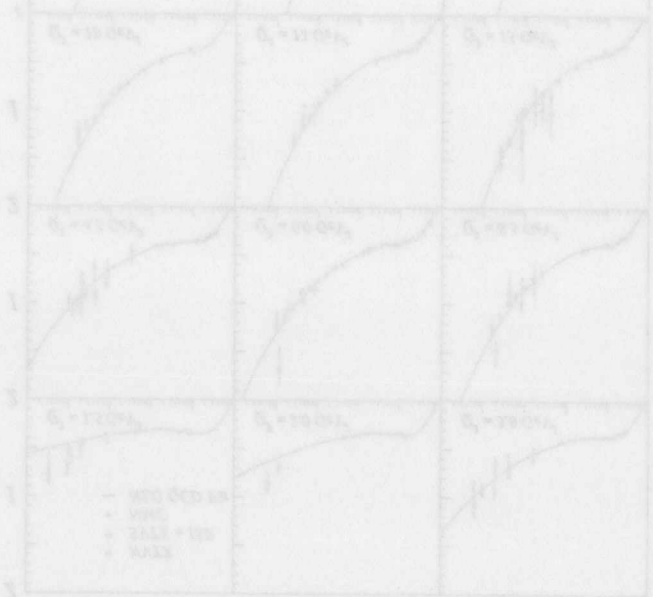
Constructing the flavour parton distributions from the grid quantities and equation 2.22 allow the calculation of<sup>1</sup>

$$F_2^p = \frac{4}{9} [u + \bar{u} + c + \bar{c}] + \frac{1}{9} [d + \bar{d} + s + \bar{s}] \quad \text{and}$$

$$F_2^n = \frac{4}{9} [d + \bar{d} + c + \bar{c}] + \frac{1}{9} [u + \bar{u} + s + \bar{s}] \quad \text{so that}$$

$$F_2^d = (F_2^p + F_2^n)/2 = \frac{5}{18} [u + \bar{u} + d + \bar{d}] + \frac{1}{9} [s + \bar{s}] + \frac{4}{9} [c + \bar{c}]$$

These values are finally compared to the data points in the way described in section 10.2.2. Further details about the program and the set of parameters referred to as MRS-R1 to MRS-R4 can be found in [135, 137].



<sup>1</sup>Shadowing corrections, taking the binding of the proton and the neutron in a deuteron into account, are expected to be small and not applied to  $F_2^d$ .

### 10.3 Results

#### 10.3.1 The Central Fit.

The central NLO QCD fit includes NVTX and SVTX  $F_2^p$  data as presented in this thesis and the NMC  $F_2^p$  and  $F_2^d$  data. As these data have been found to be rather insensitive to the non-singlet, i.e. the valence parton densities, their corresponding parameters are fixed to the values from the global QCD analysis with  $\Lambda_{\overline{MS}}^{(4)} = 344$  MeV (MRS-R2 fit) [137]. The normalisations of all data sets are initially set to unity, their variations is investigated in section 10.3.3. Only statistical errors on the measured  $F_2$  are considered, except for the NVTX data, where a quadratic sum of the statistical errors and the systematic errors originating from the unfolding procedure is used. Systematic uncertainties on  $F_2$  and the PDFs are considered in a separate section 10.3.5

Parameter	free ?	value	error	MRS-R2
$\Lambda_{\overline{MS}}^{n_f=4}$	-	0.344		0.344
$\eta_1$	-	0.61		0.61
$\eta_2$	-	3.54		3.54
$\eta_3$	-	0.24		0.24
$\eta_4 - \eta_2$	-	0.66		0.66
$A_s$	+	0.36 ± 0.19		0.37
$\eta_s$	+	7.75 ± 0.86		8.27
$(A_g)$	-	7.56		14.4
$\eta_D$	+	5.88 ± 29.5		5.51
$\gamma_u$	-	6.51		6.51
$(A_\Delta)$	-	0.54		0.036
$\gamma_g$	+	6.51 ± 4.74		6.57
$\delta_g$	+	0.40 ± 8.2		0.51
$\gamma_d$	-	29.9		29.9
$\delta_s$	+	-0.13 ± 0.52		-0.15
$\gamma_s$	+	15.33 ± 3.19		14.41
$\epsilon_u$	-	-0.98		-0.98
$\epsilon_d$	-	7.37		7.37
$\epsilon_s$	+	0.77 ± 0.93		1.13
$\epsilon_g$	+	-3.39 ± 1.63		-4.20
$\eta_\Delta$	+	0.55 ± 0.15		0.30
$\gamma_\Delta$	-	64.9		64.9

Table 10.3: Numerical values of the parameters describing the parton distribution functions at  $Q_0^2 = 1 \text{ GeV}^2$ . The values obtained in MRS-R2 are also listed for comparison. Parameters in brackets are not directly fitted but determined from sum rules.

Figures 10.3 and 10.4 show the  $F_2$  resulting from the NLO QCD fit as solid line together with the data fitted and the ISR  $F_2$ . For  $Q^2 \geq 3 \text{ GeV}^2$  the fit describes the data very well at low as well as at high  $x$ . Only at  $Q^2 \leq 2 \text{ GeV}^2$  does the fit tend to

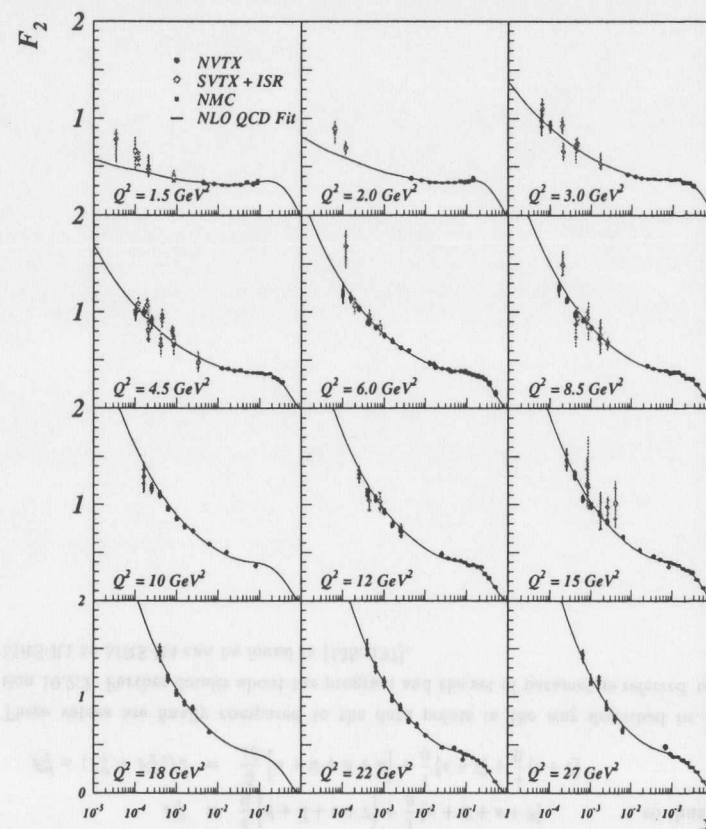


Figure 10.3:  $F_2$  versus  $x$  from the NVTX data (closed circles), the SVTX data (open circles) and NMC data (closed rectangles) together with the central NLO QCD fit (solid line).

undershoot the low- $x$  data from the SVTX and the ISR analyses due to the suppression of the charm contribution. Nevertheless the fit is consistent with the data in this region as the experimental errors are rather large at present.

The  $Q^2$  dependence of  $F_2$  for fixed  $x$  is shown in figures 10.5 and 10.6. The SVTX and ISR data are shown at  $x$ -values of the NVTX analysis, using the NLO fit for the interpolation. The NLO fit describes the rise of the  $F_2$  data with  $Q^2$  in the NMC region and HERA region very well, and in particular the change in the slope due to the scaling violations, a salient feature of NLO QCD, is very well reproduced over four orders of

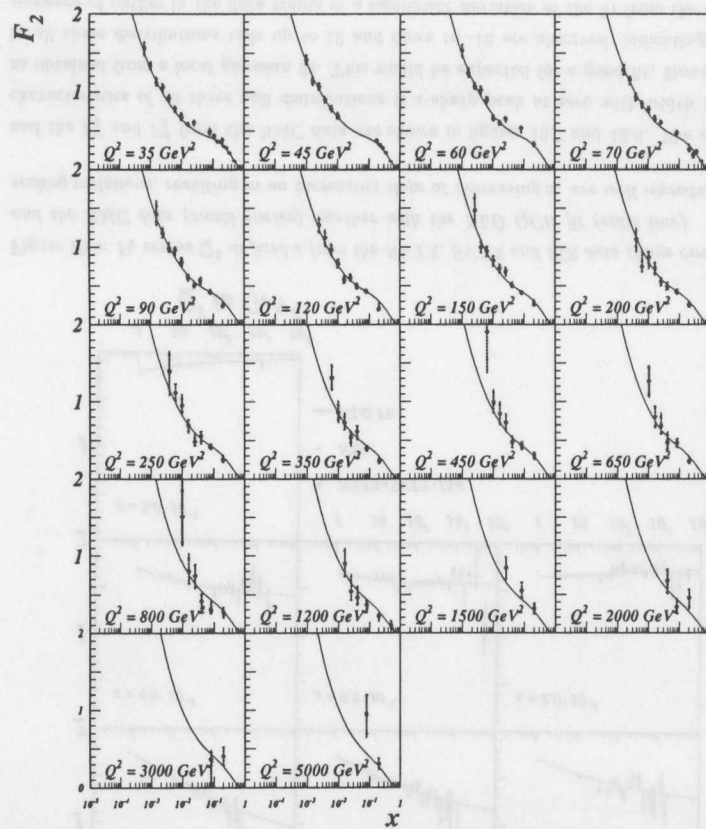


Figure 10.4:  $F_2$  versus  $x$  from the NVTX data (closed circles), the SVTX data (open circles) and NMC data (closed rectangles) together with the central NLO QCD fit (solid line).

magnitude in  $Q^2$ .

The parameters of the central fit, describing the parton distribution functions at  $Q^2 = Q_0^2 = 1 \text{ GeV}^2$  are listed in table 10.3.

The quality of the fit is quantified by a total  $\chi^2 = 1292$  for 727 data points. The  $\chi^2$ -contribution from the different data sets is given in table 10.4.

The large  $\chi^2$  for the SVTX points is due to the undershooting of the fit below  $Q^2 \approx 3 \text{ GeV}^2$ , where most of the SVTX data have been taken. Furthermore the low- $x$  SVTX points tend to be slightly high compared to the curve and, if available, NVTX

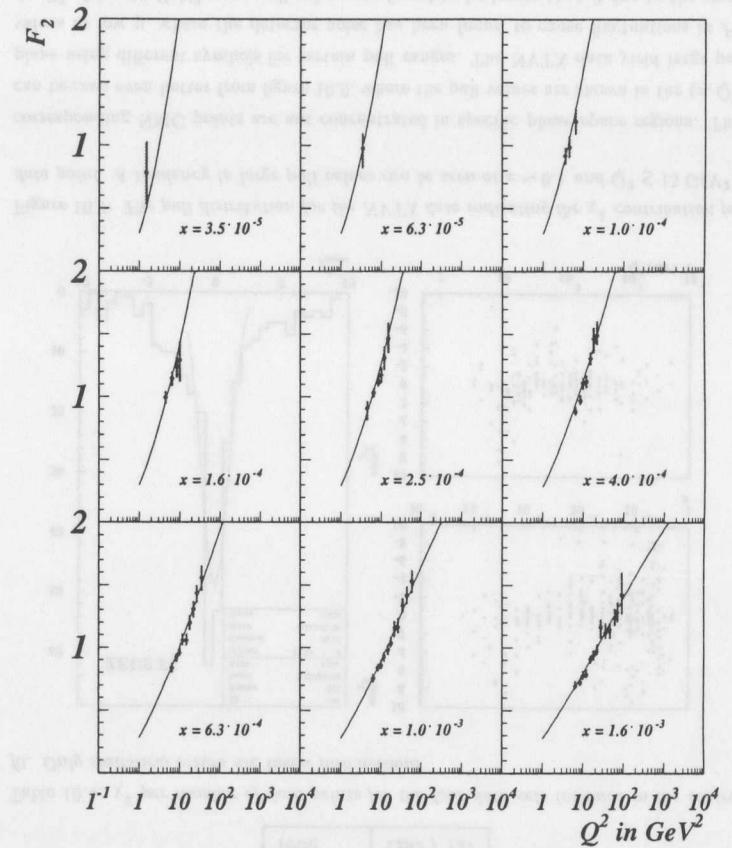


Figure 10.5:  $F_2$  versus  $Q^2$  at fixed  $x$  from the NVTX, SVTX and ISR data (large circles) and the NMC data (small circles) together with the NLO QCD fit (solid line). The scaling violations, resulting in an increasing slope at decreasing  $x$ , are well reproduced.

data, so that some points contribute  $\chi^2 \gtrsim 20$ . Taking into account that the fit has 10 free parameters a  $\chi^2/ndf = 1292/(727 - 10) = 1.8$  is obtained. This indicates that the fit is adequate, but not brilliant. In order to study the origin of this effect the quantity 'pull', which measures the  $\chi^2$  contribution per data point, is defined

$$\text{pull}(x_i, Q_i^2) = \text{sgn}(i) \cdot \left( \frac{F_2^{\text{data}}(x_i, Q_i^2) - F_2^{\text{fit}}(x_i, Q_i^2)}{\sigma_i} \right)^2 \quad \text{with } \text{sgn} = \frac{F_2^{\text{data}} - F_2^{\text{fit}}}{|F_2^{\text{data}} - F_2^{\text{fit}}|}$$

The pull distributions and scatter plots versus  $x$  and  $Q^2$  for  $F_2^p$  from the NVTX data

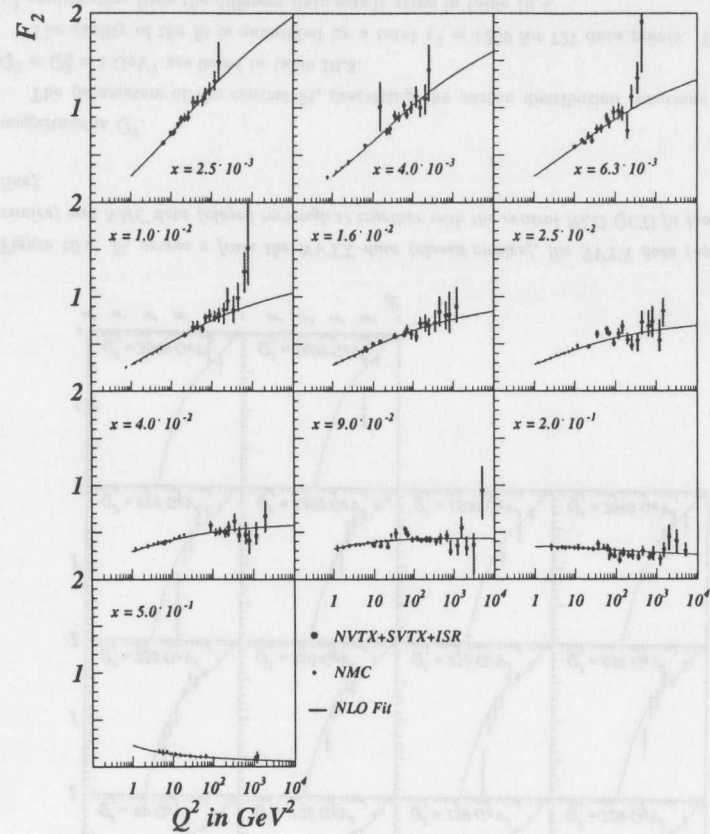


Figure 10.6:  $F_2$  versus  $Q^2$  at fixed  $x$  from the NVTX, SVTX and ISR data (large circles) and the NMC data (small circles) together with the NLO QCD fit (solid line). The scaling violations, resulting in an increasing slope at decreasing  $x$ , are well reproduced.

and the  $F_2^p$  and  $F_2^d$  from the NMC data are shown in figures 10.7 and 10.8. The main characteristics of all three pull distributions is a sharp peak at zero with width  $\simeq 1$ , as obtained from a local gaussian fit. This would be expected for a good fit. However, in all three distributions tails up to 10 and down to -10 are observed, indicating the presence of outlier in the data points or a significant deviation of the fit from the data in a particular  $(x, Q^2)$  region. The distribution of the pull as a function of  $x$  or  $Q^2$  do not show any evidence for a systematic mismatch between the data and the fit. The NVTX points with the largest pull values lie around  $x \gtrsim 10^{-1}$  and  $Q^2 \lesssim 15 \text{ GeV}^2$ . The

Data Set	$\chi^2 / n_{\text{points}}$
$F_2^p$ NVTX	287 / 191
$F_2^p$ SVTX	237 / 24
$F_2^p$ NMC	418 / 256
$F_2^d$ NMC	350 / 256
Total	1292 / 727

Table 10.4:  $\chi^2$  per number of data points for the four data sets included in the central fit. Only statistical errors are taken into account

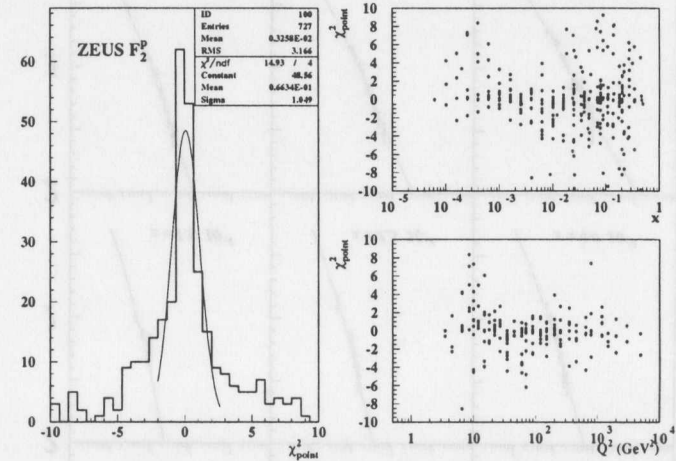


Figure 10.7: The pull distribution for the NVTX data indicating the  $\chi^2$  contribution per data point. A tendency to large pull values can be seen at  $x \sim 0.1$  and  $Q^2 \lesssim 15 \text{ GeV}^2$ .

corresponding NMC points are not concentrated in specific phase space regions. This can be seen even better from figure 10.9, where the pull values are shown in the  $(x, Q^2)$  plane using different symbols for certain pull ranges. The NVTX data yield large pull values at low  $y$ , where the detector noise has been found to cause fluctuations in  $F_2$ . At  $Q^2$  of 8 – 10  $\text{GeV}^2$  some pull values are found to be larger than 2 due to the small statistical errors ( $\sim 1.9\%$ ).

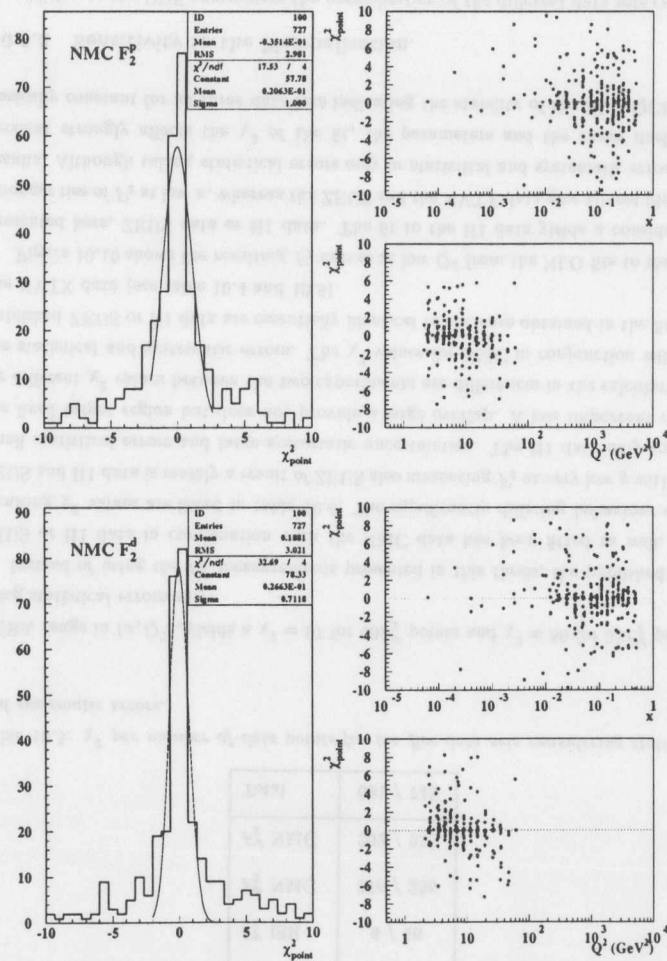


Figure 10.8: The pull distribution for the NMC  $F_2^p$  (top) and  $F_2^d$  (bottom) data sets, indicating the  $\chi^2$  contribution per data point.

### 10.3.2 Sensitivity to the Input Data.

Only including statistical errors for the NVTX data yields a  $\chi^2 = 675/191$  where the dominating contribution comes from the low- $y$  points. Using the quadratic sum of statistical and systematic errors for all data sets, now also including the ISR data in

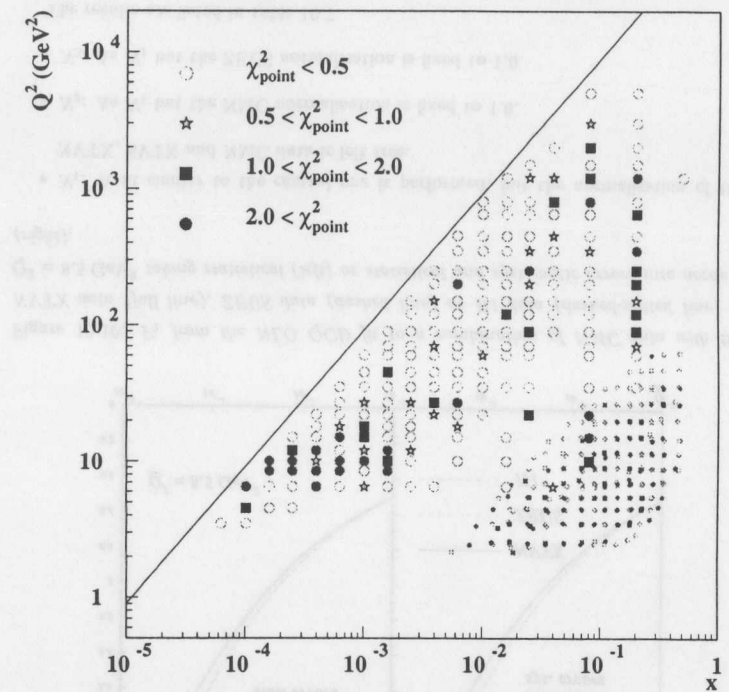


Figure 10.9:  $\chi^2$  contribution per data point for the central fit from the NVTX data (big symbols) and the NMC data (small symbols) in the  $(x, Q^2)$  plane.

addition to the NVTX and SVTX  $F_2^{ep}$  and the NMC  $F_2^{up}$  and  $F_2^{ud}$ , results in  $\chi^2$  as listed in table 10.5. Even though adding the systematic errors in quadrature improves the  $\chi^2$  significantly, indicating that the NLO fit describes the data better than the fit using statistical errors only, the corresponding PDF parameters have not changed significantly.

However, if BCDMS  $F_2^p$  and  $F_2^d$  data are included these data dominate the fit as a consequence of the very small errors for the large number of data points (175 points for  $F_2^p$  and 157 points for  $F_2^d$ ) in a comparatively small  $(x, Q^2)$  region. The  $\chi^2$  for the 191 NVTX points in such a fit increases to 1417. The fits undershoots the low- $x$  data significantly. This is not too surprising, considering that a NLO analysis of the accurate BCDMS data results in a  $\Lambda_{\overline{MS}}^{(4)}$  value of 256 MeV [164], which is much lower than the 344 MeV used here (This observation has been interpreted as an indication that a good simultaneous fit to high- $x$  and low- $x$  data requires the inclusion of  $\ln \frac{1}{x}$  terms [32]).

Including in addition E665 data, which in general lies between the BCDMS and the

Data Set	$\chi^2 / n_{points}$
$F_2^p$ NVTX	150 / 191
$F_2^p$ SVTX	47 / 24
$F_2^p$ ISR	6 / 16
$F_2^p$ NMC	276 / 256
$F_2^d$ NMC	202 / 256
Total	681 / 743

Table 10.5:  $\chi^2$  per number of data points for the five data sets considering statistical and systematic errors.

HERA range in  $(x, Q^2)$ , yields a  $\chi^2 = 97$  for  $60F_2^p$  points and  $\chi^2 = 86$  for  $53F_2^d$  points, using statistical errors only.

Instead of using the  $F_2^p$  measurements presented in this thesis, the published 1994 ZEUS or H1 data in combination with the NMC data has been fitted as well. The resulting  $\chi^2$  values are listed in table 10.6. The significantly differing behaviour of the ZEUS and H1 data is mainly a result of ZEUS also measuring  $F_2$  at very low  $y$  with very small statistical errors and large systematic uncertainties. The H1 data only touches the fixed target region but does not provide a large overlap. A less important reason for different  $\chi^2$  values between the two experiments are differences in the calculation of the statistical and systematic errors. The  $\chi^2$  values for NMC in conjunction with the published ZEUS or H1 data are essentially identical to the ones obtained in the fit with the NVTX data (see table 10.4 and 10.5).

Figure 10.10 shows the resulting  $F_2$  curves at low  $Q^2$  from the NLO fits to the data presented here, ZEUS data or H1 data. The fit to the H1 data yields a considerably stronger rise of  $F_2$  at low  $x$ , whereas the ZEUS and the NVTX data give almost identical results. Although taking statistical errors only or statistical and systematic errors into account strongly affects the  $\chi^2$  of the fit, the parameters and the curve itself stay basically constant for all three data sets indicating the stability of the NLO QCD fit.

### 10.3.3 Sensitivity to the Normalisation.

In addition to the PDF parameters the normalisation of the different data sets can also be left free. The following scenarios have been fitted in order to study whether there is some need for normalisation corrections.

Data Set	$\chi^2 / n_{points}$
1994 ZEUS (stat)	653 / 188
1994 ZEUS (stat $\oplus$ sys)	258 / 188
1994 H1 (stat)	399 / 193
1994 H1 (stat $\oplus$ sys)	97 / 193

Table 10.6:  $\chi^2$  per number of data points from separate fits to ZEUS and NMC or H1 and NMC data for different error treatments.

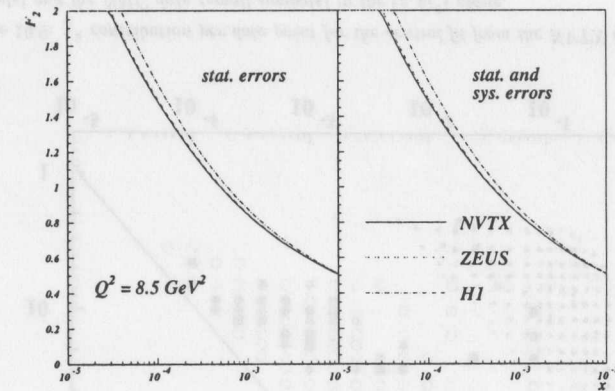


Figure 10.10:  $F_2$  from the NLO QCD fit to a combination of NMC data with the NVTX data (full line), ZEUS data (dashed line) or H1 data (dashed-dotted line) at  $Q^2 = 8.5 \text{ GeV}^2$  taking statistical (left) or statistical and systematic errors into account (right).

- $N_1$ : A fit similar to the central one is performed, but the normalisation of the NVTX, SVTX and NMC data is left free.
- $N_2$ : As  $N_1$  but the NMC normalisation is fixed to 1.0.
- $N_3$ : As  $N_1$  but the ZEUS normalisation is fixed to 1.0.

The results are listed in table 10.7.

The  $\chi^2$  variations for the ZEUS data can be quite substantial, whereas the NMC  $\chi^2$  is rather stable. Treating all normalisations as free parameters results in a downscaling of NMC data by 1.4%, while the NVTX data are scaled down by 5.4% and the SVTX

Scenario	NVTX	SVTX	NMC(p)	NMC(d)	$N_{NVTX}$	$N_{SVTX}$	$N_{NMC}$
$N_1$	226/191	255/24	404/256	319/256	$0.946 \pm 0.017$	$1.091 \pm 10^5$	$0.986 \pm 0.016$
$N_2$	231/191	230/24	422/256	356/256	$0.962 \pm 0.011$	$1.048 \pm 10^5$	1.0
$N_3$	273/191	228/24	433/256	370/256	1.0	1.0	$1.013 \pm 0.011$

Table 10.7:  $\chi^2$  dependence on the normalisation of the data sets.

data up by 9.1%. The NVTX and NMC values lie in the  $1 - 2\sigma_{norm}$  range, only the SVTX normalisation receives a larger scale factor. But in the fit no strong sensitivity to this normalisation is found, as can be seen from the large error.

Given the present normalisation uncertainties the normalisation scales vary within reasonable bounds. But the results obtained indicate that an improved understanding of the trigger efficiency and luminosity measurement as well as a larger overlap in kinematic region between the data sets will be important for global QCD analyses.

### 10.3.4 Sensitivity to $\alpha_s$ .

The NLO QCD fit requires as input the data points, the starting PDFs, the NLO splitting functions and  $\alpha_s$ . It is clear that the fit results are sensitive to the choice of  $\alpha_s$ . At large  $x$  the evolution of  $F_2$  is determined by a convolution of the valence quark distribution and  $\alpha_s$ , at low  $x$  the  $F_2$  evolution is dominated by a convolution of the gluon density and  $\alpha_s$ . In order to investigate the sensitivity of the fit to  $\alpha_s$  the NVTX, BCDMS and NMC data have been fitted with the valence quark, sea and gluon parameters left free. The statistical and systematic errors are added quadratically.

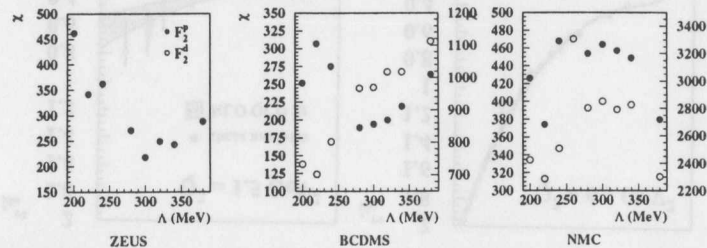


Figure 10.11:  $\chi^2$  contribution from the data sets of the ZEUS, BCDMS and NMC experiments as a function of  $\alpha_s$ . Values obtained from  $F_2^p$  are shown as full circles, values from  $F_2^d$  as open circles.

The resulting  $\chi^2$  for the different data sets are shown in figure 10.11.  $F_2^p$  sets are shown as full circles,  $F_2^d$  as open circles. The NVTX data (left plot) exhibits a rather strong  $\alpha_s$  dependence. The minimum  $\chi^2$  is reached for  $\Lambda_{\overline{MS}}^{(4)} \simeq 300$  MeV, which is in very good agreement with the  $\Lambda_{\overline{MS}}^{(4)} \simeq 278$  MeV obtained in the NLO DAS fit. The BCDMS  $F_2^p$  data seems to favour  $\Lambda \approx 270$  MeV, whereas the  $F_2^d$  data yields its lowest  $\chi^2$  for  $\Lambda \approx 220$  MeV. The NMC  $F_2^p$  and  $F_2^d$  data also seems to favour  $\Lambda \approx 220$  MeV.

The procedure applied is not completely suitable to determine  $\alpha_s$ , as the  $\alpha_s$  dependence of the different data sets influence each other. The fit minimises the total  $\chi^2$  and is therefore dominated by the data set which is most sensitive to  $\alpha_s$ . Nevertheless the general picture, that fixed target data seems to favour a low  $\alpha_s$  while HERA data tend to prefer a value closer to the world average, is confirmed in the QCD fit.

### 10.3.5 Error Estimate on the PDFs, the gluon and $F_2$ .

Global QCD analyses are not only performed in order to study and test perturbative QCD, but they also serve the purpose of extracting the universal parton densities in the proton. This information can in turn, for example, be used to perform calculations of QCD predictions for cross sections in  $\bar{p}p$  or  $pp$  collisions. The present uncertainty in the PDFs is a considerable systematic error source for the measurements of the  $W$ -mass. As pointed out in [105] this and other examples suggest that it is not sufficient to extract PDFs from global QCD fits, but that a consistent treatment of the experimental errors of the data sets is necessary to estimate the uncertainty on the PDFs and further calculations from them.

In the presented study experimental errors are considered in the following way: For the ZEUS  $F_2^p$ , the 31 systematic checks of the NVTX analysis are combined with the central NMC data; for NMC 10 systematic checks are combined with the central NVTX data. This procedure results in 41 additional data sets. Performing 42 NLO fits (1 central and 41 systematic checks) and adding positive and negative deviations of the resulting grid quantities and PDFs in quadrature provides an estimate of the uncertainty in the PDFs.

Figure 10.12 shows the  $F_2$  data versus  $x$  for four particular  $Q^2$  values together with the NLO QCD fit. The central fit is shown as dashed line, the shaded error band obtained from the prescription described above indicates the uncertainty in  $F_2$ .

As  $F_2$  is the quantity which is actually fitted it is hardly surprising that the error band is rather small. Only at  $Q^2 = 1.5$  GeV<sup>2</sup>, where the experimental errors are relatively large and constraints from lower  $Q^2$  are missing the uncertainty on  $F_2$  from the fit is as large as 20%.

Figure 10.13 shows the quark distributions as a function of  $x$  for  $Q^2$  of 10 and 1000 GeV<sup>2</sup>. Since the data set considered is not sensitive to high- $x$  PDFs, the corresponding parameters are fixed, so that the estimated error on the PDFs at  $x > 10^{-2}$  is

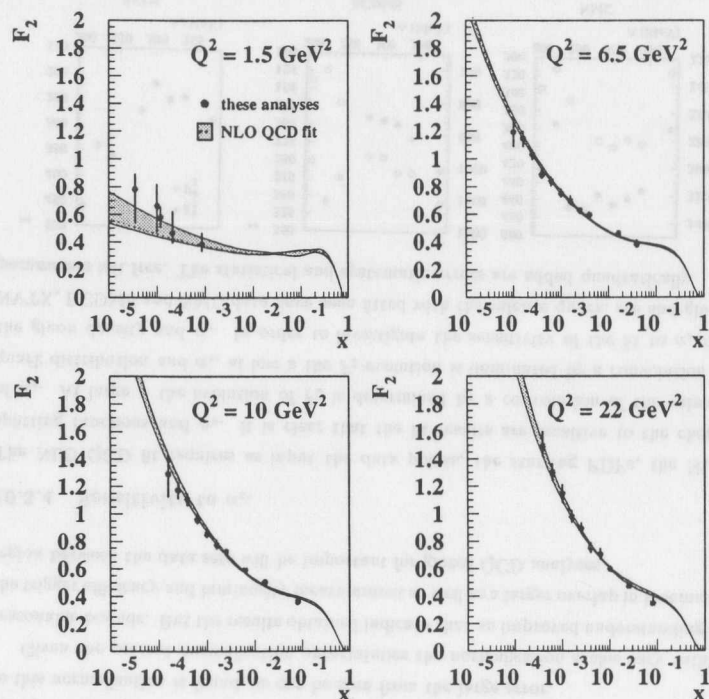


Figure 10.12: *NVTX*, *SVTX*, and *ISR*  $F_2$  data versus  $x$  together with the *NLO QCD* fit. The central fit is shown as dashed line, the uncertainty as shaded error band.

small. However, at  $Q^2 = 10 \text{ GeV}^2$  and  $x \simeq 10^{-4}$  or even lower the uncertainty on the quark densities can be larger than 10%. At  $Q^2 = 1000 \text{ GeV}^2$  and  $x \lesssim 10^{-3}$  the  $u$  and  $d$ -quark densities can only be determined to within 15%.

These  $x$  and  $Q^2$  dependences of the quark density uncertainties are also reflected in the gluon density. Figure 10.14 shows the gluon momentum distribution versus  $x$  at small and medium  $Q^2$ . Not only the evolution of the gluon density with  $Q^2$  can clearly be seen, but also its  $x$ -dependence. The error bands exhibit a prominent structure at  $x \simeq 1 - 3 \cdot 10^{-2}$  and  $1 - 2 \cdot 10^{-1}$ . The origin of this feature is the overlap between the two data sets, introducing fluctuations in  $F_2$  from the different systematic checks. The uncertainty in the gluon density at  $Q^2 = 22 \text{ GeV}^2$  and  $x = 10^{-4}$  is  $\approx 24\%$ , where the error band is also found to be strongly asymmetric. In comparison to previous determinations of the gluon momentum distribution in the proton [118] the extension of

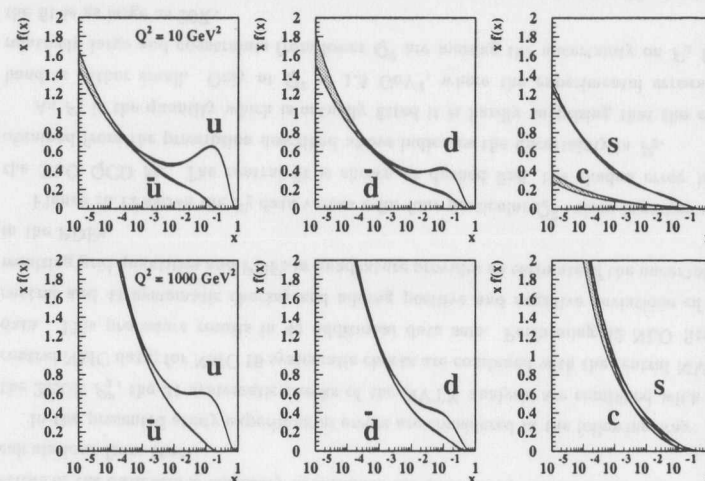


Figure 10.13: Flavour parton distribution functions (PDFs) as a function of  $x$  for  $Q^2 = 10 \text{ GeV}^2$  (top) and  $Q^2 = 1000 \text{ GeV}^2$  (bottom). The uncertainty of the PDFs as obtained from the fit are shown as shaded error bands.

the kinematic region of the  $F_2$  measurements and the reduction of the errors on the data points result in a significantly reduced uncertainty in the gluon distribution at small  $x$ .

A comparison of the gluon density obtained in this analysis to those of global QCD analyses at  $Q^2 = 22 \text{ GeV}^2$  is shown in figure 10.15. The gluon density extracted in this analysis follows very closely the one from MRSR2. Only at  $x \lesssim 10^{-2}$  MRSR2 lies slightly higher. Both parametrisations lie between those of MRSD<sub>0</sub> and MRSD<sub>-</sub>, which represent extreme assumptions of pre-HERA predictions. This analysis is also found to be in good agreement with CTEQ4, the latest parametrisation of the CTEQ collaboration. The previous CTEQ fit, and GRV give gluon densities that are higher and steeper than the one obtained here for  $x \lesssim 10^{-2}$ . This, however, is partially due to the fact that GRV and CTEQ3 use  $\Lambda_{QCD}^{(n_f=4)}$  values of 200 MeV and 247 MeV, respectively. Since the gluon splitting and hence the scaling violations at small  $x$  are proportional to the product of the strong coupling constant,  $\alpha_s$ , and the gluon density, these two quantities are anticorrelated. This effect is demonstrated in figure 10.16, where the gluon density of the central fit ( $\Lambda_{QCD}^{(n_f=4)} = 344 \text{ MeV}$ ) at low  $x$  is shown to be lower than that of a fit with a smaller  $\alpha_s$  ( $\Lambda_{QCD}^{(n_f=4)} = 241 \text{ MeV}$ ).

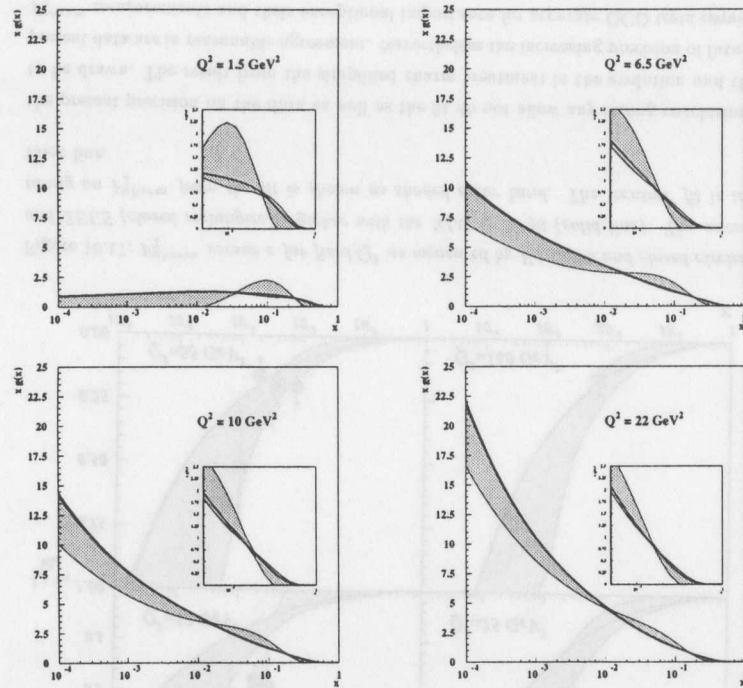


Figure 10.14: Gluon momentum distribution  $xg(x)$  at four  $Q^2$  values as extracted from the NLO QCD fit. The uncertainty on  $xg(x)$  is shown as shaded error band, the inset zooms into the region around  $x \approx 10^{-1}$  where the overlap of the NVTX and the NMC data produces the depicted feature in the error band.

### 10.3.6 $F_2^{charm}$ Comparison.

Assuming the absence of intrinsic charm, the proton's charm content originates entirely from charm production via the boson-gluon fusion mechanism. The corresponding contribution to  $F_2$ , namely  $F_2^{charm}$ , is an exclusive quantity in the sense that it is flavour specific, even though inclusive of all decays. It provides an alternative handle on the gluon density and allows additional tests of QCD. The precise measurement of  $F_2^{charm}$  at small  $x$  at HERA will eventually play a crucial role in furthering the understanding of perturbative QCD and in the determination of PDFs and their uncertainties in general.

The first measurements of  $F_2^{charm}$  at large  $x$  were made by a FNAL collaboration [167] and the EMC collaboration [168]. They were based on the identification of dimuon and trimuon events in  $\mu^+$ -iron interactions, which were dominantly caused by open

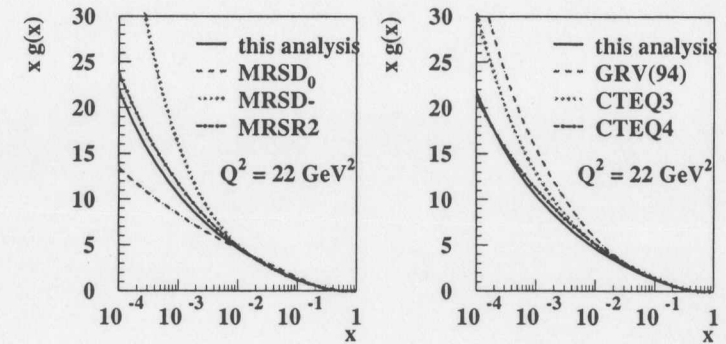


Figure 10.15: Comparison of the gluon density obtained in this analysis with those from global QCD analyses.

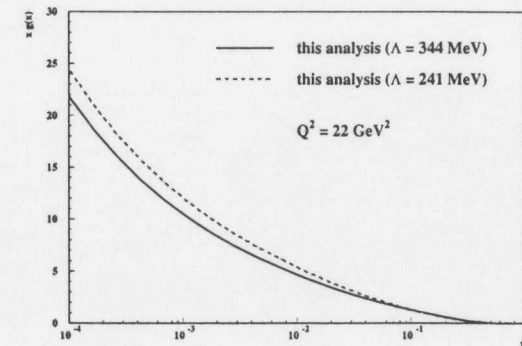


Figure 10.16: Comparison of the gluon density obtained from the central fit ( $\Lambda_{QCD}^{(n_f=4)} = 344$  MeV) to the one obtained in a fit with  $\Lambda_{QCD}^{(n_f=4)}$  reduced to 241 MeV.

charm production in which the charmed particles decayed semileptonically to muons. This measurement has recently been complemented by H1 [169] and preliminary ZEUS measurements [170]. Open charm production in DIS at HERA is tagged via the reconstruction of charged  $D^*$  mesons and their decays  $D^{*\pm} \rightarrow D^0 \pi_{\pm}^{\pm}$  with the characteristic signature of the 'slow pion' with a momentum of only 40 MeV in the  $D^{*\pm}$  rest frame and the subsequent decay of the  $D^0$  into kaons or pions. Also measurements of inclusive  $D^0$  production via their semileptonic decays are being worked on.

Figure 10.17 shows the  $F_2^{charm}$  data from H1 and ZEUS at six  $Q^2$  values together with the  $F_2^{charm}$  as obtained from the NLO QCD fit described here. Although the central fit tends to underestimate the data at low  $x$ , where a steep rise of  $F_2^{charm}$  has been found,

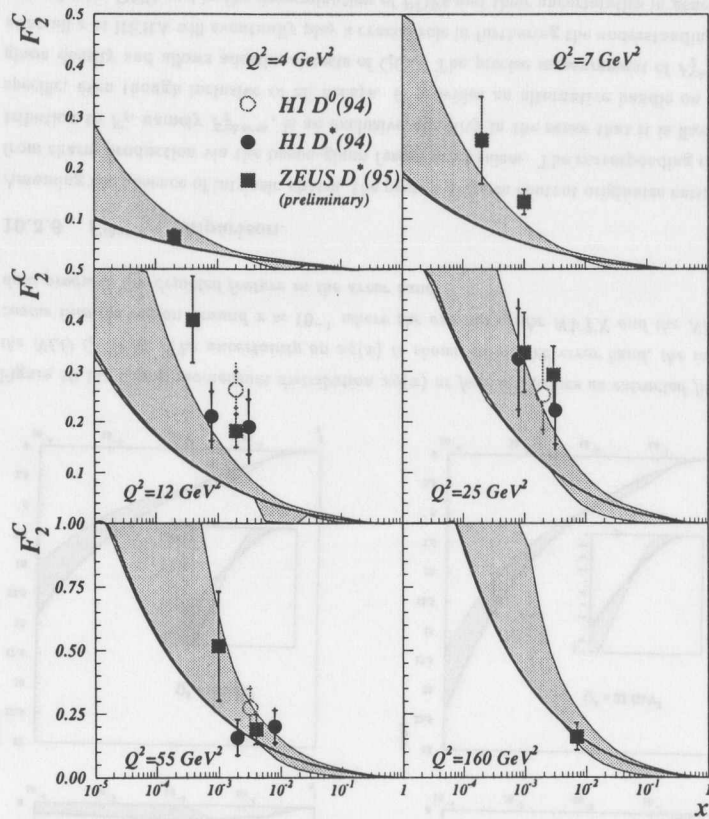


Figure 10.17:  $F_2^{charm}$  versus  $x$  for fixed  $Q^2$  as measured by H1 (open and closed circles) and ZEUS (closed rectangles) together with the NLO QCD fit (solid line). The uncertainty on  $F_2^{charm}$  from the fit is shown as shaded error band. The 'central' fit is the thick line.

the present precision on the data as well as the fit do not allow any strong conclusions to be drawn. The result from the simplified charm treatment in the evolution and the present data are in reasonable agreement. Nevertheless the increasing precision of future  $F_2^{charm}$  measurements and their exceptional importance for accurate QCD tests require a refinement of the current charm evolution, in particular of the turn-on behaviour at the mass threshold. At very high  $Q^2$  the leading order contribution of the photon gluon fusion (PGF) process  $\gamma^*g \rightarrow c\bar{c}$  to  $F_2$  behaves as  $F_2 \sim \alpha_s(\mu_r^2) \ln(Q^2/m_c^2)$ . Higher order

corrections also behave as  $(\alpha_s \ln(Q^2/m_c^2))^n$ , so that fixed order perturbation theory breaks down. Thus the charm quark will have to be included as a parton in the DGLAP evolution. The exact next to leading order corrections to the PGF structure function have been calculated in [33]. The consistent inclusion of the heavy quark mass in the DGLAP splitting functions without losing the original parton interpretation has been addressed recently in [34, 35]. Both studies are based on the generalised variable flavour number formalism [36] which provides a consistent picture from the mass threshold to the asymptotic region  $Q^2 \rightarrow \infty$ . They find a better description of the experimental data in their global analyses. These new fits and correspondingly the adopted treatment of the charm quark in the DGLAP evolution await confrontation with more and more precise  $F_2^{charm}$  data from HERA.

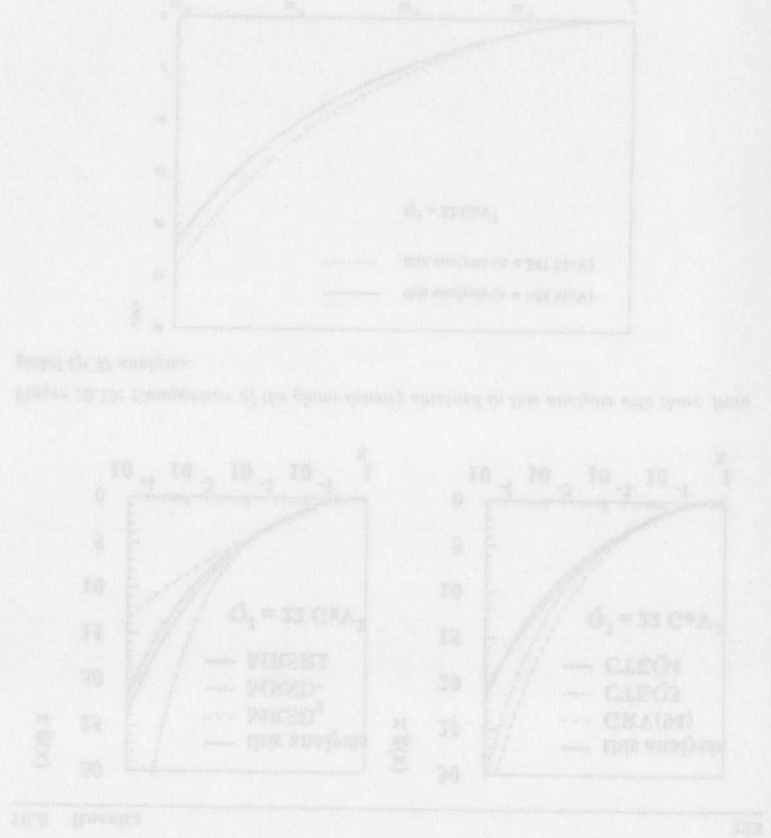


Figure 10.18:  $F_2^{charm}$  versus  $x$  for fixed  $Q^2$  as measured by H1 (open and closed circles) and ZEUS (closed rectangles) together with the NLO QCD fit (solid line). The uncertainty on  $F_2^{charm}$  from the fit is shown as shaded error band. The 'central' fit is the thick line.

## Chapter 11

### Conclusion.

This thesis has presented an independent measurement of the proton structure function  $F_2$ , studies of phenomenological models describing  $F_2$  and a determination of the gluon momentum distribution in the proton.

The  $F_2$  measurement is based on a data sample corresponding to an integrated luminosity of  $2.4 \text{ pb}^{-1}$  collected in 1994 with the ZEUS detector at HERA. It extends the accessible kinematic range to lower and higher values of  $x$  and  $Q^2$  compared to the 1993 data and provides an overlap with the fixed target region.  $F_2$  has been measured for  $3.5 \cdot 10^{-5} \leq x \leq 0.8$  and  $1.5 \leq Q^2 \leq 5000 \text{ GeV}^2$ .

The low  $Q^2$  data have been analysed using events with a shifted interaction point or with collinear photon emission in the initial state. The analysis of the medium and high  $Q^2$  data has been carried out using a new kinematic reconstruction method which provides an improved resolution. In the region of  $3 \leq Q^2 \leq 100 \text{ GeV}^2$ , where the statistical errors are  $\sim 2-4\%$ , the systematic uncertainties have been reduced to below 5%, whereas the very low and the higher  $Q^2$  regions are at present dominated by limited statistics.

The most striking feature of the measured proton structure function  $F_2$  is its strong rise with decreasing  $x$ , which has been confirmed at medium and high  $Q^2$  and has been found to persist down to  $Q^2$  as low as  $1.5 \text{ GeV}^2$ . With increasing  $Q^2$  this rise gets more pronounced, which is a result of the strong scaling violations at low  $x$ . In the region of overlap the present  $F_2$  measurement is consistent with the fixed target data.

The latest parametrisations of the parton distribution functions (MRSR and CTEQ4), which have been fitted to 1994 HERA and other data using the DGLAP evolution equations, describe the  $F_2$  data very well and are in most of the  $(x, Q^2)$  region essentially indistinguishable. Previous parametrisations show deviations from the data mainly at low  $Q^2$ . The dynamical parton model of GRV, an almost parameter free prediction of perturbative QCD using a very low starting scale and the DGLAP evolution equations, is found to be able to describe the data adequately over the entire  $Q^2$  range. The Regge-inspired parametrisation of Donnachie-Landshoff, however, undershoots the  $F_2$

data at low  $x$  and is ruled out at  $Q^2 \geq 2 \text{ GeV}^2$ .

$F_2$  at low  $x$  exhibits approximate logarithmic scaling in  $x$  and  $Q^2$  which allows a simple description of the data at low  $x$ . If this observation were found to persist to asymptotically low  $x$  the unitarity bound could get saturated, but not violated.

The perturbative QCD predictions for the behaviour of  $F_2$  at small  $x$  vary for the two scenarios, where the  $x$  dependence of the input gluon distribution at a starting scale  $Q_0^2$  is singular ( $\sim x^{-\lambda}$ ;  $\lambda \gtrsim 0.3$ ) or soft. The latter case is investigated in further detail. The low  $x$  prediction that  $F_2$  exhibits double asymptotic scaling is confirmed. Furthermore it is found that this feature of the data is described better if the calculations are carried out in next to leading order so that scaling violations, mainly observed at low  $Q^2$ , are reduced. Double asymptotic scaling provides a very economic description of the data. Assuming a soft input gluon distribution the functional form of  $F_2$  at low  $x$ , as calculated in the double asymptotic scaling approach, has been found to be sensitive to the value of the strong coupling constant  $\alpha_s$ . Exploiting this dependence the expected function is fitted to the present  $F_2$  data. The obtained value of  $\alpha_s(M_Z^2) = 0.115 \pm 0.002(\text{exp.}) \pm 0.006(\text{sys.}) \pm 0.009(\text{theor.})$  is consistent with other determinations of  $\alpha_s$  from DIS and the world average.

A QCD analysis of the present  $F_2$  data is performed. Using the DGLAP evolution equations in next to leading order the measured  $(x, Q^2)$  dependence of  $F_2$  can be very well described in the full kinematic range. Only at  $Q^2 < 3 \text{ GeV}^2$  a slight undershooting of the data indicates that a refined treatment of the heavy charm quarks becomes important in this region. From this QCD fit the gluon momentum distribution of the proton is extracted taking the error correlation of the  $F_2$  data into account. The gluon density is found to be strongly rising at low  $x$ .

Low  $x$  DIS physics has been exciting recently through the interaction of theoretical speculations and experimental HERA results. However, important questions remain to be answered. In order to investigate further how low in  $x$  the conventional DGLAP evolution can describe the data or if  $\ln \frac{1}{x}$  terms have to be included in the calculations requires an improved precision of the measurements. The rise in the gluon density at low  $x$  has to be determined with increased precision and needs to be complemented by other studies, such as  $J/\psi$  production and  $F_2^{\text{charm}}$ . A measurement of the longitudinal structure function  $F_L$ , also possible using initial state radiation events, could serve as a consistency check and provide confidence in the structure function results obtained so far.

Electron proton scattering continues to be a powerful tool in the study of the structure of the proton and in testing QCD to unprecedented detail.

## Appendix 12

## The Photon Lifetime.

The deep inelastic electron proton scattering process, depicted in figure 12.1, can be viewed as the scattering of virtual photons off the proton. The DIS  $ep$  cross section

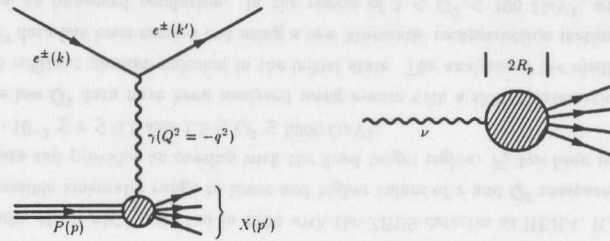


Figure 12.1: The deep inelastic  $ep$  scattering (left) can also be viewed as scattering of virtual photons off protons (right).

can be expressed as a product of the flux of virtual photons and the total cross section  $\sigma_{tot}^{\gamma p}$  for the scattering of virtual photons off protons [140]. This separation, however, is only meaningful provided that the lifetime of the virtual photon is large compared to the interaction time [141]

$$\tau_{life} \gg \tau_{interaction} \quad (12.1)$$

Let  $R_p$  be the proton radius and  $\beta$  the photons relativistic velocity,  $\nu$  its energy and  $Q^2$  its invariant mass. In the proton rest frame the interaction time of the photon proton scattering is then given by

$$\begin{aligned} \tau_{interaction} &= \frac{2R_p}{\beta} = \frac{2R_p}{(p/\nu)} = \frac{2R_p\nu}{\sqrt{\nu^2 + Q^2}} \\ &= \frac{2R_p}{\sqrt{1 + \frac{4M^2x^2}{Q^2}}} \end{aligned}$$

with the Bjorken scaling variable  $x = \frac{Q^2}{2M\nu}$  and  $M$  the proton mass.

The energy uncertainty of the photon is

$$\begin{aligned} \Delta\nu &= \left( \sqrt{\nu^2 + Q^2} - \nu \right) \\ &\approx \frac{Q^2}{2\nu} \end{aligned}$$

so that its lifetime turns out to be

$$\begin{aligned} \Delta\tau_{life} &= \frac{1}{\Delta\nu} = \frac{2\nu}{Q^2} \\ &= \frac{1}{Mx} \end{aligned}$$

Therefore, the condition 12.1 on the photon lifetime implies that the considered separation of the  $ep$  scattering into photon flux and photon-proton cross section is only valid if

$$x \ll \frac{\sqrt{1 + \frac{4M^2x^2}{Q^2}}}{2R_pM}$$

or with  $R_p \simeq 4 \text{ GeV}^{-1}$

$$x \ll 10^{-2}.$$

# Appendix 13

## $F_2$ Tables.

$Q^2$	$Q^2$ -range	$x$	$x$ -range	events	No.BG	$F_2 \pm stat. \pm syst.$
3.5	3.0-4.0	$6.3 \cdot 10^{-5}$	$5.0-8.0 \cdot 10^{-5}$	2352	127.2(0.0)	$0.973 \pm 0.058^{+0.111}_{-0.139}$
3.5	3.0-4.0	$1.0 \cdot 10^{-4}$	$0.8-1.3 \cdot 10^{-4}$	3576	103.3(40.5)	$0.921 \pm 0.039^{+0.047}_{-0.058}$
4.5	4.0-5.0	$1.0 \cdot 10^{-4}$	$0.8-1.3 \cdot 10^{-4}$	4404	222.5(20.7)	$0.991 \pm 0.025^{+0.078}_{-0.084}$
4.5	4.0-5.0	$1.6 \cdot 10^{-4}$	$1.3-2.0 \cdot 10^{-4}$	4022	79.5(18.5)	$0.997 \pm 0.024^{+0.048}_{-0.048}$
4.5	4.0-5.0	$2.5 \cdot 10^{-4}$	$2.0-3.2 \cdot 10^{-4}$	2634	7.9(10.3)	$0.911 \pm 0.029^{+0.048}_{-0.050}$
6.5	5.0-7.0	$1.0 \cdot 10^{-4}$	$0.8-1.3 \cdot 10^{-4}$	2650	127.2(37.9)	$1.190 \pm 0.034^{+0.106}_{-0.098}$
6.5	5.0-7.0	$1.6 \cdot 10^{-4}$	$1.3-2.0 \cdot 10^{-4}$	7481	174.8(91.7)	$1.145 \pm 0.019^{+0.054}_{-0.053}$
6.5	5.0-7.0	$2.5 \cdot 10^{-4}$	$2.0-3.2 \cdot 10^{-4}$	7977	87.4(61.4)	$1.034 \pm 0.016^{+0.027}_{-0.036}$
6.5	5.0-7.0	$4.0 \cdot 10^{-4}$	$3.2-5.0 \cdot 10^{-4}$	6052	0.0(129.5)	$0.885 \pm 0.018^{+0.036}_{-0.031}$
6.5	5.0-7.0	$6.3 \cdot 10^{-4}$	$5.0-8.0 \cdot 10^{-4}$	5286	0.0(26.9)	$0.839 \pm 0.017^{+0.033}_{-0.031}$
6.5	5.0-7.0	$1.0 \cdot 10^{-3}$	$0.8-1.3 \cdot 10^{-3}$	4643	0.0(10.3)	$0.753 \pm 0.015^{+0.027}_{-0.033}$
6.5	5.0-7.0	$1.6 \cdot 10^{-3}$	$1.3-2.0 \cdot 10^{-3}$	3944	0.0(37.1)	$0.695 \pm 0.017^{+0.027}_{-0.021}$
6.5	5.0-9.0	$2.5 \cdot 10^{-3}$	$2.0-3.2 \cdot 10^{-3}$	8677	0.0(116.8)	$0.630 \pm 0.010^{+0.020}_{-0.023}$
6.5	5.0-9.0	$4.0 \cdot 10^{-3}$	$3.2-8.0 \cdot 10^{-3}$	16746	0.0(114.9)	$0.599 \pm 0.008^{+0.021}_{-0.025}$
6.5	5.0-9.0	$1.6 \cdot 10^{-2}$	$0.8-3.2 \cdot 10^{-2}$	18495	0.0(149.4)	$0.462 \pm 0.006^{+0.017}_{-0.017}$
6.5	5.0-9.0	$4.0 \cdot 10^{-2}$	$0.3-1.3 \cdot 10^{-1}$	7326	0.0(92.6)	$0.382 \pm 0.008^{+0.019}_{-0.019}$
8.5	7.0-9.0	$1.6 \cdot 10^{-4}$	$1.3-2.0 \cdot 10^{-4}$	2984	119.2(28.4)	$1.240 \pm 0.031^{+0.071}_{-0.081}$
8.5	7.0-9.0	$2.5 \cdot 10^{-4}$	$2.0-3.2 \cdot 10^{-4}$	5639	95.4(50.2)	$1.117 \pm 0.022^{+0.046}_{-0.023}$
8.5	7.0-9.0	$4.0 \cdot 10^{-4}$	$3.2-5.0 \cdot 10^{-4}$	5305	7.9(32.2)	$0.974 \pm 0.019^{+0.035}_{-0.035}$
8.5	7.0-9.0	$6.3 \cdot 10^{-4}$	$5.0-8.0 \cdot 10^{-4}$	5247	0.0(0.0)	$0.918 \pm 0.017^{+0.031}_{-0.022}$
8.5	7.0-9.0	$1.0 \cdot 10^{-3}$	$0.8-1.3 \cdot 10^{-3}$	5029	0.0(78.8)	$0.837 \pm 0.017^{+0.022}_{-0.025}$
8.5	7.0-9.0	$1.6 \cdot 10^{-3}$	$1.3-2.0 \cdot 10^{-3}$	3994	0.0(45.0)	$0.721 \pm 0.017^{+0.025}_{-0.016}$
10.0	9.0-11.0	$1.6 \cdot 10^{-4}$	$1.3-2.0 \cdot 10^{-4}$	644	55.6(0.0)	$1.290 \pm 0.071^{+0.133}_{-0.149}$
10.0	9.0-11.0	$2.5 \cdot 10^{-4}$	$2.0-3.2 \cdot 10^{-4}$	3114	79.5(30.3)	$1.172 \pm 0.029^{+0.054}_{-0.053}$
10.0	9.0-11.0	$4.0 \cdot 10^{-4}$	$3.2-5.0 \cdot 10^{-4}$	3632	15.9(41.0)	$1.107 \pm 0.025^{+0.036}_{-0.036}$
10.0	9.0-11.0	$6.3 \cdot 10^{-4}$	$5.0-8.0 \cdot 10^{-4}$	3796	0.0(70.7)	$0.960 \pm 0.021^{+0.030}_{-0.021}$
10.0	9.0-11.0	$1.0 \cdot 10^{-3}$	$0.8-1.3 \cdot 10^{-3}$	3662	7.9(21.0)	$0.855 \pm 0.020^{+0.031}_{-0.016}$
10.0	9.0-11.0	$1.6 \cdot 10^{-3}$	$1.3-2.0 \cdot 10^{-3}$	3138	0.0(11.7)	$0.775 \pm 0.021^{+0.033}_{-0.023}$
10.0	9.0-11.0	$2.5 \cdot 10^{-3}$	$2.0-3.2 \cdot 10^{-3}$	3403	0.0(20.2)	$0.728 \pm 0.017^{+0.017}_{-0.023}$
10.0	9.0-13.0	$6.3 \cdot 10^{-3}$	$3.2-8.0 \cdot 10^{-3}$	11803	0.0(67.7)	$0.591 \pm 0.007^{+0.012}_{-0.012}$
10.0	9.0-13.0	$1.6 \cdot 10^{-2}$	$0.8-3.2 \cdot 10^{-2}$	15734	0.0(70.3)	$0.504 \pm 0.006^{+0.013}_{-0.013}$
10.0	9.0-13.0	$8.1 \cdot 10^{-2}$	$0.3-1.3 \cdot 10^{-1}$	6342	0.0(38.9)	$0.361 \pm 0.006^{+0.033}_{-0.016}$

Table 13.1: The  $F_2(x, Q^2)$  from the NVTX ( $p_T$ ) analysis. The bin boundaries of  $x$  and  $Q^2$  at which  $F_2$  is determined are listed. The numbers of events before background subtraction as well as the estimated photoproduction background and beam-gas background (the latter in brackets) for each bin are given. An overall normalisation error of 2% is not included

$Q^2$	$Q^2$ -range	$x$	$x$ -range	events	No.BG	$F_2 \pm stat. \pm syst.$
12.0	11.0-13.0	$2.5 \cdot 10^{-4}$	$2.0-3.2 \cdot 10^{-4}$	1746	79.5(0.0)	$1.314 \pm 0.042^{+0.075}_{-0.087}$
12.0	11.0-13.0	$4.0 \cdot 10^{-4}$	$3.2-5.0 \cdot 10^{-4}$	2408	39.7(8.7)	$1.125 \pm 0.031^{+0.043}_{-0.040}$
12.0	11.0-13.0	$6.3 \cdot 10^{-4}$	$5.0-8.0 \cdot 10^{-4}$	2657	23.8(31.4)	$1.058 \pm 0.027^{+0.048}_{-0.035}$
12.0	11.0-13.0	$1.0 \cdot 10^{-3}$	$0.8-1.3 \cdot 10^{-3}$	2698	0.0(50.4)	$0.926 \pm 0.023^{+0.035}_{-0.036}$
12.0	11.0-13.0	$1.6 \cdot 10^{-3}$	$1.3-2.0 \cdot 10^{-3}$	2217	0.0(39.5)	$0.785 \pm 0.023^{+0.016}_{-0.023}$
12.0	11.0-13.0	$2.5 \cdot 10^{-3}$	$2.0-3.2 \cdot 10^{-3}$	2373	0.0(10.3)	$0.735 \pm 0.021^{+0.037}_{-0.037}$
15.0	13.0-16.0	$2.5 \cdot 10^{-4}$	$2.0-3.2 \cdot 10^{-4}$	956	31.8(19.8)	$1.464 \pm 0.061^{+0.117}_{-0.096}$
15.0	13.0-16.0	$4.0 \cdot 10^{-4}$	$3.2-5.0 \cdot 10^{-4}$	2411	47.7(10.3)	$1.305 \pm 0.033^{+0.043}_{-0.042}$
15.0	13.0-16.0	$6.3 \cdot 10^{-4}$	$5.0-8.0 \cdot 10^{-4}$	2610	39.7(19.7)	$1.056 \pm 0.026^{+0.045}_{-0.045}$
15.0	13.0-16.0	$1.0 \cdot 10^{-3}$	$0.8-1.3 \cdot 10^{-3}$	2678	0.0(0.0)	$0.986 \pm 0.024^{+0.037}_{-0.035}$
15.0	13.0-16.0	$1.6 \cdot 10^{-3}$	$1.3-2.0 \cdot 10^{-3}$	2318	0.0(9.3)	$0.906 \pm 0.024^{+0.031}_{-0.017}$
15.0	13.0-16.0	$2.5 \cdot 10^{-3}$	$2.0-3.2 \cdot 10^{-3}$	2399	0.0(10.1)	$0.825 \pm 0.022^{+0.030}_{-0.020}$
15.0	13.0-16.0	$6.3 \cdot 10^{-3}$	$3.2-8.0 \cdot 10^{-3}$	4856	0.0(0.0)	$0.661 \pm 0.013^{+0.034}_{-0.023}$
15.0	13.0-20.0	$1.6 \cdot 10^{-2}$	$0.8-3.2 \cdot 10^{-2}$	13065	0.0(50.9)	$0.528 \pm 0.006^{+0.011}_{-0.011}$
15.0	13.0-20.0	$8.1 \cdot 10^{-2}$	$0.3-1.3 \cdot 10^{-1}$	5715	0.0(48.7)	$0.354 \pm 0.006^{+0.036}_{-0.017}$
18.0	16.0-20.0	$4.0 \cdot 10^{-4}$	$3.2-5.0 \cdot 10^{-4}$	1762	55.6(10.6)	$1.469 \pm 0.046^{+0.108}_{-0.046}$
18.0	16.0-20.0	$6.3 \cdot 10^{-4}$	$5.0-8.0 \cdot 10^{-4}$	2182	39.7(19.3)	$1.197 \pm 0.033^{+0.043}_{-0.037}$
18.0	16.0-20.0	$1.0 \cdot 10^{-3}$	$0.8-1.3 \cdot 10^{-3}$	2357	0.0(28.3)	$1.036 \pm 0.029^{+0.037}_{-0.037}$
18.0	16.0-20.0	$1.6 \cdot 10^{-3}$	$1.3-2.0 \cdot 10^{-3}$	2025	0.0(0.0)	$0.938 \pm 0.027^{+0.037}_{-0.026}$
18.0	16.0-20.0	$2.5 \cdot 10^{-3}$	$2.0-3.2 \cdot 10^{-3}$	2095	0.0(0.0)	$0.876 \pm 0.025^{+0.032}_{-0.038}$
18.0	16.0-20.0	$6.3 \cdot 10^{-3}$	$3.2-8.0 \cdot 10^{-3}$	3901	0.0(29.2)	$0.635 \pm 0.013^{+0.024}_{-0.014}$
22.0	20.0-25.0	$4.0 \cdot 10^{-4}$	$3.2-5.0 \cdot 10^{-4}$	1026	15.9(0.0)	$1.493 \pm 0.065^{+0.109}_{-0.039}$
22.0	20.0-25.0	$6.3 \cdot 10^{-4}$	$5.0-8.0 \cdot 10^{-4}$	1620	15.9(18.6)	$1.305 \pm 0.042^{+0.043}_{-0.043}$
22.0	20.0-25.0	$1.0 \cdot 10^{-3}$	$0.8-1.3 \cdot 10^{-3}$	1726	15.9(0.0)	$1.150 \pm 0.035^{+0.052}_{-0.052}$
22.0	20.0-25.0	$1.6 \cdot 10^{-3}$	$1.3-2.0 \cdot 10^{-3}$	1575	0.0(9.8)	$0.977 \pm 0.031^{+0.039}_{-0.026}$
22.0	20.0-25.0	$2.5 \cdot 10^{-3}$	$2.0-3.2 \cdot 10^{-3}$	1651	0.0(0.0)	$0.889 \pm 0.027^{+0.039}_{-0.039}$
22.0	20.0-25.0	$4.0 \cdot 10^{-3}$	$3.2-5.0 \cdot 10^{-3}$	1465	0.0(0.0)	$0.752 \pm 0.024^{+0.029}_{-0.030}$
22.0	20.0-25.0	$6.3 \cdot 10^{-3}$	$5.0-8.0 \cdot 10^{-3}$	1600	0.0(0.0)	$0.702 \pm 0.022^{+0.030}_{-0.020}$
22.0	20.0-32.0	$1.0 \cdot 10^{-2}$	$0.8-1.3 \cdot 10^{-2}$	3039	0.0(10.8)	$0.596 \pm 0.014^{+0.013}_{-0.027}$
22.0	20.0-32.0	$2.5 \cdot 10^{-2}$	$1.3-5.0 \cdot 10^{-2}$	7313	0.0(9.5)	$0.474 \pm 0.007^{+0.021}_{-0.009}$
22.0	20.0-32.0	$8.1 \cdot 10^{-2}$	$0.5-1.3 \cdot 10^{-1}$	2151	0.0(0.0)	$0.347 \pm 0.009^{+0.044}_{-0.019}$
27.0	25.0-32.0	$6.3 \cdot 10^{-4}$	$5.0-8.0 \cdot 10^{-4}$	1839	39.7(10.4)	$1.434 \pm 0.042^{+0.047}_{-0.072}$
27.0	25.0-32.0	$1.0 \cdot 10^{-3}$	$0.8-1.3 \cdot 10^{-3}$	1495	15.9(0.0)	$1.161 \pm 0.037^{+0.065}_{-0.026}$
27.0	25.0-32.0	$1.6 \cdot 10^{-3}$	$1.3-2.0 \cdot 10^{-3}$	1327	0.0(11.3)	$1.165 \pm 0.040^{+0.050}_{-0.078}$
27.0	25.0-32.0	$2.5 \cdot 10^{-3}$	$2.0-3.2 \cdot 10^{-3}$	1193	0.0(13.3)	$0.894 \pm 0.032^{+0.062}_{-0.062}$
27.0	25.0-32.0	$4.0 \cdot 10^{-3}$	$3.2-5.0 \cdot 10^{-3}$	1117	7.9(9.9)	$0.777 \pm 0.029^{+0.015}_{-0.030}$
27.0	25.0-32.0	$6.3 \cdot 10^{-3}$	$5.0-8.0 \cdot 10^{-3}$	1164	0.0(0.0)	$0.647 \pm 0.023^{+0.046}_{-0.052}$
35.0	32.0-40.0	$6.3 \cdot 10^{-4}$	$5.0-8.0 \cdot 10^{-4}$	886	15.9(9.8)	$1.557 \pm 0.066^{+0.110}_{-0.081}$
35.0	32.0-40.0	$1.0 \cdot 10^{-3}$	$0.8-1.3 \cdot 10^{-3}$	1495	7.9(0.0)	$1.337 \pm 0.043^{+0.034}_{-0.034}$
35.0	32.0-40.0	$1.6 \cdot 10^{-3}$	$1.3-2.0 \cdot 10^{-3}$	1115	0.0(0.0)	$1.120 \pm 0.041^{+0.066}_{-0.023}$
35.0	32.0-40.0	$2.5 \cdot 10^{-3}$	$2.0-3.2 \cdot 10^{-3}$	1085	0.0(0.0)	$1.057 \pm 0.040^{+0.044}_{-0.063}$
35.0	32.0-40.0	$4.0 \cdot 10^{-3}$	$3.2-5.0 \cdot 10^{-3}$	884	0.0(0.0)	$0.919 \pm 0.039^{+0.026}_{-0.026}$
35.0	32.0-40.0	$6.3 \cdot 10^{-3}$	$5.0-8.0 \cdot 10^{-3}$	842	0.0(0.0)	$0.779 \pm 0.034^{+0.027}_{-0.035}$
35.0	32.0-40.0	$1.0 \cdot 10^{-2}$	$0.8-1.3 \cdot 10^{-2}$	857	0.0(18.9)	$0.677 \pm 0.036^{+0.051}_{-0.037}$
35.0	32.0-50.0	$1.6 \cdot 10^{-2}$	$1.3-2.0 \cdot 10^{-2}$	1512	0.0(0.0)	$0.586 \pm 0.019^{+0.030}_{-0.016}$
35.0	32.0-50.0	$2.5 \cdot 10^{-2}$	$2.0-5.0 \cdot 10^{-2}$	2746	0.0(0.0)	$0.606 \pm 0.015^{+0.037}_{-0.043}$
35.0	32.0-50.0	$8.1 \cdot 10^{-2}$	$0.5-1.3 \cdot 10^{-1}$	1298	0.0(10.7)	$0.489 \pm 0.017^{+0.049}_{-0.048}$
35.0	32.0-50.0	$2.0 \cdot 10^{-1}$	$1.3-8.0 \cdot 10^{-1}$	376	0.0(9.8)	$0.378 \pm 0.025^{+0.029}_{-0.055}$

Table 13.2: NVTX- $F_2(x, Q^2)$  ( $p_T$ ), continued.

Q <sup>2</sup>	Q <sup>2</sup> -range	x	x-range	events	No.BG	F <sub>2</sub> ± stat. ± syst.
45.0	40.0-50.0	1.0 · 10 <sup>-3</sup>	0.8-1.3 · 10 <sup>-3</sup>	1335	23.8(0.0)	1.414 ± 0.051 ± 0.053
45.0	40.0-50.0	1.6 · 10 <sup>-3</sup>	1.3-2.0 · 10 <sup>-3</sup>	1117	23.8(0.0)	1.139 ± 0.042 ± 0.046
45.0	40.0-50.0	2.5 · 10 <sup>-3</sup>	2.0-3.2 · 10 <sup>-3</sup>	1087	0.0(10.5)	1.065 ± 0.041 ± 0.043
45.0	40.0-50.0	4.0 · 10 <sup>-3</sup>	3.2-5.0 · 10 <sup>-3</sup>	876	0.0(10.2)	0.899 ± 0.038 ± 0.037
45.0	40.0-50.0	6.3 · 10 <sup>-3</sup>	5.0-8.0 · 10 <sup>-3</sup>	819	0.0(10.1)	0.787 ± 0.035 ± 0.029
45.0	40.0-50.0	1.0 · 10 <sup>-2</sup>	0.8-1.3 · 10 <sup>-2</sup>	832	0.0(10.3)	0.684 ± 0.030 ± 0.034
60.0	50.0-65.0	1.0 · 10 <sup>-3</sup>	0.8-1.3 · 10 <sup>-3</sup>	752	7.9(0.0)	1.529 ± 0.073 ± 0.063
60.0	50.0-65.0	1.6 · 10 <sup>-3</sup>	1.3-2.0 · 10 <sup>-3</sup>	1122	15.9(0.0)	1.244 ± 0.046 ± 0.049
60.0	50.0-65.0	2.5 · 10 <sup>-3</sup>	2.0-3.2 · 10 <sup>-3</sup>	1154	7.9(9.3)	1.074 ± 0.039 ± 0.047
60.0	50.0-65.0	4.0 · 10 <sup>-3</sup>	3.2-5.0 · 10 <sup>-3</sup>	1014	0.0(0.0)	1.023 ± 0.041 ± 0.032
60.0	50.0-65.0	6.3 · 10 <sup>-3</sup>	5.0-8.0 · 10 <sup>-3</sup>	971	0.0(0.0)	0.901 ± 0.037 ± 0.041
60.0	50.0-65.0	1.0 · 10 <sup>-2</sup>	0.8-1.3 · 10 <sup>-2</sup>	842	0.0(0.0)	0.660 ± 0.028 ± 0.028
60.0	50.0-65.0	1.6 · 10 <sup>-2</sup>	1.3-2.0 · 10 <sup>-2</sup>	791	0.0(0.0)	0.601 ± 0.026 ± 0.035
60.0	50.0-65.0	2.5 · 10 <sup>-2</sup>	2.0-5.0 · 10 <sup>-2</sup>	1682	0.0(0.0)	0.658 ± 0.021 ± 0.009
60.0	50.0-65.0	8.1 · 10 <sup>-2</sup>	0.5-1.3 · 10 <sup>-1</sup>	1061	0.0(0.0)	0.534 ± 0.021 ± 0.021
60.0	50.0-65.0	2.0 · 10 <sup>-1</sup>	1.3-8.0 · 10 <sup>-1</sup>	231	0.0(0.0)	0.325 ± 0.027 ± 0.023
70.0	65.0-85.0	1.6 · 10 <sup>-3</sup>	1.3-2.0 · 10 <sup>-3</sup>	783	15.9(0.0)	1.279 ± 0.057 ± 0.059
70.0	65.0-85.0	2.5 · 10 <sup>-3</sup>	2.0-3.2 · 10 <sup>-3</sup>	1002	0.0(21.0)	1.149 ± 0.046 ± 0.034
70.0	65.0-85.0	4.0 · 10 <sup>-3</sup>	3.2-5.0 · 10 <sup>-3</sup>	829	0.0(0.0)	0.928 ± 0.040 ± 0.047
70.0	65.0-85.0	6.3 · 10 <sup>-3</sup>	5.0-8.0 · 10 <sup>-3</sup>	750	0.0(10.9)	0.838 ± 0.039 ± 0.035
70.0	65.0-85.0	1.0 · 10 <sup>-2</sup>	0.8-1.3 · 10 <sup>-2</sup>	767	0.0(0.0)	0.772 ± 0.035 ± 0.040
70.0	65.0-85.0	1.6 · 10 <sup>-2</sup>	1.3-2.0 · 10 <sup>-2</sup>	662	0.0(0.0)	0.657 ± 0.032 ± 0.034
70.0	65.0-85.0	2.5 · 10 <sup>-2</sup>	2.0-5.0 · 10 <sup>-2</sup>	1496	0.0(0.0)	0.613 ± 0.020 ± 0.017
70.0	65.0-85.0	8.1 · 10 <sup>-2</sup>	0.5-1.3 · 10 <sup>-1</sup>	1026	0.0(0.0)	0.473 ± 0.019 ± 0.037
70.0	65.0-85.0	2.0 · 10 <sup>-1</sup>	1.3-8.0 · 10 <sup>-1</sup>	232	0.0(0.0)	0.261 ± 0.021 ± 0.025
90.0	85.0-110.0	1.6 · 10 <sup>-3</sup>	1.3-2.0 · 10 <sup>-3</sup>	308	7.9(0.0)	1.425 ± 0.103 ± 0.148
90.0	85.0-110.0	2.5 · 10 <sup>-3</sup>	2.0-3.2 · 10 <sup>-3</sup>	678	7.9(10.3)	1.182 ± 0.057 ± 0.155
90.0	85.0-110.0	4.0 · 10 <sup>-3</sup>	3.2-5.0 · 10 <sup>-3</sup>	641	0.0(29.6)	0.989 ± 0.050 ± 0.119
90.0	85.0-110.0	6.3 · 10 <sup>-3</sup>	5.0-8.0 · 10 <sup>-3</sup>	618	0.0(0.0)	0.956 ± 0.049 ± 0.063
90.0	85.0-110.0	1.0 · 10 <sup>-2</sup>	0.8-1.3 · 10 <sup>-2</sup>	625	0.0(9.8)	0.809 ± 0.041 ± 0.025
90.0	85.0-110.0	1.6 · 10 <sup>-2</sup>	1.3-2.0 · 10 <sup>-2</sup>	456	0.0(0.0)	0.613 ± 0.036 ± 0.048
90.0	85.0-110.0	2.5 · 10 <sup>-2</sup>	2.0-3.2 · 10 <sup>-2</sup>	518	0.0(0.0)	0.509 ± 0.027 ± 0.038
90.0	85.0-110.0	4.0 · 10 <sup>-2</sup>	3.2-5.0 · 10 <sup>-2</sup>	569	0.0(0.0)	0.573 ± 0.031 ± 0.020
90.0	85.0-110.0	8.1 · 10 <sup>-2</sup>	0.5-1.3 · 10 <sup>-1</sup>	779	0.0(0.0)	0.423 ± 0.019 ± 0.058
90.0	85.0-110.0	2.0 · 10 <sup>-1</sup>	1.3-3.2 · 10 <sup>-1</sup>	170	0.0(9.4)	0.246 ± 0.023 ± 0.028
120.0	110.0-140.0	2.5 · 10 <sup>-3</sup>	2.0-3.2 · 10 <sup>-3</sup>	445	15.9(20.1)	1.280 ± 0.079 ± 0.075
120.0	110.0-140.0	4.0 · 10 <sup>-3</sup>	3.2-5.0 · 10 <sup>-3</sup>	484	7.9(31.8)	1.121 ± 0.067 ± 0.088
120.0	110.0-140.0	6.3 · 10 <sup>-3</sup>	5.0-8.0 · 10 <sup>-3</sup>	450	0.0(20.4)	0.969 ± 0.059 ± 0.050
120.0	110.0-140.0	1.0 · 10 <sup>-2</sup>	0.8-1.3 · 10 <sup>-2</sup>	400	0.0(0.0)	0.791 ± 0.050 ± 0.027
120.0	110.0-140.0	1.6 · 10 <sup>-2</sup>	1.3-2.0 · 10 <sup>-2</sup>	296	0.0(0.0)	0.580 ± 0.041 ± 0.012
120.0	110.0-140.0	2.5 · 10 <sup>-2</sup>	2.0-3.2 · 10 <sup>-2</sup>	387	0.0(0.0)	0.610 ± 0.039 ± 0.029
120.0	110.0-140.0	4.0 · 10 <sup>-2</sup>	3.2-5.0 · 10 <sup>-2</sup>	350	0.0(0.0)	0.497 ± 0.033 ± 0.043
120.0	110.0-140.0	8.1 · 10 <sup>-2</sup>	0.5-1.3 · 10 <sup>-1</sup>	597	0.0(0.0)	0.434 ± 0.022 ± 0.028
120.0	110.0-140.0	2.0 · 10 <sup>-1</sup>	1.3-3.2 · 10 <sup>-1</sup>	112	0.0(0.0)	0.201 ± 0.022 ± 0.034
150.0	140.0-185.0	2.5 · 10 <sup>-3</sup>	2.0-3.2 · 10 <sup>-3</sup>	157	0.0(0.0)	1.476 ± 0.151 ± 0.152
150.0	140.0-185.0	4.0 · 10 <sup>-3</sup>	3.2-5.0 · 10 <sup>-3</sup>	361	15.9(5.7)	0.998 ± 0.066 ± 0.115
150.0	140.0-185.0	6.3 · 10 <sup>-3</sup>	5.0-8.0 · 10 <sup>-3</sup>	389	0.0(10.7)	0.941 ± 0.061 ± 0.062
150.0	140.0-185.0	1.0 · 10 <sup>-2</sup>	0.8-1.3 · 10 <sup>-2</sup>	376	0.0(0.0)	0.825 ± 0.054 ± 0.043
150.0	140.0-185.0	1.6 · 10 <sup>-2</sup>	1.3-2.0 · 10 <sup>-2</sup>	297	0.0(0.0)	0.722 ± 0.053 ± 0.037
150.0	140.0-185.0	2.5 · 10 <sup>-2</sup>	2.0-3.2 · 10 <sup>-2</sup>	339	0.0(0.0)	0.686 ± 0.048 ± 0.033
150.0	140.0-185.0	4.0 · 10 <sup>-2</sup>	3.2-5.0 · 10 <sup>-2</sup>	294	0.0(0.0)	0.513 ± 0.037 ± 0.024
150.0	140.0-185.0	8.1 · 10 <sup>-2</sup>	0.5-1.3 · 10 <sup>-1</sup>	520	0.0(0.0)	0.415 ± 0.022 ± 0.019
150.0	140.0-185.0	2.0 · 10 <sup>-1</sup>	1.3-3.2 · 10 <sup>-1</sup>	125	0.0(0.0)	0.273 ± 0.030 ± 0.014

Table 13.3: NVTX-F<sub>2</sub>(x, Q<sup>2</sup>) (pr), continued.

Q <sup>2</sup>	Q <sup>2</sup> -range	x	x-range	events	No.BG	F <sub>2</sub> ± stat. ± syst.
200.0	185.0-240.0	4.0 · 10 <sup>-3</sup>	3.2-5.0 · 10 <sup>-3</sup>	194	0.0(10.9)	1.099 ± 0.101 ± 0.108
200.0	185.0-240.0	6.3 · 10 <sup>-3</sup>	5.0-8.0 · 10 <sup>-3</sup>	261	0.0(59.3)	0.752 ± 0.064 ± 0.134
200.0	185.0-240.0	1.0 · 10 <sup>-2</sup>	0.8-1.3 · 10 <sup>-2</sup>	252	0.0(8.3)	0.866 ± 0.070 ± 0.032
200.0	185.0-240.0	1.6 · 10 <sup>-2</sup>	1.3-2.0 · 10 <sup>-2</sup>	201	0.0(9.9)	0.724 ± 0.066 ± 0.065
200.0	185.0-240.0	2.5 · 10 <sup>-2</sup>	2.0-3.2 · 10 <sup>-2</sup>	183	0.0(0.0)	0.551 ± 0.050 ± 0.065
200.0	185.0-240.0	4.0 · 10 <sup>-2</sup>	3.2-5.0 · 10 <sup>-2</sup>	200	0.0(0.0)	0.495 ± 0.043 ± 0.037
200.0	185.0-240.0	8.1 · 10 <sup>-2</sup>	0.5-1.3 · 10 <sup>-1</sup>	376	0.0(0.0)	0.425 ± 0.027 ± 0.031
200.0	185.0-240.0	2.0 · 10 <sup>-1</sup>	1.3-3.2 · 10 <sup>-1</sup>	98	0.0(0.0)	0.255 ± 0.031 ± 0.024
250.0	240.0-310.0	4.0 · 10 <sup>-3</sup>	3.2-5.0 · 10 <sup>-3</sup>	68	0.0(0.0)	1.395 ± 0.219 ± 0.239
250.0	240.0-310.0	6.3 · 10 <sup>-3</sup>	5.0-8.0 · 10 <sup>-3</sup>	189	0.0(9.8)	1.122 ± 0.107 ± 0.085
250.0	240.0-310.0	1.0 · 10 <sup>-2</sup>	0.8-1.3 · 10 <sup>-2</sup>	194	0.0(0.0)	0.958 ± 0.088 ± 0.091
250.0	240.0-310.0	1.6 · 10 <sup>-2</sup>	1.3-2.0 · 10 <sup>-2</sup>	147	0.0(0.0)	0.697 ± 0.072 ± 0.086
250.0	240.0-310.0	2.5 · 10 <sup>-2</sup>	2.0-3.2 · 10 <sup>-2</sup>	137	0.0(10.1)	0.484 ± 0.052 ± 0.061
250.0	240.0-310.0	4.0 · 10 <sup>-2</sup>	3.2-5.0 · 10 <sup>-2</sup>	147	0.0(0.0)	0.555 ± 0.058 ± 0.014
250.0	240.0-310.0	8.1 · 10 <sup>-2</sup>	0.5-1.3 · 10 <sup>-1</sup>	278	0.0(0.0)	0.421 ± 0.031 ± 0.087
250.0	240.0-310.0	2.0 · 10 <sup>-1</sup>	1.3-3.2 · 10 <sup>-1</sup>	80	0.0(0.0)	0.253 ± 0.034 ± 0.051
350.0	310.0-410.0	6.3 · 10 <sup>-3</sup>	5.0-8.0 · 10 <sup>-3</sup>	138	0.0(0.0)	1.311 ± 0.147 ± 0.095
350.0	310.0-410.0	1.0 · 10 <sup>-2</sup>	0.8-1.3 · 10 <sup>-2</sup>	153	0.0(0.0)	0.862 ± 0.087 ± 0.079
350.0	310.0-410.0	1.6 · 10 <sup>-2</sup>	1.3-2.0 · 10 <sup>-2</sup>	123	0.0(0.0)	0.725 ± 0.082 ± 0.109
350.0	310.0-410.0	2.5 · 10 <sup>-2</sup>	2.0-3.2 · 10 <sup>-2</sup>	101	0.0(0.0)	0.543 ± 0.066 ± 0.048
350.0	310.0-410.0	4.0 · 10 <sup>-2</sup>	3.2-5.0 · 10 <sup>-2</sup>	118	0.0(0.0)	0.617 ± 0.072 ± 0.103
350.0	310.0-410.0	8.1 · 10 <sup>-2</sup>	0.5-1.3 · 10 <sup>-1</sup>	199	0.0(0.0)	0.398 ± 0.035 ± 0.033
350.0	310.0-410.0	2.0 · 10 <sup>-1</sup>	1.3-3.2 · 10 <sup>-1</sup>	75	0.0(0.0)	0.232 ± 0.032 ± 0.024
450.0	410.0-530.0	6.3 · 10 <sup>-3</sup>	5.0-8.0 · 10 <sup>-3</sup>	55	0.0(0.0)	1.907 ± 0.366 ± 0.086
450.0	410.0-530.0	1.0 · 10 <sup>-2</sup>	0.8-1.3 · 10 <sup>-2</sup>	92	0.0(0.0)	0.988 ± 0.132 ± 0.100
450.0	410.0-530.0	1.6 · 10 <sup>-2</sup>	1.3-2.0 · 10 <sup>-2</sup>	91	0.0(12.1)	0.844 ± 0.122 ± 0.046
450.0	410.0-530.0	2.5 · 10 <sup>-2</sup>	2.0-3.2 · 10 <sup>-2</sup>	92	0.0(0.0)	0.732 ± 0.098 ± 0.101
450.0	410.0-530.0	4.0 · 10 <sup>-2</sup>	3.2-5.0 · 10 <sup>-2</sup>	69	0.0(0.0)	0.472 ± 0.069 ± 0.082
450.0	410.0-530.0	8.1 · 10 <sup>-2</sup>	0.5-1.3 · 10 <sup>-1</sup>	171	0.0(0.0)	0.440 ± 0.042 ± 0.026
450.0	410.0-530.0	2.0 · 10 <sup>-1</sup>	1.3-3.2 · 10 <sup>-1</sup>	74	0.0(0.0)	0.300 ± 0.044 ± 0.055
650.0	530.0-710.0	1.0 · 10 <sup>-2</sup>	0.8-1.3 · 10 <sup>-2</sup>	89	0.0(0.0)	1.263 ± 0.179 ± 0.104
650.0	530.0-710.0	1.6 · 10 <sup>-2</sup>	1.3-2.0 · 10 <sup>-2</sup>	74	0.0(9.8)	0.806 ± 0.127 ± 0.121
650.0	530.0-710.0	2.5 · 10 <sup>-2</sup>	2.0-3.2 · 10 <sup>-2</sup>	68	0.0(0.0)	0.690 ± 0.106 ± 0.084
650.0	530.0-710.0	4.0 · 10 <sup>-2</sup>	3.2-5.0 · 10 <sup>-2</sup>	47	0.0(10.3)	0.475 ± 0.095 ± 0.023
650.0	530.0-710.0	8.1 · 10 <sup>-2</sup>	0.5-1.3 · 10 <sup>-1</sup>	132	0.0(0.0)	0.467 ± 0.051 ± 0.012
650.0	530.0-710.0	2.0 · 10 <sup>-1</sup>	1.3-3.2 · 10 <sup>-1</sup>	68	0.0(10.3)	0.233 ± 0.037 ± 0.046
800.0	710.0-900.0	1.0 · 10 <sup>-2</sup>	0.8-1.3 · 10 <sup>-2</sup>	40	0.0(0.0)	1.515 ± 0.330 ± 0.097
800.0	710.0-900.0	1.6 · 10 <sup>-2</sup>	1.3-2.0 · 10 <sup>-2</sup>	39	0.0(0.0)	0.806 ± 0.163 ± 0.211
800.0	710.0-900.0	2.5 · 10 <sup>-2</sup>	2.0-3.2 · 10 <sup>-2</sup>	45	0.0(0.0)	0.739 ± 0.140 ± 0.184
800.0	710.0-900.0	4.0 · 10 <sup>-2</sup>	3.2-5.0 · 10 <sup>-2</sup>	29	0.0(0.0)	0.412 ± 0.091 ± 0.079
800.0	710.0-900.0	8.1 · 10 <sup>-2</sup>	0.5-1.3 · 10 <sup>-1</sup>	75	0.0(10.0)	0.299 ± 0.043 ± 0.084
800.0	710.0-900.0	2.0 · 10 <sup>-1</sup>	1.3-3.2 · 10 <sup>-1</sup>	35	0.0(0.0)	0.273 ± 0.057 ± 0.106
1200.0	900.0-1300.0	1.6 · 10 <sup>-2</sup>	1.3-2.0 · 10 <sup>-2</sup>	48	0.0(0.0)	0.900 ± 0.166 ± 0.058
1200.0	900.0-1300.0	2.5 · 10 <sup>-2</sup>	2.0-3.2 · 10 <sup>-2</sup>	45	0.0(10.8)	0.539 ± 0.111 ± 0.029
1200.0	900.0-1300.0	4.0 · 10 <sup>-2</sup>	3.2-5.0 · 10 <sup>-2</sup>	34	0.0(0.0)	0.463 ± 0.096 ± 0.194
1200.0	900.0-1300.0	8.1 · 10 <sup>-2</sup>	0.5-1.3 · 10 <sup>-1</sup>	62	0.0(0.0)	0.363 ± 0.055 ± 0.019
1200.0	900.0-1300.0	2.0 · 10 <sup>-1</sup>	1.3-3.2 · 10 <sup>-1</sup>	42	0.0(0.0)	0.215 ± 0.039 ± 0.013
1200.0	900.0-1300.0	5.1 · 10 <sup>-1</sup>	3.2-8.0 · 10 <sup>-1</sup>	9	0.0(0.0)	0.107 ± 0.048 ± 0.020

Table 13.4: NVTX-F<sub>2</sub>(x, Q<sup>2</sup>) (pr), continued.

$Q^2$	$Q^2$ -range	$x$	$x$ -range	evts	No.BG	$F_2 \pm stat. \pm syst.$
1500.0	1300.0 – 1800.0	$2.5 \cdot 10^{-2}$	$2.0 - 5.0 \cdot 10^{-2}$	64	0.0(0.0)	$0.846 \pm 0.137^{+0.019}_{-0.091}$
1500.0	1300.0 – 1800.0	$8.1 \cdot 10^{-2}$	$0.5 - 1.3 \cdot 10^{-1}$	48	0.0(0.0)	$0.550 \pm 0.102^{+0.054}_{-0.038}$
1500.0	1300.0 – 1800.0	$2.0 \cdot 10^{-1}$	$1.3 - 3.2 \cdot 10^{-1}$	34	0.0(0.0)	$0.312 \pm 0.067^{+0.041}_{-0.042}$
2000.0	1800.0 – 2500.0	$4.0 \cdot 10^{-2}$	$2.0 - 5.0 \cdot 10^{-2}$	33	0.0(0.0)	$0.672 \pm 0.149^{+0.059}_{-0.081}$
2000.0	1800.0 – 2500.0	$8.1 \cdot 10^{-2}$	$0.5 - 1.3 \cdot 10^{-1}$	21	0.0(0.0)	$0.334 \pm 0.086^{+0.083}_{-0.092}$
2000.0	1800.0 – 2500.0	$2.0 \cdot 10^{-1}$	$1.3 - 3.2 \cdot 10^{-1}$	32	0.0(0.0)	$0.453 \pm 0.109^{+0.047}_{-0.102}$
3000.0	2500.0 – 3500.0	$8.1 \cdot 10^{-2}$	$0.2 - 1.3 \cdot 10^{-1}$	27	0.0(0.0)	$0.368 \pm 0.085^{+0.085}_{-0.084}$
3000.0	2500.0 – 3500.0	$2.0 \cdot 10^{-1}$	$1.3 - 8.0 \cdot 10^{-1}$	21	0.0(0.0)	$0.404 \pm 0.117^{+0.034}_{-0.066}$
5000.0	3500.0 – 15000.0	$8.1 \cdot 10^{-2}$	$0.2 - 1.3 \cdot 10^{-1}$	30	0.0(0.0)	$0.946 \pm 0.248^{+0.170}_{-0.185}$
5000.0	3500.0 – 15000.0	$2.0 \cdot 10^{-1}$	$1.3 - 8.0 \cdot 10^{-1}$	30	0.0(0.0)	$0.305 \pm 0.069^{+0.039}_{-0.000}$

Table 13.5:  $NVTX-F_2(x, Q^2)$  ( $pr$ ), continued.

$Q^2$	$Q^2$ -range	$x$	$x$ -range	events	No.BG	$F_2 \pm stat. \pm syst.$
3.5	3.0 – 4.0	$1.0 \cdot 10^{-4}$	$0.6 - 1.4 \cdot 10^{-4}$	6621	254.3(79.9)	$0.878 \pm 0.027^{+0.111}_{-0.072}$
3.5	3.0 – 4.0	$1.7 \cdot 10^{-4}$	$1.4 - 2.5 \cdot 10^{-4}$	1859	0.0(69.0)	$0.817 \pm 0.044^{+0.086}_{-0.089}$
4.5	4.0 – 5.0	$1.0 \cdot 10^{-4}$	$0.6 - 1.2 \cdot 10^{-4}$	4284	238.4(50.8)	$1.045 \pm 0.026^{+0.103}_{-0.081}$
4.5	4.0 – 5.0	$1.7 \cdot 10^{-4}$	$1.2 - 2.1 \cdot 10^{-4}$	5943	103.3(104.4)	$0.883 \pm 0.018^{+0.088}_{-0.081}$
4.5	4.0 – 5.0	$2.7 \cdot 10^{-4}$	$2.1 - 4.0 \cdot 10^{-4}$	3739	0.0(64.9)	$0.746 \pm 0.021^{+0.077}_{-0.077}$
6.5	5.0 – 7.0	$1.0 \cdot 10^{-4}$	$0.8 - 1.2 \cdot 10^{-4}$	1741	63.6(29.4)	$1.300 \pm 0.045^{+0.138}_{-0.081}$
6.5	5.0 – 7.0	$1.7 \cdot 10^{-4}$	$1.2 - 2.1 \cdot 10^{-4}$	10349	222.5(141.8)	$1.149 \pm 0.017^{+0.070}_{-0.061}$
6.5	5.0 – 7.0	$2.7 \cdot 10^{-4}$	$2.1 - 3.2 \cdot 10^{-4}$	8709	15.9(230.5)	$0.969 \pm 0.016^{+0.113}_{-0.106}$
6.5	5.0 – 7.0	$5.2 \cdot 10^{-4}$	$3.2 - 7.4 \cdot 10^{-4}$	13129	0.0(245.6)	$0.766 \pm 0.010^{+0.118}_{-0.118}$
8.5	7.0 – 9.0	$1.5 \cdot 10^{-4}$	$1.0 - 1.7 \cdot 10^{-4}$	1540	95.4(0.0)	$1.332 \pm 0.047^{+0.155}_{-0.118}$
8.5	7.0 – 9.0	$2.4 \cdot 10^{-4}$	$1.7 - 2.8 \cdot 10^{-4}$	5997	151.0(68.6)	$1.161 \pm 0.022^{+0.090}_{-0.065}$
8.5	7.0 – 9.0	$3.8 \cdot 10^{-4}$	$2.8 - 4.7 \cdot 10^{-4}$	7754	7.9(81.0)	$1.034 \pm 0.016^{+0.127}_{-0.053}$
8.5	7.0 – 9.0	$7.2 \cdot 10^{-4}$	$0.5 - 1.0 \cdot 10^{-3}$	10800	0.0(128.4)	$0.902 \pm 0.012^{+0.140}_{-0.140}$
10.0	9.0 – 11.0	$1.5 \cdot 10^{-4}$	$1.2 - 2.1 \cdot 10^{-4}$	925	63.6(0.0)	$1.354 \pm 0.064^{+0.128}_{-0.117}$
10.0	9.0 – 11.0	$2.4 \cdot 10^{-4}$	$2.1 - 3.3 \cdot 10^{-4}$	3280	63.6(20.6)	$1.242 \pm 0.030^{+0.061}_{-0.079}$
10.0	9.0 – 11.0	$5.2 \cdot 10^{-4}$	$3.3 - 5.8 \cdot 10^{-4}$	5471	7.9(93.2)	$1.042 \pm 0.019^{+0.077}_{-0.070}$
10.0	9.0 – 11.0	$7.2 \cdot 10^{-4}$	$0.6 - 1.6 \cdot 10^{-3}$	9885	0.0(140.5)	$0.968 \pm 0.014^{+0.138}_{-0.135}$
12.0	11.0 – 13.0	$1.8 \cdot 10^{-4}$	$1.5 - 2.5 \cdot 10^{-4}$	628	39.7(0.0)	$1.483 \pm 0.077^{+0.089}_{-0.127}$
12.0	11.0 – 13.0	$3.8 \cdot 10^{-4}$	$2.5 - 4.2 \cdot 10^{-4}$	2684	71.5(38.7)	$1.140 \pm 0.030^{+0.088}_{-0.070}$
12.0	11.0 – 13.0	$5.2 \cdot 10^{-4}$	$4.2 - 7.0 \cdot 10^{-4}$	3455	7.9(31.6)	$1.163 \pm 0.026^{+0.073}_{-0.096}$
12.0	11.0 – 13.0	$1.2 \cdot 10^{-3}$	$0.7 - 1.5 \cdot 10^{-3}$	4842	0.0(88.1)	$0.891 \pm 0.017^{+0.119}_{-0.119}$
15.0	13.0 – 16.0	$2.4 \cdot 10^{-4}$	$1.8 - 3.4 \cdot 10^{-4}$	1277	47.7(9.8)	$1.561 \pm 0.057^{+0.110}_{-0.110}$
15.0	13.0 – 16.0	$5.2 \cdot 10^{-4}$	$3.4 - 5.7 \cdot 10^{-4}$	3104	79.5(10.3)	$1.203 \pm 0.028^{+0.074}_{-0.074}$
15.0	13.0 – 16.0	$7.2 \cdot 10^{-4}$	$5.7 - 9.0 \cdot 10^{-4}$	3023	7.9(40.3)	$1.097 \pm 0.026^{+0.078}_{-0.076}$
15.0	13.0 – 16.0	$1.2 \cdot 10^{-3}$	$0.9 - 2.8 \cdot 10^{-3}$	7074	0.0(38.3)	$0.985 \pm 0.016^{+0.136}_{-0.145}$

Table 13.6: The measured  $F_2(x, Q^2)$  from the  $NVTX$  ( $EL$ ) analysis. The bin boundaries of  $x$  and  $Q^2$  at which  $F_2$  is determined are listed. The numbers of events before background subtraction as well as the estimated photoproduction background and beam-gas background (the latter in brackets) for each bin are given. An overall normalisation error of 2% is not included

$Q^2$	$Q^2$ -range	$x$	$x$ -range	events	No.BG	$F_2 \pm stat. \pm syst.$
18.0	16.0 – 20.0	$2.4 \cdot 10^{-4}$	$2.1 - 3.5 \cdot 10^{-4}$	444	31.8(10.6)	$1.514 \pm 0.094^{+0.157}_{-0.144}$
18.0	16.0 – 20.0	$5.2 \cdot 10^{-4}$	$3.5 - 6.4 \cdot 10^{-4}$	2780	55.6(10.1)	$1.382 \pm 0.035^{+0.074}_{-0.088}$
18.0	16.0 – 20.0	$7.2 \cdot 10^{-4}$	$0.6 - 1.0 \cdot 10^{-3}$	2500	7.9(29.5)	$1.190 \pm 0.031^{+0.072}_{-0.108}$
18.0	16.0 – 20.0	$1.2 \cdot 10^{-3}$	$1.0 - 1.8 \cdot 10^{-3}$	3335	0.0(29.3)	$1.074 \pm 0.025^{+0.111}_{-0.111}$
22.0	20.0 – 25.0	$3.8 \cdot 10^{-4}$	$2.7 - 4.3 \cdot 10^{-4}$	449	15.9(0.0)	$1.646 \pm 0.099^{+0.067}_{-0.152}$
22.0	20.0 – 25.0	$5.2 \cdot 10^{-4}$	$4.3 - 6.2 \cdot 10^{-4}$	1313	7.9(8.7)	$1.420 \pm 0.049^{+0.048}_{-0.094}$
22.0	20.0 – 25.0	$7.2 \cdot 10^{-4}$	$6.2 - 9.0 \cdot 10^{-4}$	1430	0.0(19.7)	$1.256 \pm 0.043^{+0.082}_{-0.085}$
22.0	20.0 – 25.0	$1.2 \cdot 10^{-3}$	$0.9 - 1.5 \cdot 10^{-3}$	2095	0.0(22.6)	$1.105 \pm 0.030^{+0.089}_{-0.089}$
22.0	20.0 – 25.0	$1.9 \cdot 10^{-3}$	$1.5 - 3.0 \cdot 10^{-3}$	2727	0.0(0.0)	$0.956 \pm 0.023^{+0.133}_{-0.133}$
27.0	25.0 – 32.0	$3.8 \cdot 10^{-4}$	$3.2 - 5.1 \cdot 10^{-4}$	258	31.8(0.0)	$1.448 \pm 0.144^{+0.222}_{-0.220}$
27.0	25.0 – 32.0	$7.2 \cdot 10^{-4}$	$5.1 - 7.6 \cdot 10^{-4}$	1652	55.6(10.4)	$1.398 \pm 0.043^{+0.069}_{-0.060}$
27.0	25.0 – 32.0	$9.0 \cdot 10^{-4}$	$0.8 - 1.1 \cdot 10^{-3}$	1393	15.9(0.0)	$1.271 \pm 0.042^{+0.084}_{-0.066}$
27.0	25.0 – 32.0	$1.5 \cdot 10^{-3}$	$1.1 - 1.9 \cdot 10^{-3}$	1833	0.0(19.8)	$1.145 \pm 0.034^{+0.098}_{-0.133}$
27.0	25.0 – 32.0	$3.2 \cdot 10^{-3}$	$1.9 - 5.7 \cdot 10^{-3}$	3205	7.9(31.9)	$0.871 \pm 0.019^{+0.122}_{-0.140}$
35.0	32.0 – 40.0	$5.2 \cdot 10^{-4}$	$4.6 - 7.0 \cdot 10^{-4}$	419	0.0(0.0)	$1.682 \pm 0.102^{+0.073}_{-0.073}$
35.0	32.0 – 40.0	$9.0 \cdot 10^{-4}$	$0.7 - 1.1 \cdot 10^{-3}$	1489	39.7(9.8)	$1.321 \pm 0.043^{+0.086}_{-0.082}$
35.0	32.0 – 40.0	$1.5 \cdot 10^{-3}$	$1.1 - 1.7 \cdot 10^{-3}$	1378	0.0(10.5)	$1.204 \pm 0.041^{+0.088}_{-0.088}$
35.0	32.0 – 40.0	$1.9 \cdot 10^{-3}$	$1.7 - 2.8 \cdot 10^{-3}$	1266	0.0(0.0)	$1.032 \pm 0.036^{+0.057}_{-0.141}$
35.0	32.0 – 40.0	$3.2 \cdot 10^{-3}$	$2.8 - 5.2 \cdot 10^{-3}$	1467	0.0(0.0)	$1.031 \pm 0.034^{+0.082}_{-0.107}$
45.0	40.0 – 50.0	$7.2 \cdot 10^{-4}$	$5.7 - 9.0 \cdot 10^{-4}$	438	15.9(0.0)	$1.567 \pm 0.094^{+0.163}_{-0.163}$
45.0	40.0 – 50.0	$1.2 \cdot 10^{-3}$	$0.9 - 1.3 \cdot 10^{-3}$	1120	7.9(0.0)	$1.414 \pm 0.056^{+0.053}_{-0.059}$
45.0	40.0 – 50.0	$1.5 \cdot 10^{-3}$	$1.3 - 2.0 \cdot 10^{-3}$	1286	0.0(0.0)	$1.221 \pm 0.042^{+0.076}_{-0.076}$
45.0	40.0 – 50.0	$2.4 \cdot 10^{-3}$	$2.0 - 3.0 \cdot 10^{-3}$	1083	0.0(0.0)	$1.082 \pm 0.041^{+0.083}_{-0.083}$
45.0	40.0 – 50.0	$3.2 \cdot 10^{-3}$	$3.0 - 4.8 \cdot 10^{-3}$	1080	0.0(10.1)	$0.936 \pm 0.035^{+0.083}_{-0.107}$
60.0	50.0 – 65.0	$9.0 \cdot 10^{-4}$	$0.7 - 1.1 \cdot 10^{-3}$	327	0.0(0.0)	$1.604 \pm 0.122^{+0.078}_{-0.078}$
60.0	50.0 – 65.0	$1.5 \cdot 10^{-3}$	$1.1 - 1.7 \cdot 10^{-3}$	1128	39.7(0.0)	$1.253 \pm 0.046^{+0.058}_{-0.058}$
60.0	50.0 – 65.0	$1.9 \cdot 10^{-3}$	$1.7 - 2.8 \cdot 10^{-3}$	1471	0.0(0.0)	$1.223 \pm 0.040^{+0.070}_{-0.113}$
60.0	50.0 – 65.0	$3.2 \cdot 10^{-3}$	$2.8 - 5.5 \cdot 10^{-3}$	1876	0.0(9.3)	$1.089 \pm 0.032^{+0.046}_{-0.056}$
70.0	65.0 – 85.0	$1.5 \cdot 10^{-3}$	$0.9 - 1.7 \cdot 10^{-3}$	587	15.9(0.0)	$1.320 \pm 0.068^{+0.067}_{-0.067}$
70.0	65.0 – 85.0	$1.9 \cdot 10^{-3}$	$1.7 - 2.8 \cdot 10^{-3}$	1118	7.9(10.2)	$1.244 \pm 0.047^{+0.054}_{-0.054}$
70.0	65.0 – 85.0	$3.2 \cdot 10^{-3}$	$2.8 - 4.5 \cdot 10^{-3}$	1080	0.0(20.3)	$1.022 \pm 0.039^{+0.112}_{-0.067}$
70.0	65.0 – 85.0	$5.4 \cdot 10^{-3}$	$4.5 - 7.0 \cdot 10^{-3}$	923	0.0(10.9)	$0.868 \pm 0.036^{+0.067}_{-0.067}$
70.0	65.0 – 85.0	$1.2 \cdot 10^{-2}$	$0.7 - 1.6 \cdot 10^{-2}$	1575	0.0(0.0)	$0.726 \pm 0.028^{+0.110}_{-0.110}$
90.0	85.0 – 110.0	$1.5 \cdot 10^{-3}$	$1.2 - 1.8 \cdot 10^{-3}$	162	0.0(0.0)	$1.457 \pm 0.143^{+0.199}_{-0.199}$
90.0	85.0 – 110.0	$1.9 \cdot 10^{-3}$	$1.8 - 2.8 \cdot 10^{-3}$	666	0.0(10.3)	$1.371 \pm 0.068^{+0.057}_{-0.057}$
90.0	85.0 – 110.0	$3.2 \cdot 10^{-3}$	$2.8 - 4.5 \cdot 10^{-3}$	757	0.0(10.2)	$1.069 \pm 0.049^{+0.048}_{-0.048}$
90.0	85.0 – 110.0	$5.4 \cdot 10^{-3}$	$4.5 - 7.0 \cdot 10^{-3}$	755	0.0(0.0)	$0.957 \pm 0.044^{+0.081}_{-0.081}$
90.0	85.0 – 110.0	$1.2 \cdot 10^{-2}$	$0.7 - 1.6 \cdot 10^{-2}$	1242	0.0(9.2)	$0.746 \pm 0.027^{+0.092}_{-0.092}$
120.0	110.0 – 140.0	$2.4 \cdot 10^{-3}$	$1.6 - 2.6 \cdot 10^{-3}$	273	7.9(20.1)	$1.549 \pm 0.128^{+0.163}_{-0.163}$
120.0	110.0 – 140.0	$3.2 \cdot 10^{-3}$	$2.6 - 4.4 \cdot 10^{-3}$	606	15.9(0.0)	$1.164 \pm 0.060^{+0.059}_{-0.059}$
120.0	110.0 – 140.0	$5.4 \cdot 10^{-3}$	$4.4 - 8.2 \cdot 10^{-3}$	745	0.0(30.9)	$1.040 \pm 0.049^{+0.076}_{-0.076}$
120.0	110.0 – 140.0	$1.2 \cdot 10^{-2}$	$0.8 - 2.1 \cdot 10^{-2}$	891	0.0(20.5)	$0.678 \pm 0.028^{+0.056}_{-0.056}$
150.0	140.0 – 185.0	$2.4 \cdot 10^{-3}$	$2.0 - 3.1 \cdot 10^{-3}$	142	0.0(0.0)	$1.602 \pm 0.175^{+0.090}_{-0.172}$
150.0	140.0 – 185.0	$3.2 \cdot 10^{-3}$	$3.1 - 4.8 \cdot 10^{-3}$	362	7.9(16.4)	$1.080 \pm 0.072^{+0.046}_{-0.046}$
150.0	140.0 – 185.0	$5.9 \cdot 10^{-3}$	$4.8 - 8.0 \cdot 10^{-3}$	515	0.0(30.7)	$1.003 \pm 0.058^{+0.020}_{-0.020}$
150.0	140.0 – 185.0	$1.2 \cdot 10^{-2}$	$0.8 - 1.6 \cdot 10^{-2}$	649	0.0(0.0)	$0.752 \pm 0.037^{+0.063}_{-0.063}$
150.0	140.0 – 185.0	$4.0 \cdot 10^{-2}$	$1.6 - 4.5 \cdot 10^{-2}$	631	0.0(10.4)	$0.509 \pm 0.025^{+0.061}_{-0.064}$
200.0	185.0 – 240.0	$3.2 \cdot 10^{-3}$	$2.5 - 4.0 \cdot 10^{-3}$	90	0.0(0.0)	$1.243 \pm 0.165^{+0.053}_{-0.053}$
200.0	185.0 – 240.0	$5.4 \cdot $				

$Q^2$	$Q^2$ -range	$x$	$x$ -range	evts	No.BG	$F_2 \pm stat. \pm syst.$
250.0	240.0 - 310.0	$3.7 \cdot 10^{-3}$	$3.2 - 4.8 \cdot 10^{-3}$	47	0.0(0.0)	$1.478 \pm 0.281^{+0.088}_{-0.088}$
250.0	240.0 - 310.0	$5.4 \cdot 10^{-3}$	$4.8 - 8.2 \cdot 10^{-3}$	219	0.0(0.0)	$1.181 \pm 0.102^{+0.062}_{-0.062}$
250.0	240.0 - 310.0	$1.2 \cdot 10^{-2}$	$0.8 - 1.7 \cdot 10^{-2}$	330	0.0(9.9)	$0.852 \pm 0.060^{+0.065}_{-0.065}$
250.0	240.0 - 310.0	$4.0 \cdot 10^{-2}$	$1.7 - 4.4 \cdot 10^{-2}$	310	0.0(9.8)	$0.442 \pm 0.031^{+0.053}_{-0.053}$
350.0	310.0 - 410.0	$5.4 \cdot 10^{-3}$	$4.2 - 6.5 \cdot 10^{-3}$	75	0.0(0.0)	$1.457 \pm 0.223^{+0.074}_{-0.138}$
350.0	310.0 - 410.0	$9.0 \cdot 10^{-3}$	$0.7 - 1.2 \cdot 10^{-2}$	207	0.0(9.8)	$0.913 \pm 0.082^{+0.131}_{-0.082}$
350.0	310.0 - 410.0	$2.1 \cdot 10^{-2}$	$1.2 - 3.1 \cdot 10^{-2}$	316	0.0(18.9)	$0.605 \pm 0.043^{+0.040}_{-0.040}$
350.0	310.0 - 410.0	$4.0 \cdot 10^{-2}$	$3.1 - 9.0 \cdot 10^{-2}$	173	0.0(0.0)	$0.428 \pm 0.039^{+0.020}_{-0.039}$
450.0	410.0 - 530.0	$7.3 \cdot 10^{-3}$	$5.0 - 8.8 \cdot 10^{-3}$	67	0.0(0.0)	$1.586 \pm 0.267^{+0.109}_{-0.320}$
450.0	410.0 - 530.0	$1.2 \cdot 10^{-2}$	$0.9 - 1.6 \cdot 10^{-2}$	144	0.0(0.0)	$1.083 \pm 0.119^{+0.071}_{-0.088}$
450.0	410.0 - 530.0	$2.1 \cdot 10^{-2}$	$1.6 - 3.5 \cdot 10^{-2}$	187	0.0(0.0)	$0.737 \pm 0.068^{+0.044}_{-0.044}$
450.0	410.0 - 530.0	$4.0 \cdot 10^{-2}$	$3.5 - 8.3 \cdot 10^{-2}$	137	0.0(0.0)	$0.515 \pm 0.054^{+0.087}_{-0.007}$
650.0	530.0 - 710.0	$1.2 \cdot 10^{-2}$	$0.7 - 1.3 \cdot 10^{-2}$	89	0.0(0.0)	$1.146 \pm 0.161^{+0.110}_{-0.079}$
650.0	530.0 - 710.0	$2.1 \cdot 10^{-2}$	$1.3 - 3.5 \cdot 10^{-2}$	174	0.0(32.2)	$0.638 \pm 0.066^{+0.070}_{-0.064}$
650.0	530.0 - 710.0	$4.0 \cdot 10^{-2}$	$3.5 - 8.3 \cdot 10^{-2}$	128	0.0(0.0)	$0.671 \pm 0.076^{+0.044}_{-0.116}$
800.0	710.0 - 900.0	$1.2 \cdot 10^{-2}$	$0.9 - 1.8 \cdot 10^{-2}$	62	0.0(11.3)	$0.815 \pm 0.141^{+0.135}_{-0.017}$
800.0	710.0 - 900.0	$4.0 \cdot 10^{-2}$	$1.8 - 4.5 \cdot 10^{-2}$	98	0.0(0.0)	$0.632 \pm 0.082^{+0.031}_{-0.102}$
800.0	710.0 - 900.0	$7.0 \cdot 10^{-2}$	$0.5 - 1.3 \cdot 10^{-1}$	57	0.0(10.6)	$0.254 \pm 0.042^{+0.110}_{-0.016}$
1200.0	900.0 - 1300.0	$2.1 \cdot 10^{-2}$	$1.2 - 2.6 \cdot 10^{-2}$	82	0.0(0.0)	$0.855 \pm 0.122^{+0.032}_{-0.048}$
1200.0	900.0 - 1300.0	$4.0 \cdot 10^{-2}$	$2.6 - 8.0 \cdot 10^{-2}$	92	0.0(0.0)	$0.486 \pm 0.061^{+0.029}_{-0.034}$
1200.0	900.0 - 1300.0	$1.4 \cdot 10^{-1}$	$0.8 - 2.5 \cdot 10^{-1}$	46	0.0(0.0)	$0.313 \pm 0.056^{+0.017}_{-0.043}$
1500.0	1300.0 - 1800.0	$2.1 \cdot 10^{-2}$	$1.6 - 3.6 \cdot 10^{-2}$	55	0.0(0.0)	$0.958 \pm 0.169^{+0.157}_{-0.073}$
1500.0	1300.0 - 1800.0	$4.0 \cdot 10^{-2}$	$3.6 - 8.6 \cdot 10^{-2}$	57	0.0(0.0)	$0.667 \pm 0.112^{+0.054}_{-0.061}$
1500.0	1300.0 - 1800.0	$1.4 \cdot 10^{-1}$	$0.9 - 1.9 \cdot 10^{-1}$	37	0.0(0.0)	$0.511 \pm 0.112^{+0.054}_{-0.090}$
2000.0	1800.0 - 2500.0	$4.0 \cdot 10^{-2}$	$2.3 - 4.4 \cdot 10^{-2}$	31	0.0(0.0)	$0.710 \pm 0.165^{+0.076}_{-0.020}$
2000.0	1800.0 - 2500.0	$7.0 \cdot 10^{-2}$	$0.4 - 1.2 \cdot 10^{-1}$	32	0.0(0.0)	$0.499 \pm 0.110^{+0.049}_{-0.038}$
2000.0	1800.0 - 2500.0	$1.4 \cdot 10^{-1}$	$1.2 - 2.8 \cdot 10^{-1}$	23	0.0(0.0)	$0.686 \pm 0.203^{+0.083}_{-0.238}$
3000.0	2500.0 - 3500.0	$7.0 \cdot 10^{-2}$	$3.4 - 9.0 \cdot 10^{-2}$	18	0.0(0.0)	$0.431 \pm 0.124^{+0.067}_{-0.023}$
3000.0	2500.0 - 3500.0	$1.4 \cdot 10^{-1}$	$0.9 - 2.5 \cdot 10^{-1}$	21	0.0(0.0)	$0.470 \pm 0.134^{+0.033}_{-0.106}$
5000.0	3500.0 - 15000.0	$7.0 \cdot 10^{-2}$	$0.5 - 1.1 \cdot 10^{-1}$	19	0.0(0.0)	$0.716 \pm 0.218^{+0.137}_{-0.097}$
5000.0	3500.0 - 15000.0	$1.4 \cdot 10^{-1}$	$1.1 - 3.0 \cdot 10^{-1}$	26	0.0(0.0)	$0.398 \pm 0.098^{+0.034}_{-0.034}$
5000.0	3500.0 - 15000.0	$5.0 \cdot 10^{-1}$	$0.3 - 1.0 \cdot 10^{+0}$	14	0.0(0.0)	$0.136 \pm 0.052^{+0.029}_{-0.024}$

Table 13.8:  $NVTX$ - $F_2(x, Q^2)$  (EL), continued.

$Q^2$	$Q^2$ -range	$x$	$x$ -range	No.evts	No.BG	$F_2 \pm stat. \pm syst.$
1.5	1.3 - 1.9	$3.5 \cdot 10^{-5}$	$2.8 - 5.2 \cdot 10^{-5}$	263	16.9	$0.782 \pm 0.053^{+0.095}_{-0.239}$
1.5	1.3 - 1.9	$1.2 \cdot 10^{-4}$	$0.5 - 1.6 \cdot 10^{-4}$	86	0.0	$0.581 \pm 0.065^{+0.040}_{-0.032}$
2.0	1.9 - 2.7	$6.5 \cdot 10^{-5}$	$4.0 - 9.0 \cdot 10^{-5}$	664	20.0	$0.893 \pm 0.038^{+0.067}_{-0.158}$
2.0	1.9 - 2.7	$1.2 \cdot 10^{-4}$	$0.9 - 2.0 \cdot 10^{-4}$	427	2.0	$0.693 \pm 0.036^{+0.067}_{-0.067}$
3.0	2.7 - 3.6	$6.5 \cdot 10^{-5}$	$0.6 - 1.2 \cdot 10^{-4}$	543	23.1	$1.092 \pm 0.052^{+0.107}_{-0.074}$
3.0	2.7 - 3.6	$2.0 \cdot 10^{-4}$	$1.2 - 2.3 \cdot 10^{-4}$	655	2.0	$0.926 \pm 0.041^{+0.076}_{-0.074}$
3.0	2.7 - 3.6	$4.5 \cdot 10^{-4}$	$0.2 - 1.0 \cdot 10^{-3}$	1042	0.0	$0.734 \pm 0.026^{+0.061}_{-0.075}$
4.5	3.6 - 5.0	$1.2 \cdot 10^{-4}$	$0.8 - 1.6 \cdot 10^{-4}$	436	10.1	$1.083 \pm 0.055^{+0.048}_{-0.087}$
4.5	3.6 - 5.0	$2.0 \cdot 10^{-4}$	$1.6 - 3.0 \cdot 10^{-4}$	590	1.4	$1.067 \pm 0.048^{+0.056}_{-0.083}$
4.5	3.6 - 5.0	$4.5 \cdot 10^{-4}$	$3.0 - 6.0 \cdot 10^{-4}$	670	0.0	$0.933 \pm 0.040^{+0.098}_{-0.092}$
4.5	3.6 - 5.0	$8.0 \cdot 10^{-4}$	$0.6 - 4.0 \cdot 10^{-3}$	1121	0.0	$0.802 \pm 0.026^{+0.048}_{-0.075}$
6.0	5.0 - 7.0	$1.2 \cdot 10^{-4}$	$1.1 - 1.8 \cdot 10^{-4}$	257	7.3	$1.679 \pm 0.112^{+0.120}_{-0.204}$
6.0	5.0 - 7.0	$2.0 \cdot 10^{-4}$	$1.8 - 3.2 \cdot 10^{-4}$	358	3.0	$1.069 \pm 0.061^{+0.046}_{-0.074}$
6.0	5.0 - 7.0	$4.5 \cdot 10^{-4}$	$3.2 - 5.6 \cdot 10^{-4}$	375	0.0	$0.919 \pm 0.051^{+0.094}_{-0.062}$
6.0	5.0 - 7.0	$8.0 \cdot 10^{-4}$	$0.6 - 3.0 \cdot 10^{-3}$	943	0.0	$0.835 \pm 0.029^{+0.077}_{-0.079}$
8.5	7.0 - 10.0	$2.0 \cdot 10^{-4}$	$1.5 - 3.0 \cdot 10^{-4}$	218	3.2	$1.489 \pm 0.105^{+0.095}_{-0.060}$
8.5	7.0 - 10.0	$4.5 \cdot 10^{-4}$	$3.0 - 6.0 \cdot 10^{-4}$	285	1.9	$0.933 \pm 0.058^{+0.119}_{-0.063}$
8.5	7.0 - 10.0	$8.0 \cdot 10^{-4}$	$0.6 - 1.2 \cdot 10^{-3}$	326	0.0	$0.943 \pm 0.056^{+0.068}_{-0.059}$
8.5	7.0 - 10.0	$2.6 \cdot 10^{-3}$	$1.2 - 7.0 \cdot 10^{-3}$	516	0.0	$0.675 \pm 0.031^{+0.061}_{-0.068}$
12.0	10.0 - 14.0	$4.5 \cdot 10^{-4}$	$2.5 - 6.0 \cdot 10^{-4}$	105	0.0	$1.041 \pm 0.103^{+0.081}_{-0.045}$
12.0	10.0 - 14.0	$8.0 \cdot 10^{-4}$	$0.6 - 1.2 \cdot 10^{-3}$	159	0.0	$1.037 \pm 0.085^{+0.038}_{-0.089}$
12.0	10.0 - 14.0	$2.6 \cdot 10^{-3}$	$1.2 - 5.0 \cdot 10^{-3}$	272	0.0	$0.719 \pm 0.045^{+0.085}_{-0.054}$
15.0	14.0 - 20.0	$8.0 \cdot 10^{-4}$	$0.6 - 1.5 \cdot 10^{-3}$	58	0.0	$1.210 \pm 0.161^{+0.227}_{-0.133}$
15.0	14.0 - 20.0	$2.6 \cdot 10^{-3}$	$0.2 - 1.2 \cdot 10^{-2}$	157	0.0	$0.975 \pm 0.079^{+0.070}_{-0.083}$

Table 13.9:  $F_2$ -results from the SVTX-analysis in  $(x, Q^2)$  bins. The estimated number of photoproduction background events is also tabulated. For each value of  $F_2$  the statistical and asymmetric systematic errors are given. The overall normalisation uncertainty of 3% is not included.

Q <sup>2</sup>	Q <sup>2</sup> -range	x	y-range	No.evts	No.BG	F <sub>2</sub> ± stat. ± syst.
1.5	1.2 - 1.7	4.5 · 10 <sup>-5</sup>	2.99 - 6.00 · 10 <sup>-1</sup>	194	12.3	0.745 ± 0.058 <sup>+0.081</sup> <sub>-0.286</sub>
2.0	1.7 - 2.5	1.3 · 10 <sup>-4</sup>	1.28 - 2.99 · 10 <sup>-1</sup>	334	2.0	0.656 ± 0.038 <sup>+0.095</sup> <sub>-0.059</sub>
2.0	1.7 - 2.5	4.5 · 10 <sup>-5</sup>	2.99 - 6.00 · 10 <sup>-1</sup>	591	23.7	0.910 ± 0.041 <sup>+0.058</sup> <sub>-0.177</sub>
3.0	2.5 - 3.5	4.3 · 10 <sup>-4</sup>	0.55 - 1.28 · 10 <sup>-1</sup>	672	0.0	0.708 ± 0.031 <sup>+0.086</sup> <sub>-0.063</sub>
3.0	2.5 - 3.5	1.6 · 10 <sup>-4</sup>	1.28 - 2.99 · 10 <sup>-1</sup>	973	3.0	1.013 ± 0.037 <sup>+0.053</sup> <sub>-0.073</sub>
3.0	2.5 - 3.5	8.7 · 10 <sup>-5</sup>	2.99 - 6.00 · 10 <sup>-1</sup>	614	22.9	1.053 ± 0.048 <sup>+0.082</sup> <sub>-0.067</sub>
4.5	3.5 - 5.0	4.3 · 10 <sup>-4</sup>	0.55 - 1.28 · 10 <sup>-1</sup>	933	0.0	0.999 ± 0.037 <sup>+0.094</sup> <sub>-0.121</sub>
4.5	3.5 - 5.0	2.8 · 10 <sup>-4</sup>	1.28 - 2.99 · 10 <sup>-1</sup>	826	0.7	0.961 ± 0.036 <sup>+0.055</sup> <sub>-0.047</sub>
4.5	3.5 - 5.0	0.9 · 10 <sup>-4</sup>	2.99 - 6.00 · 10 <sup>-1</sup>	514	16.1	1.240 ± 0.059 <sup>+0.063</sup> <sub>-0.174</sub>
6.0	5.0 - 7.0	0.8 · 10 <sup>-3</sup>	0.55 - 1.28 · 10 <sup>-1</sup>	572	0.0	0.839 ± 0.038 <sup>+0.103</sup> <sub>-0.081</sub>
6.0	5.0 - 7.0	2.8 · 10 <sup>-4</sup>	1.28 - 2.99 · 10 <sup>-1</sup>	543	1.3	0.989 ± 0.046 <sup>+0.054</sup> <sub>-0.061</sub>
6.0	5.0 - 7.0	1.6 · 10 <sup>-4</sup>	2.99 - 6.00 · 10 <sup>-1</sup>	412	10.3	1.546 ± 0.082 <sup>+0.078</sup> <sub>-0.181</sub>
8.5	7.0 - 10.0	1.2 · 10 <sup>-3</sup>	0.55 - 1.28 · 10 <sup>-1</sup>	382	0.0	0.839 ± 0.046 <sup>+0.081</sup> <sub>-0.077</sub>
8.5	7.0 - 10.0	4.3 · 10 <sup>-4</sup>	1.28 - 2.99 · 10 <sup>-1</sup>	355	1.3	0.985 ± 0.055 <sup>+0.096</sup> <sub>-0.039</sub>
8.5	7.0 - 10.0	1.6 · 10 <sup>-4</sup>	2.99 - 6.00 · 10 <sup>-1</sup>	223	3.7	1.544 ± 0.108 <sup>+0.098</sup> <sub>-0.070</sub>
12.0	10.0 - 14.0	1.8 · 10 <sup>-3</sup>	0.55 - 1.28 · 10 <sup>-1</sup>	193	0.0	0.836 ± 0.062 <sup>+0.087</sup> <sub>-0.054</sub>
12.0	10.0 - 14.0	8.0 · 10 <sup>-4</sup>	1.28 - 2.99 · 10 <sup>-1</sup>	169	0.0	0.937 ± 0.074 <sup>+0.048</sup> <sub>-0.065</sub>

Table 13.10: F<sub>2</sub>-results from the SVTX-analysis in (y, Q<sup>2</sup>) bins. F<sub>2</sub> is reported close to the centre of the bins and transformed into (x, Q<sup>2</sup>) for convenience. The estimated number of photoproduction background events is also tabulated. For each value of F<sub>2</sub> the statistical and asymmetric systematic errors are given. The overall normalisation uncertainty of 3% is not included.

References

Q <sup>2</sup>	Q <sup>2</sup> -range	x	x-range	No.evts	No.BG	F <sub>2</sub> ± stat. ± syst.
1.5	1.3 - 2.2	1.0 · 10 <sup>-4</sup>	0.7 - 1.5 · 10 <sup>-4</sup>	260	14.3(0.0)	0.661 ± 0.066 <sup>+0.145</sup> <sub>-0.180</sub>
1.5	1.3 - 2.2	2.1 · 10 <sup>-4</sup>	1.5 - 4.5 · 10 <sup>-4</sup>	413	4.8(10.2)	0.470 ± 0.036 <sup>+0.149</sup> <sub>-0.066</sub>
1.5	1.3 - 2.2	8.5 · 10 <sup>-4</sup>	0.4 - 1.7 · 10 <sup>-3</sup>	209	1.8(0.0)	0.386 ± 0.042 <sup>+0.069</sup> <sub>-0.030</sub>
3.0	2.2 - 3.8	2.1 · 10 <sup>-4</sup>	1.5 - 3.0 · 10 <sup>-4</sup>	349	28.3(41.2)	0.658 ± 0.055 <sup>+0.079</sup> <sub>-0.078</sub>
3.0	2.2 - 3.8	4.2 · 10 <sup>-4</sup>	3.0 - 9.0 · 10 <sup>-4</sup>	591	18.8(10.3)	0.689 ± 0.045 <sup>+0.103</sup> <sub>-0.143</sub>
3.0	2.2 - 3.8	1.7 · 10 <sup>-3</sup>	0.9 - 3.6 · 10 <sup>-3</sup>	308	7.5(0.0)	0.530 ± 0.048 <sup>+0.101</sup> <sub>-0.039</sub>
4.5	3.8 - 6.5	2.1 · 10 <sup>-4</sup>	1.5 - 3.0 · 10 <sup>-4</sup>	187	38.9(0.0)	0.806 ± 0.090 <sup>+0.168</sup> <sub>-0.093</sub>
4.5	3.8 - 6.5	4.2 · 10 <sup>-4</sup>	3.0 - 6.0 · 10 <sup>-4</sup>	262	32.2(8.1)	0.658 ± 0.062 <sup>+0.120</sup> <sub>-0.104</sub>
4.5	3.8 - 6.5	8.5 · 10 <sup>-4</sup>	0.6 - 1.8 · 10 <sup>-3</sup>	467	26.5(10.5)	0.697 ± 0.051 <sup>+0.118</sup> <sub>-0.137</sub>
4.5	3.8 - 6.5	3.4 · 10 <sup>-3</sup>	1.8 - 5.4 · 10 <sup>-3</sup>	195	8.6(0.0)	0.477 ± 0.060 <sup>+0.094</sup> <sub>-0.079</sub>
8.5	6.5 - 11.5	4.2 · 10 <sup>-4</sup>	3.0 - 6.0 · 10 <sup>-4</sup>	131	24.9(0.0)	0.868 ± 0.124 <sup>+0.139</sup> <sub>-0.191</sub>
8.5	6.5 - 11.5	8.5 · 10 <sup>-4</sup>	0.6 - 1.2 · 10 <sup>-3</sup>	178	16.5(0.0)	0.853 ± 0.104 <sup>+0.241</sup> <sub>-0.095</sub>
8.5	6.5 - 11.5	1.7 · 10 <sup>-3</sup>	1.2 - 3.6 · 10 <sup>-3</sup>	243	13.6(0.0)	0.751 ± 0.080 <sup>+0.157</sup> <sub>-0.171</sub>
15.0	11.5 - 20.0	8.5 · 10 <sup>-4</sup>	0.6 - 1.2 · 10 <sup>-3</sup>	101	13.4(0.0)	1.192 ± 0.207 <sup>+0.470</sup> <sub>-0.132</sub>
15.0	11.5 - 20.0	1.7 · 10 <sup>-3</sup>	1.2 - 2.4 · 10 <sup>-3</sup>	118	9.7(0.0)	0.886 ± 0.139 <sup>+0.208</sup> <sub>-0.052</sub>
15.0	11.5 - 20.0	4.0 · 10 <sup>-3</sup>	2.4 - 7.2 · 10 <sup>-3</sup>	132	7.3(0.0)	1.012 ± 0.162 <sup>+0.171</sup> <sub>-0.201</sub>

Table 13.11: F<sub>2</sub>-results from the ISR-analysis. The estimated number of bremsstrahlung background events is also tabulated. For each value of F<sub>2</sub> the statistical and asymmetric systematic errors are given. The overall normalisation uncertainty of 3% is not included.

## References

- [1] E. Rutherford, *Phil. Mag.* **21**, 669 (1911);  
H. Geiger and E. Marsden, *Proc. Roy. Soc.* **82**, 495 (1909).
- [2] N.F. Mott, *Proc. Roy. Soc. A* **124**, 425 (1929); *Proc. Roy. Soc. A* **135**, 429 (1932).
- [3] J. Franck and G. Hertz, *Verh. Deutschen Phys. Ges.* **16** (1914) 457.
- [4] M.N. Rosenbluth, *Phys. Rev.* **79**, 615 (1950).
- [5] R.W. McAllister and R. Hofstadter, *Phys. Rev.* **102**, 851 (1956);  
R. Hofstadter, *Rev. Mod. Phys.* **28**, 214 (1956).
- [6] M. Gell-Mann, *Phys. Rev.* **125**, 1067 (1962);  
Y. Ne'eman, *Nucl. Phys.* **26**, 222 (1961).
- [7] M. Gell-Mann, *Phys. Lett.* **8**, 214 (1964);  
G. Zweig, CERN-8192/TH 401 (1964),  
G. Zweig, CERN-8419/TH 412 (1964).
- [8] O.W. Greenberg, *Phys. Rev. Lett.* **13**, 598 (1964);  
M.Y. Han and Y. Nambu, *Phys. Rev. Lett.* **139**, 1006B (1965).
- [9] R.E. Taylor, *Phys. Rev. Lett.* **61**, 573 (1991);  
H.K. Kendall, *Phys. Rev. Lett.* **61**, 597 (1991);  
J.I. Friedmann, *Phys. Rev. Lett.* **61**, 615 (1991);
- [10] R.P. Feynman, *Phys. Rev. Lett.* **23**, 1415 (1969).
- [11] J.D. Bjorken and E.A. Paschos, *Phys. Rev.* **185**, 1975 (1969).
- [12] J. Kuti and V.F. Weisskopf, *Phys. Rev. D* **4**, 3418 (1971).
- [13] R.N. Cahn and G. Goldhaber, 'The Experimental Foundations of Particle Physics',  
Cambridge University Press (1989).
- [14] ZEUS Collab., M. Derrick et al., *Phys. Rev. Lett.* **75**, 1006 (1995).
- [15] F. Halzen and A.D. Martin, 'Quarks & Leptons', Wiley & Sons. (1984).
- [16] C.G. Callan and D. Gross, *Phys. Rev. Lett.* **22**, 156 (1969).

- [17] D.H. Perkins, 'Introduction to High Energy Physics', Addison Wesley, (1987).
- [18] Deden et al., *Nucl. Phys. B* **85**, 269 (1975).
- [19] T. Eichten et al., *Phys. Lett. B* **46**, 274 (1973).
- [20] TASSO Collab., R. Bradelik et al., *Phys. Lett. B* **86**, 243 (1979).
- [21] Y. Balitzki, L.N. Lipatov, *Phys. Rev. Lett.* **28**, 822 (1978);  
E.A. Kuraev, L.N. Lipatov, V.S. Fadin, *Phys. Rev. Lett.* **44**, 443 (1976) and  
*Phys. Rev. Lett.* **45**, 199 (1977).
- [22] Martin F. McDermott, 'An Investigation into the effects of introducing transverse momentum cutoffs on the BFKL equation', D.Phil. Thesis, Oxford University, 1995.  
M.F. McDermott and J.R. Forshaw, 'Further analysis of the BFKL equation with momentum cutoffs', DESY-96-103.
- [23] V. Fadin and L. Lipatov, DESY 96-020;  
V.S. Fadin, R. Fiore and A. Quartorolo, *Phys. Rev. D* **53**, 2729 (1996);  
V. Del Duca, *Phys. Rev. D* **54**, 989 (1996);  
G. Camici and M. Ciafaloni, DFF-250-6-96.
- [24] M. Ciafaloni, *Nucl. Phys. B* **296**, 49 (1988);  
S. Catani, F. Fiorani and G. Marchesini, *Phys. Lett. B* **234**, 339 (1990);  
*Nucl. Phys. B* **336**, 18 (1990).
- [25] J. Kwiecinski, A.D. Martin and P.J. Sutton, *Phys. Rev. D* **52**, 1445 (1995).
- [26] M.G. Ryskin and E.M. Levin, *Phys. Rep.* **189**, 267 (1990);  
A.H. Mueller, *Nucl. Phys. B* **335**, 115 (1990).
- [27] L.V. Gribov, E.M. Levin and M.G. Ryskin, *Phys. Rep.* **100**, 1 (1983),  
*Nucl. Phys. B* **188**, 155 (1981);  
A.H. Mueller and J. Qiu, *Nucl. Phys. B* **260**, 427 (1986).
- [28] F.J. Ynduráin, 'Theory of Small  $x$  Inclusive Photon Scattering',  
FTUAM 96-12, HEP-PH/9604263.
- [29] C. López, F. Barreiro and F.J. Ynduráin, 'NLO predictions for the growth of  $F_2$  at small  $x$  and comparison with experimental data',  
DESY 96-087, HEP-PH/9605395.
- [30] R. Peschanski and G. Salam, Proceedings of the Workshop on Future Physics at HERA, Hamburg, May 1996, p 110.
- [31] J. Kwieciński, 'Theoretical issues at small  $x$  physics', *J. Phys. G: Nucl. Part. Phys.* **22**, 685 (1996).

- [32] R.S. Thorne, 'A Complete Leading Order, Renormalisation-Scheme-Consistent Calculation of Small- $x$  Structure Function, Including Leading- $\ln(\frac{1}{x})$  Terms', RAL-96-065, HEP-PH/9701241.
- [33] E. Laernen et al., *Nucl. Phys. B* **392**, 162 (1993).
- [34] A.D. Martin et al., 'Consistent Treatment of Charm Evolution in Deep Inelastic Scattering', DTP/96/102, RAL-TR-96-103, HEP-PH/9612449.
- [35] H.L. Lai and W.K. Tung, 'Charm Production and Parton Distributions', MSU-HEP-61222, CTEQ-622, HEP-PH/9701256.
- [36] M. Aivazis et al., *Phys. Rev. D* **50**, 3102 (1994).
- [37] R.G. Roberts, 'The Structure of the Proton', Cambridge University Press (1990).
- [38] R.K. Ellis, W.J. Stirling and B.R. Webber, 'QCD and Collider Physics', Cambridge University Press, 1996.
- [39] A.M. Cooper-Sarkar and R.C.E. Devenish, 'Structure Functions of the Nucleon and their Interpretation', International Journal of Modern Physics A, review in preparation, 1997.
- [40] 'HERA, A proposal for a Large Electron-Proton Colliding Beam Facility at DESY', DESY HERA 81-10.
- [41] G.-A. Voss and B.H. Wiik, 'The electron-proton collider HERA', *Ann. Rev. Nucl. Part. Sci.* **44** (1994), 413-452.
- [42] ZEUS Collaboration, Status of the Detector Status Report 1993 - The Blue Book, ZEUS 93, DESY (1993).
- [43] B. Foster et al., *Nucl. Instrum. Methods A* **338**, 254 (1994).
- [44] M. Derrick et al., *Nucl. Instrum. Methods A* **309**, 77 (1991);  
A. Andresen et al., *Nucl. Instrum. Methods A* **309**, 101 (1991);  
B. Bernstein et al., *Nucl. Instrum. Methods A* **336**, 23 (1993).
- [45] J. Krüger, Habilitationsschrift, Hamburg University 1992, DESY F35-92-02.
- [46] ZEUS Collab., 'Proposal for a Small Angle Rear Tracking Detector for ZEUS', ZEUS-Note 93-016.
- [47] A. Bamberger et al., 'The Small Angle Rear Tracking Detector for ZEUS', ZEUS-Note 95-095.
- [48] H. Bethe and W. Heitler, *Proc. Roy. Soc. A* **146** (1934) 83.

- [49] J. Andruskow et al., DESY 92-066;  
K. Piotrkowski, Dissertation, DESY F35D-93-06.
- [50] 'The ZEUS Data Acquisition System', C.Youngman, DESY 92-150A.
- [51] 'The ZEUS Trigger System', W.H.Smith et al., ZEUS-Note 89-084.
- [52] Henk A.J.R.Uijterwaal, 'The Global Second Level Trigger', Ph.D. Thesis, University of Amsterdam 1992.
- [53] 'HERA: Physics, Machine and Experiments', G.Wolf, DESY 86-089.
- [54] H1 Collab., T. Ahmed et al., *Nucl. Phys. B* **419**, 477 (1994).
- [55] ZEUS Collab., M. Derrick et al., *Phys. Lett. B* **315**, 481 (1993).
- [56] ZEUS Collab., M. Derrick et al., *Z. Phys. C* **68**, 569 (1995).
- [57] HERACLES 4.4; K. Kwiatowski, H. Spiesberger and H.J. Möhring, Proceedings of the Workshop 'Physics at HERA', DESY (1992) 1294.
- [58] CDM: Y. Azimov, Y. Dokshitzer, V. Khoze, S. Troyan, *Phys. Lett. B* **165**, 147 (1985);  
G. Gustafson, *Phys. Lett. B* **175**, 453 (1986);  
G. Gustafson, U. Pettersson, *Nucl. Phys. B* **306**, 746 (1988);  
B. Anderson, G. Gustafson, L. Lönnblad, U. Pettersson, *Z. Phys. C* **43**, 625 (1989).
- [59] ARIADNE 4.0: L. Lönnblad, *Comp. Phys. Comm.* **71**, 15 (1992);  
L. Lönnblad, *Z. Phys. C* **65**, 285 (1995).
- [60] JETSET 7.4: T. Sjöstrand and M. Bergtsson, *Comp. Phys. Comm.* **43**, 367 (1987).
- [61] B. Anderson et al., *Phys. Rev.* **97**, 31 (1983).
- [62] H. Plathow-Besch, *Comp. Phys. Comm.* **75**, 396 (1993).
- [63] ZEUS Collab., The ZEUS Detector, Status Report 1993, February 1993.
- [64] ZGAN, ZEUS trigger simulation library, Els de Wolf (editor) et al.
- [65] GEANT 3.13: R. Brun, CERN DD/EE/84-1 (1987).
- [66] 'G.F. Hartner, Y. Iga, J.B. Lane, N.A. McCubbin, VCTRAK (3.06/20): Offline Output Information', ZEUS-Note 96-013.
- [67] H. Abramowicz, A. Caldwell, R. Sinkus, 'Neural Network Based Electron Identification in the ZEUS Calorimeter', DESY 95-054.  
R. Sinkus, *Nucl. Instrum. Methods A* **361**, 290 (1995).
- [68] J. Ng and W. Verkerke, 'An Overview of SRTD Analysis', ZEUS-Note 95-037.

- [69] A. Quadt, 'SRTD alignment based on rate studies & the routine ELECSHIFT', ZEUS-Note 96-002.
- [70] I. Fleck and L. Lindemann, 'Electron/positron reconstruction in the RTD and related studies using 1994 data', ZEUS-Note 95-128  
S. Mari, 'Study on alignment of CTD, RTD, SRTD with 1994 ZEUS data', ZEUS-Note 95-120.
- [71] T. Doeker, A. Frey, M. Nakao, 'Electron Position Reconstruction - Update of the ELECP0 routines', ZEUS-Note 94-123.
- [72] PYTHIA 5.7: H.-U. Bengtsson and T. Sjöstrand, *Comp. Phys. Comm.* **46**, 43 (1987);  
T. Sjöstrand, CERN TH-7112-93, (1994).
- [73] H. Abramowicz, E.M. Levin, A. Levy and U. Maor, *Phys. Lett. B* **269**, 465 (1991).
- [74] K. Piotrkowski, *Z. Phys. C* **67**, 577 (1995).
- [75] Ariane Frey, 'Messung der Protonstrukturfunktion  $F_2(x, Q^2)$  in radiativer  $ep$ -Streuung mit dem ZEUS-Detektor', Ph.D. Thesis, Bonn, 1996.
- [76] M. Vreeswijk and P. Kojman, 'On noise and  $Y_{J_B}$ ', ZEUS-Note 95-115.
- [77] J. Blitinger, 'Uranium Calorimeter Noise of 1994 Data', ZEUS-Note 95-072.
- [78] Studies by Reinhold Seifert, Ralph Sinkus, Gernard Briskin and Marcel Vreeswijk, ZEUS DIS-group.
- [79] R. Seifert, 'noise94', noise suppression routine in PHANTOM user-library, (based on [78]).
- [80] A. Caldwell et al., 'An Electron Energy Correction Method: A Preliminary Implementation and Its Effect on the  $F_2$  Measurement', ZEUS-Note 94-051.
- [81] Anna Goussiou, 'Measurement of the Proton Structure Function  $F_2$  and Extraction of the Gluon Density of the Proton at Low  $x$ , Using the ZEUS Detector at HERA', Ph.D. thesis, Wisconsin University, DESY F35D-95-13.
- [82] Christoph Amelung, 'Phasenraum-isolierte Teilchen im Endzustand tiefinelastischer  $ep$ -Reaktionen bei ZEUS', Diplom Thesis, Bonn, 1996.
- [83] F. Jacquet and A. Blondel, Proc. of the study of an  $ep$  facility for Europe, DESY 79-48 (1979), edited by U. Amaldi, p.391.
- [84] S. Bentvelsen, J. Engelen and P. Kojman, 'Reconstruction of  $(x, Q^2)$  and extraction of structure functions in neutral current scattering at HERA', Proc. Workshop on physics at HERA vol. 1(1992) 23.

- [85] M. Vreeswijk, 'Toward the Systematic Error of Hadronic Energy Corrections', Personal Note, spring 1996.
- [86] G. Briskin and A. Caldwell, 'Comparison of CAL Energy for Electrons with CTD momentum', ZEUS-Note 95-035.
- [87] U. Bassler and G. Bernardi, *Nucl. Instrum. Methods A* **361**, 197 (1995).
- [88] G. D'Agostini, 'A Multidimensional Unfolding Method Based on Bayes' Theorem', DESY 94-099;  
G. D'Agostini, 'Comments on the Bayesian Unfolding', ZEUS-Note 95-166.
- [89] W.H. Smith et al., *Nucl. Instrum. Methods A* **355**, 278 (1995).
- [90] S. Schlenstedt, EVTAK routine, PHANTOM library.
- [91] R. Sinkus, A. Quadt, DISTAKE94 routine, ZEUS DIS-group.
- [92] Krzysztof Piotrkowski and Maciej Zachara, 'Determination of the ZEUS Luminosity in 1994', ZEUS-Note 95-138.
- [93] A. Arbuzov et al., 'HECTOR 1.00, A Program for the calculation of QED, QCD and electroweak corrections to  $ep$  and  $l^\pm N$  deep inelastic neutral and charged current scattering', DESY 95-185.
- [94] M. Vreeswijk and R. Yoshida, 'Higher Order QED Radiative Correction using the PT Method for Kinematic Reconstruction of NC DIS events', ZEUS-Note 96-040.
- [95] L. Lyons, 'Statistics for Nuclear and Particle Physicists', Cambridge University Press, 1986.
- [96] EEXOTIC electron finder, Phantom user library.
- [97] LOCAL electron finder, Phantom user library.
- [98] Elec5 electron finder, Phantom user library.
- [99] K. Piotrkowski, M. Zachara, 'Determination of the ZEUS Luminosity in 1993', ZEUS-Note 94-167.
- [100] J. Kripfglanz, H.J. Möhring and H. Spiesberger; *Z. Phys. C* **40**, 501 (1991).
- [101] K. Piotrkowski, M. Zachara, 'Determination of the ZEUS Luminosity in 1994', ZEUS-Note 95-138.
- [102] M. Glück, E. Reya and A. Vogt, *Z. Phys. C* **53**, 127 (1992);  
M. Glück, E. Reya, Dortmund DO-TH 93/27 (1993);  
M. Glück, E. Reya and A. Vogt, *Phys. Lett. B* **306**, 391 (1993);  
M. Glück, E. Reya and A. Vogt, *Z. Phys. C* **67**, 433 (1995).

- [103] A. Donnachie and P.V. Landshoff, *Z. Phys. C* **61**, 139 (1994).
- [104] A. Donnachie and P.V. Landshoff, *Phys. Lett. B* **296**, 227 (1992).
- [105] P. Burrows et al., QCD: Challenges for the Future, Snowmass Conference 1996.
- [106] R.G. Roberts, private communication.
- [107] R.K. Ellis, private communication.
- [108] ZEUS- $F_2$  (1992), ZEUS Collab., M. Derrick et al., *Phys. Lett. B* **316**, 412 (1993).
- [109] ZEUS- $F_2$  (1993), ZEUS Collab., M. Derrick et al., *Z. Phys. C* **65**, 379 (1995).
- [110] ZEUS- $F_2$  (1994), ZEUS Collab., M. Derrick et al., *Z. Phys. C* **72**, 339 (1996).
- [111] L. Lindemann, talk at the ZEUS Collaboration meeting, November 1996.
- [112] ZEUS- $F_2$  (1994), ZEUS Collab., M. Derrick et al., *Z. Phys. C* **69**, 607 (1996).
- [113] ZEUS Collab., M. Derrick et al., *Z. Phys. C* **63**, 391 (1994).
- [114] H1- $F_2$  (1992), H1 Collab., I. Abt et al., *Nucl. Phys. B* **407**, 515 (1993).
- [115] H1- $F_2$  (1993), H1 Collab., T. Ahmed et al., *Nucl. Phys. B* **439**, 471 (1995).
- [116] H1- $F_2$  (1994), H1 Collab., A. Aid et al., *Nucl. Phys. B* **470**, 3 (1996).
- [117] V. Shekelyan for the H1 Collab., Proceedings of the XXVIIIth International Conference on High Energy Physics, 25.-31. July 1996, Warsaw.
- [118] ZEUS collab., M. Derrick et al., *Phys. Lett. B* **345**, 576 (1995).
- [119] ZEUS Collab., M. Derrick et al., *Phys. Lett. B* **315**, 481 (1993);  
H1 Collab., T. Ahmed et al., *Phys. Lett. B* **297**, 205 (1992).
- [120] N. Cartiglia et al., 'LPS Alignment, Calibration and Reconstruction for 1994 Data', ZEUS-Note 96-059
- [121] Emanuela Barberis, 'Measurement of the Cross Section and  $t$  Distribution in Diffractive Deep Inelastic Scattering at HERA', Ph.D. thesis, Santa Cruz, July 1996.
- [122] ZEUS Collab., M. Derrick, *Phys. Lett. B* **315**, 481 (1993).
- [123] J. A. O'Mara, 'A Determination of the gluon momentum density within the Proton and Studies of Systematic Errors and Trigger Rates for the Measurement of the Proton Structure Function,  $F_2$ ', Ph.D. thesis, Bristol 1995.
- [124] M. Vreeswijk, 'Measurement of the Structure Function  $F_2$  and the Gluon Density of the Proton.', Ph.D. thesis, Amsterdam 1996.

- [125] Martin Löwe, 'Measurement of Positron-Proton Scattering at  $Q^2 = 0.25 \text{ GeV}^2$ ', Ph.D. thesis, Hamburg 1995, DESY F35D-96-03.
- [126] Q. Zhu for the ZEUS Collaboration, Proceedings of the International Workshop on Deep Inelastic Scattering and Related Phenomena, edited by G. D'Agostini, A. Nigro (Rome, 1996).
- [127] J. Parsons for the ZEUS Collaboration, Proceedings of the XXVIIIth International Conference on High Energy Physics, 25.-31. July 1996, Warsaw.
- [128] BCDMS Collaboration, Benvenuti et al., *Phys. Lett.* **223**, 485 (1989).
- [129] NMC Collaboration, 'Measurements of the proton and deuteron structure functions,  $F_2^p$  and  $F_2^d$ , and the ratio  $\sigma(L)/\sigma(T)$ ', HEP-PH/9610231, accepted for publication in Nucl.Phys.B.
- [130] A.V. Kotwal "Proton and Deuteron Structure Functions in Muon Scattering at 470 GeV/c", presented at the XXXth Rencontres de Moriond, QCD and High Energy Interactions, March 1995, FERMILAB-Conf-95/046-Expt.;  
E665 Collaboration, M.R. Adams et al., FERMILAB-PUB-95-396-E.
- [131] SLAC  $F_2$ : L.W. Whitlow et al., *Phys. Lett. B* **282**, 475 (1992).
- [132] 'Measurement of the proton and the deuteron structure functions,  $F_2^p$  and  $F_2^d$ ', New Muon Collaboration (NMC), Physics Letters B 364 (1995) 107-115.
- [133] NMC 96, HEP-PH/9610231.
- [134] MRSD': A.D. Martin, W.J. Stirling and R.G. Roberts, *Phys. Lett. B* **306**, 145 (1993).
- [135] MRSA: A.D. Martin, W.J. Stirling and R.G. Roberts, *Phys. Rev. D* **50**, 6734 (1994).
- [136] MRSA': A.D. Martin, W.J. Stirling and R.G. Roberts, *Phys. Rev. D* **51**, 4756 (1995).
- [137] MRSR: A.D. Martin, R.G. Roberts and W.J. Stirling, 'Parton distribution: a study of the new HERA data,  $\alpha_s$ , the gluon and  $p\bar{p}$  jet production', DTP/96/44, RAL-TR-96-037.
- [138] CTEQ4: H.L. Lai et al., 'Improved Parton Distributions from Global Analysis of Recent Deep Inelastic Scattering and Inclusive Jet Data', MSUHEP-60426, CTEQ-604.
- [139] H. Abramowicz, E.M. Levin, A. Levy and U. Maor, *Phys. Lett. B* **260**, 465 (1991).

- [140] L.N. Hand, *Phys. Lett. B* **129**, 1834 (1963);  
S.D. Drell and J.D. Walecka, *Ann. Phys. (N.Y.)* **28**, 18 (1964);  
F.J. Gilman, *Phys. Rev.* **4**, 95 (1972).
- [141] B.L. Ioffe, *Phys. Lett. B* **30**, 123 (1969);  
B.L. Ioffe, V.A. Khoze and L.N. Lipatov, 'Hard Processes', North Holland (1984) p185.
- [142] ZEUS Collab., M. Derrick et al., *Phys. Lett. B* **293**, 465 (1992);  
ZEUS Collab., M. Derrick et al., *Z. Phys. C* **63**, 391 (1994).
- [143] H1 Collab., T. Ahmed et al., *Phys. Lett. B* **299**, 374 (1992);  
H1 Collab., S. Aid et al., DESY 95-162 (1995).
- [144] ZEUS Collab., M. Derrick et al., *Z. Phys. C* **59**, 231 (1993);  
ZEUS Collab., M. Derrick et al., *Phys. Lett. B* **315**, 483 (1994).
- [145] W. Buchmüller and D. Haidt, 'Double-logarithmic Scaling of the Structure Function  $F_2$  at small  $x$ ', DESY 96-061.
- [146] M. Froissart, *Phys. Rev.* **123**, 1053 (1962).
- [147] R.D. Field, 'Applications of Perturbative QCD', (Addison Wesley, New York, 1989).
- [148] V. Gribov, *Sov. Phys. JETP* **30**, 709 (1969).
- [149] J.D. Bjorken, SLAC-PUB-7096.
- [150] A. De Rújula et al., *Phys. Rev. D* **10**, 1649 (1974).
- [151] R.D. Ball and S. Forte, *Phys. Lett. B* **335**, 77 (1994);  
R.D. Ball and S. Forte, *Phys. Lett. B* **336**, 77 (1994).
- [152] S. Forte and R.D. Ball, 'Universality and Scaling in Perturbative QCD at Small  $x$ ', CERN-TH/95-323.
- [153] R.D. Ball and S. Forte, 'Determination of  $\alpha_s$  from  $F_2^p$  at HERA', CERN-TH/95-148.
- [154] CCFR Collaboration, D. Harris, talk at the XXVIII Int. Conf. on HEP, Warsaw, July 1996;  
P. Spentzoursis, talk at the DPF meeting of APS, Minnesota, August 1996.
- [155] CCFR Collaboration, A. Bazark et al., Columbia University preprint, NEVIS-1492 (1993).
- [156] NA51 Collaboration, A. Baldit et al., *Phys. Lett. B* **332**, 244 (1994).

- [157] NMC Collaboration, P. Amandruz et al., *Phys. Rev. Lett.* **66**, 2712 (1991).
- [158] G. Curcu, W. Furmanski and R. Petronzio, *Nucl. Phys. B* **175**, 27 (1980);  
W. Furmanski and R. Petronzio, *Phys. Lett. B* **97**, 437 (1980);  
E.G. Floratos, D.A. Ross and C.T. Sachrajda, *Nucl. Phys. B* **129**, 66 (1977); *Nucl. Phys. B* **139**, 545 (1978); (erratum; *Nucl. Phys. B* **152**, 493 (1979));  
A. Gonzalez-Arroyo, C. López and F.J. Ynduráin, *Nucl. Phys. B* **153**, 161 (1979);  
E.G. Floratos, R. Lacaze and C. Kounnas, *Nucl. Phys. B* **192**, 417 (1981).
- [159] W.J. Marciano, *Phys. Rev. D* **29**, 580 (1984).
- [160] G. Parisi, Proc. 11th Rencontre de Moriond, ed. J. Tran Thanhm, ed. Frontiers, 1976;  
G. Altarelli and G. Parisi, *Nucl. Phys. B* **126**, 298 (1977). G. Altarelli, *Nucl. Phys. B* **81**, 1 (1981).
- [161] V.N. Gribov and L.N. Lipatov, *Sov. J. Nucl. Phys.* **15**, 438 (1972);  
L.N. Lipatov, *Sov. J. Nucl. Phys.* **20**, 96 (1975);  
Y.L. Dokshitzer, *Sov. Phys. JETP* **46**, 641 (1977).
- [162] Particle Data Group, *Phys. Rev. D* **54**, 1 (1996).
- [163] P.Z. Quintas et al., CCFR Collaboration, *Phys. Rev. Lett.* **71**, 1307 (1993).
- [164] M. Virchaux and A. Milsztajn, *Phys. Lett. B* **274**, 221 (1992).
- [165] S. Bethke, Talk presented at the QCD Euroconference 96, Montpellier (France), PITHA 96/30.
- [166] A. DeRoeck, M. Klein and Th. Naumann, 'On the Asymptotic Behaviour of  $F_2(x, Q^2)$ ', DESY 96-063.
- [167] A.R. Clark et al., *Phys. Rev. Lett.* **45**, 1465 (1980).
- [168] EMC Collaboration, *Nucl. Phys. B* **213**, 31 (1983).
- [169] H1 Collab., C. Adloff et al., DESY-96-138.
- [170] A. Prinias, talk at the ZEUS Collaboration meeting, November 1996.